Technische Universität München
Fakultät für Elektrotechnik und Informationstechnik

# On-line Electrochemical Impedance Spectroscopy for Lithium-Ion Battery Systems

## Estimation, Compensation and Avoidance of Measurement Deviations

Diplom-Ingenieur (FH) Reinhold Koch, M. Sc.

Vollständiger Abdruck der von der Fakultät für Elektrotechnik und Informationstechnik der Technischen Universität München zur Erlangung des akademischen Grades eines Doktor-Ingenieurs genehmigten Dissertation.

Vorsitzender: Prof. Dr.-Ing. Hans-Georg Herzog

Prüfende/-r der Dissertation:
1. Prof. Dr.-Ing. Andreas Jossen
2. Prof. Dr.-Ing. Olfa Kanoun (TU Chemnitz)

Die Dissertation wurde am 23.01.2017 bei der Technischen Universität München eingereicht und durch die Fakultät für Elektrotechnik und Informationstechnik am 05.11.2017 angenommen.

# Abstract

The introduction of more electric vehicles and stationary batteries could multiply the global production of lithium-ion batteries. However, the batteries' safety and performance deterioration over their lifetime remain a concern. More sophisticated on-line measurement systems, including electrochemical impedance spectroscopy, could help address these problems.

Outside ideal laboratory conditions, electrochemical impedance spectroscopy is prone to systematic measurement deviations coming from two main sources: the cell itself and the measurement system. A high excitation amplitude improves the signal-to-noise ratio, but at the same time causes the battery to respond in a non-linear, non-stationary way. In this thesis, the deviations depending on the excitation amplitude were analyzed and an equation was derived, with which the prospective measurement deviation can be determined on an embedded controller before the measurement is taken. The calculations are mainly based on previous impedance measurements. The cause of these deviations are grouped into four categories: non-stationarity (1) of the State-of-Charge, (2) of the temperature, (3) of the Open-Circuit-Voltage and (4) non-linearity of the impedance towards the applied current. The change of the State-of-Charge causes an additional signal in the second harmonic, which is relevant for multi-sine measurements. This thesis shows, that the temperature change can be estimated from the real part of the impedance from high frequencies down to constant charge/discharge currents. The change in Open-Circuit-Voltage only introduces a deviation for the imaginary part and is independent from the excitation amplitude. Different methods to measure non-linearity are analyzed and measurements with the developed Microcycle-Impedance method are shown for the real and imaginary part of a cylindrical Lithium Iron Phosphate ($LiFePO_4$) cell. The non-linearity, described by the Butler-Volmer equation is the most critical contributor to the overall deviation for measurement deviations that come from the cell itself. But at low frequencies ($\leq 10\,\mathrm{mHz}$), the temperature increase from impedance heating also contributes a significant part to the overall deviation.

Drifts in the voltage response can make the measured impedance unusable. Different drift correction methods are compared against each other and a new one is presented in the frequency-domain. The most important types of voltage drifts are the linear and the exponential drifts. The presented new approach in the frequency-domain can correct both without the need to identify which type of drift is present. At high frequencies below the x-axis in the Nyquist plot, the real part of the impedance increases. Thus, the Nyquist curve looks like as it has been 'twisted' counter-clockwise. This effect, often referred to as the skin effect, was attributed to the parasitic shunt inductance. The excitation current of an on-line electrochemical impedance spectroscopy needs to be generated by already existing switched-mode power electronic converters in order to reduce costs. These converters cause harmonics, which can alias into the measurement frequency bandwidth and cause distortions. A distortion-free measurement frequency grid has been developed and proposed to avoid these distortions. The only downside of this grid is that for high frequencies, the measurement time needs to be increased by several measurement periods.

# Kurzfassung

Die Verbreitung von Elektrofahrzeugen und die Nutzung von stationären Speichern haben das Potenzial, die weltweite Produktion von Lithium-Ionen-Batterien zu vervielfachen. Die Alterung und die Sicherheit dieser Energiespeicher sorgen bei dieser Entwicklung für Beunruhigung. Bessere Messverfahren, wie die elektrochemische Impedanzspektroskopie welche regelmäßig während der Benutzung oder in Pausenzeiten durchgeführt werden, könnten dazu beitragen diese Probleme zu lösen.

Außerhalb von idealen Laborbedingungen ist sie allerdings mehreren systematischen Messabweichungen ausgesetzt, welche hauptsächlich aus zwei Quellen stammen: von der Batteriezelle selbst und vom Messsystem. Eine hohe Anregungsamplitude verbessert den Störspannungsabstand, führt aber gleichzeitig dazu, dass die Batterie den linearen, stationären Bereich verlässt. Die Messabweichungen abhängig von der Anregungsamplitude wurden analysiert und eine Gleichung aufgestellt, welche erlaubt, die voraussichtliche Abweichung bereits vor der eigentlichen Messung zu bestimmen. Die Berechnungen basieren zum größten Teil auf vorangegangenen Impedanzmessungen. Die Ursache der Abweichungen können in vier Kategorien eingeteilt werden: Verletzung der Stationaritätsbedingung durch (1) Veränderung des Ladezustandes, (2) der Zelltemperatur, (3) der Ruhespannung und (4) Verletzung der Linearitätsbedingung der Impedanz bezüglich der Stromamplitude. Die Änderung des Ladezustandes führt zu einer zweiten Harmonischen, was für die Anregung mit Breitbandsignalen relevant ist. Diese Arbeit zeigt, dass die Temperaturänderung über den Realteil der Impedanz über den gesamten Frequenzbereich abgeschätzt werden kann, von den hohen Frequenzen bis hin zum Konstantstrom. Die Änderung der Ruhespannung führt zu einer Messabweichung im Imaginärteil, welcher unabhängig von der Anregungsamplitude ist. Unterschiedliche Messmethoden zur Bestimmung der Nichtlinearität wurden miteinander verglichen, und die Nichtlinearität des Real- und Imaginärteils für eine zylindrische Lithium-Eisenphosphat-Zelle mit der Mikrozyklus-Impedanz Methode vermessen. Die Nichtlinearität, beschrieben mit der Butler-Volmer Gleichung, ist die kritischste Ursache für Messabweichungen, die von der Zelle selbst kommen. Bei kleinen Frequenzen ($\leq$ 10 mHz), trägt allerdings auch der Temperaturanstieg einen erheblichen Teil zur Messabweichung bei.

Eine Spannungsdrift kann eine Impedanzmessung unbrauchbar machen. Unterschiedliche Driftkorrekturen werden miteinander verglichen und eine neue, im Frequenzbereich, vorgestellt. Die wichtigsten Spannungsdriftarten sind die lineare und die exponenzielle Drift. Die neue, hier vorgestellte Methode kann beide korrigieren, ohne die Art der Drift identifizieren zu müssen. Bei hohen Frequenzen unterhalb der x-Achse in der Nyquist-Ortskurve nimmt der Realteil der Impedanz zu. Die Nyquist-Ortskurve scheint sich gegen den Uhrzeigersinn zu verdrehen. Dieser Effekt, welcher oft als “Skin Effekt” bezeichnet wird, konnte dem Einfluss der parasitären Induktivität des Stromshunts zugeordnet werden. Der Anregungsstrom einer “on-line” elektrochemischen Impedanzspektroskopie sollte aus Kostengründen möglichst von bereits vorhandenen getakteten leistungselektronischen Wandlern erzeugt werden. Diese Wandler verursachen Harmonische, deren Aliase im Bereich der Messfrequenzen stören können. Um diese Störungen zu vermeiden, wurden Regeln für ein störungsfreies Raster zur Platzierung der Messfrequenzen ausgearbeitet. Der einzige Nachteil dieses Rasters ist, dass es die Messzeit für hohe Messfrequenzen um mehrere Messperioden erhöht.

# Acknowledgement

*Carrying out this thesis and achieving the presented results has been made possible thanks to the support of various institutions and persons. The experimental work has been performed at the Campus for Research Excellence And Technological Enterprise (CREATE) in Singapore as well as at the Institute for Electrical Energy Storage (EES) Technology of the Technical University Munich.*

*Among the individuals who have contributed to this thesis I would like to thank, first of all, Professor Dr.-Ing. Andreas Jossen for his supervision of the thesis, his support and expertise. I also would like to thank all colleagues who supported me in Munich and Singapore with their knowledge and as discussion partners to test my hypotheses. I thank Patrick Osswald for the entropy measurements in this thesis recorded with the* $\delta V/\delta T$ *method and Andreas Hauser for the impedance measurement at high frequencies in figure 4.14.*

*During the time working on the doctoral thesis I supervised several Bachelor, Master and Diploma theses. Those students contributed to the success of this thesis. In particular are to mention: Sebastian Kneuer, Florian Wilde, Max Horsche, Ilya Zilberman, Christian Vergote, Patrick Dumm, Christoph Riebel and Kostadin Kotev.*

This thesis was typeset using LaTeX . It contains vector graphics created with Inkscape® version 0.91 and photos edited with GIMP® version 2.8.16. Most calculations were performed using MATLAB® version R2014a. The graphs were created using MATLAB® scripts with MATLAB2TikZ.

# Contents

**Abstract** I

**Kurzfassung** III

**1 Introduction** 1

1.1 Lifetime and Safety of Lithium-Ion Batteries 1

1.2 Crowd-sourced, Cloud-computed Battery Diagnostics 2

1.3 On-line Electrochemical Impedance Spectroscopy 2

1.4 Outline of the Thesis 4

**2 Fundamentals** 7

2.1 Lithium-ion Battery Cells 7

2.1.1 Construction and Mode of Operation 7

2.1.2 Overpotential 9

2.1.3 Entropy 12

2.1.4 State-of-Charge 14

2.2 Measurement of Inner Resistance 14

2.2.1 Current Pulses 14

2.2.2 Electrochemical Impedance Spectroscopy 16

2.2.3 Excitation Options for Electrochemical Impedance Spectroscopy 17

2.2.4 Discrete Data Analysis for Electrochemical Impedance Spectroscopy 18

2.2.5 Measurement Deviation Possibilities of the Discrete Data Analysis for Electrochemical Impedance Spectroscopy 21

**3 Excitation Amplitude Limit** 25

3.1 Measurement Deviation Caused by State-of-Charge Change 29

3.1.1 Impedance Dependency on State-of-Charge 29

3.1.2 Single-sine Measurement 29

3.1.2.1 State-of-Charge Change 29

3.1.2.2 Impedance Measurement Deviation 31

3.1.3 Multi-sine Measurement 34

3.1.3.1 State-of-Charge Change 34

3.1.3.2 Impedance Measurement Deviation 34

3.1.4 Constant Current 37

3.1.4.1 State-of-Charge Change 37

3.1.4.2 Impedance Measurement Deviation 38

3.2 Measurement Deviation Caused by Temperature Change 42

3.2.1 Impedance Temperature Dependency 43

3.2.2 Reversible Heat Generation from Sinusoidal Currents . . . . . 46
3.2.3 Irreversible Heat Generation from Sinusoidal Currents . . . . . 49
3.2.3.1 Measurement Setup . . . . . 49
3.2.3.2 Impedance as an Indicator for the Irreversible Heat Generation Rate . . 51
3.2.3.3 Impedance Measurement Deviation Caused by Alternating Part of Impedance Heating for a Single-sine Measurement . . . . . 52
3.2.4 Irreversible Heat Generation from Pulsed Currents . . . . . 55
3.2.4.1 Decomposition of Pulse Trains . . . . . 56
3.2.4.2 Irreversible Heat Generation Dependency on Pulse Frequency . . . . . 56
3.2.5 Irreversible Heat Generation from Constant Charge/Discharge Currents . . . . . 57
3.2.5.1 Time Constant of the Heat Transfer to the Cell Casing . . . . . 58
3.2.5.2 Impedance Heating . . . . . 60
3.2.5.3 Impedance Measurement Derivation Caused by Constant Current . . . 62
3.2.6 Impedance Measurement Deviation Caused by Multi-sine Measurement . . . . . 64
3.3 Measurement Deviation Caused by Open-Circuit-Voltage Displacement . . . . . 66
3.3.1 Open-Circuit-Voltage Displacement from State-of-Charge Change . . . . . 66
3.3.1.1 Open-Circuit-Voltage Displacement . . . . . 66
3.3.1.2 Impedance Measurement Deviation . . . . . 69
3.3.2 Open-Circuit-Voltage Displacement from Temperature Change . . . . . 73
3.3.2.1 Open-Circuit-Voltage Displacement . . . . . 74
3.3.2.2 Impedance Measurement Deviation . . . . . 74
3.3.3 Comparison of Measurement Deviations . . . . . 75
3.4 Measurement Deviation Caused by Impedance Non-linearity . . . . . 77
3.4.1 Double Butler-Volmer Equation . . . . . 77
3.4.2 Measurement of Non-linearity . . . . . 80
3.4.2.1 Charge/Discharge Cycles . . . . . 80
3.4.2.2 Microcycles . . . . . 81
3.4.2.3 Microcycle-Impedance . . . . . 82
3.4.2.4 Harmonics . . . . . 83
3.4.3 Magnitude of Non-linearity . . . . . 86
3.4.4 Impedance Measurement Deviation Caused by Single-sine Measurement . . . . . 91
3.4.5 Impedance Measurement Deviation Caused by Multi-sine Measurement . . . . . 94
3.4.6 Measurement Deviation from Impedance Non-linearity Caused by Constant Current . . . . . 94
3.5 Comparison of Measurement Deviation Sources . . . . . 98

**4 On-line Electrochemical Impedance Spectroscopy Measurements 105**
4.1 Drift Correction . . . . . 107
4.1.1 Time-Domain Drift Correction . . . . . 109
4.1.2 Drift Measurement Deviation Suppression by Windowing . . . . . 110
4.1.3 Drift Correction in the Frequency-Domain . . . . . 111
4.1.3.1 Linear Drift . . . . . 113
4.1.3.2 Exponential Drift . . . . . 116
4.1.4 Comparison of Correction Methods . . . . . 120
4.2 Impedance Measurement Deviation Caused by the Parasitic Current Shunt Inductance . 125
4.3 Narrowband Distortions Caused by Switched-mode Excitation . . . . . 128

4.3.1 Harmonics Caused by Switched-mode Excitation . . . . . 128
4.3.2 Impedance Measurement Deviation Caused by Narrowband Distortions . . . . . 130
4.3.3 Topologies for On-line Electrochemical Impedance Spectroscopy Implementation 133
4.3.3.1 Charger Topology . . . . . 134
4.3.3.2 Balancing Unit Topology . . . . . 137
4.3.3.3 DC-Supply Topology . . . . . 141
4.3.3.4 Comparison . . . . . 145
4.3.4 Distortion Reduction by Adjusting the DC-link Voltage . . . . . 145
4.4 Distortion-free Frequency Grid . . . . . 150
4.4.1 Process to Define Distortion-Free Grid . . . . . 150
4.4.2 Repetition of Carrier Harmonics . . . . . 151
4.4.3 Safe Lower Frequency Bandwidth . . . . . 154
4.4.4 Frequency Grid . . . . . 154
4.4.5 Example for the Distortion-Free Frequency Grid . . . . . 157

**5 Conclusion** **159**

**References** **163**

**Glossary** **173**

**Abbreviations** **177**

**Formula Symbols** **179**

**Appendix** **191**

**A Battery Cells Used** **193**
A.1 Cylindrical LFP Cell . . . . . 194
A.2 Cylindrical NMC Cell . . . . . 197
A.3 Cylindrical LCO Cell . . . . . 199
A.4 Cylindrical NCA Cell . . . . . 201
A.5 NMC Pouch Cell . . . . . 203

**B Prototype Used** **205**

**C Mathematical Lemmas** **207**
C.1 Trigonometric Identities . . . . . 207
C.2 Definite integrals . . . . . 207
C.3 Indefinite integrals . . . . . 208
C.4 Bessel Function of the First Kind . . . . . 209
C.5 Modified Bessel Function of the First Kind . . . . . 210
C.6 Imaginary Unit to the Power of a Fraction . . . . . 213

**D Mathematical Derivations for Impedance Non-linearity** **215**
D.1 Harmonics generated by Butler-Volmer equation . . . . . 215
D.2 Ratios of harmonics generated by Butler-Volmer equation . . . . . 216
D.3 Single-sine measurement . . . . . 217
D.4 Multi-sine measurement . . . . . 218

D.5 Measurement with constant current . . . . . . . . . . . . . . . . . . . . . . . . . . . . . . . . 219

**E Mathematical Derivation of Generated Harmonics by Switched Mode Excitation 221**

E.1 General Process . . . . . . . . . . . . . . . . . . . . . . . . . . . . . . . . . . . . . . . 221

E.2 Charger Topology Using DC-link adjustment . . . . . . . . . . . . . . . . . . . . . . . . . . 223

E.3 Balancing Unit Topology . . . . . . . . . . . . . . . . . . . . . . . . . . . . . . . . . . . 227

E.4 DC Supply Topology . . . . . . . . . . . . . . . . . . . . . . . . . . . . . . . . . . . . . 230

# 1 Introduction

The production and usage of lithium-ion (li-ion) batteries continues to expand [96]. The invention of the li-ion battery eased the introduction and widespread use of cell phones, it replaced, by large quantities, the usage of other types of batteries in laptops, power tools and cameras. They made new products possible, which before did not exist in that way such as the electric cigarette and the autonomous electric vacuum cleaner or mower. In transportation, the low weight of the li-ion battery made the introduction of plug-in hybrid electric vehicles and fully electric vehicles possible. Electric scooters and bikes powered by li-ion batteries created a large new market and are becoming more and more popular. The fluctuating generation of energy by renewable energy sources will make energy storage in batteries necessary in the future [109].

This increased usage of li-ion batteries is a development that should be welcomed. The new products make our life easier and create several new employment opportunities. Locally emission-free transportation, as provided by electric cars, scooters and bikes, improves our health and the quality of life in our cities. The seamless integration of renewable energy sources into the electric grid by stationary batteries will help to reduce carbon emissions and help to limit global warming.

The usage of li-ion battery packs for electric cars and stationary batteries is already gaining some ground. The potential is immense and it could multiply the worldwide production of li-ion batteries. New developments in li-ion batteries will help to pave the way for their widespread use in these applications [96; 109].

## 1.1 Lifetime and Safety of Lithium-Ion Batteries

For a continuing increase of the usage of li-ion batteries, they need to overcome certain issues. Besides the limited capacity, high costs and limited operational temperature, their deterioration over time and safety are two major concerns for the application of li-ion batteries.

The deterioration over time, or their ‘aging’, is noticeable for the user of the battery in two ways: by capacity fade and by power fade, i.e. an increase in inner resistance. However, both are to some extent intertwined [60]. Up to now, only a qualitative understanding exists of what causes li-ion batteries to age. These effects are dependent on the chemistry of the cathode and materials of the anode. A quantitative estimation of how much a certain operation pattern will deteriorate the battery is only obtained by replicating this pattern in exactly the same way in the laboratory and wait until a measurable deterioration takes place. Aging is dependent on various parameters, such as temperature, State-of-Charge (SoC), depth of discharge, and C-rate. Due to the lack of knowledge about the quantitative interrelation between these parameters, these tests require a multidimensional test plan. This means, for example, that when the aging at a new temperature is tested, it has to be tested varying all the other parameters. An interpolation from existing measurements is only valid if the already existing measurements are in close proximity. Once this matrix of measurements is obtained, it is only valid for one specific battery, which is determined by its chemistry, its electrolyte, its coating thickness of the electrodes, its mechanical construction and other battery parameters. If one of them is changed, the whole matrix needs to be redone, since the influence of this particular change on the aging is difficult to estimate.

There have been incidents of battery failures, where the battery did or could have seriously hurt humans. These incidents are rare and difficult to reproduce, even if similar batteries from the same batch are used. Usually, only little knowledge is available about the conditions of the battery before the incident.

## 1.2 Crowd-sourced, Cloud-computed Battery Diagnostics

A continuous measurement system or at least one that does measurements on a regular basis could overcome these difficulties. It could acquire measurement data from the battery and upload it to a server. Various batteries of the same type would pool their data on this server, where the data could be analyzed and compared. By doing this, the knowledge of the quantitative deterioration of this battery under various conditions would be obtained. If another battery is about to run a similar pattern as the batteries before, the prospective deterioration could be estimated.

For example, to increase grid stability, there exists the idea that electric cars could be charged during the times of the day when electricity prices are low. By doing this the car owner could save money and has an incentive to help stabilizing the grid. In general, however, charging a li-ion battery with a lower current will deteriorate it less [61]. Taking advantage of low energy prizes will always mean that the battery is not charged during a certain time interval and therefore charged with a higher current during another time interval. If deterioration is not taken into account, the car owner might end up losing more money due to wear and tear of the battery than he saves through the lower electricity prices.

If the information would exist about how much deterioration a certain charging process will cause, this could be avoided. This information could be obtained from several other batteries of the same kind, which already experienced similar charging patterns.

In case of a destructive battery failure, the data gathered on a server would not be destroyed with the battery. Moreover, that data would not be limited by a small memory of the device. Most importantly, it would be possible to compare the state of a failed battery with batteries of the same type in similar applications. By using that information, rare failures could be better understood, reconstructed or even prevented because a similar pattern is recognized.

## 1.3 On-line Electrochemical Impedance Spectroscopy

Crowd-sourced, cloud-computed battery diagnostics are only possible if measurements, which until now are restricted to the laboratory, are available on-line. This means that these measurements can be done continuously or at least in regular time intervals. It should not be necessary to take out the battery from its usual location in the application. The measurements should also be done automatically and without human intervention.

Electrochemical impedance spectroscopy (EIS) is such a measurement, which could be applied on-line and deliver valuable information about the battery. Since a battery usually does not run full cycles, the total capacity is difficult to measure. EIS measurements could serve as an additional parameter for the assessment of battery aging. Kazuhiko et al. showed in [60] a strong correlation between impedance and capacity. Wei Chou filed a patent on the utilization of this relationship for lead-acid batteries [126]. Tröltzsch et al. showed in [118] that model parameters derived from impedance measurements, such as the series resistance $R_{\Omega}$, the charge transfer resistance $R_{ct}$ and the Warburg coefficient $\sigma_W$, are a good proxy for the number of charge/discharge cycles a battery experiences. He used a combination of the evolution and Levenberg-Marquardt algorithm to extract these model parameters [23; 58]. Schranzhofer et al. [107] showed that EIS can detect an increase of the Solid-Electrolyte-Interface (SEI) layer better than any other known non-destructive measurement method. The distribution of relaxation times, can be derived from impedance spectra and isolate processes with different time constants to give a better insight into the dynamics of the battery [22; 28; 124]. Cuadras and Kanoun showed in [29] that for the battery cells they studied the modulus and phase can be used to determine the SoC. Nowadays, only the temperature of the most critical cells in a battery pack is measured because of the costs associated with measuring the temperature of all cells. EIS gives the possibility to measure temperature without any additional sensors [69; 93; 105; 114].

Even without the additional benefit of pooling the data on a server, on-line EIS could improve the state-estimation of a battery done by the battery management system (BMS) [75; 89–91]. On-line EIS could also improve the operation of a battery. It is necessary to adapt the management of the battery and the operation of the supplied system depending on the state of the battery [122]. The maximum power capability should be determined depending on the current inner resistance of the battery, especially when the battery is cold [16; 17].
Maintenance and replacement of batteries could be done dependent on the necessity and not on a regular basis, which is typically done much earlier than a battery failure can occur. On-line EIS could identify batteries of critical performance. This is especially beneficial for batteries that never run full cycles or are hardly used, such as batteries in uninterruptible power supplys (UPSs). In these cases, the current performance of the battery is difficult to determine. EIS measurements, however, can even be performed with these batteries [63].

The requirements for an on-line EIS system for li-ion battery packs are different from their laboratory counterparts. The frequency range is more limited, but should still covers several decades. The frequencies should range from 10 mHz, to monitor aging proposed by Tröltzsch et al. [118], up to 1 kHz, to measure sensor-less the cell temperature as proposed in [67; 93; 114]. The current has two boundaries. On one side, it should be large to cause a voltage response high enough to be resolved by the voltage analog-to-digital converter (ADC) available and high enough to guarantee a sufficient signal-to-noise ratio (SNR). On the other side, it should not cause the battery cell to respond in a non-linear way or cause the state of the battery to change. The boundary of linearity is commonly assumed with the 10 mV-Criterion [9], which states that the battery should not respond with a voltage amplitude higher than 10 mV. This criterion only considers the non-linearity described by the Butler-Volmer equation.

Several attempts have already been made to prove the applicability of on-line EIS. The always present noise on the power buslines was used as an excitation signal to evaluate the battery impedance by Christophersen et al. in [26; 27]. The DC/DC converter, managing the energy between a photovoltaic panel and a lead-acid battery, superimposed a sinusoidal current on the battery current to measure the impedance of the lead-acid battery [31]. A small motor controller generated pseudo-random noise in order to measure the impedance of the li-ion battery stack that supplied it [52]. The output of a switched-mode amplifier mimicked an electric vehicle charger to generate a sinusoidal current for the stimulus of an EIS measurement on a li-ion battery stack [65]. A specifically designed charger was used to estimate the state-of-health (SoH) by using EIS on a lead-acid battery. All of these EIS measurements were intended as a proof of concept. However, several ones showed quite large deviations to the reference curve the on-line EIS measurement was compared to. All of them used some kind of switched-mode excitation generation instead of an analog amplifier typically used in laboratory impedance meters.

The biggest difficulty for implementing a measurement system like on-line EIS is to achieve a reliable measurement by keeping the implementation cost low at the same time. In this thesis, the systematic measurement deviations of interest for an on-line EIS measurement are analyzed and their quantitative estimation is shown. New methods to compensate or avoid measurement deviations are introduced and, when applicable, compared to existing ones.

## 1.4 Outline of the Thesis

This thesis is separated into two main parts. The first discusses the measurement deviations introduced from the cell itself and the second from the on-line EIS implementation. Figure 1.1 gives a graphical overview of the topics and how they are related to each other.
In the fundamentals, the first part gives the theoretical background for chapter 3 and the second part for chapter 4. Chapter 3 discusses the 10 mV-Criterion and its applicability to li-ion batteries. It includes three additional effects to the impedance non-linearity: the change in SoC (section 3.1), the change of the cell temperature (section 3.2) and of the Open-Circuit-Voltage (OCV) (section 3.3). These effects cause the battery to be non-stationary. In section 3.4 it evaluates the actual impedance non-linearity of a li-ion battery cell. In summary, it will combine these four effects in section 3.5 and conclude that the 10 mV-Criterion is too strict, at least for the battery evaluated.

Chapter 4 will discuss three sources of measurement deviation, which are of specific interest for on-line EIS meters. Section 4.1 gives a summary over drift corrections and introduces a new one in the frequency-domain. Section 4.2 explains the measurement deviation caused by the parasitic current shunt inductance. This potential source of measurement deviation, applicable to all EIS meters, is particularly relevant when comparing the results of high frequency measurements between an on-line EIS meter and a laboratory impedance meter, which uses a different current shunt. Section 4.3 shows which magnitude of harmonics are generated by a switched-mode excitation for the three different topologies: Battery Charger Topology, Balancing Unit Topology and DC Supply Topology. In order to avoid these distortions, section 4.4 proposes a distortion-free frequency grid.

This thesis does not discuss measurement noise, i.e. random measurement deviations caused by a low SNR and their implications on the measurement or on the design of the on-line EIS meter. It also does not discuss long term drifts of the battery under test. One example of such a drift is the still changing impedance even after long hours of relaxation as published by Kindermann et al. in [64].

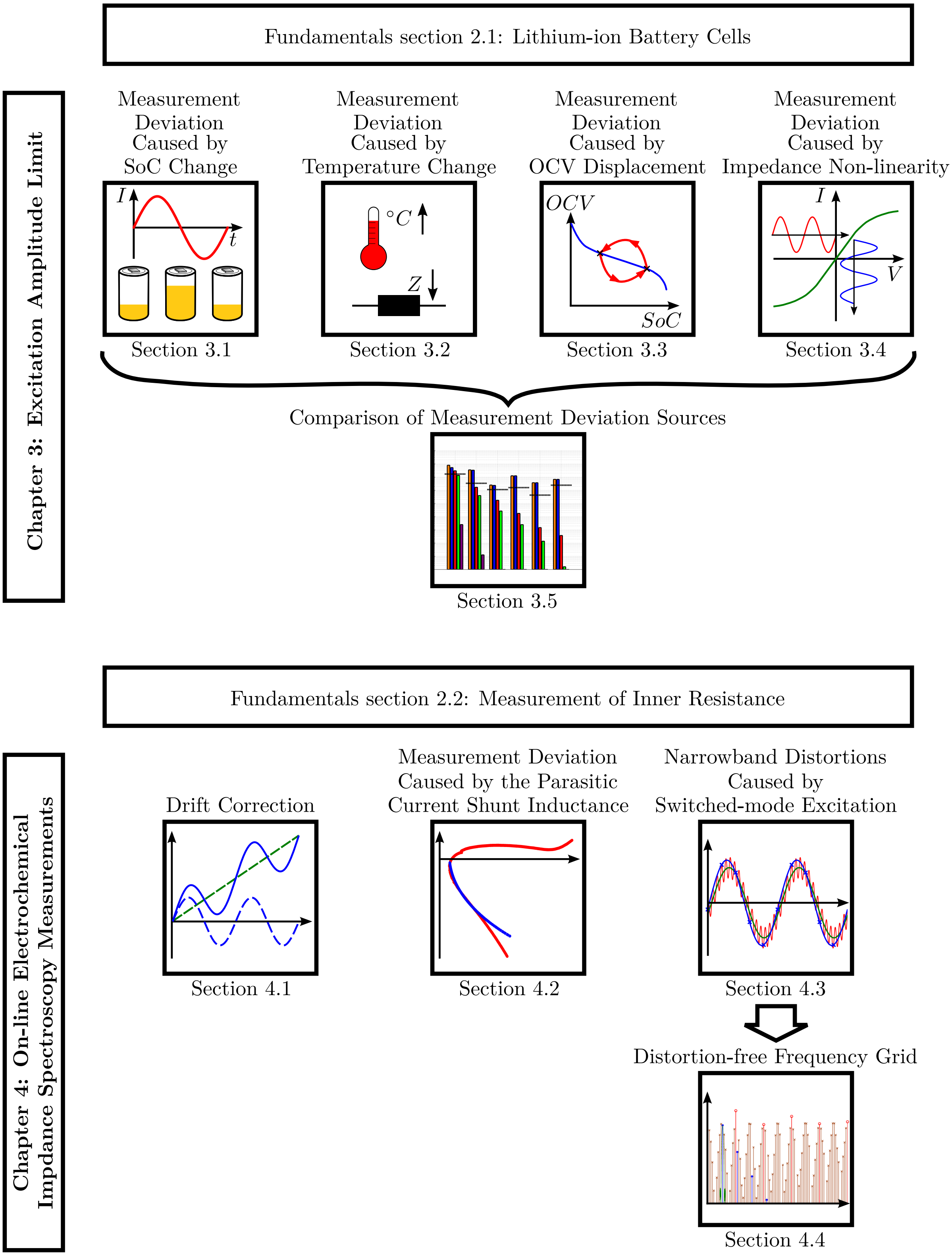

Figure 1.1: Graphical overview of the thesis.

# 2 Fundamentals

**Abstract**

*The construction of a lithium-ion battery cell determines the components of the inner resistance. The first part of this chapter introduces these components and discusses the two most critical ones responsible for the non-linearity of the inner resistance in detail: the double layer capacitance* $C_{dl}$ *and the charge transfer resistance* $R_{ct}$*. The first part concludes with introducing the entropy, two ways of measuring entropy, and the State-of-Charge of a battery cell. In this way the first part gives the fundamental understanding necessary for chapter 3 of this thesis.*

*The second part of this fundamentals chapter introduces various ways to measure the impedance of the inner resistance. Starting with the interpretation and the Linear-Time-Invariant condition for an electrochemical impedance spectroscopy measurement, going over different excitation methods and finishing with the data analysis for the calculation of the impedance. It serves as the fundamental knowledge necessary for chapter 4 of this thesis.*

## 2.1 Lithium-ion Battery Cells

### 2.1.1 Construction and Mode of Operation

A li-ion battery has two electrodes: a negative and a positive one. The electrodes consist of active material and current collectors. The negative electrode contains the li-ions before discharge. During the discharge the li-ions move into the positive one. In today's most common commercial li-ion batteries the active material of the negative electrode is made of graphite. A new active material for the negative electrode for high power applications is lithium titanate (see table 2.1).

Different chemistries can be used for the active material of the positive electrode, which are identified by three letter acronyms. The most common ones are shown in table 2.2. Between the two electrodes is a separator, which is usually made of polymer. The two electrodes and the separator are covered in liquid electrolyte. This is the medium which is necessary for the li-ion to flow. It is a liquid, consisting of an organic solvent, salt and additives. It has no water, since water would decompose into Hydrogen and Oxygen at 1.229 Volt. A li-ion battery has a voltage between 2.0 and 4.35 Volt. The exact window of operation depends on the used active materials and the cell design. A commonly used electrolyte in batteries is EC:DEC (ethylene carbonate : diethyl carbonate) or EC:DMC (ethylene carbonate : dimethyl carbonate) [57] and the most commonly dissolved salt is $LiPF_6$ [57].

The current collectors are layers of a thin conductive material, to connect the active material to an outside device. Typically aluminum is used for the positive electrode and copper is used for the negative electrode. In a cylindrical cell, the two electrodes and the separator in between are rolled up to form a jelly roll or coil. This jelly roll is then connected to the casing via connection flags.

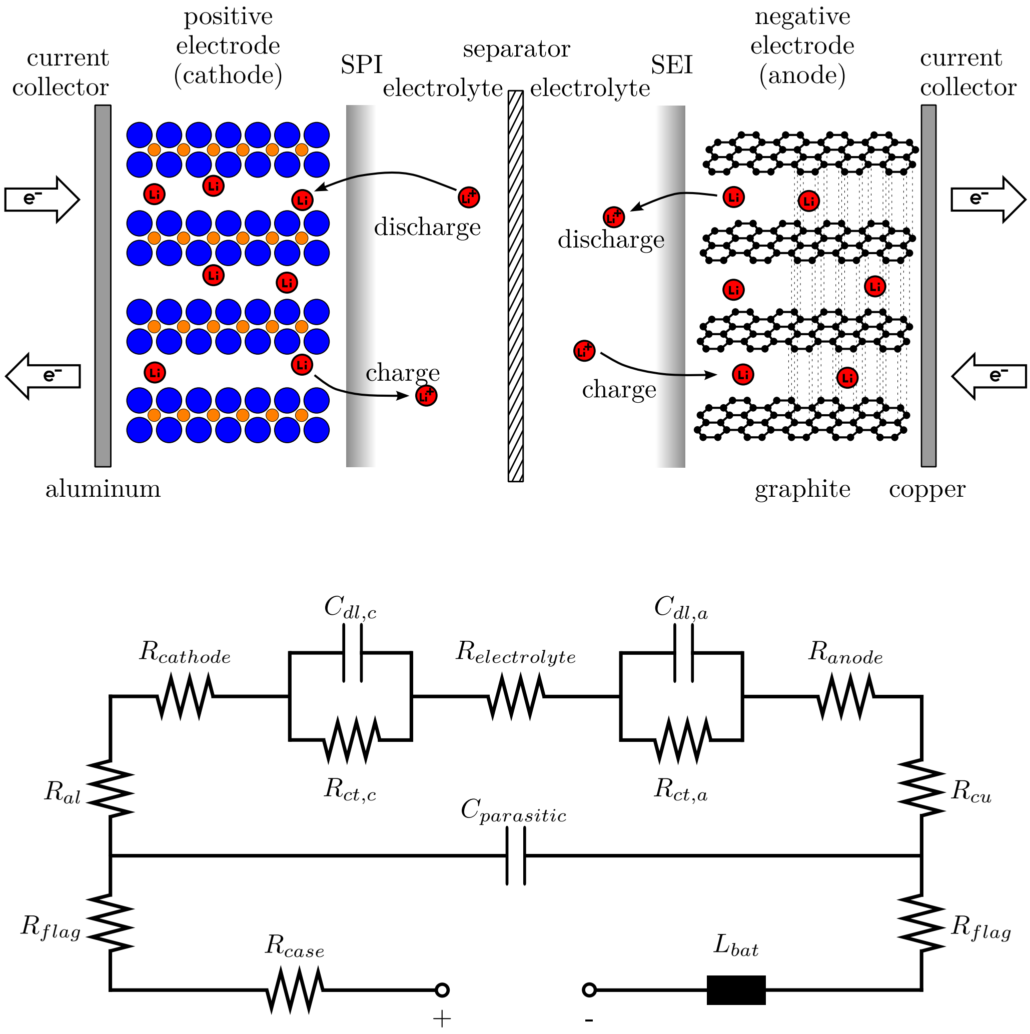

Figure 2.1: Construction of a li-ion battery cell and its equivalent electrical circuit for the inner resistance.

When the li-ions are in the negative electrode they do not react with the graphite. The graphite acts as a host lattice for the li-ions. The absorption of the li-ions by the graphite host lattice is called intercalation. During discharging, the li-ions are reduced on the positive electrode. During charging the roles are reversed.

The positive electrode is commonly called the cathode and the negative the anode. However, this nomenclature is not strictly correct. By definition the cathode is the electrode to which the positively charged li-ion move towards to. Therefore, the nomenclature is only correct when the battery cell is discharged. For charging the names would need to be reversed. Since it is commonly accepted to stick with the nomenclature which applies for the discharge case, this thesis will also do so.

The separator only lets li-ions pass through. The electrons of the lithium atom, as they are stored in

| **Acronyms** | **Description** | **Chemical formula** |
|---|---|---|
| Carbon | graphite | $C_6$ |
| LTO | lithium titanate | $Li_4Ti_5O_{12}$ |

Table 2.1: Negative electrode types, their acronyms and chemical formulas.

| **Acronyms** | **Description** | **Chemical formula** |
|---|---|---|
| LCO | lithium cobalt oxide | $LiCoO_2$ |
| LFP | lithium iron phosphate | $LiFePO_4$ |
| LMO | lithium manganese oxide | $LiMn_2O_4$ |
| NMC | lithium nickel manganese cobalt oxide | $Li(Ni_xMn_yCo_z)O_2$ |
| NCA | lithium nickel cobalt aluminum oxide | $LiNiCoAlO_2$ |

Table 2.2: Positive electrode types, their acronyms and chemical formulas.

the anode, have to move outside the battery through the device or application. In that way this device or application is powered by the battery cell.

In the first initial cycles in the life of freshly assembled li-ion battery cell, the electrolyte decomposes at the anode under the consumption of lithium. This forms an insulating layer over the anode, which is called the SEI. The electrode surface area forms a capacitor, as charge on the electrode is face to face with the ions of the electrolyte. This capacitor is called the double layer capacitor $C_{dl}$. In parallel to the double layer capacitor $C_{dl}$ the charge transfer takes place. This is the transfer from electronic condictivity to ionic conductivity which is caused by a Faraday process: This process is described by a resistance, the charge transfer resistance $R_{ct}$. In most commonly used batteries the surface layer exists twice, once on the cathode and once on the anode.

Dispersed through the whole battery cell are ohmic resistances. Starting with the ionic resistance of the electrolyte $R_{electrolyte}$, followed by the ionic and electronic resistance of the electrode material ($R_{cathode}$, $R_{anode}$), the electronic resistance of the copper and aluminium current collectors ($R_{cu}$, $R_{al}$), the resistance of the connection flags $R_{flag}$, from the jelly roll to the casing, and ending at the resistance of the casing $R_{case}$ itself [56].

Any conductor which creates a loop also creates an inductance $L_{bat}$. Creating an inductance in batteries is inevitable. Firstly, as for any electrical system, the battery needs some distance between its two poles as an insulation distance. Secondly, in the case of a cylindrical cell for a certain desired capacity, it is inevitable to put long electrodes inside the battery. Therefore, their distance is very small but their length is very long and mainly causes the inductance.

During charging and discharging the li-ions are moved from one electrode to the other. This mass transfer does not occur infinitely fast and causes additional overpotential. The Warburg resistance $Z_W$ describes this diffusion effect.

### 2.1.2 Overpotential

In order to charge the cell, a voltage higher than the current OCV of the cell has to be applied. This overpotential is the difference between the OCV of the cell and battery voltage at its terminals. It is the voltage drop over all the resistances in the cell introduced in the previous section 2.1.1.

With the exception of the charge transfer resistance $R_{ct}$, they do not change with changing current magnitudes [63]. The dependency of the overpotential on the magnitude of the current for a single electrode can be described with the Butler-Volmer equation 2.1 [80]. It consists of two terms, one for the anodic current and one for the cathodic current. Figure 2.2 shows that for higher overpotentials, one of the terms can be neglected since its impact becomes small, leading to the so-called Tafel equation

[8], which only considers one of the terms.

$$i_{ct} = \underbrace{i_0 \cdot e^{\frac{(1-\alpha)zF(V_{bat}-V_{OCV})}{RT}}}_{=i_{anode}} \underbrace{-i_0 \cdot e^{\frac{-\alpha zF(V_{bat}-V_{OCV})}{RT}}}_{=i_{cathode}} \tag{2.1}$$

With $\alpha$ being the charge transfer coefficient, $z$ the number of electrons exchanged in the electrochemical system and $F$ the Faraday constant. The two parameters that determine the shape of the Butler-Volmer curve are the charge transfer coefficient $\alpha$ and the exchange current $i_0$. The charge transfer coefficient $\alpha$ can be considered as the symmetry factor. It determines whether a reaction happens quicker in one current direction than in the other. The exchange current $i_0$ is an indicator for the general speed of the reaction and calculated according to equation 2.2 [80]

$$i_0 = z\,F\,A\,k_a^{\alpha}\,k_c^{1-\alpha}\,c_R^{\alpha}c_O^{1-\alpha} \tag{2.2}$$

This equation is usually given for the current exchange density. This is why the electrode surface $A$ was included in order to arrive at the exchange current. $k_a$ and $k_c$ are the rate constants for the anodic and cathodic current and dependent on the porosity and the tortuosity of the electrode material. $c_R$ and $c_O$ are the concentrations of the reduced and oxidized species.

The charge transfer resistance is SoC and strongly temperature dependent [56]. The temperature appears in the denominator of the exponential argument of the Butler-Volmer equation and therefore increases the resistance for higher temperature. However, the dominant effect comes from the exchange current determining rate constant. This one depends on temperature by an exponential function with the temperature in the denominator of the negative exponential argument. The Arrhenius equation 2.3 states this dependency. It makes the resistance decrease with increasing temperature.

$$k = A \cdot e^{-\frac{E_A}{RT}} \tag{2.3}$$

For very large currents the concentrations which are used in the calculation of the exchange current $i_0$ in equation 2.2 are changing. For large currents the mass transport of li-ion inside the battery is not occurring fast enough and the concentration gradient from the bulk to the electrode surface becomes noticeable.

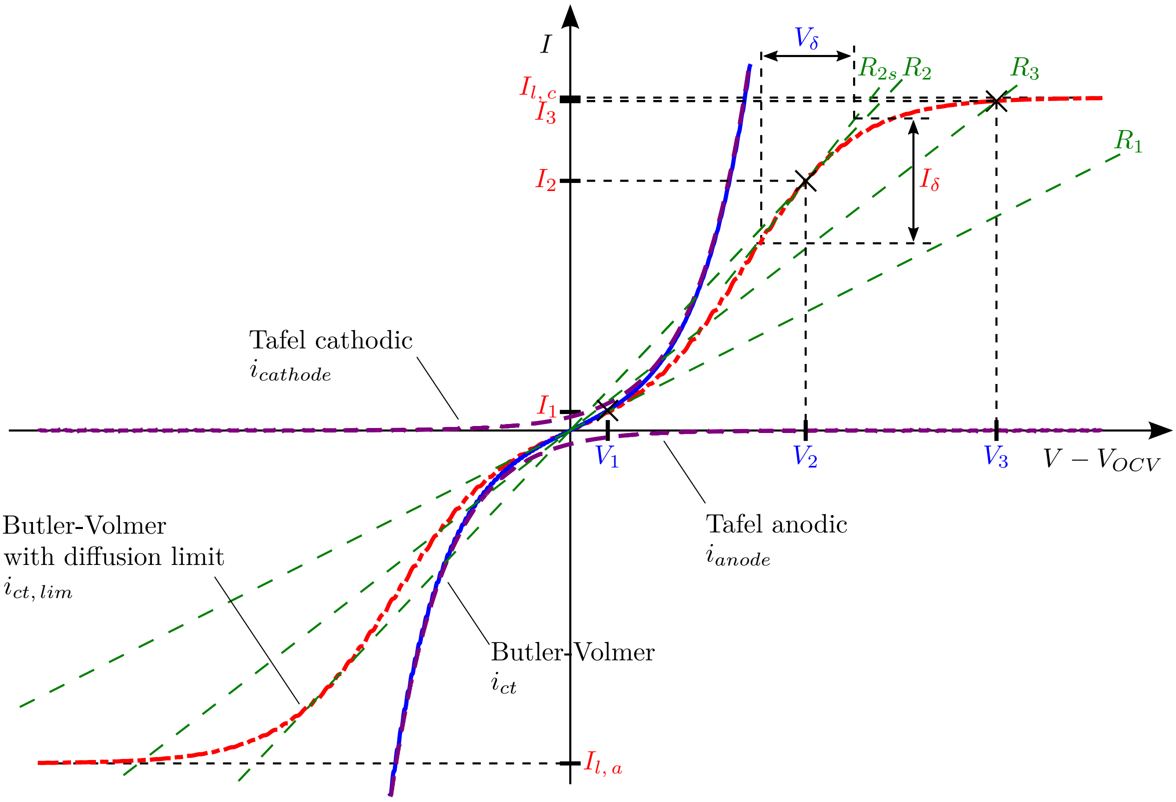

Figure 2.2: Overpotential of charge transfer reaction following a Butler-Volmer equation.

In order to accommodate for this diffusion effect, the Butler-Volmer equation needs to be modified to equation 2.4 [8; 18].

$$i_{ct,lim} = i_0 \cdot \left(1 - \frac{i}{i_{l,a}}\right) \cdot e^{\frac{(1-\alpha)zF(V_{bat}-V_{OCV})}{RT}} - i_0 \cdot \left(1 - \frac{i}{i_{l,c}}\right) \cdot e^{\frac{-\alpha zF(V_{bat}-V_{OCV})}{RT}} \tag{2.4}$$

The limiting currents $i_{l,c}$ , $i_{l,a}$ are the theoretical maximum currents when the concentration at the electrode-electrolyte interface becomes zero.
Figure 2.2 shows all four different curves, the Tafel cathodic and anodic current, the Butler-Volmer curve and the Butler-Volmer curve with diffusion limitation.

For a small current $I_1$ a relatively high overpotential $V_1$ is needed. This can be considered as the region of activation loss, similar to the one in fuel cells when operated at low current. The large signal resistance, shown by a straight line through $V_1$ and $I_1$, is therefore high (line $R_1$ is shallow). The large signal resistance for a higher current, as shown by the line through $V_2$ and $I_2$, is much smaller (line $R_2$ is steeper than line $R_1$). The small signal resistance is the resistance, which the electrochemical system would show for an incremental change in overpotential. It depends on the present operation point. In figure 2.2 the small signal resistance shown at $I_2$ and $V_2$ is with the ratio of $V_\delta$ and $I_\delta$, even smaller than the large signal resistance at that operation point (line $R_{2s}$ is steeper than line $R_2$). When the battery cell operates in the area limited by diffusion, the large signal resistance increases again as shown in figure 2.2 at $V_3$ and $I_3$ (line $R_3$ is shallower than line $R_2$). The diffusion and its associated parameter $i_{l,c}$ , $i_{l,a}$ is dependent on the SoC caused by several effects. For example, in lead acid batteries, the porosity decreases during discharge which leads to a lower diffusion [56].

### 2.1.3 Entropy

The Gibbs' free energy $G$ describes the usable electrical energy of a reaction. It is defined as the reaction enthalpy $\Delta H$ minus the reversible heat $T \cdot \Delta S$ (see equation 2.5).

$$\Delta G = \Delta H - T \cdot \Delta S \tag{2.5}$$

Equation 2.6 shows how the Gibbs' free energy $G$ is dependent on the OCV.

$$\Delta G = -zF \cdot V_{OCV} \tag{2.6}$$

Entropy can be measured in two different ways: by the OCV change for a given temperature change ($\delta V/\delta T$ method [84]) or by the reversible heat generated for a given electric charge charged and/or discharged ($Q_{rev}$ method [70], [106]). The first $\delta V/\delta T$ method takes advantage of the fact that in equation 2.5 if the SoC of a battery is held constant, the only summand which can change is $T \cdot \Delta S$. In this case a change in OCV is only dependent on the term $T \cdot \Delta S$. Figure 2.3a shows how after a temperature change $\Delta\vartheta$ the OCV adjusts to a new value. With this voltage change $\Delta V$, the entropy change $\Delta S$ can be calculated by combining equation 2.5 and equation 2.6 to equation 2.7 [30; 94].

$$\Delta S = z\,F \cdot \frac{\Delta V_{OCV}}{\Delta\vartheta} \tag{2.7}$$

With $F$ being the Faraday constant and $z$ the number of exchanged electrons. For li-ion batteries z equals 1.

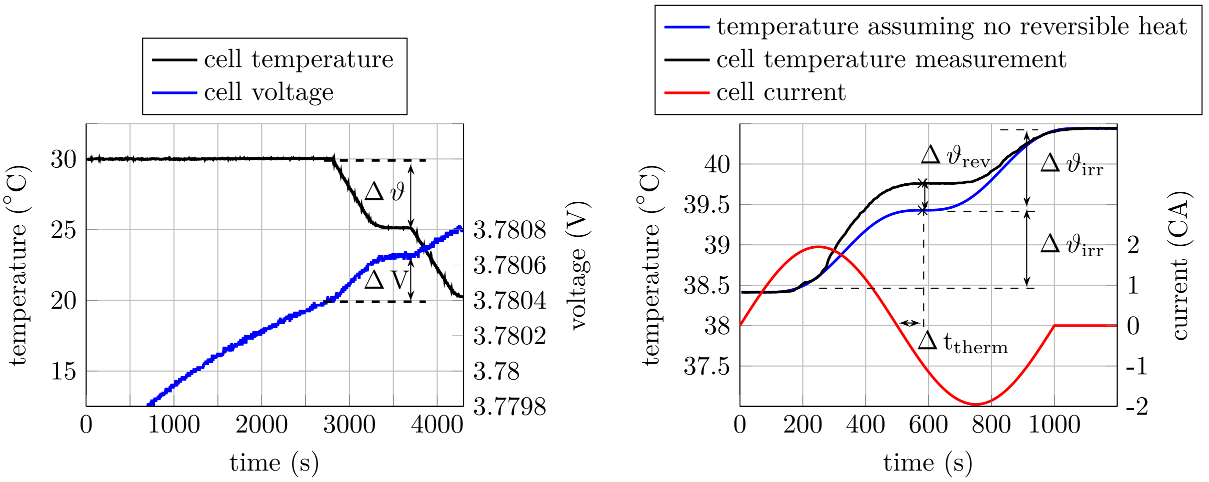

(a) $\delta V/\delta T$ method

(b) $Q_{rev}$ method

Figure 2.3: $\Delta S$ measurement methods (cylindrical NMC-cell A.2, $\hat{I}_m = 3\,\mathrm{CA}$, $SoC_{start} = 50\,\%$, $f_m = 1\,\mathrm{mHz}$)

.

The second $Q_{rev}$ method determines the reversible heat generated by the change of a certain electric charge by subtracting the irreversible heat $Q_{irr}$ from the total heat. This is best done by applying a current in the one direction and then the same current in the other direction. Figure 2.3b shows this for a sinusoidal signal applied to a battery cell in a calorimeter. The calorimeter makes sure that all the heat generated contributes to an increase of the cell temperature. The irreversible heat generated is equally large for the positive half-sine wave as it is for the negative half-sine wave. However, a difference in temperature increase can be observed. This difference is coming from the irreversible heat generated because a certain amount of electric charge passed through the battery cell during the time of the positive half-sine wave. Since only the temperature of the casing of the battery cell can be measured, a small time delay $t_{therm}$ occurs between the zero crossing of the sinusoidal current and the point at which no temperature increase is observed (see figure 2.3b). Equation 2.8 shows how the entropy can be calculated by this method.

$$\begin{aligned} \Delta Q_{rev} &= \Delta\vartheta_{rev} \cdot C_{th} \\ \Delta Q_{rev} &= \frac{T}{z\,F} \cdot \int_0^{\frac{T_m}{2}} i(t)\,\mathrm{d}t \\ \Delta S &= \Delta\vartheta_{rev} \cdot C_{th} \cdot \frac{z\,F}{T} \cdot \frac{1}{\int_0^{\frac{T_m}{2}} i(t)\,\mathrm{d}t} \end{aligned} \tag{2.8}$$

Where $C_{th}$ is the thermal capacity of the battery cell. Figure 2.4 shows that the results of both measurement methods correspond well with each other. The entropy is strongly dependent on the SoC. The comparison of the two measurement methods and the figures in this section have been presented in [70]. Schmidt et al. published a similar $Q_{rev}$ measurement method using a temperature chamber instead of a calorimeter in [106]. Murashko et al. [77] was able to use the same principle without the use of an expensive calorimeter or temperature chamber, but by using a gradient heat flux sensor at room temperature. The time needed for the two different measurement methods is about 150 minutes per SoC-point for the $\delta V/\delta T$ method [84] and 5.6 minutes per SoC-point for the $Q_{rev}$ method [106] when both methods are optimized for speed.

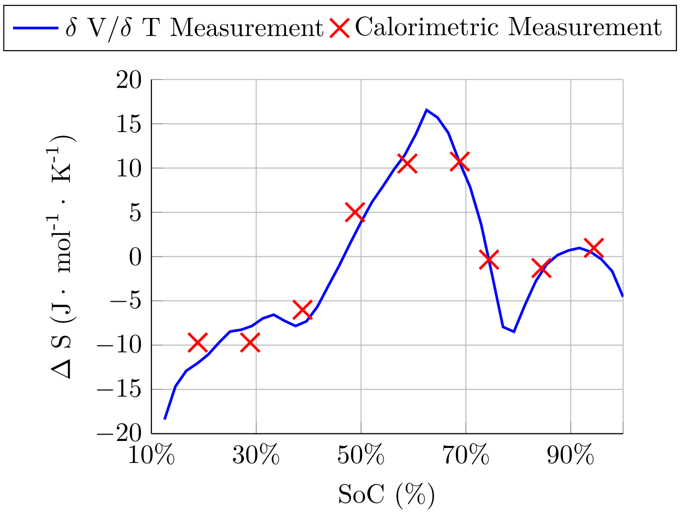

Figure 2.4: Comparison of the results of the $\delta V/\delta T$ method and the $Q_{rev}$ method with $f_m = 1\,\mathrm{mHz}$ (cylindrical Lithium Nickel Manganese Cobalt Oxide ($\mathrm{Li(Ni}_x\mathrm{Mn_yCo_z)O_2}$) (NMC)-cell A.2).

### 2.1.4 State-of-Charge

During charging and discharging, the li-ions are moving from one host structure $<Host>$ to another host structure following the general chemical equation [128]:

$$<Host> + xLi^{+} + xe^{-} <--> Li_{x}<Host> \tag{2.9}$$

x, can take values from zero to one. In practical designs the range of x is not going down to zero and stays below one. These can be translated, in case of the anode, into the SoC of a battery going from 0% to 100%. Therefore SoC corresponds to the amount of charge and not to the amount of energy available in the battery cell. However, during the change of the SoC, also the available energy, the Gibbs' free energy, of the cell changes, which corresponds to the change in OCV as shown by equation 2.6.

## 2.2 Measurement of Inner Resistance

The inner resistance of a battery determines by how much the voltage at the terminals drops if a current is drawn from the battery cell. It determines the maximum power capability of a battery, which can be drawn from it before a minimum voltage necessary for the device to operate is undercut. During charging it determines when the battery charger has to switch from constant-current (CC) to constant-voltage (CV) mode and thus significantly increases the charging time. This resistance is not constant but dependent on the current, SoC, temperature, and age of the battery cell [122]. There are various ways to measure the inner resistance. These methods differ in terms of the physical measurement method but also in terms of the data treatment of the measured voltage and current waveforms. Figure 2.5 shows the two categories of measurement methods: current pulses and electrochemical impedance spectroscopy.

### 2.2.1 Current Pulses

Current pulses can be used to study the inner resistance of a battery. The observed voltage response can be fitted to the expected response from an assumed equivalent circuit. Figure 2.5 shows this for a simple equivalent circuit with an ohmic resistance $R_{\Omega}$ and an RC-element of the double layer capacitance $C_{dl}$ and the charge transfer resistance $R_{ct}$. Their values are obtained by assuming a very quick voltage step from the ohmic resistance $R_{\Omega}$ and an exponential function from the RC-element.

Barsoukov et al. [10] and Yoon et al. [129] showed that this approach is also possible in the frequency-domain via Laplace transformation. This method uses any kind of excitation signal as long as there exists a Laplace transform for it. He fitted the voltage response not to the time-domain data but to a 'carrier-function' which he obtained by multiplying the applied current excitation function with the assumed equivalent circuit as Laplace transforms $(Z(s) \cdot I(s))$. By proposing this method he introduced a lot of versatility to the current pulse method. With his Laplace transformation method, it is easier to apply any kind of current excitation signal or assume any kind of equivalent circuit which can be described by a linear network.

It is possible to determine the impedance of at various frequencies from the fitted equivalent circuit and receive a similar result as obtained by an EIS measurement. However, Gabrielli et al. [44] showed

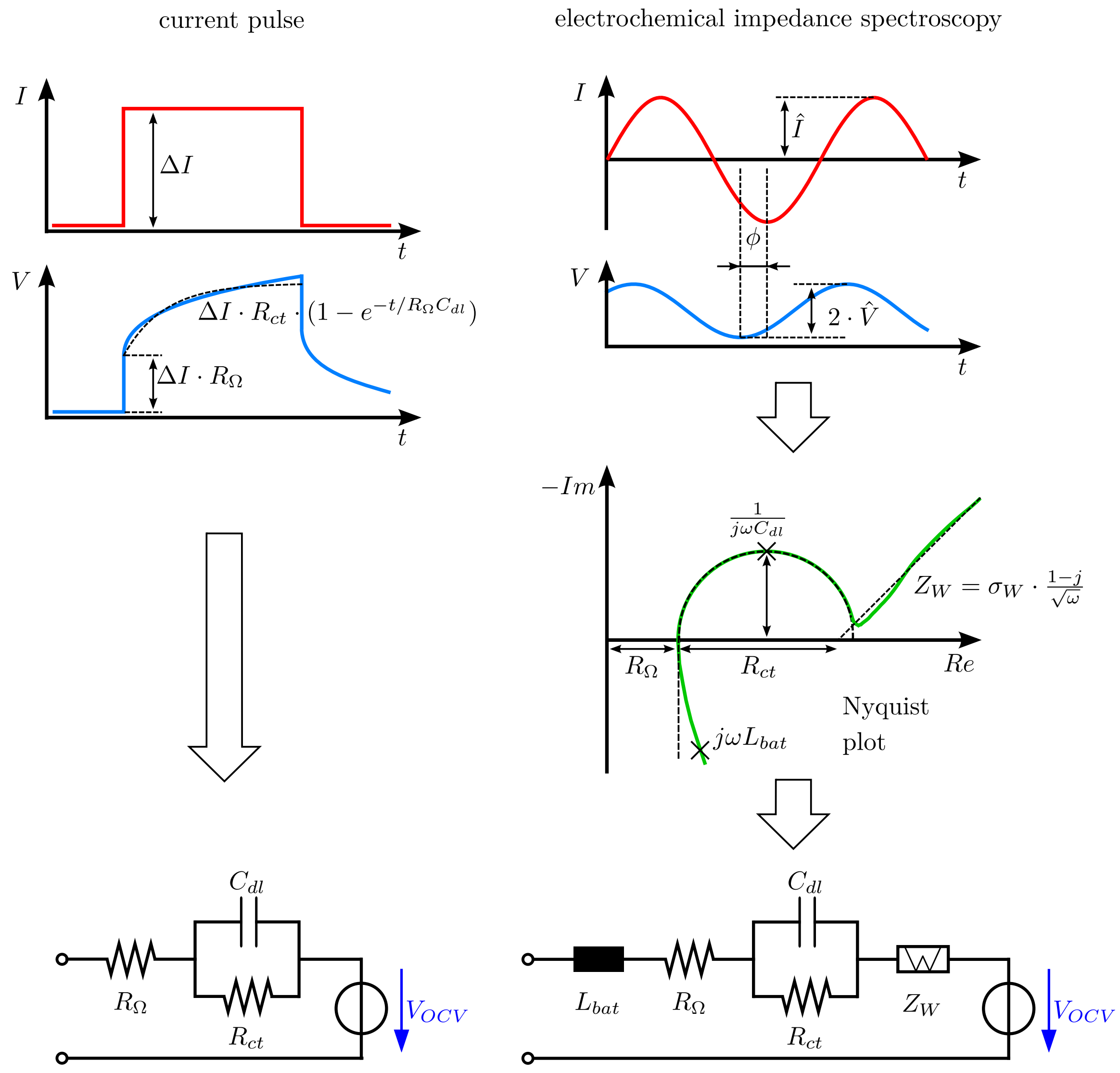

Figure 2.5: Current pulse method versus electrochemical impedance spectroscopy.

that the deviation of the identified impedance rises strongly at higher frequencies. Barsoukov et al. [10] came to the same conclusion when using the Laplace transformation method.

The fitting of the equivalent circuit to the observed voltage response, whether in time-domain or frequency-domain, is limited by how well the selected equivalent circuit does represent the inner resistance of the battery cell. It also requires in both cases a fitting algorithm which can have a long computation time. The frequency-domain method relies heavily on the correct application of the excitation signal, e.g. the current pulse. A long rise time in a current pulse, for example, would change the voltage response. The method however, still assumes an infinitely fast rise time.

Using current pulses is effective when the final outcome of the measurement should be an equivalent circuit. It is not very effective for any pattern recognition or single frequency measurement in order to monitor aging as in [63] or to measure the inner temperature of a battery cell [69; 93; 105; 114].

### 2.2.2 Electrochemical Impedance Spectroscopy

The analysis of the inner resistance at various frequencies in the frequency-domain is called electrochemical impedance spectroscopy. This measurement technique generates current excitations $I_m$ of certain frequencies $f_m$ and measures the voltage response $V_{Zm}$ (galvanostatic mode). Or it generates voltage excitations and measures the current response (potentiostatic mode). The galvanostatic mode makes sure that the SoC does not drift during the measurement, and is therefore preferred for battery cells. With the voltage and current readings, the complex impedance can be calculated as the transfer function of the battery:

$$Z_m(j\omega) = \frac{V_{Zm}(j\omega)}{I_m(j\omega)} = \frac{\hat{V}_{Zm} \cdot e^{(j\phi_V)}}{\hat{I}_m \cdot e^{(j\phi_I)}} = |Z_m| \cdot e^{j(\phi_Z)} = Z_{real} + jZ_{imag} \tag{2.10}$$

The time lag of the voltage response, as seen for the current pulse method, causes a phase delay of the voltage to the current excitation during the frequency measurement. The result is a complex impedance with a real and an imaginary part. Impedance is only defined for linear systems. Nevertheless, it can be applied to a non-linear system as a battery, if its impedance can be approximated as being linear and time-invariant (Linear-Time-Invariant (LTI) - condition). This means that the complex impedance was linear and did not change over time during the measurement, or at least was very close to linear and did almost not change over time. This is usually the case when the following conditions are met:

1. The battery is charged or discharged as little as possible during the measurement. This changes the state of charge (SOC) during the measurement and is unavoidable since the excitation current itself is charging and discharging the battery.
2. The temperature of the cell does only slightly change during the measurement. Temperature changes are unavoidable due to the excitation current itself generating heat during the measurement.
3. The Open-Circuit-Voltage does not change during the measurement. The OCV is dependent on SoC and temperature. As their change the change in OCV is unavoidable as well.
4. The inner resistance behaves linearly during the measurement. This is generally assumed if the excitation current does not cause the battery to respond with a voltage amplitude higher than 10 mV (10 mV-Criterion [9]).

All these requirements are impossible to perfectly fulfill, a detailed analysis of the measurement deviation caused by the violation of these rules is given in chapter 3.

The amplitudes of the current stimulus should be low enough in order for the battery voltage response to stay linear, but large enough to provide a sufficient signal-to-noise ratio. The frequencies of most interest for batteries are between $f_{min} = 10\,\text{mHz}$ and $f_{max} = 2\,\text{kHz}$ [9].

After measuring several frequencies, the complex impedance can be drawn in the characteristic Nyquist plot, in which -$Z_{imag}$ is plotted over $Z_{real}$ as shown in figure 2.5. From certain sections of the Nyquist plot the equivalent circuit parameters of the battery cell are derived. The inductance $L_{bat}$ of the battery cell is derived from the imaginary impedance of the high frequency measurements. The purely ohmic inner resistance $R_\Omega$ is identified at the frequency, when the imaginary part becomes zero. The values for the double layer capacitance $C_{dl}$ and the charge transfer resistance $R_{ct}$ are derived from the semicircle between the point where the imaginary part becomes zero and the local minima. For most

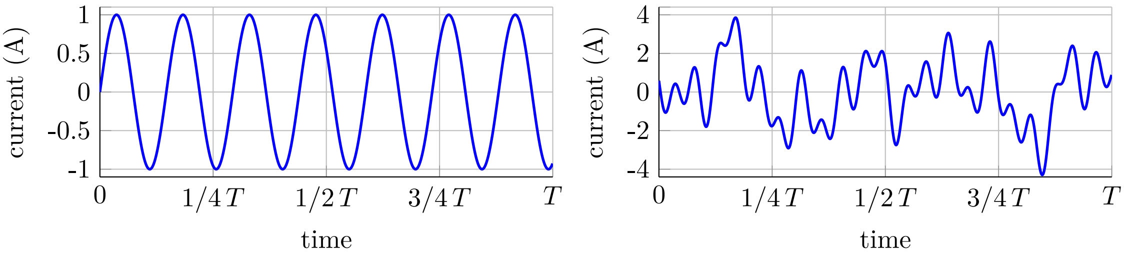

(a) single-sine measurement

(c) multi-sine measurement

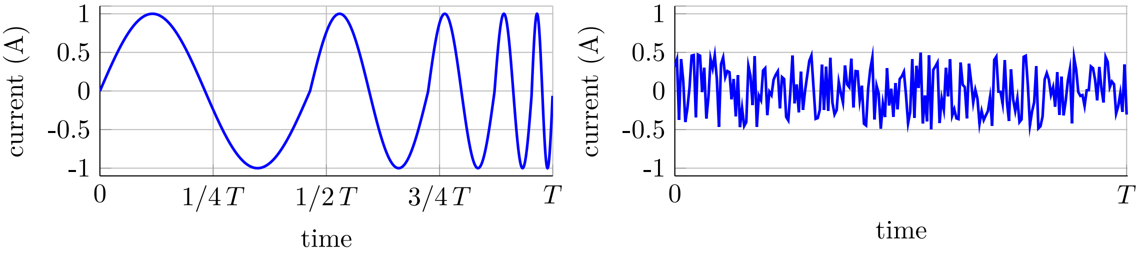

(b) sinus-sweep measurement

(d) Random Noise Excitation

Figure 2.6: Excitation Signals used for EIS measurements (synthetic data).

battery cells, however, the semicircle is usually depressed and needs to be fitted with special equivalent circuit elements or a series of RC-elements [21]. At the frequencies below the local minima the diffusion arc for low frequencies can be fitted with a Constant Phase Element (CPE) like the Warburg impedance $Z_W$. The Warburg impedance is defined by the Warburg coefficient over the square root of the angular frequency ($\sigma_W/\sqrt{\omega}$). The total transfer function of the equivalent circuit shown on the right side in figure 2.5 can be stated with:

$$Z(\omega) = R_\Omega + \frac{R_{ct}}{1+\omega^2 {C_{dl}}^2 {R_{ct}}^2} + \frac{\sigma_W}{\sqrt{\omega}} + j \cdot \left[\omega L_{bat} - \frac{\omega C_{dl} {R_{ct}}^2}{1+\omega^2 {C_{dl}}^2 {R_{ct}}^2} - \frac{\sigma_W}{\sqrt{\omega}}\right] \tag{2.11}$$

## 2.2.3 Excitation Options for Electrochemical Impedance Spectroscopy

For the excitation signal, several options are possible. Figure 2.6 gives an overview of the four dominant excitation categories. The single-sine measurement only measures one frequency. The sinus-sweep measurement applies several frequencies one after another. The inevitable transition between one frequency to another does introduce a deviation into the measurement [44]. Continuing the same trajectory of the excitation in order to keep these transition effects as small as possible, can avoid steps and its associated measurement deviations.

In order to identify the dynamics of processes inside an electrochemical device, with time constants which are magnitudes apart from each other, the measurement frequencies for EIS are logarithmically distributed according to equation 2.12.

$$f_k = \alpha_f \cdot f_{k-1}, \quad with \quad \alpha_f = e^{\left[\frac{\ln f_{max} - \ln f_{min}}{N-1}\right]} \tag{2.12}$$

Where $k$ is the index of every single frequency, $N$ is the number of frequencies to be measured, $f_{min}$ is the the minimum measurement frequency and $f_{max}$ the maximum measurement frequency. Every single frequency $f_k$ is determined by setting the first frequency to $f_{min}$ and using equation 2.12 for calculating every subsequent frequency based on the previous frequency $f_{k-1}$. The N$^{\text{th}}$ frequency $f_N$ will be equal to $f_{max}$. The single measurement periods $T_m$ form a geometric series with $\alpha_f^{-k} T_{min}$ whose sum over all measurements gives the total measurement time $T_{m,\,total}$ when only one period per frequency is applied.

$$T_{m,\,total} = T_{min} \sum_{k=0}^{N-1} \alpha_f^{-k} = T_{min} \frac{1 - \alpha_f^{-N}}{1 - \alpha_f^{-1}} \tag{2.13}$$

$T_{min}$ is the corresponding period of the minimum measurement frequency $f_{min}$ and therefore the longest period of all applied frequencies. The multi-sine measurement promises to reduce that time to only the measurement period of the lowest frequency $T_{min}$. It is a broadband signal, which tries to apply all measurement frequencies in one signal [88]. Figure 2.6 shows a signal with only five frequencies. The limit for the number of frequencies is a sufficient SNR ratio while still trying to comply with the 10 mV-Criterion. In order to comply with the 10 mV-Criterion the phase of the single frequencies are optimized to reduce the crest factor of the signal [88; 100].

Another broadband signal category is any kind of random signal. This can be a pseudo-random binary sequence, a chirp signal or simply random noise. The benefit of this kind of signal is achieving a large frequency resolution and even the simplicity of the excitation if already present noise is used [88].

### 2.2.4 Discrete Data Analysis for Electrochemical Impedance Spectroscopy

The Fourier transformation converts a signal in the time-domain into its frequency-domain representation. Equation 2.14 shows the definition for a continuous signal.

$$\mathrm{F}\{x(t)\} = X(j\omega) = \int_{-\infty}^{+\infty} x(t) \cdot e^{-j\omega \cdot t} \mathrm{d}t \tag{2.14}$$

Although it is possible to measure impedance with a fully analog circuitry, it is quite complex, inflexible and costly. The vast majority of impedance analyzers today are based on an analog-to-digital conversion of the current and voltage measurements and an analysis of the measured data by a digital processor. The main workload of the analysis is the frequency transformation of the time-domain measurement data into the frequency-domain. In this section six different methods for this transformation are presented:

1. Discrete Fourier Transformation
2. Fast Fourier Transform
3. Goertzel algorithm
4. sliding Discrete Fourier Transformation
5. sliding Goertzel algorithm
6. power spectrum of the cross-correlation

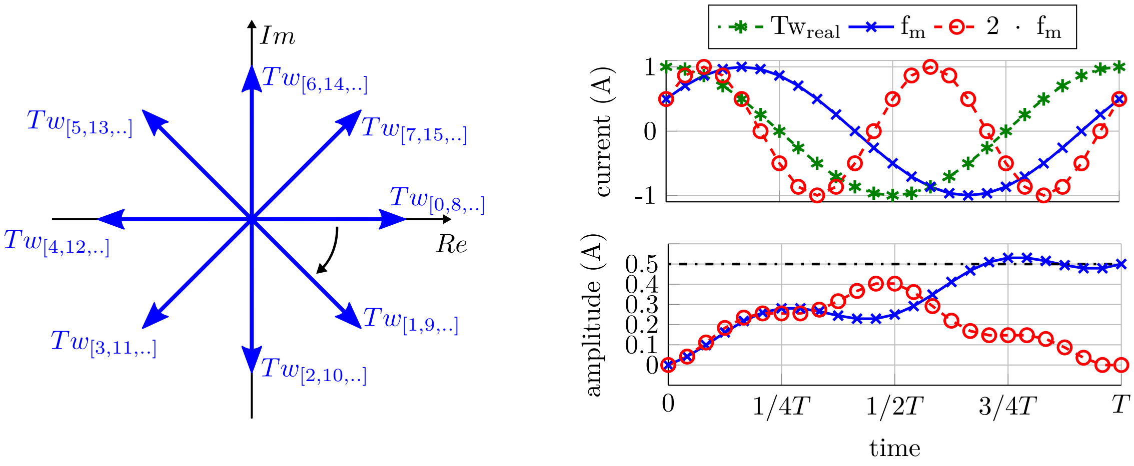

(a) Twiddle factors $Tw_{[x]} = e^{-j\cdot 2\pi/N\cdot n\cdot k}$ of the DFT for $N = 8$ (after [74]).

(b) Top: time-domain signal of the twiddle factors, a signal with the evaluated frequency, and a signal with twice the evaluated frequency. Bottom: development of the summation of both signals during a Fourier transformation.

Figure 2.7: DFT principle.

The Discrete Fourier Transformation (DFT) is the Fourier transformation for discrete signals as it is needed on an embedded controller or any other electronic computer which analyses data that had been discretized by an ADC. Equation 2.15 shows the definition of the DFT [113].

$$\mathrm{F}\{x(t)\}[k] = X_k = \sum_{n=0}^{N} x(n)\cdot e^{-j\overbrace{2\pi/N}^{\omega_0}\cdot k\cdot n}\mathrm{d}t \tag{2.15}$$

With $N$ being the maximum number of samples taken, it determines the smallest possible frequency $\omega_0$ which can be analyzed. k determines the multiple, or harmonics, of the smallest frequency which is analyzed. k can take values from 0 to $N-1$. Figure 2.7a shows the term $e^{-j2\pi/N\cdot n\cdot k}$ as a phasor which turns at the frequency $\omega_0 \cdot k$. Since the phasor does not turn continuously but only exists for discrete values, these discrete values are called twiddle factors. These twiddle factors are multiplied with the sampled datapoints. If a part of the measurement signal turns with the same speed as the twiddle factors, all of the multiplications add up, creating a very high value. If the measurement signal does not turn with the same speed some of the multiplications add up and some multiplications compensate them (see figure 2.8).

A single-sine measurement or a sinus-sweep measurement can be best analysed with a DFT or the Goertzel algorithm.

The Fast Fourier Transform (FFT) optimises the DFT by measuring several frequencies at the same time. For several frequencies some of the twiddle factor multiplications performed are the same. The FFT takes advantage of that fact and calculates intermediate results, which it then can reuse for several other intermediate results until it combines all the input sample points to the output values in the frequency-domain. There are several ways to improve either storage or processing time depending on what is more limited on the used processor [25; 92]. One of the largest drawbacks of the FFT is the strict requirement of having $N = 2^x$ sample points. If not all sample points are filled with measurement data, zero padding is applied, i.e. filling up the remaining sample points with zeros. This process leads to spectral leakage and to an inexact interpretation of the measured data. If not all frequencies are needed and the excitation frequency is known, the DFT is still quicker and should be preferred. For multi-sine measurement the FFT could be an option if it is guaranteed that all the frequencies end up finishing an integer multiple of their period at $N = 2^x$ sample points.

Gerald Gortzel [48] introduced an algorithm which allows a more efficient way to calculate the DFT in terms of computation effort. It can be described by a infinite impulse response (IIR) filter with the transfer function [54]

$$H_G(z) = \frac{1 - e^{-j2\pi k/N \cdot z^{-1}}}{1 - 2 \cdot cos(2\pi k/N) \cdot z^{-1} + z^{-2}} \tag{2.16}$$

The sliding DFT, similar to the Goertzel algorithm, is also an IIR filter with the filter transfer function [54]

$$H_{SDFT}(z) = \frac{1 - z^{-N}}{1 - e^{-j2\pi k/N \cdot z^{-1}}} \tag{2.17}$$

The sliding Goertzel algorithm is a combination of the sliding DFT and the Goertzel algorithm which creates a filter with the finite impulse response (FIR) filter transfer function [24; 54; 83]

$$H_{SG}(z) = \frac{(1 - e^{-j2\pi k/N \cdot z^{-1}})(1 - z^{-N})}{1 - 2 \cdot cos(2\pi k/N) \cdot z^{-1} + z^{-2}} \tag{2.18}$$

The ‘power spectrum of the cross-correlation’ method is best used for measurement signals with no definite frequency component. Therefore it is the method of choice for any noise signal excitation. Even if a frequency in a noise signal would be known, it could cancel itself out by shifting its phase during the measurement. To apply this method, first, the auto-correlation of the input (for galvanostatic EIS the current $i(t)$) and the cross-correlation of the input with the output need to be calculated [113].

$$r_{ii}(\tau) = \int_{-\infty}^{+\infty} i(t) \cdot i(t+\tau)\mathrm{d}t \tag{2.19}$$

$$r_{iv}(\tau) = \int_{-\infty}^{+\infty} i(t) \cdot v(t+\tau)\mathrm{d}t \tag{2.20}$$

The desired impedance is the division of the power spectrum of the cross-correlation with the one of the auto-correlation [52].

$$Z_m(j\omega) = \frac{S_{iv}(j\omega)}{S_{ii}(j\omega)} = \frac{\int_{-\infty}^{+\infty} r_{iv}(\tau) \cdot e^{-j\omega\tau}\mathrm{d}\tau}{\int_{-\infty}^{+\infty} r_{ii}(\tau) \cdot e^{-j\omega\tau}\mathrm{d}\tau} \tag{2.21}$$

For obvious reasons, the correlation has to be done for a finite amount of samples and for the calculation in a microprocessor, discrete values have to be used. Howey et al. applied this method in [52] to an on-line EIS system.

The FFT and the ‘power spectrum of the cross-correlation’ need both the whole measurement data in order to perform their calculations on it. This is a huge disadvantage for the use in an embedded system where memory, especially fast one, is scarce. All the other four methods can discard the incoming measurements once they went through their algorithm.

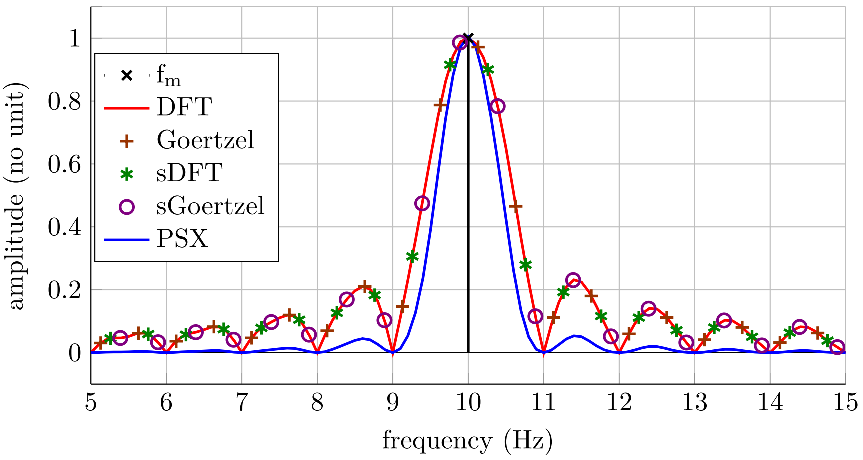

Figure 2.8: Comparison of the frequency response of the DFT (DFT), the Goertzel algorithm (Goertzel), the sliding DFT (sDFT), the sliding Goertzel algorithm (sGoertzel) and the 'power spectrum of the cross-correlation' (PSX) used with a rectangular box window ( $f_m = 10\,\mathrm{Hz}$, $T_a = 10 \cdot T_m$ ).

The Goertzel algorithm, the sliding DFT and the sliding Goertzel algorithm can lead to instabilities from rounding errors due the their recursive nature. However, the introduction and availability of controllers and processors with word lengths of 16, 32 or even 64 bits make this disadvantage hardly relevant.

The sliding DFT and the sliding Goertzel algorithm calculate for every new incoming measurement sample $x(n)$ a new value for $X_k(n)$ in the frequency-domain. In order to get the first value for the impedance calculation, $N$ samples need to have gone through these filters. The calculation for the first frequency-domain value is more time consuming than for their respective non-sliding version. But every next value comes with just another iteration step and is therefore extremely efficient when compared to the non-sliding alternative. Because of this, they are especially beneficial when used for monitoring a single impedance value. This has been done by Nevaranta et al. for monitoring a mechanical system in [79] by using the sliding DFT.

Figure 2.8 shows the frequency response of the different transformations and filters in the frequency-domain. There is no difference between the different methods in terms of frequency response, except for the 'power spectrum of the cross-correlation'. The cross- and the auto-correlation of this method multiply the excitation data with itself or the excitation with the response data. This causes the observed difference in the frequency response.

### 2.2.5 Measurement Deviation Possibilities of the Discrete Data Analysis for Electrochemical Impedance Spectroscopy

The algorithms introduced in the last section 2.2.5 are the only way to use the Fourier transformation in a real world setting, since the continuous form of the Fourier transformation demands an integration from negative infinity to positive infinity and a theoretical infinite resolution. Both requirements are impossible to implement in practice. These algorithms, therefore only assumes a finite sampling time and a finite length of recording. Both simplifications lead to the two main difficulties when applying these algorithms. The first one is Aliasing and the second one is spectral leakage.

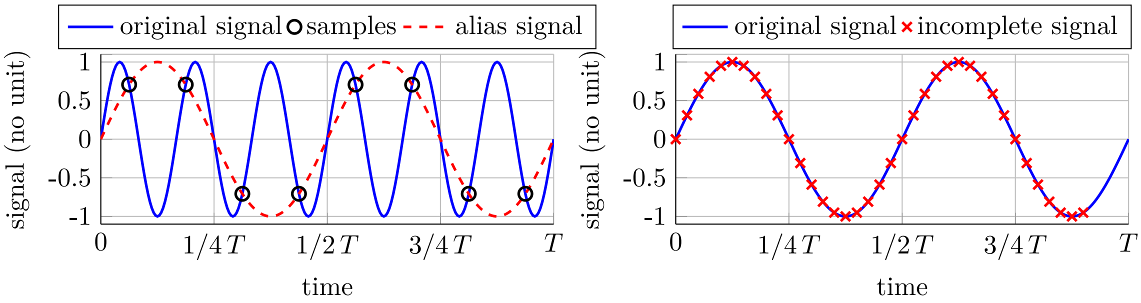

(a) Aliasing in time-domain.

(c) Spectral leakage in time-domain.

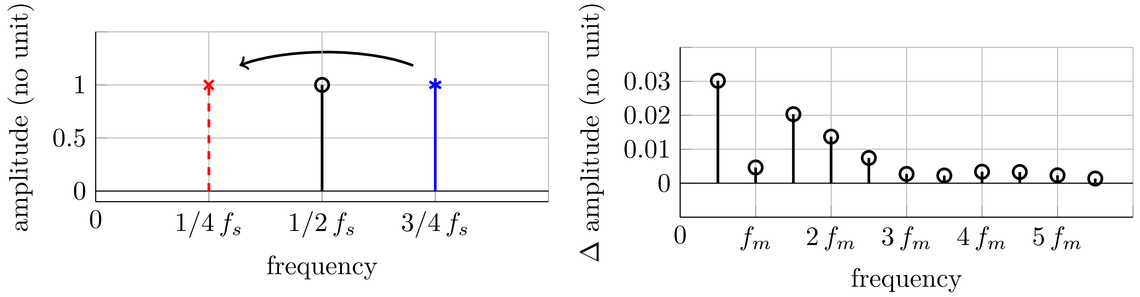

(b) Aliasing in frequency-domain.

(d) Spectral leakage in frequency-domain.

Figure 2.9: Possible measurement deviations occurring by the Fourier transformation with DFT (synthetic data).

The maximum frequency which can be measured is determined by the Nyquist-Shannon sampling theorem with half the sampling frequency $f_s$. Figure 2.9a shows how a signal, sampled with a too low sampling frequency (black circles) can be interpreted with a wrong frequency (red dashed line) which is much lower than the original frequency (blue line).

Figure 2.9b shows how the actual frequency is mirrored at $\frac{f_s}{2}$ and interpreted in a lower frequency band with the wrong frequency [113]. Figure 2.9d shows what happens, when the DFT is not done over integer multiples of the measurement period $T_m$ (see incomplete signal in figure 2.9c). The twiddle factor from figure 2.7a does not make a full rotation with the measurement data. Therefore some values are not summed up and others which have been already summed up cannot be compensated during the remaining part of the rotation. This leads to the actual applied frequency not being measured with its full amplitude and various other frequencies not ending up at a zero value.

**Chapter Conclusion**

*The impedance of the inner resistance is determined by the construction and the chemistry of the battery cell. The charge transfer reaction causes the most important non-linearity of a battery cell, which can be mathematically described by the Butler-Volmer equation. Other important values that characterize a battery are the entropy $S$ and the State-of-Charge.*

*The impedance can be measured by current pulses or by electrochemical impedance spectroscopy, which applies a sinusoidal current and compares it to the voltage response. For electrochemical impedance spectroscopy, several algorithms exist to transform the sampled measurement data from the time-domain into the frequency-domain. Most of these algorithms have the same frequency response and are prone to the same measurement deviations like Aliasing and spectral leakage. Therefore calculations on measurement deviations can be done with one of them, e.g. the Discrete Fourier Transformation, and the results are valid for all algorithms with the same characteristics.*

*This thesis always assumes that integer multiples of all applied frequencies are measured. Except for section 4.4 of chapter 4, it assumes a sufficiently high sampling rate to resolve all applied frequencies. In this case, the result of the continuous Fourier transformation and the Discrete Fourier Transformation or other algorithms with the same characteristics are the same. Because of this, all Fourier transformations in this thesis are only done using the continuous form of the Fourier transformation over an integer number of periods.*

# 3 Excitation Amplitude Limit

**Abstract**

*Impedance is only defined for a Linear-Time-Invariant system. This means that the impedance is not changing during the time of the measurement. A prerequisite of this requirement is that there is no current flowing into or out of the battery and that it is at a completely relaxed state, i.e. the terminal voltage was allowed to stabilize at the open circuit voltage for several hours.*

*Strictly speaking, this requirement is impossible to fulfill, since the measurement method itself causes the impedance to change during the time of the measurement. The sinusoidal current that is applied for the excitation of the battery changes the State-of-Charge by a sinusoidal function. The impedance is dependent on the State-of-Charge and therefore changes during the measurement. Every current that runs through a battery, as well as the excitation current for the impedance measurement, causes the cell to heat up. The impedance of a battery cell is strongly dependent on the temperature and therefore even small changes in temperature can significantly change the impedance measurement. The Open-Circuit-Voltage changes with the State-of-Charge and temperature and therefore distorts the voltage reading by an additional sinusoidal signal. An ideal impedance would have a linear dependency between the applied magnitude of the current and the voltage response. Although being very linear, lithium-ion batteries are not perfectly linear.*

*Because of these effects, the magnitude of the excitation current should be as small as possible in order to keep the described measurement deviations as low as possible. But a small excitation current results in a small voltage response. This in turn means that the voltage readings have to be very accurate in order not to obtain a noisy voltage measurement. Because of this, the optimum is neither a very large excitation current nor a very small one.*

*In order to make impedance measurements on-line, the measurement has to be done during the operation of the battery or during charging. Alternatively they could be done with a multi-sine signal in the short breaks when the battery is not in use. This leads to constant currents or additional current signals at other frequencies than the measurement frequency which are present during the measurement.*

*In this chapter the impact on the measurement caused by these effects is discussed, analyzed and its deviation on the measurement quantitatively evaluated. With these results, a deviation estimation can be given before the measurement is taken based on previous measured battery parameters, the measurement frequency and the excitation amplitude.*

The final result of this chapter is an equation, which gives a complete and detailed picture of the measurement deviations occurring during an impedance measurement. With it, the deviation made by selecting a certain excitation current amplitude and an underlying constant current can be determined. Setting maximum measurement deviation thresholds allows the determination of the maximum permissible excitation current. The equation relies on an extensive characterization of the battery. The equation and this chapter only covers deviations that come from the cell itself and are not caused by the measurement sequence, the excitation current generation, how the current and the voltage are measured or the measured data is analyzed. Figure 3.1 shows the four different categories into which the sources of these measurement deviations can be separated. These four categories built the first four sections of this chapter.

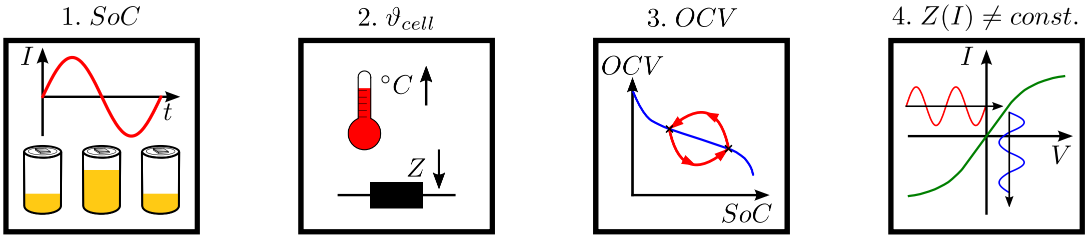
1. $SoC$ 2. $\vartheta_{cell}$ 3. $OCV$ 4. $Z(I) \neq const.$

Figure 3.1: Possible sources of measurement deviation during an electrochemical impedance measurement.

The first section 3.1 analyzes the dependency of the impedance on the SoC and the measurement deviation which is introduced by this dependency. Section 3.2 covers the effect that any current, whether the excitation current itself or an additional constant current, generates heat in the cell and causes the temperature to rise. It shows the dependency of the impedance from temperature and introduces a way to estimate the temperature increase from sinusoidal and constant currents with impedance measurements. Section 3.3 takes into consideration that the OCV changes with changing SoC and temperature. A change in OCV, which results in a different OCV at the end of the measurement, is called voltage drift, and can be compensated as shown in the next chapter in section 4.1. The impedance measurement assumes a linear relationship between the excitation current and the voltage measurement. The larger the excitation current, the more this relationship deviates from this assumption. Section 3.4 shows the magnitude of this impedance non-linearity and discusses different ways to measure it.

Each section derives the equations to determine the measurement deviation of the impedance measurement introduced by each effect. These equations are derived for single-sine measurements, multi-sine measurements and underlying constant currents. The last section 3.5 summarizes the measurement deviation equations for a single-sine measurement and an underlying constant current into one equation. The contribution of every effect is compared to each other and discussed.

Most commercially available impedance meters define a maximum impedance modulus deviation of less than 1 % and a maximum phase deviation of less than 1 ° [14; 40]. In order to assess the maximum permissible excitation current the same thresholds are used. For section 3.1 to 3.4 thresholds of 0.1 % for the modulus deviation and 0.1 ° for the phase deviation are considered critical. Setting the threshold for each category by a factor of 10 lower as the final deviation threshold is reasonable since in this chapter already four sources of measurement deviations are introduced and chapter 4 will introduce three more.

This chapter makes the following simplifications in order to determine an analytical expressions for the impedance measurement deviation:

1. If not further specified, the excitation current $I_m$ is given by its peak value and not by its effective value.
2. The transformation of the time-domain measurement data into the frequency-domain uses the Fourier transformation in its continuous form (see equation 2.14).
3. An underlying constant current, which can be present additional to the excitation current, is charging or discharging the battery for the whole impedance measurement time. Random changing currents introduce an additional frequency component. Since this frequency is unknown, it cannot be guaranteed that a full period of this frequency is recorded. This results in measurement deviations for all evaluated frequencies caused by spectral leakage.
4. The proposed method can be extended to multi-sine measurements. But only if the measured frequencies are integer multiples or integer fractions of each other. The reason is that full periods of each frequency have to be recorded in order to avoid spectral leakage.
5. The impedance dependency on SoC for any given impedance measurement at a specific SoC can be approximated by a linear function. This means that the impedance decreases/increases by a constant value for the same capacity charged or discharged according to equation 3.1).

   $$Z_{0+\Delta SoC} = \left.\frac{\Delta Z}{\Delta SoC}\right|_{T,\Delta SoC} \cdot \Delta SoC + Z_0 \tag{3.1}$$

   Where $\left.\frac{\Delta Z}{\Delta SoC}\right|_{T,\Delta SoC}$ is the linear dependency of the impedance on SoC for a given temperature, SoC and change of SoC. This simplification is assumed for the real and the imaginary part of the impedance. The error made by this assumption is small as long as the SoC change during the measurement is small, i.e. $< 1\,\%$.
6. The impedance dependency on temperature for any given impedance measurement at a specific temperature can be approximated by an exponential function. This means that the impedance decreases/increases according to the Arrhenius equation 2.3. This assumption is valid as long as the temperature change during the measurement is small, i.e. $< 1\,°\mathrm{C}$.
7. The OCV dependency on SoC for any given impedance measurement at a specific SoC can be approximated by a linear function. This means that the OCV decreases/increases by a constant value for the same capacity charged or discharged. The error made by this assumption is small as long as the SoC change during the measurement is small, i.e. $< 1\,\%$.

The method used to derive the single components of the total measurement deviation equation is to use characterized cells whose impedance over SoC and temperature as well as entropy, OCV and impedance non-linearity was determined under various conditions. Based on this characterization, the deviation equations are derived assuming a simplified mathematical model to describe the battery. The characterization allows to verify the derived deviation equations with simulations. Purely experimental studies do not allow to extract the contribution to the measurement deviation of every single effect since all the effects contribute at the same time, especially at high currents, and are impossible to separate.

The sections 3.1 to 3.4 assess the effect of a changing parameter, like SoC, OCV, temperature and current magnitude on the impedance measurement deviation by evaluating the Fourier transformation of the voltage measurement. For deriving the respective equations the Fourier transformation is separated into the real and imaginary part as shown in equations 3.2 to 3.6. The continuous form of the Fourier transformation is used with finite limits. In this chapter, measurement deviations from spectral leakage are not considered.

The measured impedance is calculated by dividing the Fourier transformation of the voltage evaluated at the measurement frequency through the one of the current. In this chapter the current is assumed to be perfectly sinusoidal therefore it can be replaced by the amplitude of the sinusoidal excitation current. Only sinusoidal currents which start at $i(t) = 0\,\mathrm{A}$ with the positive half-sine wave are used. This is why, after the Fourier transformation the current is purely imaginary (equation 3.7). Each section ends with the statement of the relative impedance measurement deviation according to equation 3.8. For cases when the wrongly measured voltage can be determined directly, equation 3.9 applies.

$$\mathrm{F}\{v(t)\} = \frac{2}{T_m}\int_0^{T_m} v(t)\cdot e^{-j\omega_m t}\mathrm{d}t \tag{3.2}$$

$$\mathrm{F}\{v(t)\} = \frac{2}{T_m}\int_0^{T_m} v(t)\cdot\left(\cos(\omega_m t) - j\sin(\omega_m t)\right)\mathrm{d}t \tag{3.3}$$

$$\mathrm{F}\{v(t)\} = a_1 - jb_1 \tag{3.4}$$

$$a_1 = \frac{2}{T}\int_0^{T_m} v(t)\cdot\cos(\omega_m t)\mathrm{d}t \tag{3.5}$$

$$b_1 = \frac{2}{T}\int_0^{T_m} v(t)\cdot\sin(\omega_m t)\mathrm{d}t \tag{3.6}$$

$$Z_m = \frac{\mathrm{F}\{v(t)\}|_{fm}}{\mathrm{F}\{i(t)\}|_{fm}} = \frac{\mathrm{F}\{v(t)\}|_{fm}}{-j\hat{I}_m} \tag{3.7}$$

$$e_Z = \frac{Z_e}{Z_0} = \frac{Z_m - Z_0}{Z_0} = \frac{\mathrm{F}\{v(t)\}}{-j\hat{I}_m\cdot Z_0} - 1 \tag{3.8}$$

$$e_Z = \frac{\mathrm{F}\{v_e(t)\}}{-j\hat{I}_m\cdot Z_0} \tag{3.9}$$

## 3.1 Measurement Deviation Caused by State-of-Charge Change

### 3.1.1 Impedance Dependency on State-of-Charge

The impedance of any battery cell is dependent on SoC. Only electrochemical systems with a theoretically infinite source such as fuel cells or redox-flow-batteries do not show this kind of dependency. Impedance values at very high and low SoC values are difficult to measure when the battery cell voltage should stay within its operating voltage window. For this reason this section will focus on the SoC-range from 10 % to 90 %. Most cells show an increase in impedance towards low and high SoCs as shown in Figure 3.2a. Figure 3.2b shows that the relative change of impedance for a 1 % SoC change is in a similar range independent whether the cell has in general a high impedance (e.g. shown Lithium Cobalt Oxide ($LiCoO_2$) (LCO) cell) or low impedance (e.g. shown Lithium Iron Phosphate ($LiFePO_4$) (LFP) cell).

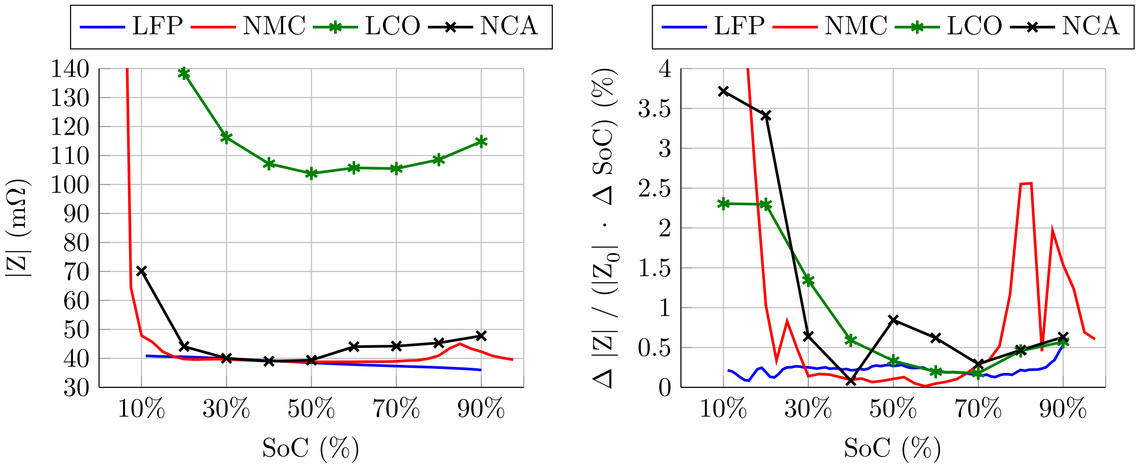

(a) Impedance modulus.

(b) Relative impedance modulus change per 1 % SoC change.

Figure 3.2: Impedance dependency on SoC for cylindrical cells with different li-ion chemistries (LFP-cell A.1, NMC-cell A.2, LCO-cell A.3, NCA-cell A.4, $\vartheta = 25\,°C$, $f_m = 10\,mHz$).

### 3.1.2 Single-sine Measurement

#### 3.1.2.1 State-of-Charge Change

The excitation current itself is responsible for a change of the SoC during the measurement. Depending on whether the sinus starts with the positive half-sine wave (as shown in Figure 3.3a) or negative half-sine wave, the change in SoC during the measurement is either positive or negative. This leads to a change of the cell impedance during the measurement. Figure 3.3a shows a quite significant change in SoC during the impedance measurement. For an unusually high excitation current of 3 CA and a measurement frequency of 10 mHz the SoC changes by up to 2.65 %. This results in a changing impedance over the time of the impedance measurement. Figure 3.3b shows the relative real and imaginary impedance change over the measurement time. Because of the changing impedance the voltage response is not perfectly sinusoidal. The blue line in figure 3.3b shows the relative deviation of the measured voltage response from the response if no SoC change would occur. Due to the non-zero phase of the impedance itself, the relative deviation is not a sinusoid with a single frequency.

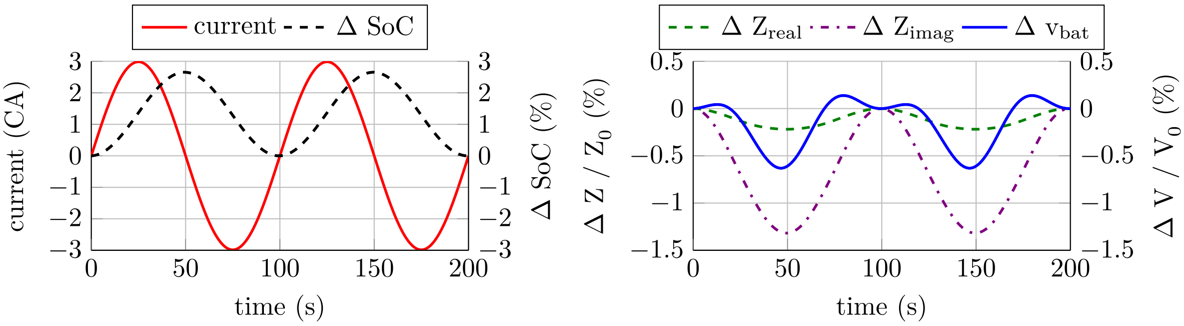

(a) Current and SoC change.

(b) Subsequent real and imaginary part impedance change and voltage response difference derived from impedance over SoC measurements.

Figure 3.3: Changes of SoC and subsequent simulated changes in impedance and voltage response during an impedance measurement. (cylindrical LFP-cell A.1, $\hat{I}_m = 3.0\,\text{CA}$, $SoC_{start} = 30\,\%$, $\vartheta = 25\,°\text{C}$, $f_m = 10\,\text{mHz}$).

Equations 3.10, 3.12 and 3.11 respectively show the equations for the maximum SoC-change (SoC sweep $\Delta\widehat{SoC}_m$), the mean SoC-change (SoC shift $\Delta\overline{SoC}_m$) and the SoC-change dependent on time during the impedance measurement.

$$\begin{aligned}
\Delta\widehat{SoC}_m &= \frac{\hat{I}_m}{C_{el}} \cdot \int_0^{\frac{T_m}{2}} \sin(2\pi f_m t + \varphi)\,\mathrm{d}t \\
&= \frac{\hat{I}_m}{C_{el}} \cdot \left[ -\frac{T_m}{2\pi} \cos\left(2\pi \frac{1}{T_m} t + \varphi\right)\right]_0^{\frac{T_m}{2}} \\
&= -\frac{T_m}{2\pi}\frac{\hat{I}_m}{C_{el}} \cdot \left[\cos\left(\pi + \varphi\right) - \cos\left(0 + \varphi\right)\right] \\
&= -\frac{T_m}{2\pi}\frac{\hat{I}_m}{C_{el}} \cdot \left[\underbrace{\cos\pi}_{-1} \cdot \cos\varphi - \underbrace{\sin\pi}_{0} \cdot \sin\varphi - \cos\varphi\right] \\
&= -\frac{T_m}{2\pi}\frac{\hat{I}_m}{C_{el}} \cdot \left[-\cos\varphi - \cos\varphi\right] \\
&= \frac{T_m}{\pi}\frac{\hat{I}_m}{C_{el}} \cdot \cos\varphi && (3.10) \\
\Delta\overline{SoC}_m &= \frac{T_m}{2\pi}\frac{\hat{I}_m}{C_{el}} \cdot \cos\varphi && (3.11) \\
\Delta SoC_m(t) &= \frac{\hat{I}_m}{C_{el}} \cdot \int \sin(2\pi f_m t + \varphi)\,\mathrm{d}t \\
&= \frac{\hat{I}_m}{C_{el}} \cdot \left[-\frac{T_m}{2\pi}\cos(2\pi f_m t + \varphi)\right] + c \\
&= -\frac{T_m}{2\pi}\frac{\hat{I}_m}{C_{el}} \cdot \cos(2\pi f_m t + \varphi) + \frac{T_m}{2\pi}\frac{\hat{I}_m}{C_{el}} \cdot \cos\varphi \\
&= \frac{T_m}{2\pi}\frac{\hat{I}_m}{C_{el}} \cdot \left[-\cos(2\pi f_m t + \varphi) + \cos\varphi\right] && (3.12)
\end{aligned}$$

#### 3.1.2.2 Impedance Measurement Deviation

In order to determine the equation for the measurement deviation, the impedance change is simplified to change linearly over SoC for a given temperature. The two end points of that linear interpolation are the starting SoC and the SoC at maximum deviation. The linear factor is then calculated according to equation 3.13:

$$\left.\frac{\Delta Z}{\Delta SoC}\right|_{T,\Delta SoC} = \frac{Z_{SoC_{start}+\Delta \widehat{SoC}_m} - Z_{SoC_{start}}}{\Delta \widehat{SoC}_m} \tag{3.13}$$

With that value the impedance deviation over time of the measured impedance from a change in SoC caused by the sinusoidal excitation current can be described according to equation 3.15:

$$Z_e(t) = \left.\frac{\Delta Z}{\Delta SoC}\right|_{T,\Delta SoC} \cdot \Delta SoC_m(t) \tag{3.14}$$

$$Z_e(t) = \left.\frac{\Delta Z}{\Delta SoC}\right|_{T,\Delta SoC} \cdot \frac{T_m}{2\pi}\frac{\hat{I}_m}{C_{el}} \cdot [-\cos(\omega_m t + \varphi) + \cos(\varphi)] \tag{3.15}$$

For this calculation the excitation current is assumed to be a sinusoid with no initial phase $\varphi = 0$. The voltage and voltage deviation respectively can be determined by multiplying the time changing impedance deviation by the excitation current:

$$v(t) = Z(t) \cdot \hat{I}_m \cdot \sin(\omega_m t) = (Z_0 + Z_e(t)) \cdot \hat{I}_m \cdot \sin(\omega_m t) = v_0(t) + v_e(t) \tag{3.16}$$

$$v_e(t) = \left.\frac{\Delta Z}{\Delta SoC}\right|_{T,\Delta SoC} \cdot \frac{T_m}{2\pi}\frac{\hat{I}_m}{C_{el}} \cdot [-\cos(\omega_m t) + 1] \cdot \hat{I}_m \cdot \sin(\omega_m t) \tag{3.17}$$

The equations for the total impedance and voltage response (equation 3.16) are only presented to show where the equations for the impedance deviation and voltage come from. Going forward, only the equation of the voltage deviation 3.17 is needed. The Fourier transformation of the voltage deviation is best calculated by separating the real part $a_1$ from the imaginary part $b_1$:

$$\mathrm{F}\{v_e(t)\} = \frac{2}{T_m}\int_0^{T_m} v_e(t) \cdot e^{-j\omega_m t}\mathrm{d}t = a_1 - jb_1 \tag{3.18}$$

$$\begin{aligned}\mathrm{F}\{v_e(t)\} = \frac{1}{\pi}\frac{\hat{I}_m{}^2}{C_{el}}\left.\frac{\Delta Z}{\Delta SoC}\right|_{T,\Delta SoC} \cdot \\ \int_0^{T_m} [-\cos(\omega_m t) + 1] \cdot \sin(\omega_m t) \cdot e^{-j\omega_m t}\mathrm{d}t\end{aligned} \tag{3.19}$$

$$\begin{aligned}a_1 = \frac{1}{\pi}\frac{\hat{I}_m{}^2}{C_{el}}\left.\frac{\Delta Z}{\Delta SoC}\right|_{T,\Delta SoC} \cdot \underbrace{\int_0^{T_m} -\cos(\omega_m t) \cdot \underbrace{\sin(\omega_m t) \cdot \cos(\omega_m t)}_{\frac{1}{2}\cdot\sin(2\omega_m t)\text{ with C.3}}\mathrm{d}t}_{=0} \\ + \frac{1}{\pi}\frac{\hat{I}_m{}^2}{C_{el}}\left.\frac{\Delta Z}{\Delta SoC}\right|_{T,\Delta SoC} \cdot \underbrace{\int_0^{T_m} \underbrace{\sin(\omega_m t) \cdot \cos(\omega_m t)}_{\frac{1}{2}\cdot\sin(2\omega_m t)\text{ with C.3}}\mathrm{d}t}_{=0}\end{aligned} \tag{3.20}$$

$$a_1 = 0 \tag{3.21}$$

$$
\begin{aligned}
b_1 = \frac{1}{\pi}\frac{\hat{I}_m^{\,2}}{C_{el}}\left.\frac{\Delta Z}{\Delta SoC}\right|_{T,\Delta SoC} &\cdot \underbrace{\int_0^{T_m} -\cos(\omega_m t)\cdot \underbrace{\sin(\omega_m t)\cdot\sin(\omega_m t)}_{\frac{1}{2}\cdot(1-\cos(2\omega_m t))\text{ with C.4}}\ \mathrm{d}t}_{=0} \\
+ \frac{1}{\pi}\frac{\hat{I}_m^{\,2}}{C_{el}}\left.\frac{\Delta Z}{\Delta SoC}\right|_{T,\Delta SoC} &\cdot \underbrace{\int_0^{T_m} \underbrace{\sin(\omega_m t)\cdot\sin(\omega_m t)}_{\frac{1}{2}\cdot(1-\cos(2\omega_m t))\text{ with C.4}}\ \mathrm{d}t}_{=\frac{1}{2}\cdot T_m}
\end{aligned}
\tag{3.22}
$$

$$b_1 = \frac{T_m}{2\pi}\frac{\hat{I}_m^{\,2}}{C_{el}}\left.\frac{\Delta Z}{\Delta SoC}\right|_{T,\Delta SoC} \tag{3.23}$$

$$\mathrm{F}\{v_e(t)\} = -j\frac{T_m}{2\pi}\frac{\hat{I}_m^{\,2}}{C_{el}}\left.\frac{\Delta Z}{\Delta SoC}\right|_{T,\Delta SoC} \tag{3.24}$$

With equation 3.9 the relative deviation from SoC change caused by a single sinusoidal current can be stated as:

$$e_Z = \frac{\mathrm{F}\{v_e(t)\}}{-j\hat{I}_m\cdot Z_0} = \frac{T_m}{2\pi}\frac{\hat{I}_m}{C_{el}}\left.\frac{\Delta Z/Z_0}{\Delta SoC}\right|_{T,\Delta SoC} \tag{3.25}$$

Although the change in imaginary impedance in figure 3.3b of over 1.3 % is quite significant, the resulting measurement deviation of the impedance modulus and phase are smaller. The impedance deviation is the averaged impedance change over which the SoC has swept. For the modulus deviation the imaginary part only makes a minor contribution. The phase deviation is measured in absolute terms and is therefore less affected by a large relative imaginary impedance change on a rather small imaginary impedance value compared to the real impedance value.

Figure 3.4 shows that the permissible excitation current amplitude for staying below an impedance modulus deviation of 0.1 % is lower than for staying below an impedance phase deviation of 0.1 °. As equation 3.25 shows, the measurement deviation is linearly dependent on $\hat{I}_m$ as well as on $T_m$. The higher the frequency $f_m$, the higher the permissible excitation current becomes.

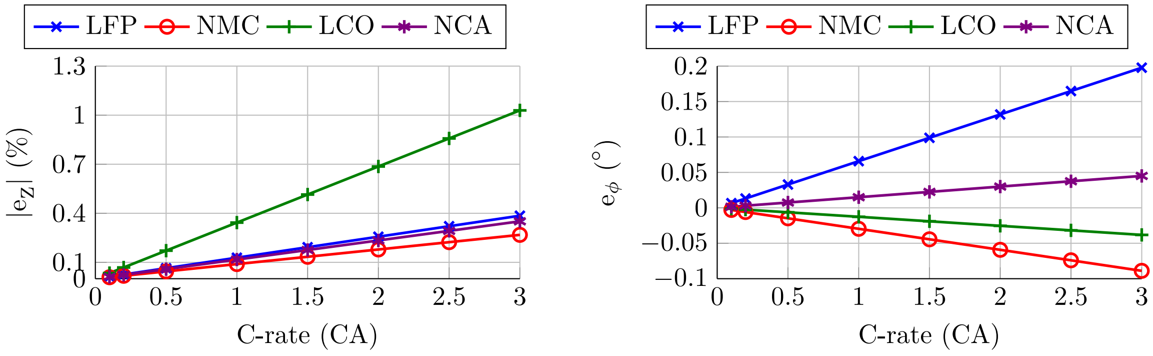

(a) Modulus deviation.

(b) Phase deviation.

Figure 3.4: Measurement deviation caused by SoC change during impedance measurements with different excitation current magnitudes. (cylindrical cells A.1 to A.4, $SoC_{start} = 30\,\%$, $\vartheta = 25\,°\mathrm{C}$, $f_m = 10\,\mathrm{mHz}$).

Figure 3.5 reconfirms that it is easier to stay below the phase deviation threshold of 0.1 ° than below the one of the impedance modulus threshold of 0.1 %. Especially for SoC values below 30 % and above 80 % the modulus deviation breaks through this threshold.

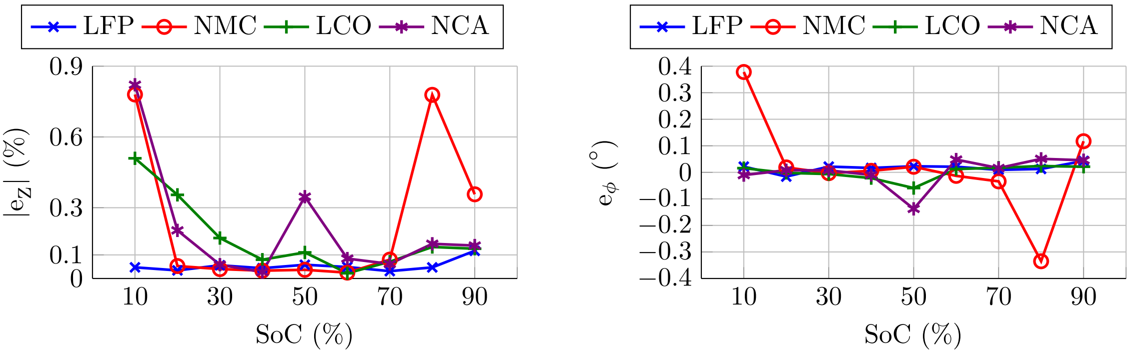

(a) Modulus deviation.

(b) Phase deviation.

Figure 3.5: Measurement deviation caused by SoC change during impedance measurements at different SoCs. (cylindrical cells A.1 to A.4, $\hat{I}_m = 0.5\,\mathrm{CA}$, $\vartheta = 25\,°\mathrm{C}$, $f_m = 10\,\mathrm{mHz}$).

An option for eliminating this measurement deviation is simply not to assume that the measurement is taken at the start-SoC, but at the start-SoC plus the SoC shift $\Delta\overline{SoC}$. The more $\frac{\Delta Z}{\Delta SoC}$ is a constant value, the more this assumption is correct. If this is done the deviation reduces to the non-linearity of the $\frac{\Delta Z}{\Delta SoC}$ relationship, which is negligible for small SoC changes below 1 %. Figure 3.6 proves this. It is based on impedance measurement data for every 1 % SoC change. The first curve $Z_{sim}$ of this figure is obtained by using the measurement data in a simulation. In this simulation the voltage response for a given excitation current amplitude is calculated by multiplying the current with the impedance which changes with the SoC. Between the measurement points spaced with 1 % SoC resolution the impedance was linearly interpolated. The simulated voltage response is then Fourier transformed divided by the excitation current to obtain the impedance. The shown deviation is the difference between the impedance determined by this simulation and the impedance which was measured at the SoC where the simulation started. The second curve $Z_{lin}$ calculates the deviation based on the linear interpolation between the start-SoC and the end-SoC, which is $\Delta\widehat{SoC}_m$ higher than the start-SoC by using the equations 3.13 and 3.25. The third curve $Z_{diff}$ is the difference between $Z_{sim}$ and $Z_{lin}$. The figure shows that the non-linearity is negligible and the measurement deviation stays below 0.1 % and 0.1 °, even for an SoC shift of up to 10 %, when the measured impedance is considered to be taken at $SoC_{start} + \Delta\overline{SoC}_m$. Another option to eliminate this deviation introduced by SoC change is to use a cosine function to stimulate the battery. The drawback of this method is the sudden current ‘jump’ at the beginning of the measurement which would lead to a very long settling time until the battery follows the excitation current. If used, a whole period would need to be waited for the battery to settle. A settling time of less than a period would result in an SoC at the end of the measurement that is different from that at the beginning. If several frequencies are applied in a sinus-sweep measurement, every single frequency measurement would then be measured at a slightly different SoC.

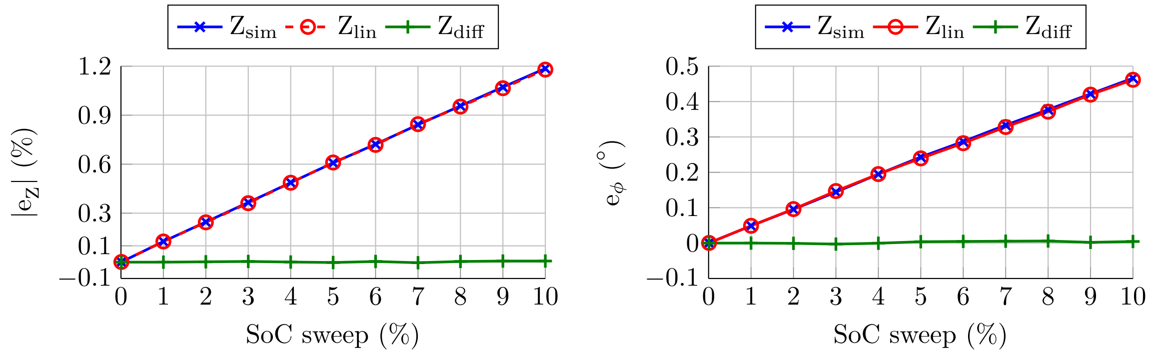

(a) Modulus deviation.

(b) Phase deviation.

Figure 3.6: Comparison of equation 3.25 with a linear impedance to SoC dependency to a simulation with an impedance resolution of 1 % (cylindrical LFP-cell A.1, $SoC_{start} = 30\,\%$, $\vartheta = 25\,°\mathrm{C}$, $f_m = 10\,\mathrm{mHz}$).

### 3.1.3 Multi-sine Measurement

#### 3.1.3.1 State-of-Charge Change

For a multi-sine signal the SoC displacement is dependent on all of its single components. The maximum displacement cannot be easily determined as its calculation involves solving a function with several local minimas [49; 100]. However, the time dependency of the SoC shown by equation 3.26 is enough to derive the equations for the introduced measurement deviation in the next section.

$$\Delta SoC_{m,\,MS}(t) = \sum_{n=1}^{N} \frac{T_n}{2\pi}\frac{\hat{I}_n}{C_{el}} \cdot [-\cos(2\pi f_n t + \varphi_n) + \cos(\varphi_n)] \tag{3.26}$$

#### 3.1.3.2 Impedance Measurement Deviation

In contrast to section 3.1.2.2 the measurement deviation for multi-sine measurement is derived with an initial phase $\varphi_n$ for all the single components of the multi-sine signal. The initial phase is important, since it is often used to reduce the Crest factor [20; 108]. The measurement deviation of the impedance $Z_e(t)$ and the associated voltage deviation $v_e(t)$ are calculated by assuming a linear dependency of the impedance to SoC.

$$Z_e(t) = \left.\frac{\Delta Z}{\Delta SoC}\right|_{T,\Delta SoC} \cdot \sum_{n=1}^{N} \frac{T_n}{2\pi}\frac{\hat{I}_n}{C_{el}} \cdot [-\cos(\omega_n t + \varphi_n) + \cos(\varphi_n)] \tag{3.27}$$

$$v_e(t) = \left.\frac{\Delta Z}{\Delta SoC}\right|_{T,\Delta SoC} \cdot \sum_{n=1}^{N} \frac{T_n}{2\pi}\frac{\hat{I}_n}{C_{el}} \cdot [-\cos(\omega_n t + \varphi_n) + \cos(\varphi_n)] \cdot \hat{I}_n \cdot \sin(\omega_n t + \varphi_n) \tag{3.28}$$

In a multi-sine signal all frequencies are applied at the same time. The time $T_a$ for which these frequencies are applied is equal to the period of the lowest frequency component of the multi-sine signal $T_{min}$. This is the reason for calculating the Fourier transformation of the voltage deviation over this period. Any of the frequency components $f_n$ indicated with the index $n$ of the multi-sine signal could have an influence on the Fourier transformation of the measurement frequency $f_m$ indicated with the index $m$. Therefore, the following equations have to be considered for every measurement frequency $f_m$.

$$\mathrm{F}\{v_e(t)\} = \frac{2}{T_{min}} \int_0^{T_{min}} v_e(t) \cdot e^{-j\omega_m t}\mathrm{d}t = a_1 - jb_1 \tag{3.29}$$

$$\begin{aligned}\mathrm{F}\{v_e(t)\} = {} & \frac{1}{\pi}\frac{1}{T_{min}}\frac{1}{C_{el}}\left.\frac{\Delta Z}{\Delta SoC}\right|_{T,\Delta SoC} \cdot \\ & \int_0^{T_{min}} \sum_{n=1}^{N} T_n \hat{I}_n^2 \cdot [-\cos(\omega_n t+\varphi_n)+\cos(\varphi_n)] \cdot \sin(\omega_n t+\varphi_n) \cdot e^{-j\omega_m t}\mathrm{d}t\end{aligned} \tag{3.30}$$

$$\begin{aligned}a_1 = {} & \frac{1}{\pi}\frac{1}{T_{min}}\frac{1}{C_{el}}\left.\frac{\Delta Z}{\Delta SoC}\right|_{T,\Delta SoC} \cdot \\ & \underbrace{\int_0^{T_{min}} \sum_{n=1}^{N} -T_n \hat{I}_n^2 \cdot \underbrace{\cos(\omega_n t+\varphi_n)\cdot\sin(\omega_n t+\varphi_n)}_{\frac{1}{2}[\sin(2\omega_n t)\cos(2\varphi_n)+\cos(2\omega_n t)\sin(2\varphi_n)] \text{ with C.6}} \cdot \cos(\omega_m t)\mathrm{d}t}_{=-\frac{1}{4}T_n\hat{I}_n^2\cdot T_{min}\cdot\sin(2\varphi_n) \text{ with C.7 and C.9 for } \omega_n=\frac{1}{2}\omega_m\text{, otherwise } =0} \\ & + \frac{1}{\pi}\frac{1}{T_{min}}\frac{1}{C_{el}}\left.\frac{\Delta Z}{\Delta SoC}\right|_{T,\Delta SoC} \cdot \\ & \underbrace{\int_0^{T_{min}} \sum_{n=1}^{N} T_n \hat{I}_n^2 \cos(\varphi_n)\cdot\sin(\omega_n t+\varphi_n)\cdot\cos(\omega_m t)\mathrm{d}t}_{=\frac{1}{2}T_n\hat{I}_n^2\cdot T_{min}\cdot\cos(\varphi_n)\cdot\sin(\varphi_n) \text{ with C.10 for } \omega_n=\omega_m\text{, otherwise } =0}\end{aligned} \tag{3.31}$$

$$\begin{aligned}b_1 = {} & \frac{1}{\pi}\frac{1}{T_{min}}\frac{1}{C_{el}}\left.\frac{\Delta Z}{\Delta SoC}\right|_{T,\Delta SoC} \cdot \\ & \underbrace{\int_0^{T_{min}} \sum_{n=1}^{N} -T_n \hat{I}_n^2 \cdot \underbrace{\cos(\omega_n t+\varphi_n)\cdot\sin(\omega_n t+\varphi_n)}_{\frac{1}{2}[\sin(2\omega_n t)\cos(2\varphi_n)+\cos(2\omega_n t)\sin(2\varphi_n)] \text{ with C.6}} \cdot \sin(\omega_m t)\mathrm{d}t}_{=-\frac{1}{4}T_n\hat{I}_n^2\cdot T_{min}\cdot\cos(2\varphi_n) \text{ with C.8 and C.7 for } \omega_n=\frac{1}{2}\omega_m\text{, otherwise } =0} \\ & + \frac{1}{\pi}\frac{1}{T_{min}}\frac{1}{C_{el}}\left.\frac{\Delta Z}{\Delta SoC}\right|_{T,\Delta SoC} \cdot \\ & \underbrace{\int_0^{T_{min}} \sum_{n=1}^{N} T_n \hat{I}_n^2 \cos(\varphi_n)\cdot\sin(\omega_n t+\varphi_n)\cdot\sin(\omega_m t)\mathrm{d}t}_{=\frac{1}{2}T_n\hat{I}_n^2\cdot T_{min}\cdot\cos(\varphi_n)\cdot\cos(\varphi_n) \text{ with C.11 for } \omega_n=\omega_m\text{, otherwise } =0}\end{aligned} \tag{3.32}$$

With equation 3.9 the relative impedance measurement deviation from SoC change caused by a multisinusoidal current is:

$$e_Z = \begin{cases} \frac{1}{2\pi}\frac{1}{C_{el}}\left.\frac{\Delta Z/Z_0}{\Delta SoC}\right|_{T,\Delta SoC} \cdot \left[-T_m \frac{\hat{I}_n^2}{\hat{I}_m}(\cos(2\varphi_n)+j\cdot\sin(2\varphi_n))\right] & \text{for } \omega_n = \frac{1}{2}\omega_m \\ \frac{1}{2\pi}\frac{1}{C_{el}}\left.\frac{\Delta Z/Z_0}{\Delta SoC}\right|_{T,\Delta SoC} \cdot T_m\hat{I}_m\cdot\cos(\varphi_n)\cdot(\cos(\varphi_n)+j\cdot\sin(\varphi_n)) & \text{for } \omega_n = \omega_m \end{cases} \tag{3.33}$$

The analysis in this section applies for multi-sinus signals if the measured frequencies of the multi-sinus are even integer multiples or fractions of each other. From the derivation of the measurement deviation it becomes evident that the SoC dependency of the impedance causes deviations at different frequencies. One in the baseband frequency $f_m$ and one in the second harmonic $2\cdot f_m$. Figure 3.7 shows the harmonics of a single-sine signal based on a simulation with an impedance over SoC resolution for every 1 % SoC change. With the assumption of a linear change of the impedance with the SoC change only the first and the second harmonic should have non-zero values. However, figure 3.7 shows also small values compared to the first and second harmonic for the third harmonic and above. These values are caused by the deviation from the linear behavior of the impedance change with the SoC change.

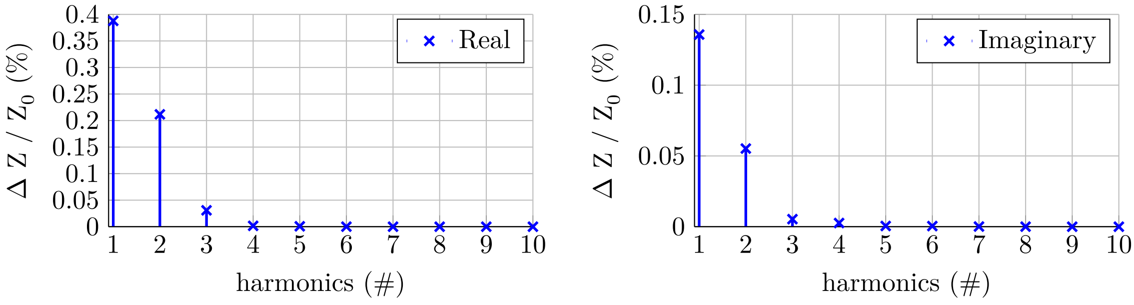

(a) Real part.

(b) Imaginary part.

Figure 3.7: Harmonics caused by a change in voltage response due to the SoC change during impedance measurements. (cylindrical LFP-cell A.1, $\hat{I}_m = 3\,\mathrm{CA}$, $SoC_{start} = 30\,\%$, $\vartheta = 25\,°\mathrm{C}$, $f_m = 10\,\mathrm{mHz}$).

This effect opens up the possibility for compensating the deviations introduced by the SoC dependency of the impedance. If a signal with half the measurement frequency would be superpositioned onto the actual measurement signal, the second harmonic of the additional signal at half the measurement frequency could compensate the deviation of the measurement frequency. Equation 3.33 indicates that the additional signal would need an initial phase of zero, or an integer multiple of $\pi$, and that both amplitudes need to have the same value and either the same or opposite sign. Figure 3.8 shows the two signals, their sum and their combined resulting SoC change.

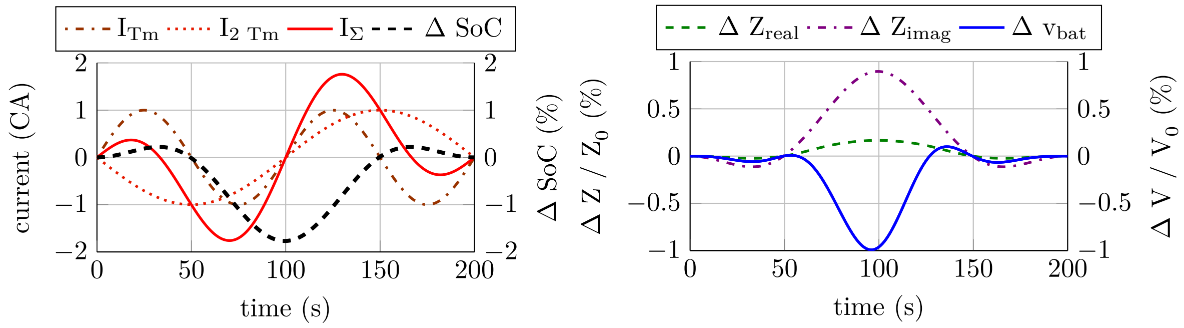

(a) Current and SoC change.

(b) Subsequent impedance and voltage response change.

Figure 3.8: Introducing an additional current at half the measurement frequency eliminates the measurement deviation introduced by SoC change. Figure shows change in SoC and subsequent changes in impedance and voltage response during an impedance measurement (cylindrical LFP-cell A.1, $\hat{I}_{Tm} = 1\,\mathrm{CA}$, $\hat{I}_{2 \cdot Tm} = -1\,\mathrm{CA}$, $\varphi_{2 \cdot Tm} = 0\,°$, $SoC_{start} = 30\,\%$, $\vartheta = 25\,°\mathrm{C}$, $f_m = 10\,\mathrm{mHz}$).

In this case the signal with the measurement frequency $f_m$ would perform two periods in the time in which the underlying signal with a frequency of $\frac{1}{2} f_m$ only performs one period. The measurement of the

actual measurement signal with $f_m$ is done twice, once with the SoC changed by the superpositioned signal with $\frac{1}{2}f_m$ towards negative SoC values and once towards positive SoC values, the deviations of these two measurements cancel each other out.
The total SoC shift and the SoC sweep is certainly higher than before. This is only critical if the assumption of a linear impedance to SoC relationship does not hold true. Section 3.1.2.2 showed that with this assumption the modulus deviation can be kept below 1 % and the phase deviation below 1 ° over the entire SoC range from 10 % to 90 %. However, other sources, such as temperature increase (see section 3.2) and impedance non-linearity (see section 3.4), will introduce a larger deviation because of the additional signal.

## 3.1.4 Constant Current

### 3.1.4.1 State-of-Charge Change

An underlying constant current that charges or discharges the battery violates the Linear-Time-Invariant-condition. The SoC not only changes during the measurement as it happens with the sinusoidal excitation current, but also the end-SoC is different from the start-SoC. The possibility to perform EIS measurements during charging would be a great opportunity for on-line EIS measurements since the battery goes through a number of different SoCs during the charging process at which the battery could be characterized. For constant currents during the EIS measurement, equation 3.34, 3.35 and 3.36 respectively show the SoC sweep, the SoC shift and the time dependency of the SoC change.

$$\Delta\widehat{SoC}_{dc} = \frac{I_{dc}}{C_{el}} \cdot T_m \tag{3.34}$$

$$\Delta\overline{SoC}_{dc} = \frac{1}{2}\frac{I_{dc}}{C_{el}} \cdot T_m \tag{3.35}$$

$$\Delta SoC_{dc}(t) = \frac{I_{dc}}{C_{el}} \cdot t \tag{3.36}$$

Figure 3.9 shows a constant current causing the same average SoC shift as the 3 CA excitation current from figure 3.3a.

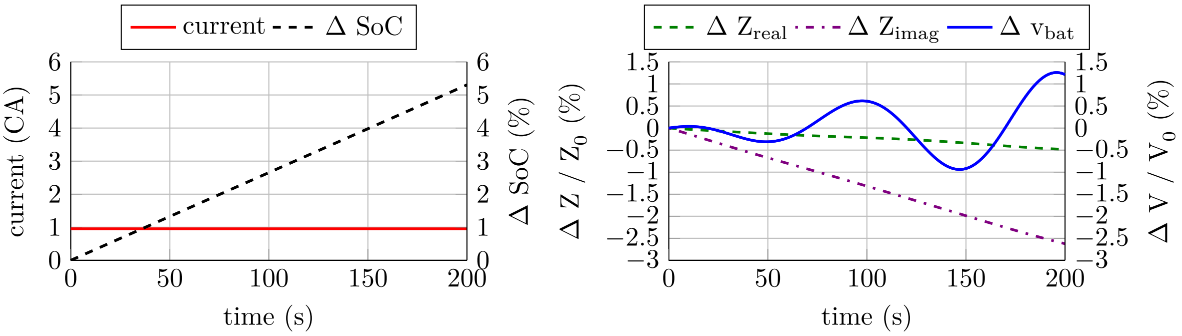

(a) Current and SoC change.

(b) Subsequent impedance and voltage response change.

Figure 3.9: Changes of SoC and subsequent changes in impedance and voltage response due to constant charging during an impedance measurement. (cylindrical LFP-cell A.1, $I_{dc} = \frac{3.0}{\pi}$CA, $SoC_{start} = 30\,\%$, $\vartheta = 25\,°\mathrm{C}$, $f_m = 10\,\mathrm{mHz}$). The figure shows simulated values and only the effect of the constant current. $\Delta v_{bat}$ assumes a sinusoidal excitation current of 0.5 CA but only shows the effect of the impedance change caused by the constant current. The figure therefore omits for all waveforms the changing SoC effect of the sinusoidal excitation current.

Please note that for illustrative the graph shows the constant over two periods. However, the equations derived in this section only consider one period. The constant current is by a factor of $\frac{1}{\pi}$ smaller than the amplitude of the excitation current. A constant current is therefore much more critical than a large excitation current.

#### 3.1.4.2 Impedance Measurement Deviation

This section derives the measurement deviation from the SoC dependency of the impedance caused by a constant current for a single-sine measurement. The initial phase of the sinusoidal excitation current is again considered to be $\varphi = 0$. The deviation of the impedance $Z_e(t)$ and the voltage $v_e(t)$ are calculated by assuming a linear dependency of the impedance to SoC and that the SoC shift is only caused by the constant current. The two end points for the linear interpolation are the start-SoC and the end-SoC and their respective impedances. The gradient is calculated similar to equation 3.13 with equation 3.37.

$$\left.\frac{\Delta Z}{\Delta SoC}\right|_{T,\Delta SoC} = \frac{Z_{start+\Delta\widehat{SoC}_{dc}} - Z_{start}}{\Delta\widehat{SoC}_{dc}} \tag{3.37}$$

$$Z_e(t) = \left.\frac{\Delta Z}{\Delta SoC}\right|_{T,\Delta SoC} \cdot \frac{I_{dc}}{C_{el}} \cdot t \tag{3.38}$$

$$v_e(t) = \left.\frac{\Delta Z}{\Delta SoC}\right|_{T,\Delta SoC} \cdot \frac{I_{dc}}{C_{el}} \cdot t \cdot \hat{I}_m \cdot \sin(\omega_m t) \tag{3.39}$$

The Fourier transformation of the voltage deviation is calculated over the period of the impedance excitation current $T_m$. The real part $a_1$ and the imaginary part $b_1$ are calculated separately.

$$\mathrm{F}\{v_e(t)\} = \frac{2}{T_m}\int_0^{T_m} v_e(t)\cdot e^{-j\omega_m t}\mathrm{d}t = a_1 - jb_1 \tag{3.40}$$

$$\mathrm{F}\{v_e(t)\} = \frac{2}{T_m}\frac{I_{dc}\cdot\hat{I}_m}{C_{el}}\frac{\Delta Z}{\Delta SoC}\bigg|_{T,\Delta SoC}\cdot\int_0^{T_m} t\cdot\sin(\omega_m t)\cdot e^{-j\omega_m t}\mathrm{d}t \tag{3.41}$$

$$a_1 = \frac{2}{T_m}\frac{I_{dc}\cdot\hat{I}_m}{C_{el}}\frac{\Delta Z}{\Delta SoC}\bigg|_{T,\Delta SoC}\cdot \underbrace{\int_0^{T_m} t\cdot\underbrace{\sin(\omega_m t)\cdot\cos(\omega_m t)}_{\frac{1}{2}\cdot\sin(2\omega_m t)\text{ with C.3}}\mathrm{d}t}_{=\frac{1}{2}\left[\underbrace{\frac{\sin(2\omega_m t)}{(2\omega_m)^2}}_{=0}-\frac{t\cdot\cos(2\omega_m t)}{2\omega_m}\right]_0^{T_m}=-\frac{1}{2}\frac{T_m^2}{4\pi}\text{ with C.12}} \tag{3.42}$$

$$a_1 = \frac{T_m}{2}\frac{I_{dc}\cdot\hat{I}_m}{C_{el}}\frac{\Delta Z}{\Delta SoC}\bigg|_{T,\Delta SoC}\cdot\left[-\frac{1}{2\pi}\right] \tag{3.43}$$

$$b_1 = \frac{2}{T_m}\frac{I_{dc}\cdot\hat{I}_m}{C_{el}}\frac{\Delta Z}{\Delta SoC}\bigg|_{T,\Delta SoC}\cdot \underbrace{\int_0^{T_m} t\cdot\underbrace{\sin(\omega_m t)\cdot\sin(\omega_m t)}_{\frac{1}{2}\cdot(1-\cos(2\omega_m t))\text{ with C.4}}\mathrm{d}t}_{=\underbrace{\left[\frac{1}{4}t^2\right]_0^{T_m}}_{=\frac{T_m{}^2}{4}}-\left[\underbrace{\frac{\cos(2\omega_m t)}{(2\omega_m)^2}}_{=0}+\underbrace{\frac{t\cdot\sin(2\omega_m t)}{2\omega_m}}_{=0}\right]_0^{T_m}=\frac{T_m{}^2}{4}\text{ with C.13}} \tag{3.44}$$

$$b_1 = \frac{T_m}{2}\frac{I_{dc}\cdot\hat{I}_m}{C_{el}}\frac{\Delta Z}{\Delta SoC}\bigg|_{T,\Delta SoC} \tag{3.45}$$

With equation 3.9, the relative deviation from SoC change caused by a constant current can be written as:

$$e_Z = \frac{T_m}{2}\frac{I_{dc}}{C_{el}}\frac{\Delta Z/Z_0}{\Delta SoC}\bigg|_{T,\Delta SoC}\cdot\left[1-\frac{j}{2\pi}\right] \tag{3.46}$$

Figure 3.10 shows the measurement deviation caused by a constant current charge at different C-rates. For very low constant currents the deviation already goes over the 0.1 % and 0.1 ° threshold. As for the single-sine measurement, the modulus deviation increases much quicker with increasing current amplitude as the phase deviation.

Figure 3.11 shows the dependency of the deviation on the start-SoC. An excitation current, which starts with a positive half-sine wave, was assumed for this simulation. The figure is similar as figure 3.5 but not the same. The 0.1 % modulus deviation threshold is violated almost over the entire SoC range from 10 % to 90 %. The 0.1 ° phase deviation threshold is easier to comply with.

In order to get the combined measurement deviation from constant current and excitation current, the deviation derived here needs to be added to the deviation derived in section 3.1.2.2 or 3.1.3.2. The best way to avoid the deviation introduced by a constant current and the excitation current is to assume

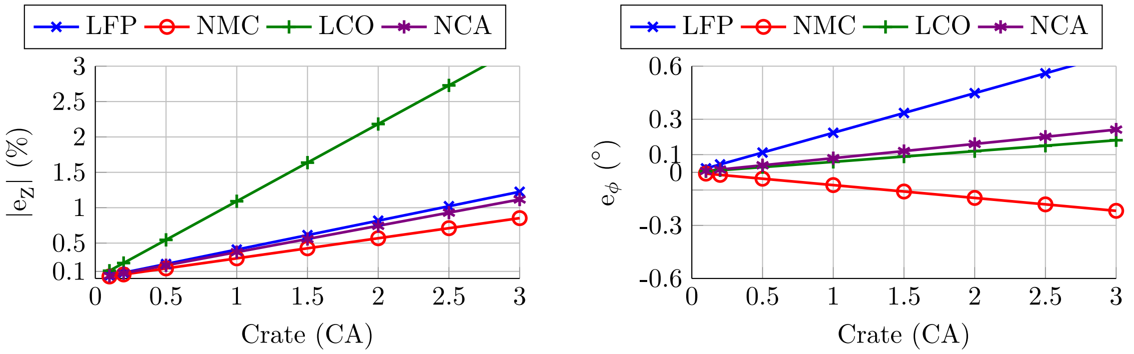

(a) Modulus deviation.

(b) Phase deviation.

Figure 3.10: Measurement deviation from SoCs change caused by constant current charging during impedance measurements. (LFP-cell A.1, NMC-cell A.2, LCO-cell A.3, NCA-cell A.4, $SoC_{start} = 30\,\%$, $\vartheta = 25\,°\mathrm{C}$, $f_m = 10\,\mathrm{mHz}$).

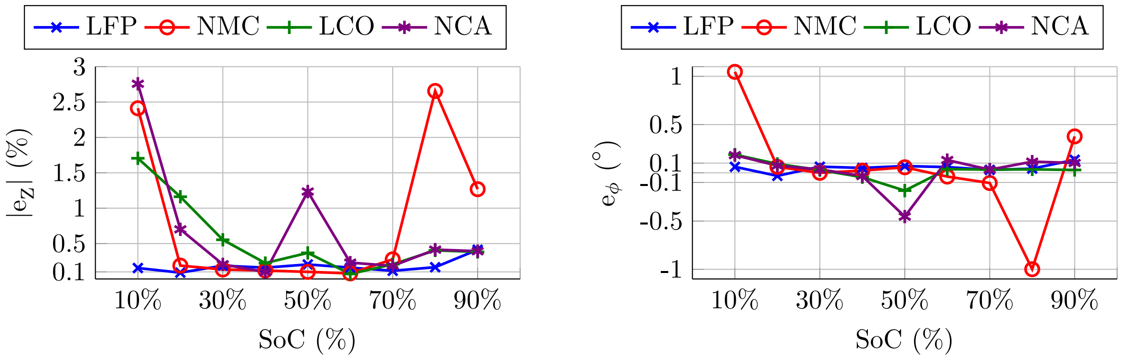

(a) Modulus deviation.

(b) Phase deviation.

Figure 3.11: Measurement deviation caused by SoC change due to a constant charging current during the impedance measurement at different SoCs (LFP-cell A.1, NMC-cell A.2, LCO-cell A.3, NCA-cell A.4, constant current charge rate $= \frac{3}{\pi}$CA, $SoC_{start} = 30\,\%$, $\vartheta = 25\,°\mathrm{C}$, $f_m = 10\,\mathrm{mHz}$).

that the measurement is taken at the start-SoC plus the average SoC shift of the excitation current $\Delta\overline{SoC}_m$ and the constant current $\Delta\overline{SoC}_{dc}$ as shown in equation 3.47.

$$Z_m = Z_0 + Z_e = Z_0 + \left.\frac{\Delta Z}{\Delta SoC}\right|_{T,\Delta SoC} \cdot \left(\Delta\overline{SoC}_m + \Delta\overline{SoC}_{dc}\right) \tag{3.47}$$

For calculating the linear factor $\left.\frac{\Delta Z}{\Delta SoC}\right|_{T,\Delta SoC}$ equation 3.48 applies.

$$\left.\frac{\Delta Z}{\Delta SoC}\right|_{T,\Delta SoC} = \frac{Z_{start+\Delta\widehat{SoC}} - Z_{start}}{\Delta\widehat{SoC}} \tag{3.48}$$

When choosing between $\Delta\widehat{SoC}_m$ and $\Delta\widehat{SoC}_{dc}$, the one with the larger deviation from the starting SoC should be used. This is because a wrong assumption of the linear behavior of the impedance over SoC is then less critical. When $\Delta\widehat{SoC}_m$ is smaller as $\Delta\widehat{SoC}_{dc}$, then during the impedance measurement the sinusoidal SoC sweep will also be along the line between the start-SoC and the end-SoC. If $\Delta\widehat{SoC}_m$ is larger than $\Delta\widehat{SoC}_{dc}$, then the SoC sweep of the impedance measurement will surpass the SoC change caused by the constant current and will be more important for the total measurement deviation.

**Section Conclusion**

*A change in State-of-Charge during the impedance measurement changes its result. Any current flowing out or into the battery causes the State-of-Charge to change. Due to the nature of the impedance measurement, which relies on a sinusoidal current, even a single sine measurement is changing the State-of-Charge during the measurement. Especially excitation currents, which follow a sinus function and not a cosinus function, cause an additional deviation. Underlying constant currents that might be present during charging or discharging cause a similar effect.*

*This section derived the theoretical measurement deviations caused by a single-sine measurement, multi-sine measurement and an underlying constant current. The equations are derived under the assumption of a linear dependency of the impedance on the State-of-Charge. This assumption was verified by a comparison between a high resolution simulation and the linear assumption. Due to this simplification, the deviation can also be reduced significantly by assuming that the impedance measurement was taken at the starting State-of-Charge plus the average State-of-Charge shift.*

## 3.2 Measurement Deviation Caused by Temperature Change

The impedance of a battery is temperature dependent. Section 3.2.1 introduces a mathematical description of this dependency. This dependency causes measurement deviations when the temperature is changing during the impedance measurement. Any current charging or discharging a battery causes it to heat up, also the alternating excitation current of an EIS measurement. Section 3.2.2 covers the influence of entropy heating of a sinusoidal current as a reversible heat source and the impedance measurement deviation it causes. Section 3.2.3 covers the influence of impedance heating of a sinusoidal current as an irreversible heat source and the impedance measurement deviation it causes. Section 3.2.4 shows how the results shown in section 3.2.3 can be expanded to pulsed currents. Section 3.2.5 introduces the expansion of section 3.2.4 to constant currents and the impedance measurement deviation they cause. The derived equations estimate the heat generation, the temperature increase and the deviation of an impedance measurement based on the information of previous impedance measurements, the entropy and the impedance temperature dependency.

As introduced in the fundamentals chapter 2, there are several ways to measure entropy. The entropy data used in this thesis were acquired by the $\delta U/\delta T$ measurement method [84]. Several heat generation studies have been carried out so far. Bandhauer et al. [7] provides an extensive summary of these studies. Most of them are conducted under isothermal conditions. In section 3.2.3 to section 3.2.5 the irreversible heat generated by an NMC cell (see appendix A.2) is studied under adiabatic conditions. Al Hallaj et al. [2] studied the temperature increase of several cells under adiabatic conditions, but only for full charge/discharge cycles. Physiochemical models rely on an accurate heat generation model. Xiao and Choe [127] used four different heat sources to model the heat generated by the battery cell in its physiochemical model:

1. **Entropy heating:** The reversible heat caused by entropy and a current running through the battery. It either cools or heats the battery depending on the direction of the current and the sign of the entropy value.
2. **Ohmic heating:** Irreversible heat generated by the ohmic resistances of electronic and ionic conductors inside the battery.
3. **Heat by charge transfer and ionic transport:** Irreversible heat generated by the the intercalation of lithium into graphite and the phase changes on the cathode.
4. **Heat of mixing:** The formation and relaxation of concentration gradients creates heat. This irreversible heat represents the fact that the battery cell still keeps generating heat after the current has been turned off. It only represents a minor heat source [117].

Section 3.2.3 and 3.2.5 will show that for simpler models at least the two irreversible heat sources, ohmic and heat by charge transfer and ionic transport can be grouped together and modelled by only the heat generated over the real part of the impedance. Section 3.2.5 shows that this is possible over the whole frequency range down to constant currents. A similar approach was done by Nieto et al. [82] but instead of using impedance data he used the ohmic drop measured from current pulse measurements.

### 3.2.1 Impedance Temperature Dependency

In the fundamental chapter, section 2.1.2 already introduced the exponential temperature dependency of the exchange current. Figure 3.12 shows an exponential dependency of the impedance real and imaginary part on temperature for different measurement frequencies.

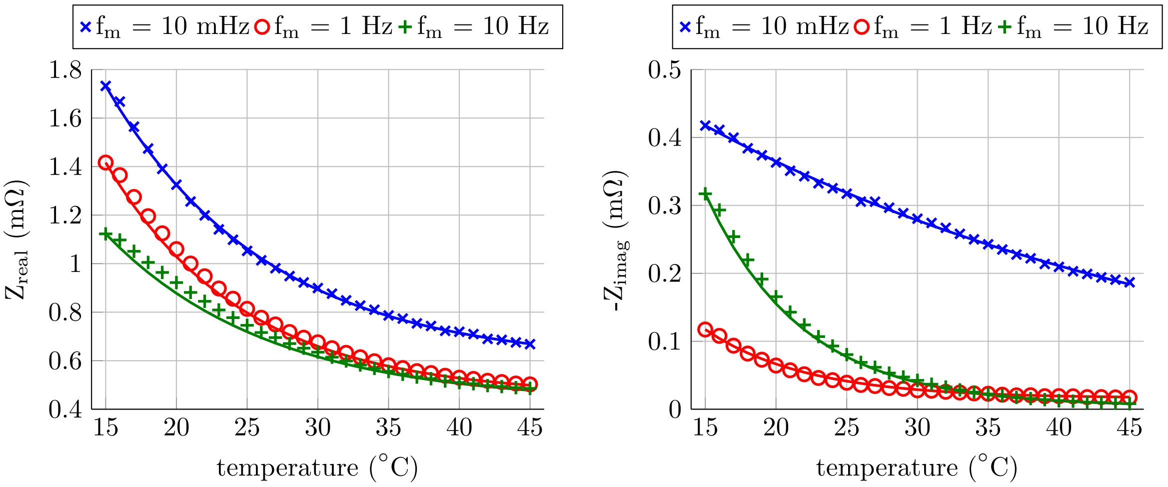

(a) Impedance real part.

(b) Impedance imaginary part.

Figure 3.12: Temperature dependency of the impedance at different measurement frequencies. (NMC pouch cell A.5, $SoC = 50\,\%$).

Andre et al. reported in [3] an exponential temperature dependency for all measured frequencies. Eddahech et al. [37] showed this effect for the resistances of equivalent circuits for li-ion batteries. Linden and Reddy showed in [73] the same behavior for Nickel-Metal Hydride (NiMH) batteries.

Although exponential, the impedance at every measurement frequency has a differently strong dependence on temperature. The dependency can be expressed by equation 3.49, with different values of Θ for each measurement frequency.

$$Z = Z_{\Theta} + Z_{\not\Theta} = A \cdot e^{T/\Theta} + Z_{\not\Theta} \tag{3.49}$$

By fitting the impedance measurements at different temperatures with the equation 3.49 the solid lines in figure 3.12 were drawn with the values in table 3.1.

| | | 10 mHz | 1 Hz | 10 Hz |
|---|---|---|---|---|
| real part | Θ (K) | -11.5104 | -9.9625 | -12.4715 |
| | $Z_{\Theta}$ (mΩ) | 0.6267 | 0.5000 | 0.4642 |
| imaginary part | Θ (K) | -24.1531 | -7.8905 | -8.1989 |
| | $Z_{\Theta}$ (mΩ) | -0.0620 | -0.0178 | -0.0079 |

Table 3.1: Parameters Θ and $Z_{\not\Theta}$ used for drawing the solid lines in figure 3.12.

The parameter $A$ in equation 3.49 is not calculated since the impedance at one temperature is determined starting with the knowledge of the impedance of another temperature and by using the fitted parameters Θ, $Z_{\not\Theta}$ with equation 3.50. The calculation has to be done separately for the real and for the imaginary part.

$$Z_2 - Z_{\not\Theta} = e^{(T_2-T_1)/\Theta} \cdot (Z_1 - Z_{\not\Theta}) \tag{3.50}$$

$Z_{\not\Theta}$ is the temperature independent part, which also has a physical representation. In a battery some of the resistance is created by the current collectors and wires, which have a negligible temperature dependency. A temperature independent negative phase shift is introduced by the parasitic capacitor which is created by the two current collectors. These are two sheets which are packed closely together and are insulated against each other. A temperature independent positive phase shift is introduced by the loop created by the current collectors and wires inside the battery. Dependent on the frequency, the negative or the positive phase shift is more present. $Z_\Theta = Z - Z_{\not\Theta}$ is the temperature dependent part of the impedance. The exponential temperature dependency can also be derived from the Arrhenius equation 3.51. Equation 3.52 to 3.57 show how an equation 3.57 similar to equation 3.50 can be derived from the Arrhenius equation. However, the parameters of equation 3.50 cannot be directly compared with the ones of the Arrhenius equation, but would need to be adjusted by the constant factors $c_1$, $c_2$ and $c_3$ in order to get a direct correspondence between them.

$$\begin{align}
k &= A \cdot e^{-E_A/(RT)} \tag{3.51}\\
\frac{k_1}{k_2} &= e^{\left[\left(\frac{-E_A}{RT_1}\right)-\left(\frac{-E_A}{RT_2}\right)\right]} \tag{3.52}\\
ln\frac{k_1}{k_2} &= -\frac{E_A \cdot (T_2 - T_1)}{RT_1T_2} \tag{3.53}\\
-\frac{RT_1T_2}{E_A}\left(ln(k_1) - ln(k_2)\right) &= T_2 - T_1 \tag{3.54}\\
T_1T_2 \cdot ln(k_2) - T_1T_2 \cdot ln(k_1) &= \frac{T_2 - T_1}{R/E_A} \tag{3.55}\\
\frac{\left(e^{ln(k_2)}\right)^{T_1T_2}}{\left(e^{ln(k_1)}\right)^{T_1T_2}} &= e^{\frac{T_2-T_1}{R/E_A}} \tag{3.56}\\
\underbrace{k_2^{T_1T_2}}_{c_1\cdot(Z_2-Z_{\not\Theta})} &= e^{(T_2-T_1)/\overbrace{\left(\frac{R}{E_A}\right)}^{c_3\cdot\Theta}} \cdot \underbrace{k_1^{T_1T_2}}_{c_2\cdot(Z_1-Z_{\not\Theta}} \tag{3.57}
\end{align}$$

Figure 3.13 shows the frequency dependency of the complex parameter $\Theta$ for 10 % and 50 % SoC. Low negative values of $\Theta$ signify a high temperature dependency. High negative values of $\Theta$ signify a low temperature dependency. The temperature dependency decreases sharply above a measurement frequency of 30 Hz for the real part and above a measurement frequency of 100 Hz for the imaginary part. A negative value indicates that the impedance decreases with increasing temperature, which is the case for all frequencies.

Figure 3.14 shows the frequency dependency of the complex parameter $Z_{\not\Theta}$ for 10 % and 50 % $SoC$. This value determines how much of the impedance is subject to temperature change. $(Z_1 - Z_{\not\Theta})$ is affected by the temperature change, whereas $Z_{\not\Theta}$ is not. The temperature dependent part $(Z_1 - Z_{\not\Theta})$ changes depending on the starting temperature $T_1$ used in equation 3.50. The value $Z_{\not\Theta}$, however, stays the same over the whole temperature range. The quickly rising real and imaginary part of $Z_{\not\Theta}$ above the intercept frequency create a smaller temperature dependency. This and the simultaneously quickly

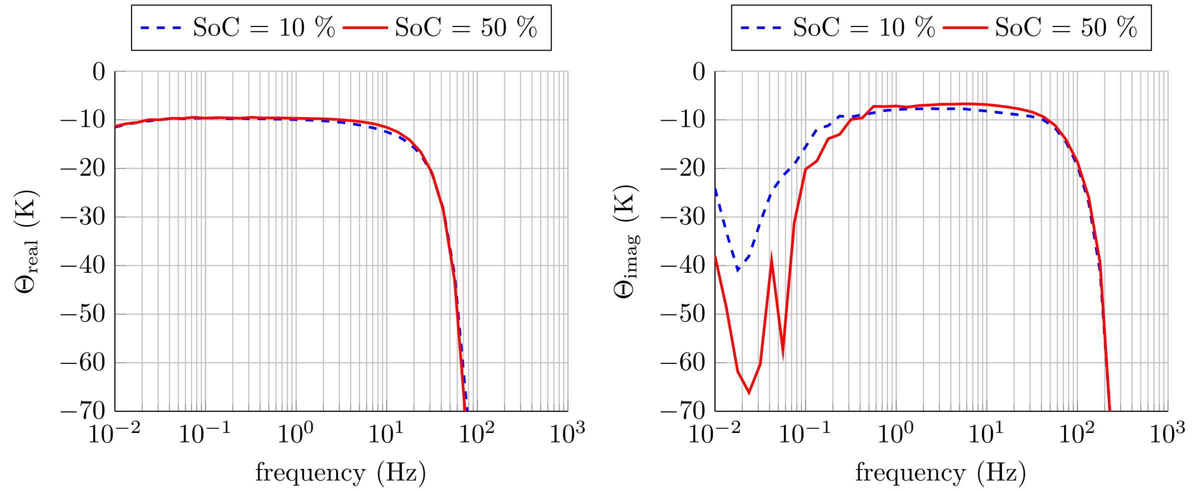

(a) Θ of the impedance real part.

(b) Θ of the impedance imaginary part.

Figure 3.13: Frequency dependency of the parameter Θ for the real and imaginary part of the impedance at 10 % and 50 % *SoC* (NMC pouch cell A.5, fitting range $\vartheta = 15$ to 45 °C).

rising exponential factor Θ indicate that the overall temperature dependency reduces so strongly above the intercept frequency that the temperature dependency is negligible. Above intercept frequency, the generated heat in the battery can also be neglected since the impedance measurements at these high frequencies can be done very quickly.

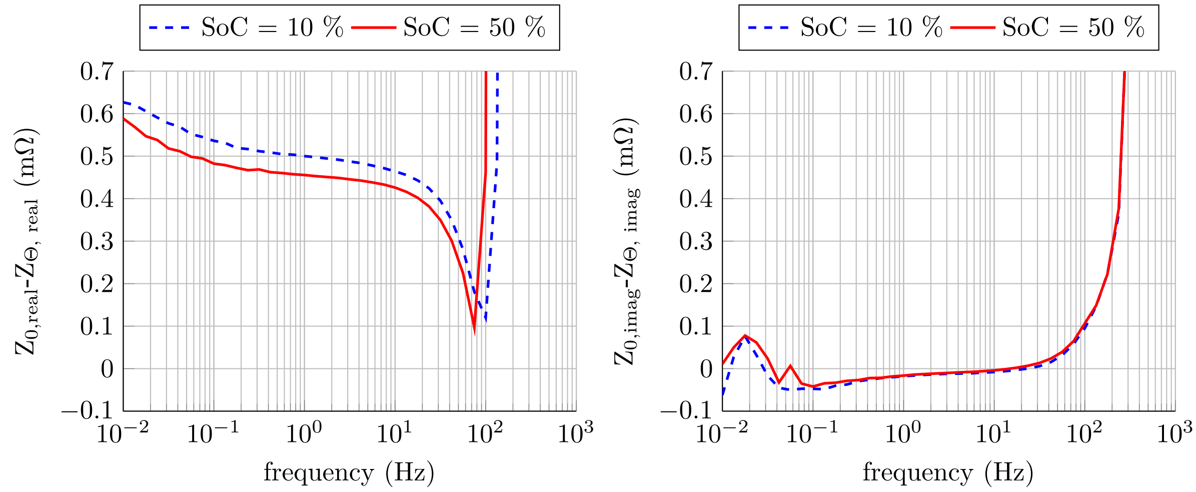

(a) Real part of $Z_{\not\vartheta}$.

(b) Imaginary part of $Z_{\not\vartheta}$.

Figure 3.14: Frequency dependency of the temperature independent part of the impedance $Z_{\not\vartheta}$ at 10% and 50% *SoC* (NMC pouch cell A.5, fitting range $\vartheta = 15$ to $45°C$).

### 3.2.2 Reversible Heat Generation from Sinusoidal Currents

This section shows by how much a sinusoidal current can heat up a cell during a single-sine measurement by entropy heating and the deviation it introduces to the measured impedance. Entropy heating is a reversible heating, meaning it can heat or cool a battery depending on the direction of the current flow. During charging, the battery is heated if the entropy value is positive, the battery is cooled if the entropy is negative. The effect is reversed during discharging. Equation 3.58 shows the temperature change over time when a current is flowing through the battery. Entropy is SoC dependent, but can be assumed constant for small SoC changes of less than one percent.

$$\Delta\vartheta(t) = \int \underbrace{\Delta S(SoC)\frac{T}{zF}}_{=HGR_e} \cdot \frac{1}{C_{th}} \cdot I(t) \cdot \mathrm{d}t \tag{3.58}$$

For simplifying the equation an entropic heat generation rate $HGR_e$ is defined. It describes the amount of heat generated in Joule per Coulomb, which is charged into or discharged from the battery cell. The ratio $HGR_e$ over $C_{th}$ is the temperature increase in Kelvin per Coulomb, which is charged into or discharged from the battery cell. By integrating the current over time equation 3.59 gives the time dependent temperature change during an impedance measurement.

$$\Delta\vartheta(t) = \int \frac{HGR_e}{C_{th}} \cdot \hat{I}_m \cdot \sin(\omega_m t) \cdot \mathrm{d}t = -\frac{HGR_e}{C_{th}} \frac{\hat{I}_m \cdot T_m}{2\pi} \cdot \cos(\omega_m t) \tag{3.59}$$

Section 3.2.1 derived the temperature dependency of the impedance. It separated the impedance into a temperature dependent part $Z_{\Theta}$ and a temperature independent part $Z_{\not\Theta}$. The response voltage can be equally separated into a temperature dependent part $v_{\Theta}(t)$ and a temperature independent part $v_{\not\Theta}(t)$.

$$Z(t) = Z_{\Theta} \cdot e^{\frac{\Delta T(t)}{\Theta}} + Z_{\not\Theta} \tag{3.60}$$

$$Z(t) = Z_{\Theta} \cdot e^{-\frac{HGR_e}{C_{th}} \frac{\hat{I}_m \cdot T_m}{2\pi \cdot \Theta} \cdot cos(\omega_m t)} + Z_{\not\Theta} \tag{3.61}$$

$$v(t) = Z(t) \cdot \hat{I}_m \cdot \sin(\omega_m t) \tag{3.62}$$

$$v(t) = \underbrace{Z_{\Theta} \cdot e^{-\frac{HGR_e}{C_{th}} \frac{\hat{I}_m \cdot T_m}{2\pi \cdot \Theta} \cdot \cos(\omega_m t)} \cdot \hat{I}_m \cdot \sin(\omega_m t)}_{=v_{\Theta}(t)} + \underbrace{Z_{\not\Theta} \cdot \hat{I}_m \cdot \sin(\omega_m t)}_{=v_{\not\Theta}(t)} \tag{3.63}$$

For the derivation of the deviation caused by entropy heating, the temperature dependent part $v_{\Theta}(t)$ is the one that causes the measurement deviation and is transformed into the frequency-domain by separating the Fourier transformation into the real part $a_1$ and imaginary part $b_1$.

$$\mathrm{F}\{v_{\Theta}(t)\} = \frac{2}{T_m} \int_0^{T_m} \underbrace{Z_{\Theta} \cdot e^{-\frac{HGR_e}{C_{th}} \frac{\hat{I}_m \cdot T_m}{2\pi \cdot \Theta} \cdot \cos(\omega_m t)} \cdot \hat{I}_m \cdot \sin(\omega_m t)}_{=v_{\Theta}(t)} \cdot e^{-j\omega_m t} \mathrm{d}t = a_1 - jb_1 \tag{3.64}$$

$$a_1 = \frac{Z_\Theta \hat{I}_m}{T_m} \cdot 2 \int_0^{T_m} e^{-\frac{HGR_e}{C_{th}} \frac{\hat{I}_m \cdot T_m}{2\pi \cdot \Theta} \cdot \cos(\omega_m t)} \cdot \underbrace{\sin(\omega_m t) \cdot \cos(\omega_m t)}_{\frac{1}{2} \cdot \sin(2\omega_m t) \text{ with C.3}} \mathrm{d}t \tag{3.65}$$

$$= \frac{Z_\Theta \hat{I}_m}{T_m} \underbrace{\int_0^{T_m} e^{-\frac{HGR_e}{C_{th}} \frac{\hat{I}_m \cdot T_m}{2\pi \cdot \Theta} \cdot \cos(\omega_m t)} \cdot \sin(2\omega_m t) \mathrm{d}t}_{0 \text{ with C.26}} \tag{3.66}$$

$$= 0 \tag{3.67}$$

$$b_1 = \frac{Z_\Theta \hat{I}_m}{T_m} \cdot 2 \int_0^{T_m} e^{-\frac{HGR_e}{C_{th}} \frac{\hat{I}_m \cdot T_m}{2\pi \cdot \Theta} \cdot \cos(\omega_m t)} \cdot \underbrace{\sin^2(\omega_m \cdot t)}_{\frac{1}{2} \cdot (1 - \cos(2\omega_m t)) \text{ with C.4}} \mathrm{d}t \tag{3.68}$$

$$= \frac{Z_\Theta \hat{I}_m}{T_m} \underbrace{\int_0^{T_m} e^{-\frac{HGR_e}{C_{th}} \frac{\hat{I}_m \cdot T_m}{2\pi \cdot \Theta} \cdot \cos(\omega_m t)} \mathrm{d}t}_{T_m \cdot \mathcal{I}_0\left(\frac{HGR_e}{C_{th}} \frac{\hat{I}_m \cdot T_m}{2\pi \cdot \Theta}\right) \text{ with C.29}}$$

$$- \frac{Z_\Theta \hat{I}_m}{T_m} \underbrace{\int_0^{T_m} e^{-\frac{HGR_e}{C_{th}} \frac{\hat{I}_m \cdot T_m}{2\pi \cdot \Theta} \cdot \cos(\omega_m t)} \cdot cos(2\omega_m t) \mathrm{d}t}_{(-1)^2 T_m \cdot \mathcal{I}_2\left(\frac{HGR_e}{C_{th}} \frac{\hat{I}_m \cdot T_m}{2\pi \cdot \Theta}\right) \text{ with C.24}} \tag{3.69}$$

$$= Z_\Theta \hat{I}_m \cdot \left( \mathcal{I}_0 \left( \frac{HGR_e}{C_{th}} \frac{\hat{I}_m \cdot T_m}{2\pi \cdot \Theta} \right) - \mathcal{I}_2 \left( \frac{HGR_e}{C_{th}} \frac{\hat{I}_m \cdot T_m}{2\pi \cdot \Theta} \right) \right) \tag{3.70}$$

$$\mathrm{F}\{v_\Theta(t)\} = -j \cdot Z_\Theta \hat{I}_m \cdot \left( \mathcal{I}_0 \left( \frac{HGR_e}{C_{th}} \frac{\hat{I}_m \cdot T_m}{2\pi \cdot \Theta} \right) - \mathcal{I}_2 \left( \frac{HGR_e}{C_{th}} \frac{\hat{I}_m \cdot T_m}{2\pi \cdot \Theta} \right) \right) \tag{3.71}$$

The measured impedance consists of both the response of the temperature dependent part $\mathrm{F}\{v_\Theta(t)\}$ from equation 3.71 and the temperature independent part, which does not introduce any measurement deviation (see equation 3.72). Therefore, the temperature independent part reduces the deviation by the ratio $\frac{Z_{\not\Theta}}{Z_0}$. Equation 3.73 shows a modified version of equation 3.8. With it, the relative measurement deviation from entropy heat generation caused by a sinusoidal current can be stated as shown in equation 3.74.

$$Z_m = \frac{\mathrm{F}\{v_\Theta(t)\}}{-j\hat{I}_m} + Z_{\not\Theta} \tag{3.72}$$

$$e_Z = \frac{\mathrm{F}\{v_\Theta(t)\}}{-j\hat{I}_m \cdot Z_0} + \frac{Z_0 - Z_\Theta}{Z_0} - 1 = \frac{\mathrm{F}\{v_\Theta(t)\}}{-j\hat{I}_m \cdot Z_0} - \frac{Z_\Theta}{Z_0} \tag{3.73}$$

$$e_Z = \frac{Z_\Theta}{Z_0} \cdot \left[ \mathcal{I}_0 \left( \frac{HGR_e}{C_{th}} \frac{\hat{I}_m \cdot T_m}{2\pi \cdot \Theta} \right) - \mathcal{I}_2 \left( \frac{HGR_e}{C_{th}} \frac{\hat{I}_m \cdot T_m}{2\pi \cdot \Theta} \right) - 1 \right] \tag{3.74}$$

Figure 3.15 shows the change in impedance during an impedance measurement caused by entropy heating. With a 3 CA current amplitude, the maximum impedance change during the measurement goes beyond 0.1 % for both, the real part and the imaginary part.

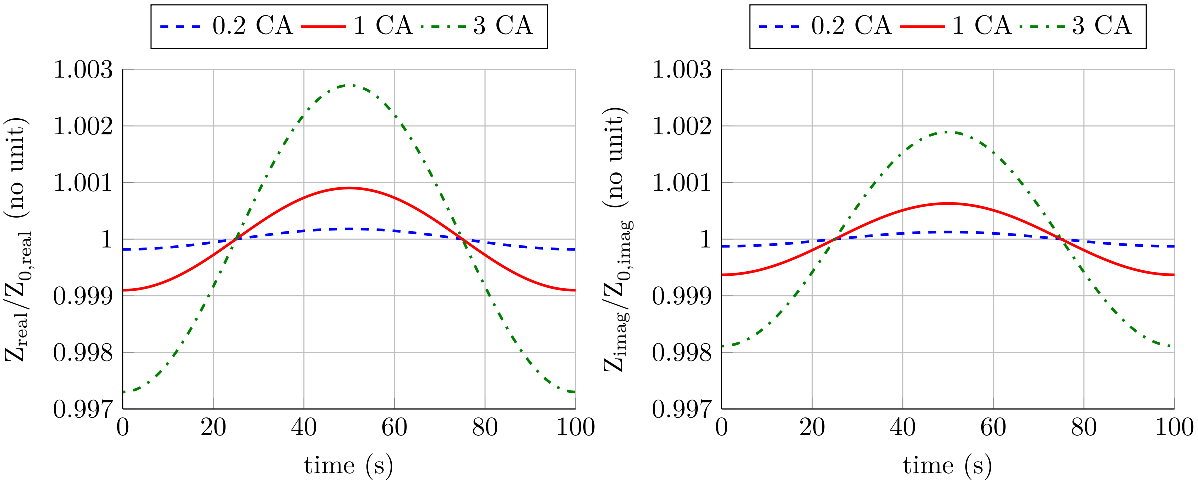

(a) Impedance real part.

(b) Impedance imaginary part.

Figure 3.15: Simulated impedance change from entropy heating caused by the excitation current during the impedance measurement. The graphs show no transitory effect but show one period of a theoretically infinitely long applied excitation current (NMC pouch cell A.5, $SoC = 50\,\%$, $f_m = 10\,\mathrm{mHz}$).

With the derived equation the deviations for the modulus and the phase can be calculated directly. Figure 3.16 shows these two deviations over the measurement frequency for different excitation current amplitudes. The modulus deviation for a 3 CA excitation current amplitude with 10 mHz measurement frequency is below $10^{-3}\,\%$ and the phase deviation even around $10^{-5}\,°$. Both are well below the initially set thresholds of 0.1 % and 0.1 °, the phase deviation even more than the modulus deviation.

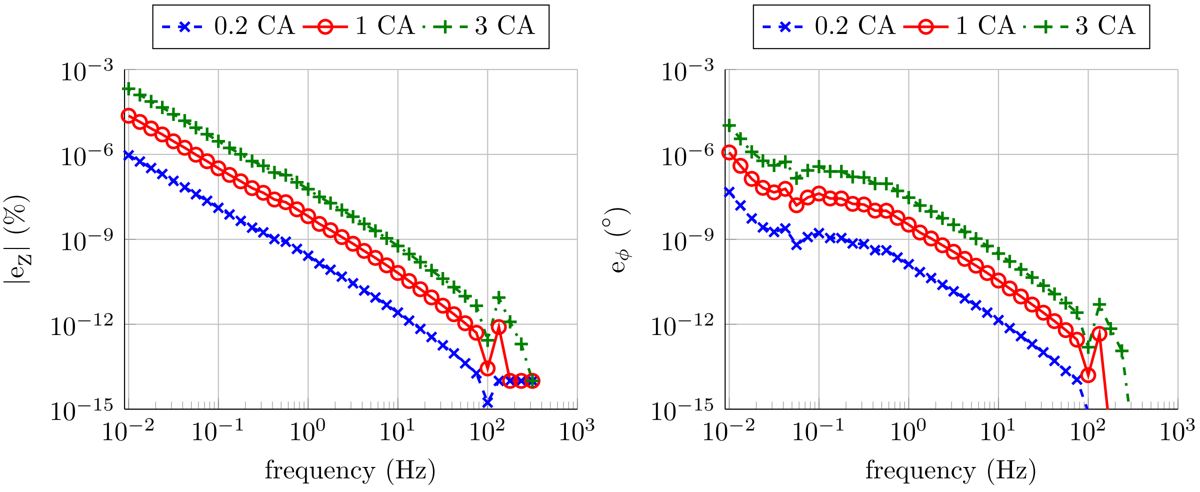

(a) Modulus deviation.

(b) Phase deviation.

Figure 3.16: Maximum measurement deviation by temperature change from entropy heating caused by the excitation current dependent on the measurement frequency and C-rates (NMC pouch cell A.5, $SoC = 50\,\%$, $\vartheta = 25\,°\mathrm{C}$).

The reason why the rather large change in impedance from figure 3.15 did not result in a large modulus and phase deviation is that the change in impedance has a phase shift of $\frac{\pi}{2}$ to the phase of the excitation current. Therefore, the change in impedance of the real part shown in figure 3.15a does affect the measured impedance of the imaginary part. Since the imaginary part has a minor contribution to the modulus, any deviation in the imaginary impedance hardly changes the impedance modulus. It has, however, a large effect on the relative deviation of the impedance phase. But in this case only the absolute value is considered, to which the imaginary part, again, has little effect.

### 3.2.3 Irreversible Heat Generation from Sinusoidal Currents

A preliminary study and measurements have been carried out during the supervision of the Master Thesis of Vergote [121]. The measurements shown here are from a different battery cell and data set, which were not acquired or used in his Master Thesis.

This section discusses by how much a sinusoidal current can increase the temperature of a battery cell. It introduces a method for estimating this temperature change from the real part of the impedance. It derives an equation for the associated deviation of the impedance measurement, which can be assessed before the measurement is even taken based on past impedance measurements. Section 3.2 already introduced several different heat sources. Section 3.2.2 discussed the measurement deviation introduced by entropy heating. This section will summarize all the other heating types introduced at the beginning of section 3.2 to the term impedance heating, since their heat contribution can be estimated from the impedance measurement. As opposed to entropy heating, which is reversible, the impedance heating is irreversible. Section 3.2.3.1 will introduce the measurement setup, which was used to produce the results in this and the following two sections 3.2.4 and 3.2.5. Section 3.2.3.2 will show that the impedance measurement is a possible predictor of the irreversible heat generated by a sinusoidal current throughout the whole frequency range. The heat generated during a sinusoidal current is not constant, it has its maximum during the negative or positive amplitude and a minimum when the current passes through zero. Section 3.2.3.3 takes this effect into account and derives the deviation on the impedance measurement caused by a sinusoidal excitation current.

#### 3.2.3.1 Measurement Setup

The heat generation rate under different conditions was determined in the following measurement setup. By running a large current signal through a battery cell, the cell heat itself by its inner resistance. At the same time, the change in cell temperature under adiabatic conditions was monitored. Figure 3.17 shows the measurement as it was carried out in an Accelerated Rate Calorimeter (ARC). This device simulates an adiabatic environment for which no heat is transferred between the system under test and the outside world. A battery cell (cylindrical LFP-cell A.1) was placed in the ARC. A signal generator (Agilent 33500B Waveform Generator) and an amplifier (Servowatt DCP780/30) connected to the cell charged and discharged the cell with sinusoidal currents, current pulses and constant currents of various current amplitudes and frequencies at several SoCs. Besides the power wires with which the cell was connected to the amplifier, the cell was connected with sense wires to a high resolution data acquisition system (DEWEsoft®). Besides the temperature sensors of the ARC, a thermocouple was placed directly on the steel casing of the cell. Due to the adiabatic environment of the ARC, the cell could not cool itself by a heat transfer to the surrounding air. The ARC's heating coils ensured that the air temperature in the compartment in which the cell was placed always followed the temperature measured on the casing of the cell. The excitation current, voltage response and cell temperature were recorded at the same time.

Figure 3.18 shows the measurement principle. A current signal is applied to the cell. Because of the functionality of the ARC, all the heat generated in the cell goes into an increase in temperature of the cell. As long as current is flowing, the temperature of the cell increases continuously over the measurement time. The more heat is generated, the steeper is the slope of the temperature increase. The current signal can have any form: sinusoidal, pulsed or constant. For the further explanation of the measurement principle, a sinusoidal current is assumed.

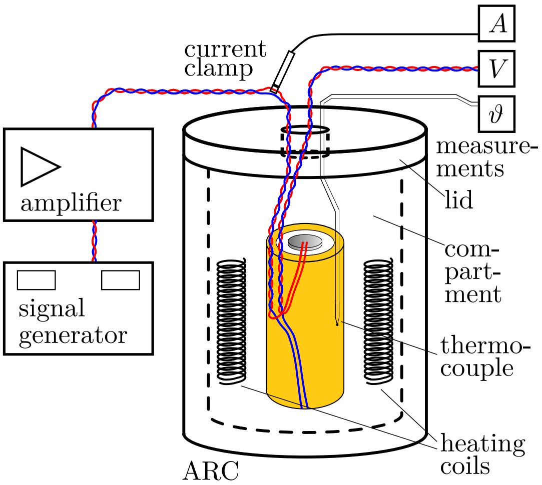

Figure 3.17: Measurement Setup.

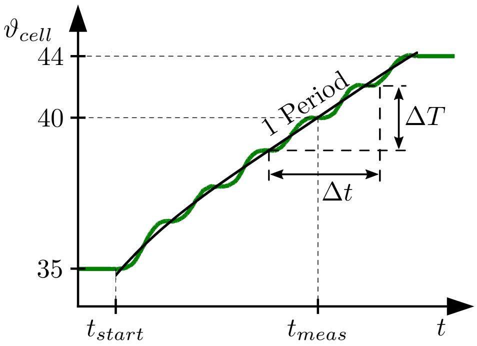

Figure 3.18: Measurement Principle.

The inclination of this slope is an indicator of the amount of heat generated. The total heat flux can be calculated by equation 3.75 and should be equal to the estimation derived from the real part of the impedance as shown in equation 3.76. The heat generation rate $HGR$ used throughout this chapter is the heat generated in Watt normalized by the square of the effective current that generates it (see equation 3.77). For a single frequency sinusoidal current, it is equal to the real part of the impedance $Z_{real}$.

$$\dot{Q} = C_{th} \cdot \frac{\Delta\vartheta}{\Delta t} \tag{3.75}$$

$$P = \dot{Q} = Z_{real} \cdot I_{eff}^2 \tag{3.76}$$

$$HGR = Z_{real} = \frac{C_{th}}{I_{eff}^2} \cdot \frac{\Delta\vartheta}{\Delta t} \tag{3.77}$$

At this point it seems unnecessary to define a new term when the value corresponds to the impedance real part at a particular frequency. In the next two sections 3.2.4 and 3.4.6, this will not be the case anymore and the definition of the heat generation rate $HGR$ will become beneficial. In order to stay consistent with that terminology and the entropic heat generation rate from the last section 3.2.2 it is already used here.

For most frequencies, the change of temperature occurs in a straight line, since the time constant of the heat transfer from the jelly roll to the casing is much larger than the period of the excitation current. For low frequencies this is not the case anymore. Figure 3.18 shows this effect for a measurement frequency of $f_m = 1\,\text{mHz}$. In this case, the temperature rise is no longer a straight line but superpositioned with a sinusoidal signal with double the frequency of the measurement frequency. The superpositioned signal has double the measurement frequency since the heat is generated equally during the positive and the negative half-sine wave. It is actually only almost equal as section 3.4 will show, but sufficiently equal for this measurement. Over the course of the test, the temperature of the cell changes significantly. With the increase in temperature the impedance value of the cell decreases. Figure 3.18 shows this effect. The superpositioned sinusoidal signal causes the temperature to increase in 'steps' for every half-sine wave of the sinusoidal excitation current. The strongest inclination occurs during the amplitude of the current and the 'plateaus' are reached once the excitation current crosses through zero. The first 'step', when the cell was at $35°C$ to $36°C$, is larger than the next and any other subsequent 'step' after that.

This changing impedance over the course of the measurement requires special care during the analysis of the measurement data. For high frequencies, the period is much shorter than the heat transfer time from the jelly roll to the casing. For them the measurement of the inclination at the measurement temperature should include a few periods in order to eliminate noise. For low frequencies, the period is longer than the heat transfer time from the coil to the casing. The measurement of the inclination should include only one period, with half a period before and after the measurement temperature. It is important that the slope of the temperature increase is measured over one whole period of the excitation current. Half of the sine wave is not sufficient, since an entropy value different from zero can make the heat contribution from the positive and the negative sine wave diverge.

The measurement setup did not secure perfect adiabatic conditions since the cables needed for the excitation current, the measurement of the voltage response and the cell temperature constituted a path for heat to escape the adiabatic system. The calibration of the ARC before the experiment series takes this into account as any other heat flux, which escapes the system through the imperfect insulation of the test compartment. The measurements of the heat generation rate were therefore not affected. However, the thermal capacity used in the experiments was affected. A separate measurement of the thermal capacity of the bare cell could not be used in the equation 3.75. The heat capacity of the bare cell was higher than the heat capacity of the actual cell used. All the wires attached helped the heat to escape. Therefore the measurement at 1 kHz was used in order to determine the effective thermal capacity of the cell and the connected wires for the experiments undertaken. Equation 3.78 determined a thermal capacity of $33.8\,\mathrm{Ws\,K^{-1}}$. This value is used for all following calculations.

$$C_{th} = \left.\frac{Z_{real}}{\frac{\Delta\vartheta}{\Delta t}}\right|_{1\,\mathrm{kHz}} \cdot \left(\frac{\hat{I}_m}{\sqrt{2}}\right)^2 \tag{3.78}$$

The thermal capacity of the bare cell was determined by a standard calorimetric measurement performed in the same calorimeter used for the experiments in this section. The measured thermal capacity was $38.4\,\mathrm{Ws\,K^{-1}}$, which is closer to other values reported in the literature for 18650 cells [46]. Since the determined value is a bit lower, it confirms that heat was lost over the wires connected to the cell.

#### 3.2.3.2 Impedance as an Indicator for the Irreversible Heat Generation Rate

Figure 3.19 plots the heat generation rate measured in the experiment by red crosses. It was calculated by equation 3.77 using the thermal capacity $C_{th} = 33.8\,\mathrm{Ws\,K^{-1}}$. It compares these measurements with the real part of the impedance $Z_{real}$. The figure proves the possibility of using the real part of the impedance as an estimator for the generated heat. The two values compare very well with each other.

Only for the lower frequencies the heat generation rate derived from $Z_{real}$ overestimates the generated heat.

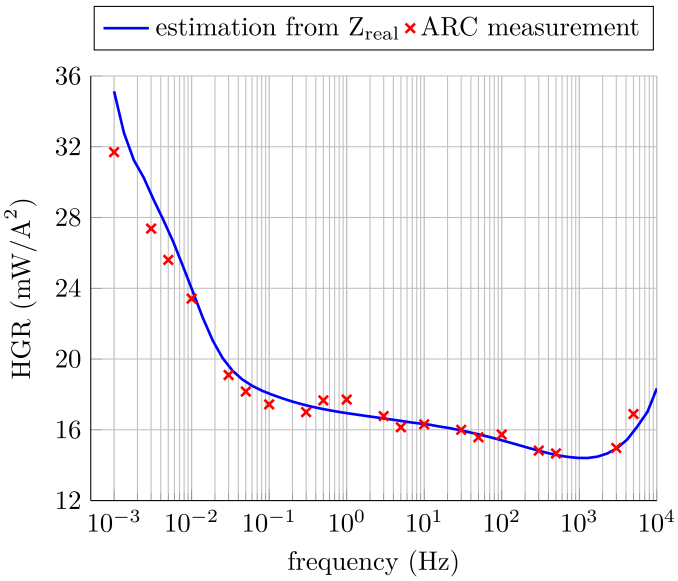

Figure 3.19: Heat generation rate for sinusoidal currents. measured by direct measurements in an ARC and indirect measurements by EIS (cylindrical LFP-cell A.1, $SoC = 50\,\%$, $\vartheta = 40\,°\mathrm{C}$, $\hat{I}_m = 3\,\mathrm{CA}$).

This conclusion also holds true for different SoC levels. Figure 3.20a shows the same match for an experiment series at 90 % SoC. Figure 3.20b shows that the measurement values from the ARC and the estimation with $Z_{real}$ match each other over the temperature range measured and for different current amplitudes. The best consistency is achieved when the impedance is measured with the same amplitude as the current with which the ARC experiment is performed. The measurement deviation that is obtained by using a different amplitude is governed by the same sources as discussed throughout this chapter.

#### 3.2.3.3 Impedance Measurement Deviation Caused by Alternating Part of Impedance Heating for a Single-sine Measurement

With the heat generation rate from equation 3.77 and the thermal capacity the time dependent temperature increase over the course of an impedance measurement can be expressed by integrating over the square of the current signal:

$$\Delta\vartheta(t) = \int \frac{HGR_{fm}}{C_{th}} \cdot \underbrace{\left(\hat{I}_m \cdot \sin(\omega_m t)\right)^2}_{=\frac{\hat{I}_m{}^2}{2}(1-\cos(2\omega_m t)) \text{ with C.4}} \cdot \mathrm{d}t \tag{3.79}$$

$$\Delta\vartheta(t) = \underbrace{\frac{HGR_{fm}}{C_{th}} \cdot \hat{I}_m{}^2 \frac{t}{2}}_{\text{constant part}} \underbrace{- \frac{HGR_{fm}}{C_{th}} \cdot \frac{\hat{I}_m{}^2 \cdot T_m}{8\pi} \cdot \sin(2\omega_m t)}_{\text{alternating part}} \tag{3.80}$$

The constant part of the impedance heating during the impedance measurement follows the same rules as an additional constant current. This is why it will be dealt with in the section 3.2.5. This section only focuses on the alternating part. The voltage response is the voltage drop caused by the sinusoidal

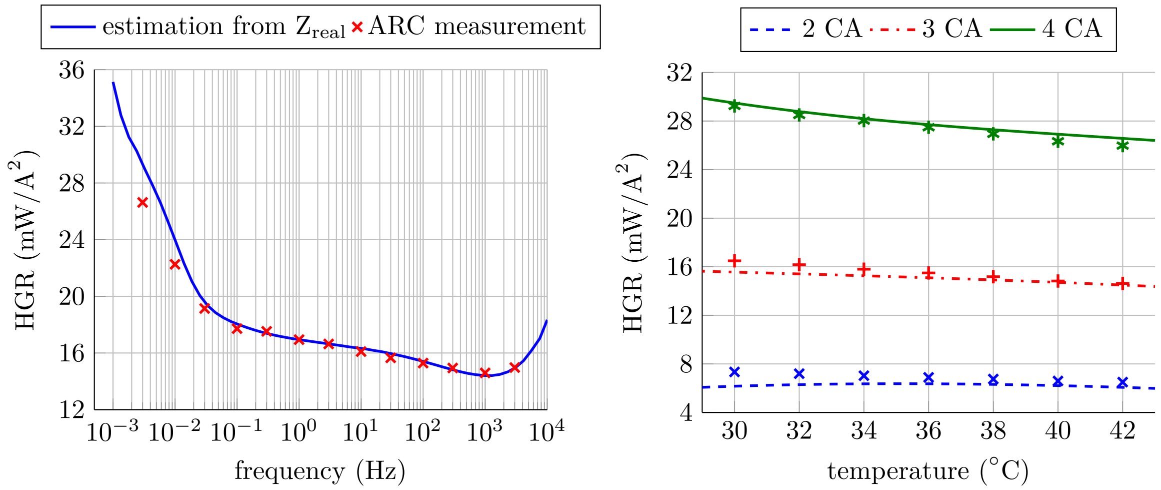

(a) Heat generation rate for 90 % SoC ($\vartheta = 40\,°\mathrm{C}$, $\hat{I}_m = 3\,\mathrm{CA}$).

(b) Heat generation rate over temperature dependent on the current amplitude. ($SoC = 50\,\%$, $f_m = 300\,\mathrm{Hz}$). Solid lines indicate the estimation from $Z_{real}$ and the dots the values obtained from the ARC measurement.

Figure 3.20: Proof of the consistency of the EIS measurement as an indicator for the heat generation rate for different SoCs, current amplitudes and temperatures (cylindrical LFP-cell A.1).

measurement current over the impedance. For deriving the deviation, only the voltage response of the temperature dependent impedance part $Z_\Theta$ is changed by the alternating temperature change from equation 3.80. Only this part is of interest and transformed into the frequency-domain via the Fourier transformation (see equation 3.81). The Fourier transformation is separated into the real $a_1$ and into the imaginary part $b_1$:

$$\mathrm{F}\{v_\Theta(t)\} = \frac{2}{T_m}\int_0^{T_m} Z_\Theta \cdot e^{-\frac{HGR_{fm}}{C_{th}}\cdot\frac{\hat{I}_m{}^2\cdot T_m}{8\pi\cdot\Theta}\cdot\sin(2\omega_m t)}\cdot \hat{I}_m\cdot\sin(\omega_m t)\cdot e^{-j\omega_m t}\mathrm{d}t = a_1 - jb_1 \tag{3.81}$$

$$a_1 = \frac{Z_\Theta \hat{I}_m}{T_m}\cdot 2\int_0^{T_m} e^{-\frac{HGR_{fm}}{C_{th}}\cdot\frac{\hat{I}_m{}^2\cdot T_m}{8\pi\cdot\Theta}\cdot\sin(2\omega_m t)}\cdot\underbrace{\sin(\omega_m t)\cdot\cos(\omega_m t)}_{\frac{1}{2}\cdot\sin(2\omega_m t)\text{ with C.3}}\mathrm{d}t \tag{3.82}$$

$$= \frac{Z_\Theta \hat{I}_m}{T_m}\int_0^{T_m} e^{-\frac{HGR_{fm}}{C_{th}}\cdot\frac{\hat{I}_m{}^2\cdot T_m}{8\pi\cdot\Theta}\cdot\sin(2\omega_m t)}\cdot\sin(2\omega_m t)\mathrm{d}t \tag{3.83}$$

$$= -Z_\Theta \hat{I}_m\cdot\mathcal{I}_1\left(\frac{HGR_{fm}}{C_{th}}\cdot\frac{\hat{I}_m{}^2\cdot T_m}{8\pi\cdot\Theta}\right)\quad\text{with C.25} \tag{3.84}$$

$$b_1 = \frac{Z_\Theta \hat{I}_m}{T_m} \cdot 2 \int_0^{T_m} e^{-\frac{HGR_{fm}}{C_{th}} \cdot \frac{\hat{I}_m{}^2 \cdot T_m}{8\pi \cdot \Theta} \cdot \sin(2\omega_m t)} \cdot \underbrace{\sin^2(\omega_m t)}_{\frac{1}{2}\cdot(1-\cos(2\omega_m t)) \text{ with C.4}} \mathrm{d}t \tag{3.85}$$

$$\begin{aligned} &= \frac{Z_\Theta \hat{I}_m}{T_m} \underbrace{\int_0^{T_m} e^{-\frac{HGR_{fm}}{C_{th}} \cdot \frac{\hat{I}_m{}^2 \cdot T_m}{8\pi \cdot \Theta} \cdot \sin(2\omega_m t)} \mathrm{d}t}_{T_m \cdot \mathcal{I}_0\left(\frac{HGR_{fm}}{C_{th}} \cdot \frac{\hat{I}_m{}^2 \cdot T_m}{8\pi \cdot \Theta}\right) \text{ with C.29}} \\ &\quad - \frac{Z_\Theta \hat{I}_m}{T_m} \underbrace{\int_0^{T_m} e^{-\frac{HGR_{fm}}{C_{th}} \cdot \frac{\hat{I}_m{}^2 \cdot T_m}{8\pi \cdot \Theta} \cdot \sin(2\omega_m t)} \cdot \cos(2\omega_m t) \mathrm{d}t}_{=0 \text{ with C.27}} \end{aligned} \tag{3.86}$$

$$= Z_\Theta \hat{I}_m \cdot \mathcal{I}_0\left(\frac{HGR_{fm}}{C_{th}} \cdot \frac{\hat{I}_m{}^2 \cdot T_m}{8\pi \cdot \Theta}\right) \tag{3.87}$$

$$\mathrm{F}\{v_\Theta(t)\} = -Z_\Theta \hat{I}_m \cdot \left[\mathcal{I}_1\left(\frac{HGR_{fm}}{C_{th}} \cdot \frac{\hat{I}_m{}^2 \cdot T_m}{8\pi \cdot \Theta}\right) + j\mathcal{I}_0\left(\frac{HGR_{fm}}{C_{th}} \cdot \frac{\hat{I}_m{}^2 \cdot T_m}{8\pi \cdot \Theta}\right)\right] \tag{3.88}$$

As in section 3.2.2, equation 3.89 introduces again the temperature independent part of the impedance, which reduces the relative deviation by the ratio $\frac{Z_\Theta}{Z_0}$. Equation 3.90 shows the measurement deviation introduced by impedance heating caused by the alternating part of the excitation current.

$$e_Z = \frac{\mathrm{F}\{v_\Theta(t)\}}{-j\hat{I}_m \cdot Z_0} + \frac{Z_0 - Z_\Theta}{Z_0} - 1 = \frac{\mathrm{F}\{v_\Theta(t)\}}{-j\hat{I}_m \cdot Z_0} - \frac{Z_\Theta}{Z_0} \tag{3.89}$$

$$e_Z = \frac{Z_\Theta}{Z_0} \cdot \left[\mathcal{I}_0\left(\frac{HGR_{fm}}{C_{th}} \cdot \frac{\hat{I}_m{}^2 \cdot T_m}{8\pi \cdot \Theta}\right) - j\mathcal{I}_1\left(\frac{HGR_{fm}}{C_{th}} \cdot \frac{\hat{I}_m{}^2 \cdot T_m}{8\pi \cdot \Theta}\right) - 1\right] \tag{3.90}$$

Figure 3.21 shows the change in impedance during an impedance measurement caused by impedance heating. With a 3 CA measurement current amplitude at a measurement frequency of 10 mHz, the maximum impedance change during the measurement goes beyond 0.1 % for the real part and the imaginary part.

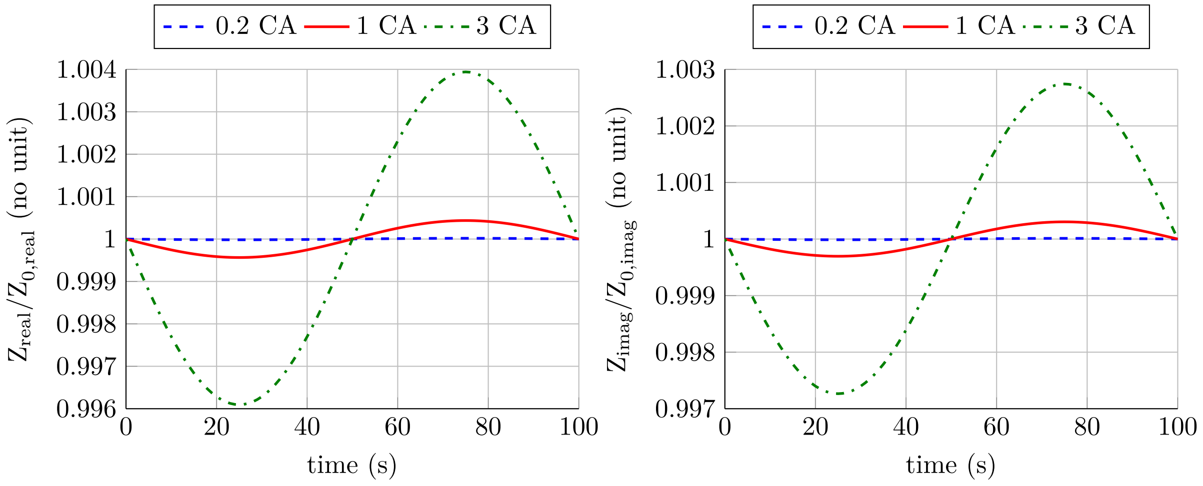

(a) Impedance real part.

(b) Impedance imaginary part.

Figure 3.21: Simulated impedance change from the alternating part of the impedance heating caused by the excitation current during the impedance measurement (NMC pouch cell A.5, $SoC = 50\,\%$, $f_m = 10\,\text{mHz}$).

Figure 3.22 shows the resulting modulus and phase deviation directly calculated with the equation 3.90. The maximum modulus deviation is 0.46 % and the maximum phase deviation is 0.26 ° for an excitation current of 3 CA and a measurement frequency of 10 mHz.

The deflection of the real and imaginary impedance shown in figure 3.21 is only around 30% larger than the ones shown in figure 3.15. The modulus deviation is by a factor of 100 and the phase deviation by a factor of $10^4$ larger. This is mainly caused by the fact that the deflection in the real and imaginary impedance only has a small phase delay. $\mathcal{I}_0$ is much larger as $\mathcal{I}_1$ for the same argument (see appendix C.5). This makes the deflection in real impedance directly affect the real impedance measurement. The same is true for the imaginary impedance. The deflection of the real impedance for entropy heating shown in figure 3.15a had a phase delay of $\frac{\pi}{2}$ and therefore affected the imaginary impedance measurement. The same is true for the deflection in imaginary impedance and the real impedance measurement. This indirect effect on the impedance measurement causes the low modulus and phase deviations in the case of entropy heating. For impedance heating the deviations shown in figure 3.22 correspond well with the deflections shown in figure 3.21.

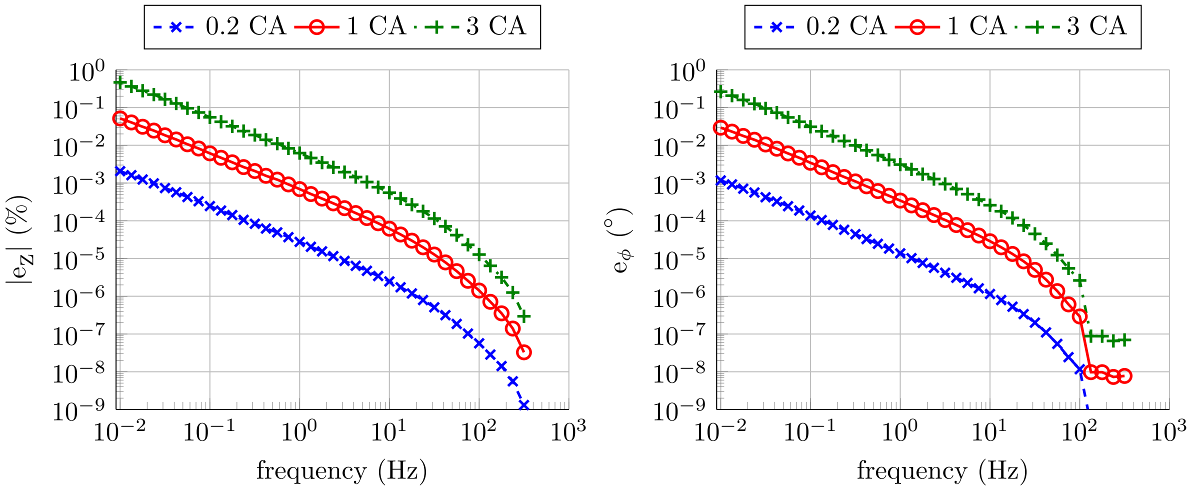

(a) Modulus deviation.

(b) Phase deviation.

Figure 3.22: Measurement deviation by temperature change from impedance heating caused by the excitation current dependent on the measurement frequency and measurement current amplitude (NMC pouch cell A.5, $SoC = 50\,\%$).

### 3.2.4 Irreversible Heat Generation from Pulsed Currents

A preliminary study and measurements have been carried out during the supervision of the Master Thesis of Vergote [121]. The measurements shown here are from a different battery cell and data set, which was not acquired or used in his Master Thesis.

Real sinusoidal currents as shown in the previous section 3.2.3 usually do not occur in a real application. Load currents are rather random functions, pulses or long constant currents. Frequency decomposition is a method in which the frequency components of signal are examined separately. In this section the applicability of this method is proven for the determination of the heat generated inside a battery cell. Section 3.2.4.1 uses a pulse to exemplify this method. Section 3.2.4.2 proofs the applicability of this method for the determination of the heat generation rate of pulses.

### 3.2.4.1 Decomposition of Pulse Trains

When decomposing a signal into its frequency parts it is transformed into the frequency-domain. Which constitutes an equivalent representation of the same signal. Figure 4.7 shows this method for the example of a pulse train with a duty cycle of 50 %.

The frequency-domain in figure 3.23b shows the fundamental frequency in red, which is the same frequency as the one of the pulse. Besides the fundamental there are several harmonics that occur at uneven multiples of the harmonic frequency. Equation 3.91 to 3.93 give the rules for the magnitude of the harmonics.

$$D = \frac{t_{on}}{t_{on} + t_{off}} = \frac{1}{2} \tag{3.91}$$

$$a_k = \frac{2}{k} \cdot \frac{2I}{\pi} \cdot \sin(k\pi D) = \frac{2}{k} \cdot \frac{2I}{\pi} \cdot \sin\left(k\frac{\pi}{2}\right) \tag{3.92}$$

$$|a_k| = \begin{cases} 0 & \text{for } k = 0, 2, 4, \dots \\ \frac{2}{k} \cdot \frac{2I}{\pi} & \text{for } k = 1, 3, 5, \dots \end{cases} \tag{3.93}$$

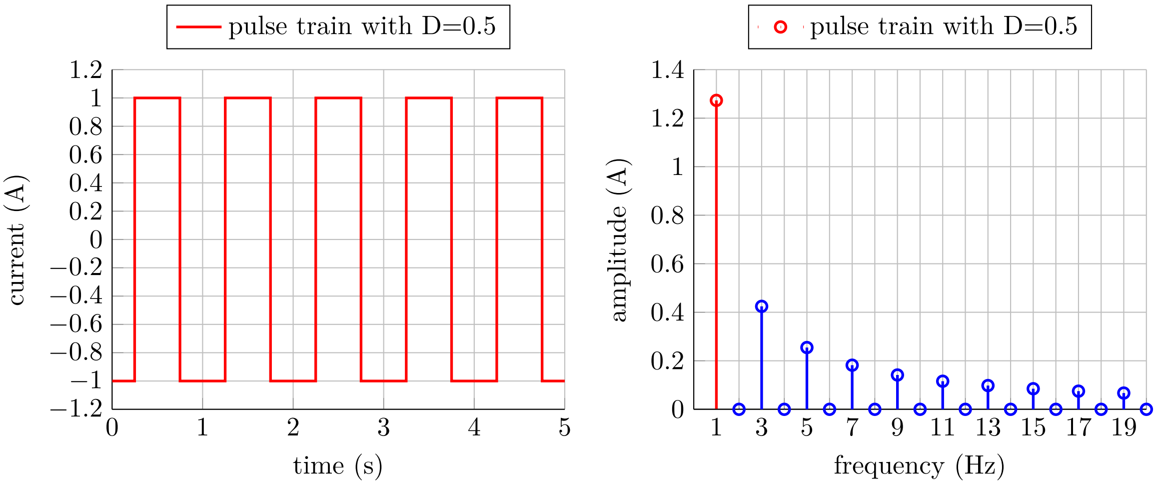

(a) Time-domain.

(b) Frequency-domain.

Figure 3.23: Decomposition of pulse trains into their harmonic components (synthetic data).

### 3.2.4.2 Irreversible Heat Generation Dependency on Pulse Frequency

With the knowledge of the amplitude of the frequency components the equation 3.76 is applied to all the harmonics present.

$$P = \dot{Q} = \sum_{k=1}^{N} Z_{real}\Big|_{k \cdot f_{pulse}} \cdot \left(\frac{a_k}{\sqrt{2}}\right)^2 \tag{3.94}$$

Figure 3.24 shows the result of applying this method. The estimated heat has a similar shape as figure 3.19 but shifted towards higher heat generation rates. The measured heat generation rates from the ARC measurements do match the estimated power from the frequency decomposition of the pulse.

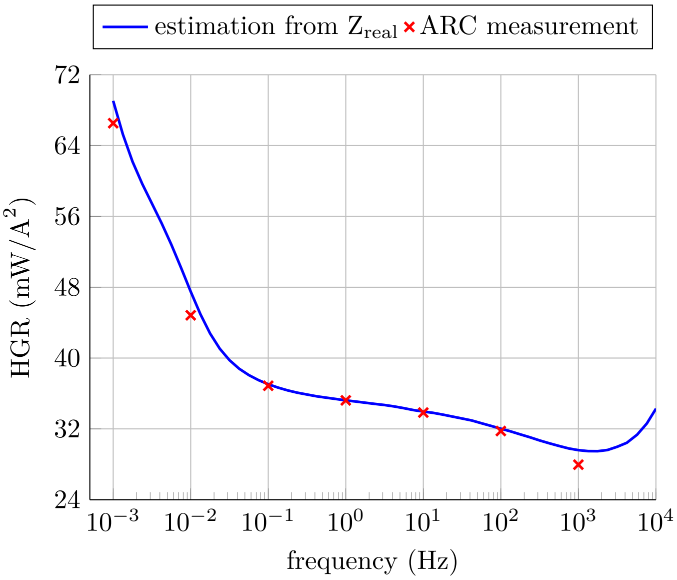

Figure 3.24: Heat generation rate of a pulsed current measured by direct measurements in an ARC and indirect EIS measurements of $Z_{real}$ (cylindrical LFP-cell A.1, $SoC = 50\,\%$, $\vartheta = 40\,°\mathrm{C}$, $\hat{I}_{pulse} = 3\,\mathrm{CA}$, $D = 50\,\%$).

This proves that the estimation of the heat generated from the real part of the impedance is also possible when applying it to pulses that are decomposed into their frequency components. It can be assumed that the same method will also work if the pulse has a duty cycle not equal to 50 % or the signal, is a random signal which is decomposed into its frequency components.

### 3.2.5 Irreversible Heat Generation from Constant Charge/Discharge Currents

Heat generated from constant currents is more difficult than that from sinusoidal currents. The approach used here is to extrapolate the method of the last section 3.2.4 and assume that a constant charge event is a very long pulse, for which the negative current part never happens. Similarly, a constant discharge event is a very long pulse, for which the positive part never happens.

Two main problems make the immediate application of this approach difficult. Firstly, the impedance needs to be measured at various SoCs and at frequencies below 1 mHz. For a constant charge of 1 CA the time needed is 3600 s. The positive and negative part of a full pulse with $D = 0.5$ would need 7200 s. This means the frequency that needs to be measured is around 139 µHz. In order to obtain consistent measurements, it would be best if that frequency would be measured with a measurement current amplitude of $\frac{4}{\pi} = 1.27\,\mathrm{CA}$ and this at several well-spaced SoCs. This requirement is impossible to fulfill, since the SoC sweep is around 81 %. Section 3.2.5.2 will discuss this problem and its solution in detail.

Secondly, the effect of the entropy is no longer compensated. The previous two sections 3.2.3 and 3.2.4 could take advantage of the fact that thanks to the alternating signal applied, the effect of the entropy was compensated. The entropy causes the cell to heat up or cool down depending on its sign and the direction of the current flow. When the signal has a mean value of zero the effect of the positive current exactly cancels out the effect of the negative current. When applying a signal, which has a mean component this is no longer the case and the entropy needs to be considered as well. Figure 3.25

shows how these two heat sources add up to a total temperature increase of the jelly roll inside the cell.

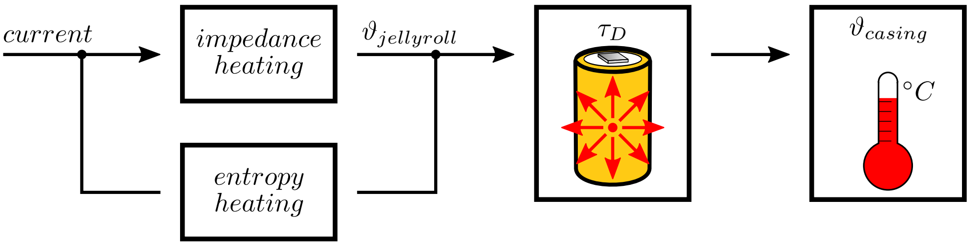

Figure 3.25: Principle of the temperature prediction during a constant charge/discharge event.

For the verification of the introduced method, the temperature increase is predicted for one constant charge and for one constant discharge with a current of 1 CA. Since only the outside temperature of the cell casing can be measured during the experiment, the time constant of the heat transfer from the jelly roll inside the cell to the outer casing is determined in section 3.2.5.1. A cylindrical NMC cell was used for the development of the method and its verification. Its detailed characteristics are available in appendix A.2. The equation for the measurement derivation from entropy and impedance heating caused by a constant current is derived in section 3.2.5.3.

#### 3.2.5.1 Time Constant of the Heat Transfer to the Cell Casing

A battery cell or any other compact item can thermally be approximated by a $1^{st}$-order lag element (PT1 element). This behavior can be seen in the results of Schmidt et al. in [104] and from Fleckenstein et al. in [42]. They performed thermal impedance $Z_{th}$ measurement over a whole frequency range calling it electrothermal impedance spectroscopy. Some higher order thermal model than a $1^{st}$-order lag element were needed to exactly model all the measurement points they showed without any deviation. Barsoukov et al. [10] showed for higher frequencies that the $1^{st}$-order lag element needs to be complemented with another $1^{st}$-order lag element for high frequencies making it a $2^{nd}$-order lag element by showing a second arc in the Nyquist plot for some battery cells he studied. He was able to measure this second arc by using single heat pulses up to 10 Hz as an excitation and the Laplace transform to evaluate the measured data. Schmidt et al. [104] and Fleckenstein et al. [42] used continuous sinusoidal excitation. With that method they could not measure below 100 mHz (Schmidt et al.) or 50 mHz (Fleckenstein et al.). All three publications show that for low frequencies when the accuracy does not have to be extremely high, as it is for this section and the next, an approximation with a $1^{st}$-order lag element is sufficient.

The determination of the time constant is based on the same concept of the comparison of action and reaction during heat generation experiment with a sinusoidal current. The time measured between the heat generating current and the temperature increase of the casing is the time constant $\tau_D$ of the heat transfer from the jelly roll to the casing of the cell. It is equal to the exponential time constant of an exponential function according to which the casing temperature would adapt to the jelly roll temperature after a current pulse was applied (see figure 3.26). Assuming a $1^{st}$-order lag element, it is unnecessary to perform a whole spectroscopy as done in [104], [42] and [10], when only the corner frequency or the time constant $\tau_D$ is needed. This value was determined from a heat generation experiment at a frequency of 1 mHz. Figure 3.27 shows the steps necessary for this calculation.

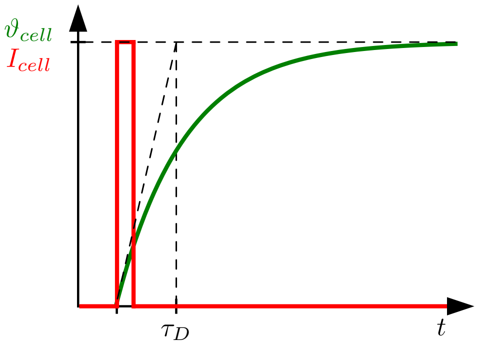

Figure 3.26: $I_{cell}$ in this graph is a short current pulse in order to generate a heat pulse inside the cell. $\vartheta_{cell}$ is the temperature measured on the casing of the cell, which increases according to a 1st-order lag element. The phase delay $\tau_D$ is the time constant of this 1st-order lag element (synthetic data).

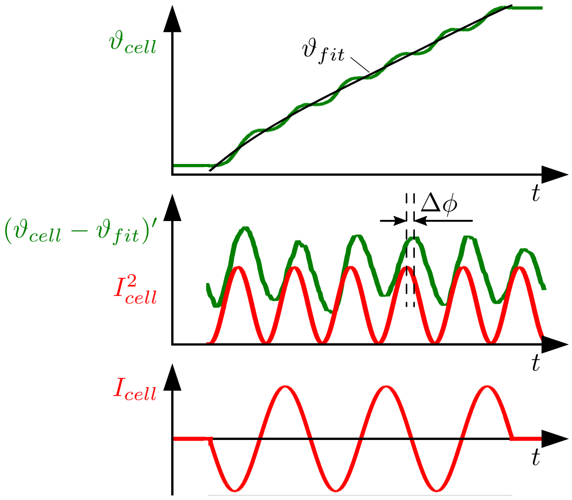

Figure 3.27: Determination of phase delay $\Delta\Phi$ due to heat transfer in the cell.

First, the temperature data has to be transformed into the heat data which generated it. Every heat generated inside the cell ended up accumulating as temperature of the cell $\vartheta_{cell}$. The transformation back is done by fitting the temperature slope of the casing with an average rise $\vartheta_{fit}$, which neglects the sinusoidal temperature changes within the excitation period. Then this fitted slope is subtracted from the temperature of the casing $(\vartheta_{cell} - \vartheta_{fit})$. The heat generated has originally been transformed into temperature by the integration of a $\sin^2(x)$ function. This integration yields a cosinus function with twice the frequency. This means the phase shift of $\frac{\pi}{2}$ came naturally with the integral behavior of the transformation between heat generation and cell temperature. This is why the resulting signal $(\vartheta_{cell} - \vartheta_{fit})$ has to be shifted backward by $\frac{\pi}{2}$ (see signal $(\vartheta_{cell} - \vartheta_{fit})'$ in the middle graph of figure 3.27). The resulting signal is a good proxy for the heat generated inside the jelly roll plus a time delay due to the heat transfer from the jelly roll to the cell casing. Squaring the current values gives a signal with double the frequency of the sinusoidal current, which exactly represents the heat generated inside the jelly roll without the time delay. Comparing this signal to the modified cell temperature $(\vartheta_{cell} - \vartheta_{fit})'$ gives the phase delay $\Delta\Phi$ between the two signals.

The phase delay $\Delta\Phi$ needs to be turned into the time delay constant $\tau_D$ shown in figure 3.26. The similar time delay constant for an RC-low-pass filter would be $R \cdot C$. The angle between the imaginary and the real part of this circuit follows the equation $\tan \Delta\Phi = \frac{Z_{imag}}{Z_{real}} = \frac{1}{\omega C \cdot R} = \frac{1}{\omega \tau_D}$. The same relationship between $\Delta\Phi$ and $\tau_D$ applies in this case. Equation 3.95 calculates the time delay constant $\tau_D$ with the measured phase delay $\Delta\Phi$. The time delay constant $\tau_D$ of the used cylindrical NMC cell was 77 s.

$$\tau_D = \left( \tan \underbrace{\left( \Phi_{Icell^2} - (\Phi_{Tcell-Tfit} + \frac{\pi}{2}) \right)}_{\Delta\Phi} \cdot 2\pi \cdot \underbrace{2 f_{Icell}}_{f_m} \right)^{-1} \tag{3.95}$$

### 3.2.5.2 Impedance Heating

A constant charge or discharge event sweeps over all the SoCs. In order to take the changing impedance with SoC into account, the impedance needs to be measured at a decent amount of SoC levels. In this section, nine measurements from 10 % to 90 % were used. For frequencies below 1 mHz, the measurement takes very long and the impedance cannot be measured anymore with the amplitude equivalent to the constant current magnitude. This is because the capacity that will be charged during the positive half-sine wave is more than the remaining free capacity that can absorb charge when the measurement is done at 90 % SoC. This is why the frequencies below 1 mHz cannot be taken at the same current amplitude as the other frequencies.

In real applications, making measurements at frequencies below 1 mHz would result in a very long measurement time in which the battery would not be available for operation. The diffusion part at low frequencies of most cells follows a linear slope in the logarithmic-domain. Instead of actually measuring at these low frequencies the value of $Z_{real}$ can simply be extrapolated from impedance measurements at higher frequencies. This method is shown in figure 3.28.

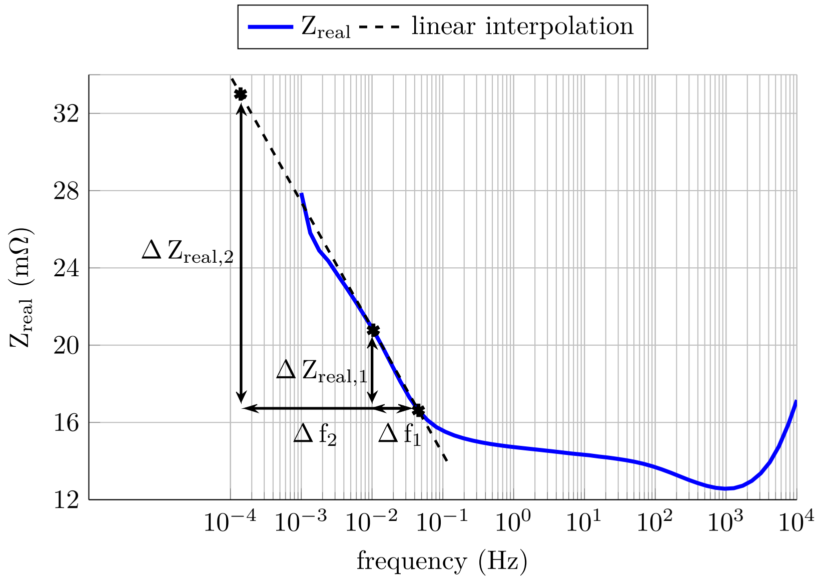

Figure 3.28: Determining the charge/discharge impedance heating by extrapolating the diffusion branch of the graph of the heat generation rate (cylindrical NMC-cell A.2, $SoC_{start} = 50\,\%$, $\vartheta = 40\,°\mathrm{C}$, $\hat{I}_m = 1.27\,\mathrm{CA}$).

By knowing $\Delta f_1$ and $\Delta Z_{real,1}$, the real part of the impedance at a lower frequency with $\Delta f_2$ can simply be calculated by using equation 3.96.

$$\Delta Z_{real,1} = \frac{\log(\Delta f_1)}{\log(\Delta f_2)} \cdot \Delta Z_{real,2} \tag{3.96}$$

In order to verify this approach, the heat generated from a constant charge and a constant discharge event with a current of 1 CA is estimated and compared to the real measurement data in an adiabatic environment of an ARC. Figure 3.29a shows the estimated heat flux $\dot{Q}$ of the entropy heating $HGR_e \cdot I$ and of the impedance heating $HGR_{dc} \cdot I^2$, which was determined from the directly measured impedance at $\frac{1}{7200}$ Hz and its higher harmonics. It also shows the sum of the two $\dot{Q}_\Sigma$ and the heat flux directly measured from the temperature increase by the ARC $\dot{Q}_{ARC}$.

A direct comparison of the last two values is difficult to make, since the heat flux measured from the ARC experiment is derived from the measurement on the outside of the cell casing. The estimated heat flux, however, is the estimated heat generated in the jelly roll of the cell. Because of this shortcoming figure 3.29b shows the heat flux $\dot{Q}_\Sigma$ turned into the temperature of the cell casing. The estimated heat flux $\dot{Q}_\Sigma$ is then delayed by the heat transfer constant $\tau_D$ as determined in section 3.2.5.1. $\Delta\vartheta_{\Sigma,1000s}$ shows the estimation by extrapolating from impedance measurements at $\frac{1}{1000}$ Hz and $\frac{1}{300}$ Hz. The temperature estimation can only make an estimation of the temperature difference but not on the absolute temperature. This is why the temperatures of the measurement in the ARC $\Delta\vartheta_{ARC}$ and the estimations $\Delta\vartheta_{\Sigma,7200s}$ and $\Delta\vartheta_{\Sigma,1000s}$ were pegged at 50 % SoC. To peg both data sets at 0 % SoC, a higher resolution between 0 % and 10 % would have been necessary, since the impedance and the entropy change significantly at low SoCs.

Figure 3.29b shows that the estimation of the temperature swing caused by the constant charge event corresponds quite well with the measured progress of the temperature. The estimation done with extrapolated data from measurements at 1 mHz and its harmonics overestimates the temperature swing by around 0.25 °C.

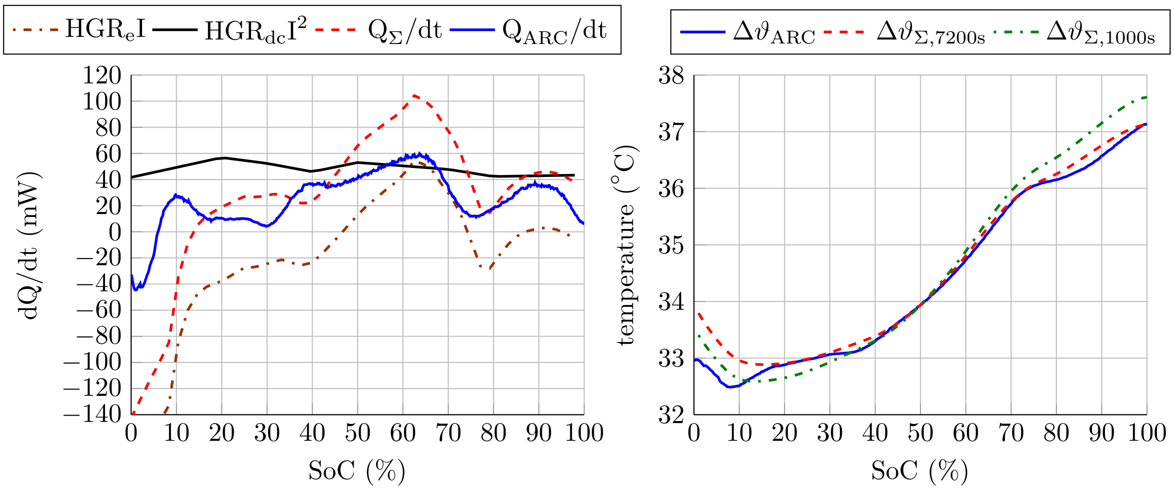

(a) Heat flux $\dot{Q}$ from impedance heating $HGR_{dc} \cdot I^2$, entropy heating $HGR_e \cdot I$, the sum of the two $\dot{Q}_\Sigma$ and from the temperature increase measured by the ARC $\dot{Q}_{ARC}$.

(b) Temperature change measured by the ARC $\Delta\vartheta_{ARC}$ and from the estimations $\Delta\vartheta_{\Sigma,7200s}$ and $\Delta\vartheta_{\Sigma,1000s}$.

Figure 3.29: Measured and estimated heat flux and temperature over SoC for a constant current charge event with 1 CA (cylindrical NMC-cell A.2).

Figure 3.30 shows the same data as figure 3.29 for the constant discharge event. The data sets of the measurement in the ARC) $\Delta\vartheta_{ARC}$ and the two estimations $\Delta\vartheta_{\Sigma,7200s}$ and $\Delta\vartheta_{\Sigma,1000s}$ were pegged at 100 % SoC. The estimation done with extrapolated data from measurements at 1 mHz and its harmonics, again, overestimates the temperature swing for the discharging event by around 1 °C.

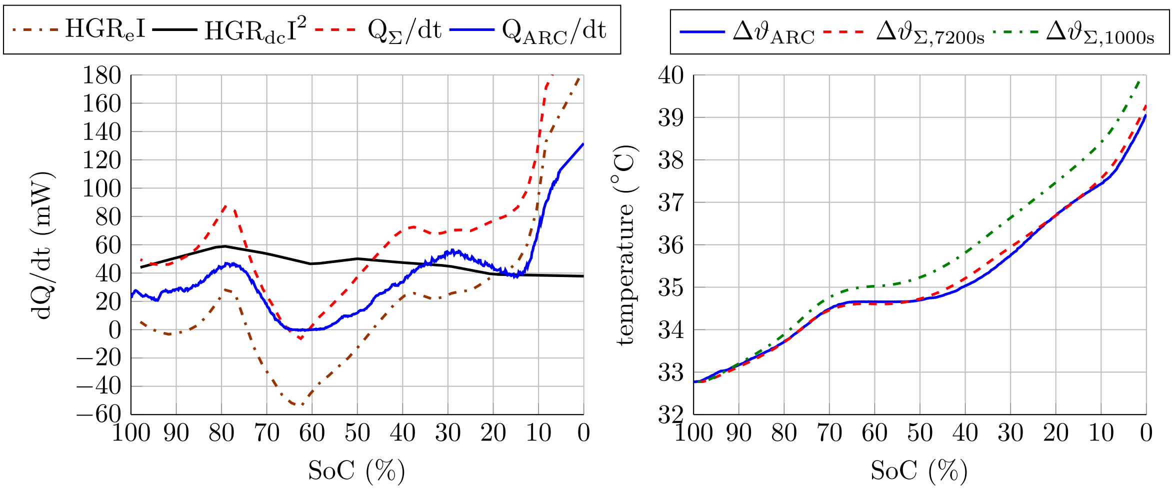

(a) Heat flux $\dot{Q}$ from impedance heating $HGR_{dc} \cdot I^2$, entropy heating $HGR_e \cdot I$, the sum of the two $\dot{Q}_\Sigma$ and from the temperature increase measured by the ARC $\dot{Q}_{ARC}$.

(b) Temperature change measured by the ARC $\Delta\vartheta_{ARC}$ and from the estimations $\Delta\vartheta_{\Sigma,7200s}$ and $\Delta\vartheta_{\Sigma,1000s}$.

Figure 3.30: Measured and estimated heat flux and temperature over SoC for a constant current discharge event with 1 CA (cylindrical NMC-cell A.2).

Nieto et al. [82] recorded similar measurements in an adiabatic environment of a calorimeter. By adding irreversible heat and entropic heat he estimated the total heat produced by the battery cell. He determined the irreversible heat by a 1 CA discharge pulse. Unfortunately he did not give the exact length of the pulse, but from his figure 4, it can be estimated that it was between 15 and 20 s in length.

### 3.2.5.3 Impedance Measurement Derivation Caused by Constant Current

The temperature increase from a constant current is caused by entropy heating and by impedance heating. The same effect is also caused by the constant part of the temperature change of a sinusoidal excitation current. Equation 3.97 sums up the three sources of a constant temperature increase during an impedance measurement.

$$\frac{\Delta T(t)}{\Delta t} = \underbrace{\frac{HGR_e}{C_{th}} \cdot I_{dc}}_{\substack{\text{constant}\\\text{entropy heating}}} + \underbrace{\frac{HGR_{dc}}{C_{th}} \cdot {I_{dc}}^2}_{\substack{\text{constant}\\\text{impedance heating}}} + \underbrace{\frac{HGR_{fm}}{C_{th} \cdot 2} \cdot {\hat{I}_m}^2}_{\substack{\text{constant part caused}\\\text{by the excitation current}}} \tag{3.97}$$

The impedance drift caused by an increasing temperature throughout the impedance measurement time is exponentially decreasing but only affects the temperature dependent part of the impedance $Z_\Theta$. Figure 3.31 shows an example for such an impedance drift caused by constant impedance heating of a constant current. The measurement frequency used in this figure is still too high in order to see clearly the exponential decrease of the impedance value.

For determining the measurement derivation caused by the temperature dependency, the temperature dependent part of the voltage response $v_\Theta(t)$ is transformed into the frequency-domain by separating real part $a_1$ and imaginary part $b_1$:

$$\mathrm{F}\{v_\Theta(t)\} = \frac{2}{T_m}\int_0^{T_m} Z_\Theta e^{\frac{\Delta T(t)}{\Delta t}\cdot\frac{1}{\Theta}\cdot t}\cdot\hat{I}_m\sin(\omega_m t)\cdot e^{-j\omega_m t}\mathrm{d}t = a_1 - jb_1 \tag{3.98}$$

$$a_1 = \frac{Z_\Theta\hat{I}_m}{T_m}\cdot 2\int_0^{T_m} e^{\frac{\Delta T(t)}{\Delta t}\cdot\frac{1}{\Theta}\cdot t}\cdot\underbrace{\sin(\omega_m t)\cdot\cos(\omega_m t)}_{\frac{1}{2}\cdot\sin(2\omega_m t)\text{ with C.3}}\mathrm{d}t \tag{3.99}$$

$$= \frac{Z_\Theta\hat{I}_m}{T_m}\cdot\int_0^{T_m} e^{\frac{\Delta T(t)}{\Delta t}\cdot\frac{1}{\Theta}\cdot t}\cdot\sin(2\omega_m t)\mathrm{d}t \tag{3.100}$$

By using lemma C.14:

$$= \frac{Z_\Theta\hat{I}_m}{T_m}\cdot\frac{e^{\frac{\Delta T(t)}{\Delta t}\cdot\frac{1}{\Theta}\cdot T_m}\cdot\left(\frac{\Delta T(t)}{\Delta t}\cdot\frac{1}{\Theta}\cdot 0 - \frac{4\pi}{T_m}\cdot 1\right) - e^{\frac{\Delta T(t)}{\Delta t}\cdot\frac{1}{\Theta}\cdot 0}\left(\frac{\Delta T(t)}{\Delta t}\cdot\frac{1}{\Theta}\cdot 0 - \frac{4\pi}{T_m}\cdot 1\right)}{\left(\frac{\Delta T(t)}{\Delta t}\cdot\frac{1}{\Theta}\right)^2 + \frac{16\pi^2}{T_m{}^2}}$$

$$= \frac{Z_\Theta\hat{I}_m}{T_m}\cdot\frac{4\pi T_m\left(1 - e^{\frac{\Delta T(t)}{\Delta t}\cdot\frac{1}{\Theta}\cdot T_m}\right)}{\left(\frac{\Delta T(t)}{\Delta t}\cdot\frac{1}{\Theta}\right)^2 T_m{}^2 + 16\pi^2} \tag{3.101}$$

$$b_1 = \frac{Z_\Theta\hat{I}_m}{T_m}\cdot 2\int_0^{T_m} e^{\frac{\Delta T(t)}{\Delta t}\cdot\frac{1}{\Theta}\cdot t}\cdot\underbrace{\sin^2(\omega_m\cdot t)}_{\frac{1}{2}\cdot(1-\cos(2\omega_m t))\text{ with C.4}}\mathrm{d}t \tag{3.102}$$

$$= \frac{Z_\Theta\hat{I}_m}{T_m}\cdot\left[\int_0^{T_m} e^{\frac{\Delta T(t)}{\Delta t}\cdot\frac{1}{\Theta}\cdot t}\mathrm{d}t - \int_0^{T_m} e^{\frac{\Delta T(t)}{\Delta t}\cdot\frac{1}{\Theta}\cdot t}\cdot cos(2\omega_m t)\mathrm{d}t\right] \tag{3.103}$$

By using lemma C.15:

$$= \frac{Z_\Theta\hat{I}_m}{T_m}\cdot\left[\frac{e^{\frac{\Delta T(t)}{\Delta t}\cdot\frac{1}{\Theta}\cdot T_m} - 1}{\frac{\Delta T(t)}{\Delta t}\cdot\frac{1}{\Theta}} - \frac{\frac{\Delta T(t)}{\Delta t}\cdot\frac{1}{\Theta}\cdot T_m{}^2\cdot\left(e^{\frac{\Delta T(t)}{\Delta t}\cdot\frac{1}{\Theta}\cdot T_m} - 1\right)}{\left(\frac{\Delta T(t)}{\Delta t}\cdot\frac{1}{\Theta}\right)^2 T_m{}^2 + 16\pi^2}\right] \tag{3.104}$$

With equation 3.89 the deviation caused by a constant increase in temperature during the impedance measurement can be stated as:

$$e_Z = \frac{Z_\Theta}{Z_0}\cdot\left[\left[\frac{e^{\frac{\Delta T(t)}{\Delta t}\cdot\frac{1}{\Theta}\cdot T_m} - 1}{\frac{\Delta T(t)}{\Delta t}\cdot\frac{1}{\Theta}\cdot T_m} - \frac{\frac{\Delta T(t)}{\Delta t}\cdot\frac{1}{\Theta}\cdot T_m\cdot\left(e^{\frac{\Delta T(t)}{\Delta t}\cdot\frac{1}{\Theta}\cdot T_m} - 1\right)}{\left(\frac{\Delta T(t)}{\Delta t}\cdot\frac{1}{\Theta}\right)^2 T_m{}^2 + 16\pi^2} + j\cdot\frac{4\pi\left(1 - e^{\frac{\Delta T(t)}{\Delta t}\cdot\frac{1}{\Theta}\cdot T_m}\right)}{\left(\frac{\Delta T(t)}{\Delta t}\cdot\frac{1}{\Theta}\right)^2 T_m{}^2 + 16\pi^2}\right] - 1\right] \tag{3.105}$$

Equation 3.97 includes the constant part of the excitation current's impedance heating. This means that this kind of deviation is always present, except for the rare case when the entropy cooling of a constant current would exactly compensate the impedance heating. This is why this part always needs to be considered. Figure 3.31 shows the change in impedance for the real and the imaginary part. Compared to the change in impedance caused by the alternating part and the excitation current's temperature increase in figure 3.21, the magnitude of the change is around ten times higher.

The impedance measurement deviation shown in figure 3.32 is compared to the one from the alternating part of the excitation current's temperature increase in figure 3.22 also by a factor of around ten higher. The phase deviation, however, changes quite significantly for lower frequencies making the phase deviation from the alternating part for some frequencies more important than the constant part.

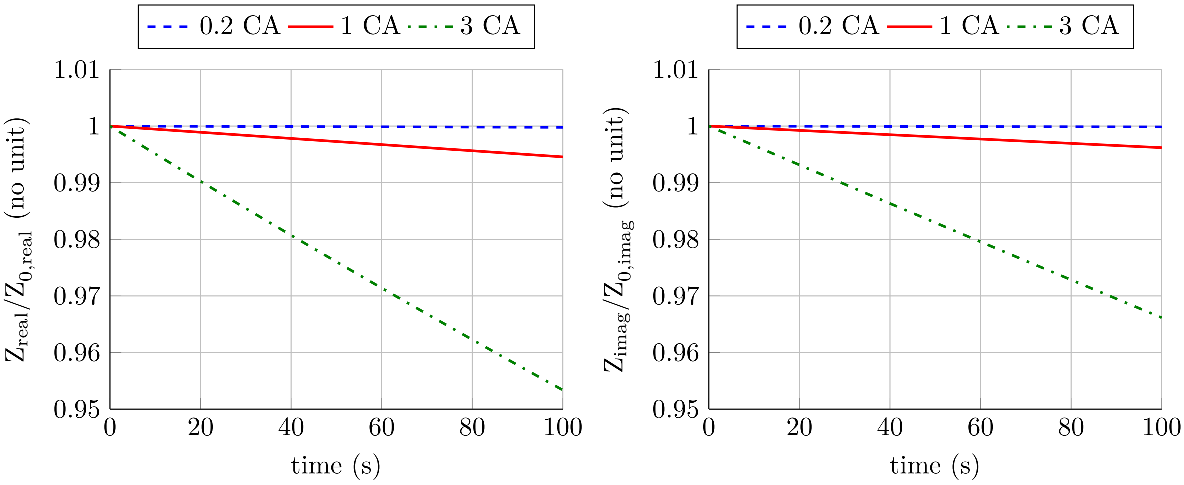

(a) Impedance real part

(b) Impedance imaginary part

Figure 3.31: Impedance change caused by the constant part of the excitation current's impedance heating during the impedance measurement (NMC pouch cell A.5, $SoC = 50\,\%$, $f_m = 10\,\mathrm{mHz}$).

The modulus measurement deviation caused by the constant part of the excitation current's temperature increase is the most critical one for all amplitudes for the shown NMC pouch cell (A.5).

The measurement deviation for an additional constant current is not shown here, since they would qualitatively behave similar to the constant part of the excitation current's temperature increase. The additional constant current would make the deviation much worse. The temperature change from the constant part of the excitation current's temperature increase is much smaller than the temperature change from an additional constant current. Equation 3.97 shows this. $HGR_{fm}$ is determined by the impedance part at higher frequencies than $HGR_{dc}$. When only considering frequencies above 1 Hz, at higher frequencies, the real part of the impedance is lower. Additionally, $HGR_{dc}$ includes its harmonics and $HGR_{fm}$ is divided by the factor of two, whereas $HGR_{dc}$ is not.

### 3.2.6 Impedance Measurement Deviation Caused by Multi-sine Measurement

There is no closed algebraic solution for the alternating part of the temperature change caused by a multi-sine excitation. The part of the constant temperature increase, however, can still be included. The term $\frac{\Delta T(t)}{\Delta t}$ needs to be extended by the temperature increase caused by every single frequency component of the multi-sine excitation signal:

$$\frac{\Delta T(t)}{\Delta t} = \underbrace{\frac{HGR_e}{C_{th}} \cdot I_{dc}}_{\substack{\text{constant}\\ \text{entropy heating}}} + \underbrace{\frac{HGR_{dc}}{C_{th}} \cdot {I_{dc}}^2}_{\substack{\text{constant}\\ \text{impedance heating}}} + \underbrace{\Sigma_{k=1}^{N} \frac{HGR_{fk}}{C_{th} \cdot 2} \cdot \hat{I}_k^2}_{\substack{\text{constant part caused}\\ \text{by all components of the}\\ \text{multi-sine excitation current}}} \tag{3.106}$$

Section 3.2.5.3 showed that the constant part of the temperature change is much more significant for the measured impedance deviation as the alternating part. Therefore, considering only the con-

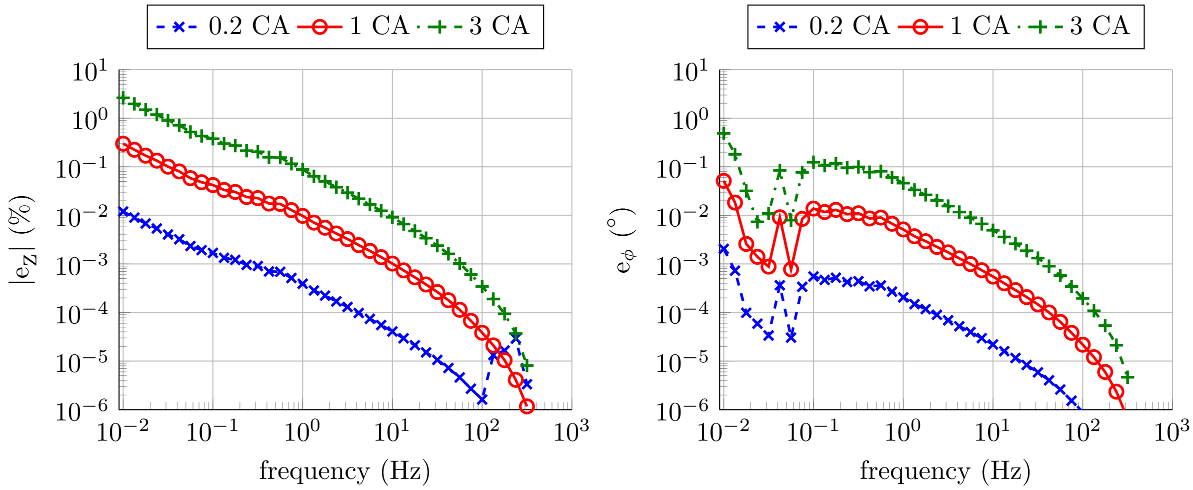

(a) Modulus deviation.

(b) Phase deviation.

Figure 3.32: Measurement deviation by temperature change from the constant part of the excitation current's impedance heating dependent on the measurement frequency and excitation current amplitude (NMC pouch cell A.5, $SoC = 50\,\%$).

stant temperature increase during a multi-sine measurement is a sufficient approximation of the total measurement deviation.

### Section Conclusion

*This section showed that the impedance of a cell can be separated into a temperature dependent part and a temperature independent part. The temperature dependent part follows an exponential function.*

*Xiao and Choe [127] separate the heat generated into joule and reaction heating. This section showed that, for non-physico-chemical models, this method is unnecessary since both joule and reaction heating can be determined by the real part of the impedance throughout the whole frequency range down to very low constant currents. This method can be applied over the whole State-of-Charge range and at different temperatures and amplitudes. This section also proved that this method not only can be applied to a sinusoidal current but to any type of signal by using the method of frequency decomposition. For charge/discharge events, the entropy and the thermal conductivity of the cell need to be taken into account, when predicting the temperature of the cell casing.*

*A changing temperature during the impedance measurement introduces a deviation into the measured impedance. From the initially set deviation thresholds of* $0.1\,\%$ *modulus deviation and* $0.1\,°$ *phase deviation, the modulus deviation is the more difficult one to comply with. A sinusoidal excitation current changes the temperature of a cell in three ways: alternating temperature change caused by entropy heating, alternating temperature change caused by impedance heating and constant temperature increase caused by impedance heating. Out of these three, the constant temperature increases caused by impedance heating is the most critical one in order to comply with the* $0.1\,\%$ *modulus deviation and* $0.1\,°$ *phase deviation thresholds.*

## 3.3 Measurement Deviation Caused by Open-Circuit-Voltage Displacement

Any current flowing in or out of a battery cell displaces the SoC and with it the OCV of the battery cell under test. This section assesses the measurement deviation introduced by a sinusoidal excitation current, which is changing the OCV in an equally sinusoidal way during the EIS measurement. This section does not assess the measurement deviation caused by a constant current. The OCV change introduced by it is called a voltage drift. A voltage drift is characterized by a different voltage at the end of the measurement compared to the voltage at which the measurement started. This OCV displacement can be identified and corrected. Section 4.1 introduces various ways to correct deviations caused by drift.

### 3.3.1 Open-Circuit-Voltage Displacement from State-of-Charge Change

Figure 3.33 shows how a deviation is caused by the SoC displacement. The excitation current causes the SoC to change. With it changes the enthalpy and entropy of the cell. As shown in the fundamentals section 2.1.4, enthalpy and entropy are related to the OCV of a battery cell. During positive currents, the excitation current is charging the battery and therefore increases the OCV. During negative currents, the excitation current is discharging the battery and therefore decreases the OCV. This behavior results in an additional signal measured by the EIS measurement. This deviation can only be determined and compensated with the knowledge of the OCV curve over the SoC.

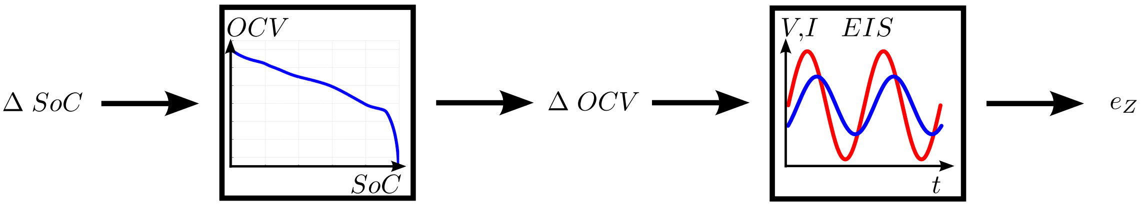

Figure 3.33: The origin of the OCV displacement is a change in SoC in combination with the OCV curve of the cell.

#### 3.3.1.1 Open-Circuit-Voltage Displacement

Section 3.1.2.1 already derived the change in SoC caused by the excitation current. When starting with the positive half-sine wave, the effective SoC at which the cell is measured is higher than the starting SoC. If started with the negative half-sine wave the effective SoC is lower. In contrast to the measurement deviation caused by the impedance dependency on SoC, the deviation caused by the open circuit voltage displacement occurs no matter with which phase the excitation current is started. Equation 3.107 shows the additional signal which is introduced by the OCV change and which is measured simultaneously with the voltage response of the impedance of the battery. The change in SoC described by equation 3.12 directly translates into an OCV change with the linear dependency of the OCV on SoC $\frac{\mathrm{d}V_{OCV}}{\mathrm{d}SoC}$. Since the SoC change is the integration of the excitation current, it trails by $\frac{\pi}{2}$ behind the excitation current. Therefore the additional signal also has a phase delay of $\frac{\pi}{2}$ to the excitation current. This phase delay is independent of the phase of the measured impedance.

$$i_m(t) = \hat{I}_m \cdot \sin(2\pi f_m t + \varphi)$$

$$v_{\Delta SoC}(t) = \frac{\mathrm{d}V_{OCV}}{\mathrm{d}SoC} \cdot \frac{T_m}{2\pi} \frac{\hat{I}_m}{C_{el}} \cdot [-\cos(2\pi f_m t + \varphi) + \cos\varphi] \tag{3.107}$$

Figure 3.34 shows for an LFP lithium-ion battery and for an NMC lithium-ion battery the original response of the actual impedance of the battery $V_{Z0}$, the displacement in open circuit voltage $V_{OCV}$ and the sum of the two $V_{Zm}$. The effect is usually very small and difficult to see, this is why a measurement frequency of $f_m = 1\,\mathrm{mHz}$ and an excitation current magnitude of $\hat{I}_m = 3\,\mathrm{CA}$ was chosen. This results in an SoC sweep of 26.5 %. The simulation was started at 50 % SoC where the LFP-cell has a very shallow slope, therefore figure 3.34a does not show much difference between the pristine impedance response and the one which also includes the change in Open-Circuit-Voltage. For the NMC cell however, figure 3.34b shows a noticeable difference. This is why for the remainder of this section the NMC cell is used to illustrate the deviations coming from an OCV displacement.

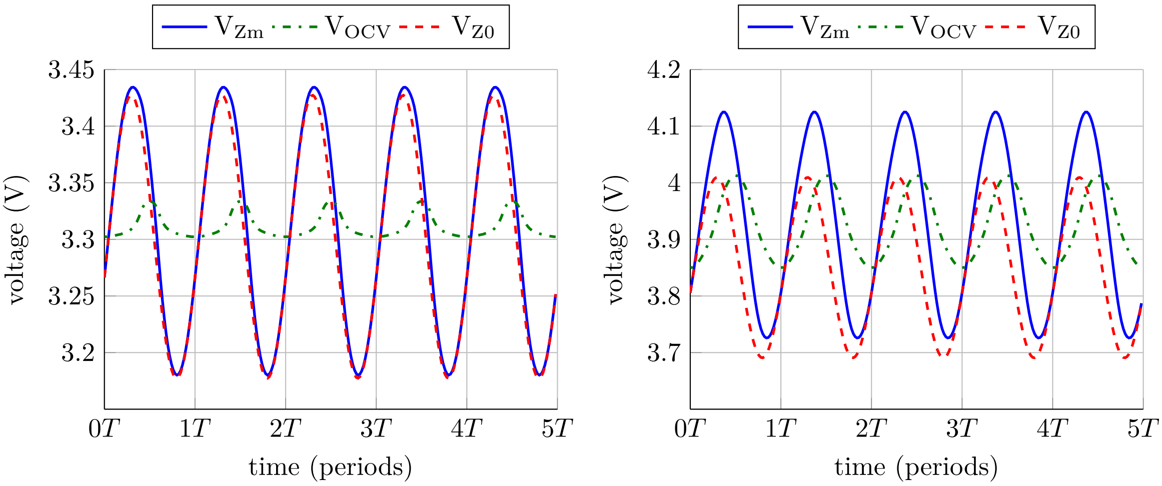

(a) Cylindrical LFP-cell A.1.

(b) Cylindrical NMC-cell A.2.

Figure 3.34: Time-domain voltages during an EIS measurement of the pristine impedance response $V_{Z0}$, the displacement in open circuit voltage $V_{OCV}$ and the sum of the two $V_{Zm}$. Simulation in which the SoC sweeps from 50 % to around 76.5 % during the measurement making it possible to see the effect of the OCV displacement. ($\hat{I}_m = 3\,\mathrm{CA}$, $SoC_{start} = 50\,\%$, $\vartheta = 25\,°\mathrm{C}$, $f_m = 1\,\mathrm{mHz}$).

Figure 3.34 was generated by a simulation with an OCV-curve resolved with around 3,000 points. For deriving equations in this section, the linear approximation of equation 3.108 is used, which approximates the OCV-curve linearly between the starting SoC and the point of maximum OCV displacement, which is $SoC_{start} + \Delta\widehat{SoC}_m$ for a sinusoidal excitation current with zero initial phase.

$$V_{OCV,\, SoC_{start}+\Delta\widehat{SoC}_m} = \left.\frac{\Delta V_{OCV}}{\Delta SoC}\right|_{T,\Delta SoC} \cdot \Delta\widehat{SoC}_m + V_{OCV} \tag{3.108}$$

$$\left.\frac{\Delta V_{OCV}}{\Delta SoC}\right|_{T,\Delta SoC} = \frac{V_{OCV,\, SoC_{start}+\Delta\widehat{SoC}_m} - V_{OCV}}{\Delta\widehat{SoC}_m} \tag{3.109}$$

A real battery cell has a non-constant slope, as figure 3.35 shows for four battery cells with different chemistries. With the exception of a LFP battery cell, most li-ion cells are operated in a similar voltage window. This similar window and the normalized capacity by using SoC on the x-axis keeps the change of OCV per 1 % SoC change almost at the same magnitude for all battery chemistries. For small changes in SoC, it can be even considered constant.

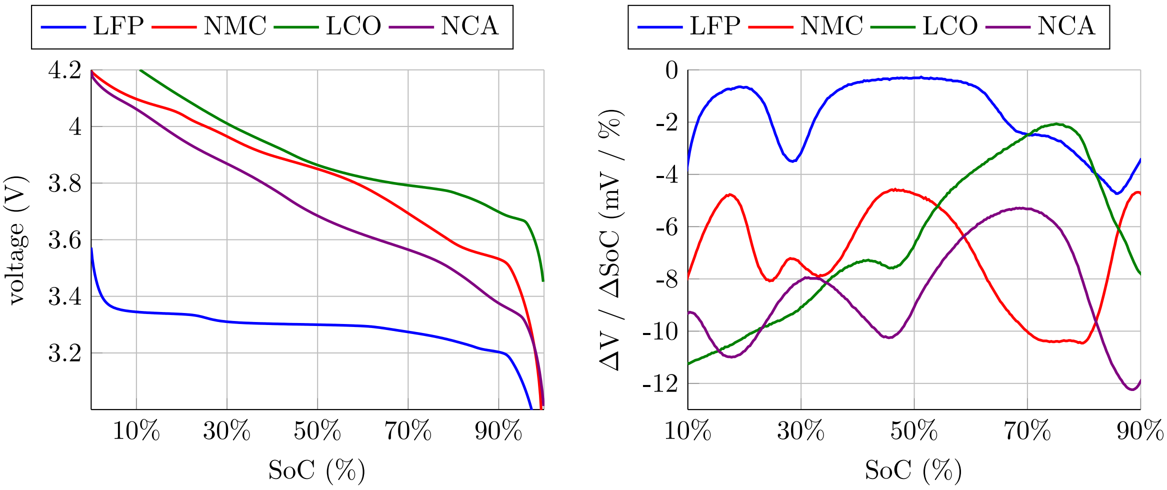

(a) Open-Circuit-Voltage.

(b) Open-Circuit-Voltage change per 1%-point of SoC change.

Figure 3.35: OCV and Change of OCV for cylindrical cells with different li-ion chemistries (LFP-cell A.1, NMC-cell A.2, LCO-cell A.3, NCA-cell A.4, $\vartheta = 25\,°\mathrm{C}$).

The non-constant slope results in a non-linear response caused by the change in OCV. This non-linearity can be examined in the frequency-domain. Figure 3.36 shows the harmonics of the real and the imaginary part for the combined response from the voltage drop over the impedance and the OCV change for the time-domain voltages of figure 3.34b.

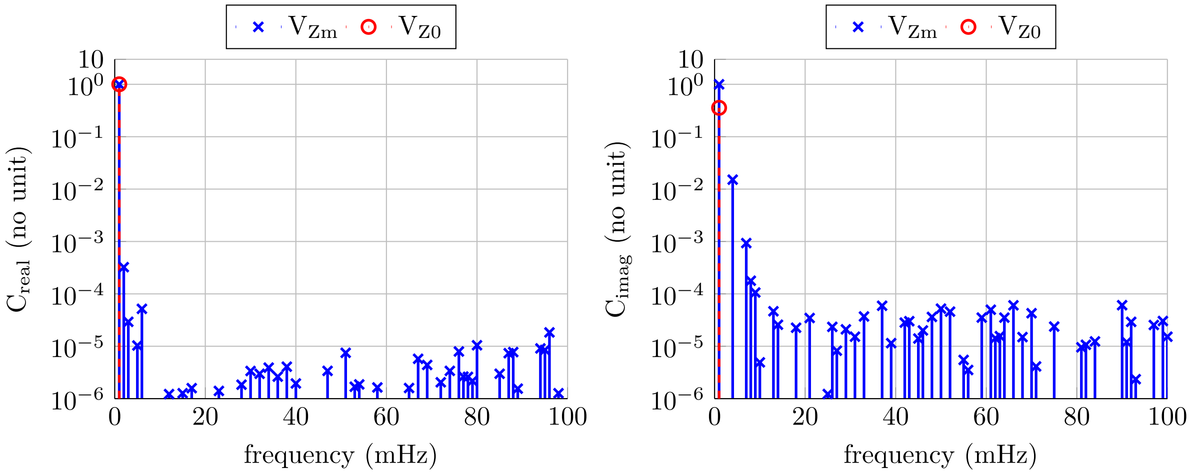

(a) Real part.

(b) Imaginary part.

Figure 3.36: Harmonics of the real and imaginary part normalized to the amplitude of the fundamental for the combined response of the voltage drop over the impedance and the OCV change from figure 3.34b (cylindrical NMC-cell A.2, $\hat{I}_m = 3\,\text{CA}$, $SoC_{start} = 50\,\%$, $\vartheta = 25\,°\text{C}$, $f_m = 1\,\text{mHz}$).

The harmonics and therefore the distortion is higher for the imaginary part as for the real part. The total harmonic distortion (THD) shown in table 3.2 also shows the higher values for the imaginary part. This causes the deviation of the imaginary part to be higher even if the deviation is compensated by the equation 3.120 derived in the next section 3.3.2.2. Table 3.2 gives a summary of the THD values for the LFP and NMC cell.

| | $THD_{real}$ | $THD_{imag}$ |
|---|---|---|
| LFP | 0.0004 | 0.1319 |
| NCM | 0.0004 | 0.0638 |

Table 3.2: Comparison of the THD caused by an OCV change during an EIS measurement (LFP-cell A.1, NMC-cell A.2, $f_m = 1\,\text{mHz}$, $\hat{I}_m = 3\,\text{CA}$).

### 3.3.1.2 Impedance Measurement Deviation

The measurement current $I_m$, the pristine impedance response $V_{Z0}$ and the displacement in Open-Circuit-Voltage $V_{OCV}$ change during the impedance measurement with the same frequency. Because of this, their frequency component can be disregarded and they can be seen as static phasors. The phasor diagram in figure 3.37 illustrates their location in the complex plane and the superposition of $V_{Z0}$ with $V_{OCV}$. For the diagram and further calculation, the excitation current is assumed to be sinusoidal with no initial phase $\varphi = 0$.

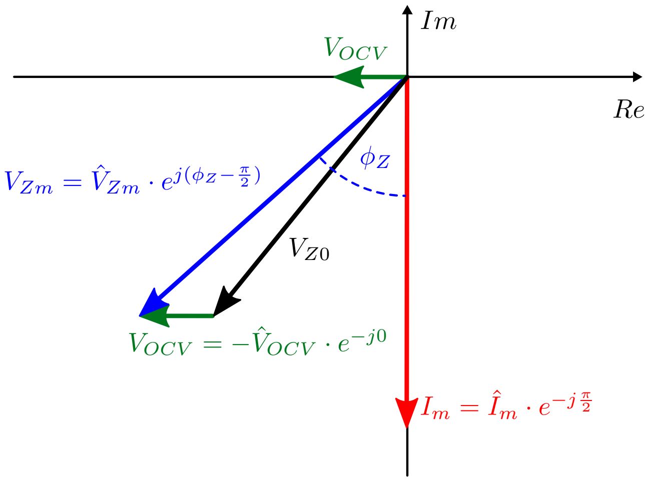

Figure 3.37: Visualization of the superposition of the real Impedance voltage $V_{Z0}$, the impact of the change in Open-Circuit-Voltage $V_{OCV}$ and the resulting measured voltage $V_{Zm}$.

The current starts on the negative imaginary axis (equation 3.110), $V_{OCV}$ trails $\frac{\pi}{2}$ behind the current (equation 3.111). The location of the pristine impedance response $V_{Z0}$ in the phasor diagram depends on the impedance phase value $\phi_Z$. It trails behind the current for negative values and precedes the current for positive values (equation 3.112).

The actual voltage response which can be measured at the battery terminals $V_{Zm}$ is the sum of $V_{Z0}$ and $V_{OCV}$ (equation 3.113).

$$\mathbf{I_m} = \hat{I}_m \cdot e^{-j\frac{\pi}{2}} = -j\hat{I}_m \tag{3.110}$$

$$\mathbf{V_{OCV}} = \hat{V}_{OCV} \cdot e^{-j\pi} = -\hat{V}_{OCV} \cdot e^{-j0} \tag{3.111}$$

$$\mathbf{V_{Z0}} = \hat{V}_{Z0} \cdot e^{j(\phi_{Z0} - \frac{\pi}{2})} \tag{3.112}$$

$$\mathbf{V_{Zm}} = \hat{V}_{Zm} \cdot e^{j(\phi_Z - \frac{\pi}{2})} = \mathbf{V_{Z0}} + \mathbf{V_{OCV}} \tag{3.113}$$

With these phasors, the measured impedance $Z_m$ can be determined according to equation 3.114 and 3.115. The two equations assume a constant slope $\frac{\Delta OCV}{\Delta SOC}$ and use equation 3.12 derived in section 3.1.2.1 for the time dependency of the SoC during an impedance measurement.

$$Z_m = \frac{\mathbf{V_{Zm}}}{\mathbf{I_m}} = \frac{\mathbf{V_{Z0}} + \mathbf{V_{OCV}}}{\mathbf{I_m}} \tag{3.114}$$

$$Z_m = \frac{\hat{V}_{Z0} e^{j(\phi_{Z0} - \frac{\pi}{2})} - \left.\frac{\Delta OCV}{\Delta SoC}\right|_{T,\Delta SoC} \frac{\hat{I}_m T_m}{2\pi C_{el}} e^{-j0}}{\hat{I}_m e^{-j\frac{\pi}{2}}} \tag{3.115}$$

In order to eliminate the complex current in the denominator, the nominator and denominator are multiplied by the conjugate-complex value of the current (equation 3.116 and 3.117).

$$Z_m = \frac{\left[\hat{V}_{Z0}\cdot\cos\left(\phi_{Z0}-\frac{\pi}{2}\right)+j\hat{V}_{Z0}\cdot\sin\left(\phi_{Z0}-\frac{\pi}{2}\right)-\frac{\Delta OCV}{\Delta SoC}\Big|_{T,\Delta SoC}\frac{\hat{I}_m T_m}{2\pi C_{el}}\right]\cdot j\hat{I}_m}{-j\hat{I}_m\cdot j\hat{I}_m} \tag{3.116}$$

$$Z_m = j\frac{\hat{V}_{Z0}\hat{I}_m}{\hat{I}_m{}^2}\underbrace{\cos\left(\phi_{Z0}-\frac{\pi}{2}\right)}_{+\sin(\phi_Z)} - \frac{\hat{V}_{Z0}\hat{I}_m}{\hat{I}_m{}^2}\underbrace{\sin\left(\phi_{Z0}-\frac{\pi}{2}\right)}_{-cos(\phi_Z)} - j\frac{\hat{I}_m{}^2}{\hat{I}_m{}^2}\cdot\frac{\Delta OCV}{\Delta SoC}\Big|_{T,\Delta SoC}\frac{T_m}{2\pi C_{el}} \tag{3.117}$$

The summands of the resulting equation 3.118 can be attributed to the particular parts of the impedance measurement.

$$Z_m = \underbrace{\underbrace{\frac{\hat{V}_{Z0}}{\hat{I}_m}\cos(\phi_{Z0})}_{Z_{real}} + j\underbrace{\frac{\hat{V}_{Z0}}{\hat{I}_m}\sin(\phi_{Z0})}_{Z_{imag}}}_{Z_0}\underbrace{-j\frac{\Delta OCV}{\Delta SoC}\Big|_{T,\Delta SoC}\frac{T_m}{2\pi C_{el}}}_{Z_{OCV/SoC}} \tag{3.118}$$

The impedance measurement therefore consists of two parts, the pristine impedance $Z_0$ and the deviation $Z_{OCV/SoC}$ which is measured due to the change in OCV. The deviation is only imaginary, as its root cause is the change in SoC and OCV, which trails by $\frac{\pi}{2}$ behind the measurement current.

$$Z_m = Z_0 + Z_{OCV/SoC} \tag{3.119}$$

$$Z_{OCV/SoC} = -j\frac{\Delta OCV}{\Delta SoC}\Big|_{T,\Delta SoC}\frac{T_m}{2\pi C_{el}} \tag{3.120}$$

If a constant slope of the OCV is assumed there is no effect on other frequencies or harmonics than the measurement frequency. For a multi-sine measurement there is no difference in the deviation which is generated since the effect of the other frequencies is suppressed by the narrowband selectivity of the Fourier transformation.

Figure 3.38a shows the imaginary part of impedance measurements performed at several start-SoCs. The imaginary deviation $Z_{OCV/sim}$ is simulated by using an OCV curve with over 3,000 points. It is compared to $Z_{OCV/SoC}$ calculated by equation 3.120, which assumes a linear slope of the OCV between the start-SoC and the SoC at maximum deviation from the start-SoC. Both results are almost identical. In figure 3.38b the difference between the two approaches is shown by $\Delta e_{imag}$. It represents the remaining deviation assuming the measured imaginary impedance was corrected by equation 3.119. The $e_{real}$ curve shows the measurement deviation present on the real part of the impedance without any correction. This curve confirms that the deviation only affects the imaginary part. The deviation of both curves comes from the incorrect assumption that the OCV is a straight line. The fact that both deviations are mainly between 0 % an 0.3 % percent shows that this assumption approximates the actual behavior very well.

Figure 3.39a shows that this also holds true when the imaginary part is plotted over the measurement frequency, with all measurements starting from the same SoC. The only difference in the correction equation 3.120 is then the measurement period, which causes $Z_{OCV/SoC}$ to form a straight line on a double logarithmic scale. The small dent between 10 mHz and 30 mHz comes from changes in the

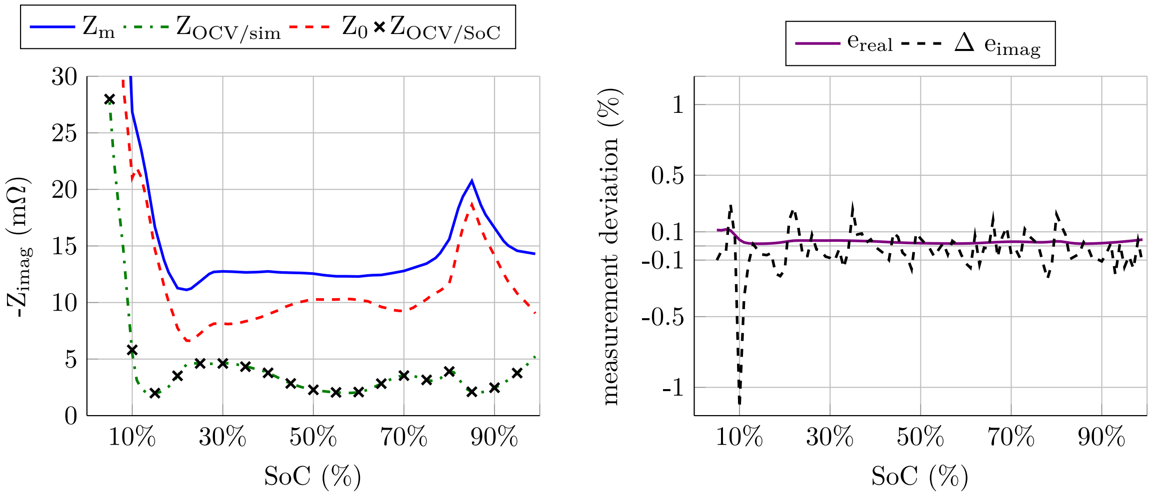

(a) Imaginary part.

(b) Deviation of the real part and the difference of the imaginary part between the linear OCV approach and the real OCV approach.

Figure 3.38: Measurement deviation due to the change in OCV during an impedance measurement. The figure shows the measured impedance $Z_m$, the deviation caused by OCV displacement determined by a simulation $Z_{OCV/sim}$ and by the linear estimation $Z_{OCV/SoC}$ according to equation 3.120 and the corrected impedance $Z_0$ (cylindrical NMC-cell A.2, $\hat{I}_m = 0.5\,\text{CA}$, $\vartheta = 25\,°\text{C}$, $f_m = 10\,\text{mHz}$).

assumed linear slope of the OCV. This is because the end SoC changes with every frequency. The Nyquist plot in figure 3.39b shows how the diffusion branch comes down towards the x-axis, when the imaginary impedance part is corrected.

Equation 3.120 shows that the measurement deviation is dependent only on the OCV-slope and on the measurement period. There is no dependency on the amplitude of the measurement current $\hat{I}_m$. The measurement current increases the SoC sweep during an impedance measurement but at the same time it also increases the voltage response $V_{Zm}$ in general. Since both are linearly dependent on the amplitude of the measurement current $\hat{I}_m$ the two effects cancel each other out.

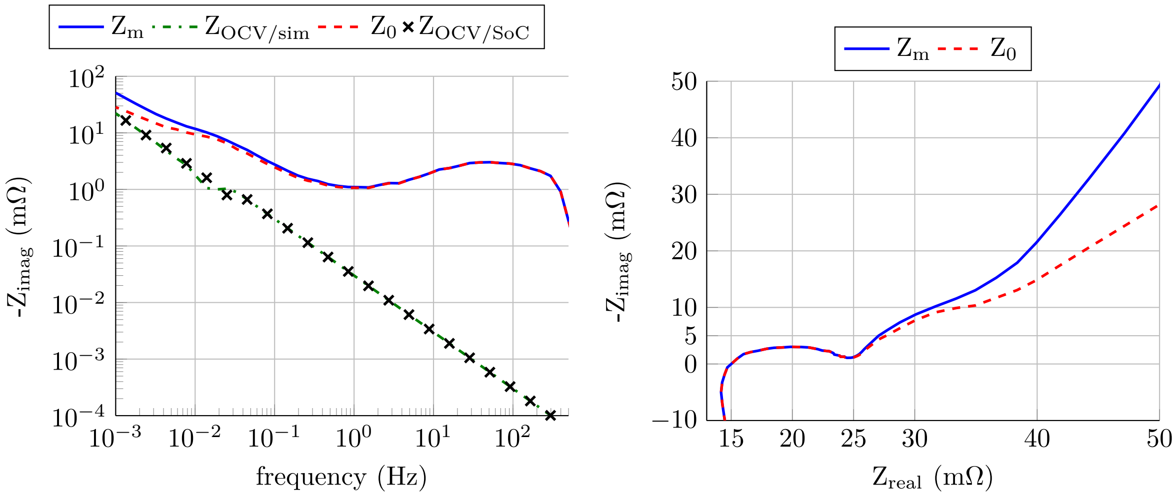

(a) Logarithmic plot.

(b) Nyquist plot.

Figure 3.39: Imaginary measurement deviations for EIS measurement frequencies from 1 mHz to 500 Hz (cylindrical NMC-cell A.2, $\hat{I}_m = 0.5\,\text{CA}$, $SoC_{start} = 50\,\%$, $\vartheta = 25\,°\text{C}$).

Because of this independence on the measurement current, the measurement deviations introduced by an OCV displacement cannot really be treated as a false measurement. It must be considered as an intrinsic effect that is dependent on the slope of the OCV, i.e. the SoC and the period of the measurement $T_m$, i.e. the measurement frequency $f_m$.

## 3.3.2 Open-Circuit-Voltage Displacement from Temperature Change

Figure 3.40 shows the difference between the effect discussed in this section and the one in the previous section 3.3.1. In this section the OCV displacement does not result from the change in SoC but in the change in temperature in combination with the entropy of the cell. The excitation current causes the temperature of the cell to change. The temperature dependent OCV therefore changes during the measurement and results in an additional signal measured by the EIS measurement. This deviation can only be determined and compensated with the knowledge of the entropy of the reaction $\Delta S$.

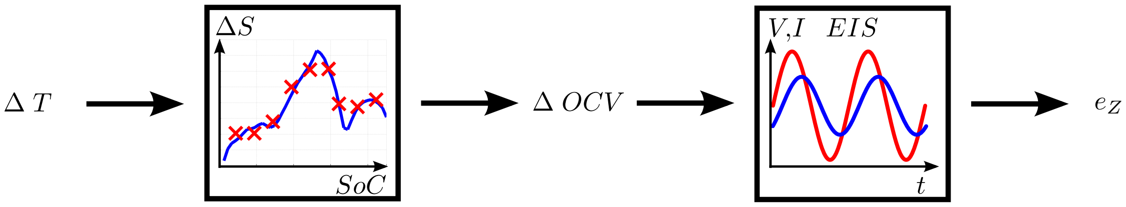

Figure 3.40: The origin of the OCV displacement is a change in temperature in combination with the entropy $\Delta S$ of the cell.

#### 3.3.2.1 Open-Circuit-Voltage Displacement

In the fundamentals, section 2.1.3 already showed that for small temperature changes, the OCV can be considered to be linearly dependent on the temperature. The change in OCV can be stated as:

$$\Delta V_{OCV} = \frac{\Delta S}{z\,F} \cdot \Delta\vartheta \tag{3.121}$$

The result is a changing OCV dependent on temperature. Figure 3.41 compares the the OCV difference of an NMC cell at 5, 15 and 35 °C to the OCV at 25 °C, which is obtained by a slow charge/discharge cycle of 0.1 CA, but where the battery is charged and discharged at 25 °C in between in order to have the same starting point for all OCV curves. If the starting SoC is not set with the same temperature, the end of charge SoC is slightly higher and the cut-off voltage is slightly lower at higher temperatures. The difference is in the range of a few 0.01 % of the SoC but crucial for the right alignment of the different curves in figure 3.41. The OCV difference is in most SoC ranges positive when temperature difference and entropy have both equal signs and is negative when they have opposite signs. The comparison is not perfect since the continuous charge current smears the edges of the entropy profile and it also heats the battery itself making it difficult to keep the temperature constant. This effect is especially dominant at low SoCs where entropy and impedance heating are especially high. Although not perfect, figure 3.41 shows that the OCV is dependent on the temperature of the cell.

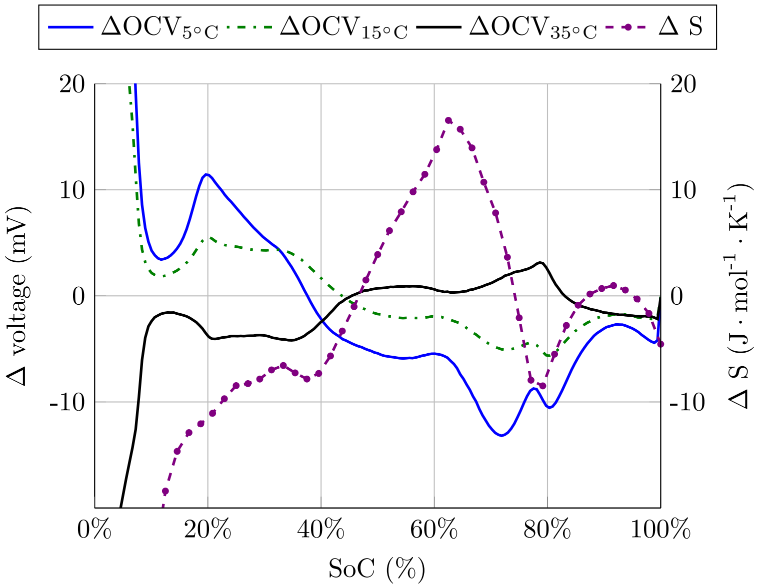

Figure 3.41: Comparison between the entropy $\Delta S$ and the OCV difference to $\vartheta = 25\,°\mathrm{C}$ at 5 °C, 15 °C and 35 °C (cylindrical NMC-cell A.2).

#### 3.3.2.2 Impedance Measurement Deviation

Since the temperature dependency of the OCV is, for small temperature changes, linear, any steady increase in temperature leads directly to a linear voltage drift of the voltage. A drift can be identified and compensated. Section 4.1 introduces various ways to correct them. This section only deals with the sinusoidal part of the temperature change. Equation 3.122 shows the two sinusoidal parts of the temperature change, one comes from impedance heating and the other one from entropy heating.

The first shows a behavior of double the EIS measurement frequency. This part is irrelevant for the measurement since the Fourier transformation will suppress it. The second part has the same frequency as the EIS measurement. With this remaining part, the OCV change due to temperature change is similar to the OCV change due to SoC change (see equation 3.120 and 3.123). It also has a phase shift of $\frac{\pi}{2}$ to the excitation current. This means the same considerations from section 3.3.2 apply and the same equations can be used. Equation 3.124 shows the impedance measurement deviation introduced by an OCV displacement caused by a temperature change. Similar to the one caused by an SoC change it is purely imaginary.

$$\Delta\vartheta(t) = \underbrace{-\frac{HGR_{fm}}{C_{th}} \cdot \frac{\hat{I}_m{}^2 \cdot T_m}{8\pi} \cdot \sin(2\omega_m t)}_{\text{impedance heating}} \underbrace{-\frac{\Delta S \cdot T}{z\,F \cdot C_{th}} \frac{\hat{I}_m \cdot T_m}{2\pi} \cdot cos(\omega_m t)}_{\text{entropy heating}} \tag{3.122}$$

$$v_{\Delta\vartheta}(t) = -\frac{\Delta S}{zF} \cdot \frac{\Delta S \cdot T}{z\,F \cdot C_{th}} \frac{\hat{I}_m \cdot T_m}{2\pi} \cdot \cos(\omega_m t) \tag{3.123}$$

$$Z_{OCV/\vartheta} = -j\frac{\Delta S^2}{z^2\,F^2}\frac{T}{C_{th}}\frac{T_m}{2\pi} \tag{3.124}$$

### 3.3.3 Comparison of Measurement Deviations

During an EIS measurement, both sources of measurement deviations, SoC change and temperature change occur at the same time (see equation 3.125). They have different magnitudes for different battery cell types. In general, the square of the Faraday constant significantly reduces the magnitude of the deviation, which comes from a temperature change. Figure 3.42 compares the magnitude of both effects. The deviation due to temperature dependency $e_{OCV/\vartheta}$ is by a factor of $10^{-4}$ smaller than the deviation due to SoC dependency $e_{OCV/SoC}$. Therefore, its contribution can be neglected and the impedance change $Z_{OCV}$ can be considered to be only caused by OCV displacement from SoC change (see equation 3.127).

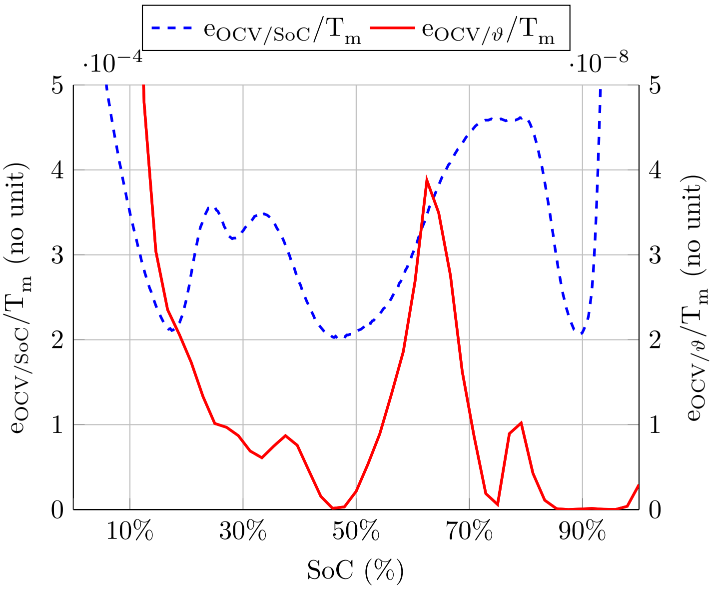

Figure 3.42: Comparison of the measurement deviation introduced by SoC change $e_{OCV/SoC}$ and introduced by temperature change $e_{OCV/\vartheta}$ (cylindrical NMC-cell A.2, $\vartheta = 25\,°\mathrm{C}$).

$$Z_{OCV} = Z_{OCV/SoC} + Z_{OCV/\vartheta} \tag{3.125}$$

$$Z_{OCV} = -j\frac{T_m}{2\pi} \cdot \left[ \left.\frac{\Delta OCV}{\Delta SoC}\right|_{T,\Delta SoC} \frac{1}{C_{el}} + \frac{\Delta S^2(T,SoC)}{z^2\,F^2} \frac{T}{C_{th}} \right] \tag{3.126}$$

$$Z_{OCV} \approx Z_{OCV/SoC} \tag{3.127}$$

For a multi-sine measurement, the part with double the measurement frequency of equation 3.122 would be relevant. But since the effect is in general negligible, a discussion about the impact the deviation has on a multi-sine measurement is omitted.

**Section Conclusion**

*This section has shown that the change of the Open-Circuit-Voltage introduces an additional signal besides the signal that is caused by the voltage drop over the complex impedance. This Open-Circuit-Voltage change can come from two different sources. The first one is the change in State-of-Charge. The second source is the change in temperature. The entropy* $\Delta S$ *of a cell is a measure of how much the Open-Circuit-Voltage changes with a change of temperature.*

*The additional signal introduced by both sources has a phase delay of* $\frac{\pi}{2}$*. Therefore, this additional signal only introduces a change in the imaginary part of the impedance. This is only true as long as the battery cell parameters* $\frac{\Delta OCV}{\Delta SoC}$ *or the entropy* $\Delta S$ *can be considered constant during the measurement. Even if this is not the case, the measurement deviation on the real part is small compared to the imaginary part. This is again because of the phase delay of* $\frac{\pi}{2}$*.*

*A comparison of the magnitude of the two sources revealed that the deviation introduced by temperature change is negligible compared to the deviation introduced by a State-of-Charge change. In both cases the deviation introduced is not dependent on the excitation current amplitude but mainly on the measurement frequency. This deviation is always present and can be considered as an inherent State-of-Charge and measurement frequency dependent part of the impedance of the cell. Due to this fact it is not relevant for further considerations on the amplitude of the excitation current and section 3.5 in which all the different impedance measurement deviations are compared with each other, will not consider it.*

## 3.4 Measurement Deviation Caused by Impedance Non-linearity

Diard et al. [34], [32] built a theoretical framework to describe the measurement deviation introduced by an impedance measurement over a polarisation resistance governed by the Butler-Volmer equation. In order to derive his equations, he used the MacLaurin series and assumed that $\alpha = 0.5$. The MacLaurin series approximates the Butler-Volmer equation at an overvoltage of zero with a Taylor series expansion [8]. In [34] he verified his theory experimentally with a semiconductor diode and in [32] with an electrochemical redox system.

### 3.4.1 Double Butler-Volmer Equation

There are two electrode/electrolyte surfaces in a commercial li-ion battery full cell: one on the cathode and one on the anode. The current passing through this interface can be described by the Butler-Volmer equation. These electrode/electrolyte surfaces are the main source of non-linear behavior of the impedance itself. Most other components in the cell, such as the electronic conducting current collectors and the ionic conducting separator have a almost constant ohmic resistance. This means that the non-linear behavior can be described by two non-linear resistances, related to the two electrode/electrolyte surfaces in series whose current is described for each one by the Butler-Volmer equation. Equation 3.128 shows the difficulty to solve this equation. The voltage distribution over the two electrode/electrolyte surfaces cannot be easily determined. One of the two equations would need to be solved for the voltage $v_C$ or $v_A$ and then entered into the exponent of the exponential function of the other equation. This cannot be done in a closed form and would need to be done iteratively.

$$i_{2xct} = i_{0C} \cdot \left[ e^{\frac{(1-\alpha_C)zF(v_C - v_0)}{RT}} - e^{\frac{(-\alpha_C)zF(v_C - v_0)}{RT}} \right] = i_{0A} \cdot \left[ e^{\frac{(1-\alpha_A)zF(v_A - v_0)}{RT}} - e^{\frac{(-\alpha_A)zF(v_A - v_0)}{RT}} \right] \quad (3.128)$$

Most studies on Nernstian- or Tafel-systems, which follow the Butler-Volmer equation, are performed for a system in which only one redox-couple is present. Applied to batteries, it means that only one electrode of a li-ion full cell is studied. When using complex models, which are capable of iterative calculations, full cells with two electrode/electrolyte surfaces and two Butler-Volmer equations are used [98].

The main difficulty is that there is no mathematical rule with which two exponential functions can be simplified to a single exponential function. However, a simplification is necessary since the equation 3.128 is too complex for further calculations. Figure 3.43 shows two Butler-Volmer equations, the series connection of the two and a single Butler-Volmer equation fitted to the series connection of the two.

The fitted single Butler-Volmer equation is hardly capable of approximating the series connection of the two original Butler-Volmer equations. The resulting curve is more linear. This makes sense, considering the the 10 mV-Criterion rests mainly on the fact that the Butler-Volmer curve can be approximated with a linear function at voltage values below 10 mV. If now several similar equations are combined, this approximation holds true for a wider voltage range. Adding a linear function to it could therefore result in a better fit. This added linear function is equivalent to adding an ohmic resistance to the resulting equivalent circuit.

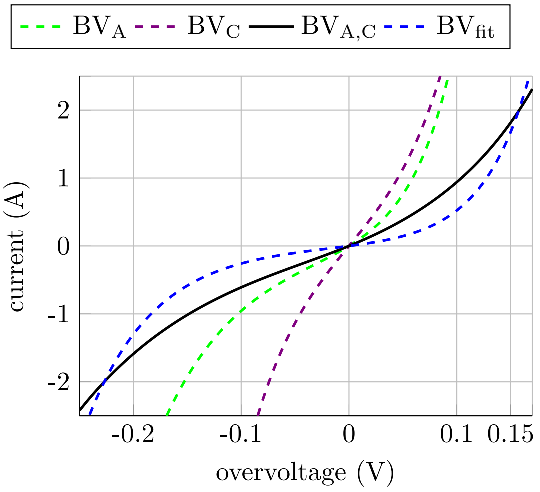

Figure 3.43: Two single Butler-Volmer equations, their series connection and the attempt to fit the series connection with a single Butler-Volmer equation. ($i_{0C} = 0.5$, $i_{0A} = 0.25$, $\alpha_C = 0.5$, $\alpha_A = 0.35$).

Figure 3.44 summarizes all the three options by showing their equivalent circuit. The first one is the already discussed single Butler-Volmer equation. The second one is the Butler-Volmer equation in series with an ohmic resistance. The third one is the Butler-Volmer equation with an ohmic resistance in parallel.

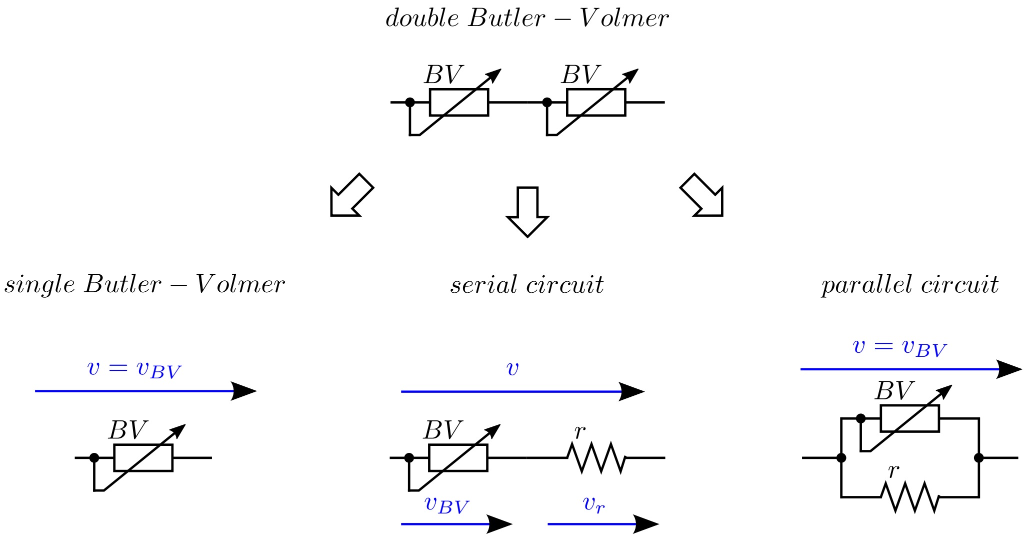

Figure 3.44: Different options to approximate two in-series Butler-Volmer equations.

The respective mathematical descriptions of these three options are shown by equation 3.129, 3.130 and 3.131.

$$i_{BV} = i_0 \cdot \left[ e^{\frac{(1-\alpha)zFv_{BV}}{RT}} - e^{\frac{-\alpha zFv_{BV}}{RT}} \right] \tag{3.129}$$

$$i_{ser} = i_0 \cdot \left[ e^{\frac{(1-\alpha)zFv_{BV}}{RT}} - e^{\frac{-\alpha zFv_{BV}}{RT}} \right] = \frac{v - v_{BV}}{r} \tag{3.130}$$

$$i_{par} = i_0 \cdot \left[ e^{\frac{(1-\alpha)zFv_{BV}}{RT}} - e^{\frac{-\alpha zFv_{BV}}{RT}} \right] + \frac{v_{BV}}{r} \tag{3.131}$$

Figure 3.45 shows the comparison of the different equivalent circuits to the sum of the two Butler-Volmer equations already introduced before. The single Butler-Volmer equation shows the biggest deviation of all three equivalent circuits. The series and parallel equivalent circuit result in an equal quality of the fit.

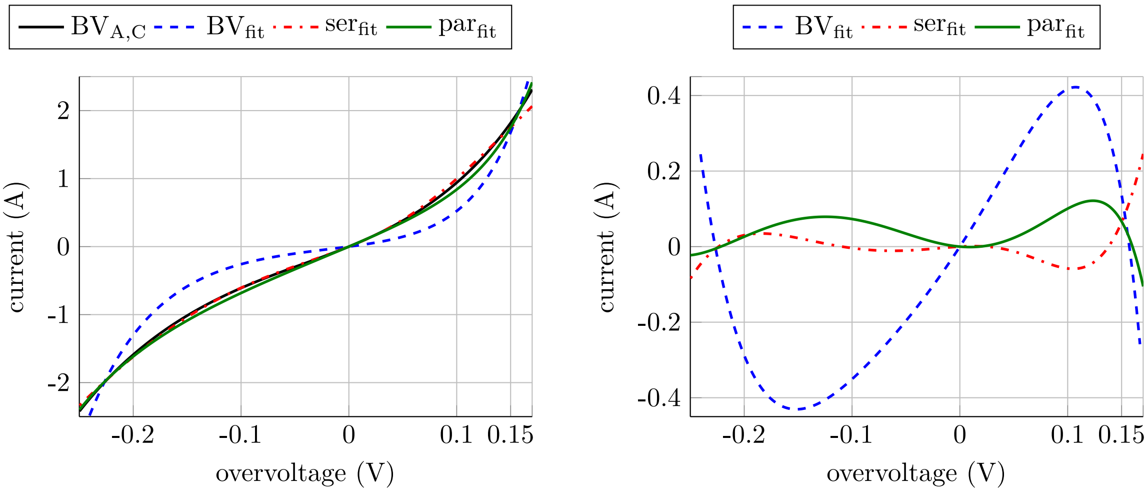

(a) Current over overvoltage.

(b) Difference to $BV_{\Sigma}$.

Figure 3.45: Sum of two Butler-Volmer equations according to equation 3.128, fitted by a single Butler-Volmer equation, a serial and a parallel circuit ($i_{0C} = 0.5\,\mathrm{A}$, $i_{0A} = 0.25\,\mathrm{A}$, $\alpha_C = 0.5$, $\alpha_A = 0.35$). The fitting was done for the current interval from $-2.5\,\mathrm{A}$ to $2.5\,\mathrm{A}$.

Figure 3.46 shows the r$^2$ value as a measure of the quality of the fit for various parameter values of $i_{0A}/i_{0C}$, $\alpha_A$ and $\alpha_C$.

All three equivalent circuits work best if the $\alpha$ and the $i_0$ values of the anode and cathode are close to each other. The more they differ, the worse the fit quality becomes. Especially for $\alpha_A < 0.25$ or $\alpha_A > 0.75$ the fit quality deteriorates. However, $\alpha$ values for a single Butler-Volmer equation are reported to be in close vicinity of 0.5 [41].

Considering that $\alpha$ has only values in the interval from 0.25 to 0.75, the following conclusions can be drawn: For the parallel and serial circuit, both are consistently better than a single Butler-Volmer equation. For most parameter values, the parallel circuit has a slightly better fit quality than the serial circuit.

For equation 3.130 of the serial equivalent circuit, only the current through the non-linear BV-equation or the ohmic resistance has to be determined, since the two currents are identical. The problem is that the distribution of the voltage drop between the non-linear resistance governed by the Butler-Volmer equation and the linear resistance $r$ is unknown and can only be determined by an iterative process.

The goal of this chapter is to derive equation for the measurement deviation in closed algebraic form.

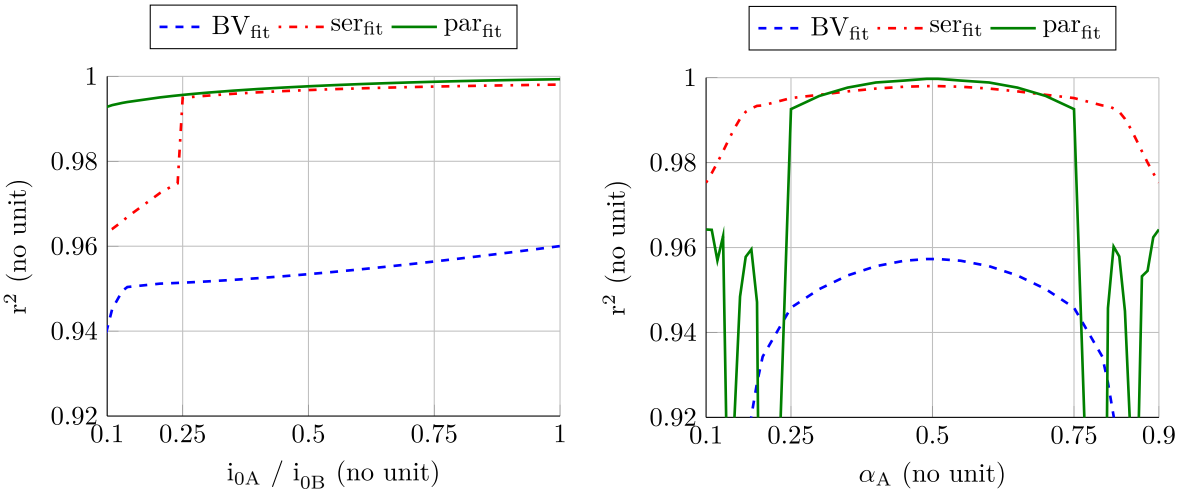

(a) r$^2$ over $i_{0A}/i_{0C}$ for $\alpha_A = 0.35$, $\alpha_C = 0.5$.

(b) r$^2$ over $\alpha_A$ for $i_{0A} = 0.25\,\mathrm{A}$, $i_{0C} = 0.5\,\mathrm{A}$, $\alpha_C = 0.5$.

Figure 3.46: r$^2$ value for the fitting of a double Butler-Volmer equation 3.128 with a single Butler-Volmer equation 3.129, with the serial circuit (equation 3.130) and with the parallel circuit (equation 3.131).

This is only possible for the parallel equivalent circuit, for which the voltage over the linear resistance $r$ is the same as the voltage over the non-linear resistance governed by the Butler-Volmer equation. For an easier mathematical use of the parallel circuit and the fact that the parallel circuit achieves generally a better fit quality, this equivalent circuit is used.

## 3.4.2 Measurement of Non-linearity

The measurement of non-linearity is difficult since several effects take place at the same time. In order to get into the non-linear region high currents have to be applied to the battery cell. These currents cause the battery and especially the electrode/electrolyte interface to heat up [12]. This again changes the measurement result. Additionally the current is changing the SoC during the measurement, which can be significant depending on how long the current is applied. There are four different ways to measure non-linearity of a battery half or full cell:

1. Charge/Discharge cycles
2. Microcycles
3. Microcycle-Impedance
4. Harmonics

### 3.4.2.1 Charge/Discharge Cycles

The measurement method follows the following sequence: Firstly, the OCV is determined for the battery. Secondly, a battery is charged and discharged by various currents in order to obtain the overvoltage at that particular current for all SoCs. For a particular SoC, the currents are plotted over the obtained overvoltage.

There is no measurement deviation introduced by a change in SoC since this deviation is ruled out when the various charge/discharge curves are aligned. However, the deviation by a change in temperature is significant. The method requires the current to be applied for an entire charge or discharge cycle of the cell. During that time the temperature increases. Even if the temperature is measured at the same time the measurement points are all at different temperatures and cannot be compared with each other.

Figure 3.47 shows a measurement with this method without any temperature compensation. The graph reveals two other shortcomings of the method. Very small currents and voltages take a long time to measure. The lowest current in Figure 3.47 is 0.02 CA, for which it takes around 100 hours to complete the charge/discharge cycle. This is why a high resolution close to zero Ampere is very difficult to achieve.

The other disadvantage is that positive currents can only be measured as long as they do not cause the cell voltage to exceed the maximum voltage of the cell, i.e. as long as the battery does not go into constant-voltage mode. This caused the current-voltage curve for 80 % SoC in figure 3.47 to stop at around 2.5 A. The last drawback of this method is that it can only measure the non-linearity for a constant current signal, and not, for example, a 1 kHz signal. This means, that the non-linearity of very large time constants is measured for which also the diffusion effect due to charge transport occurs. This is an additional non-linear effect besides the one described by the Butler-Volmer equation. The benefit on the other hand is that it is easy to use since the non-linearity can be derived from simple charge/discharge curves, which might be already available from other measurements.

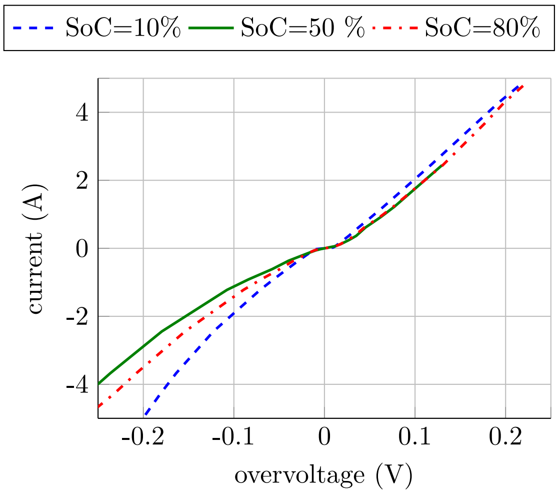

Figure 3.47: Non-linearity for different SoCs measured with the charge/discharge method (cylindrical NMC-cell A.2).

### 3.4.2.2 Microcycles

In this method not entire charge/discharge cycles are applied, but shorter pulses are used. Farmann et al. in [41] and Gaberscek et al. [43] used this method with pulses around 2 to 20 s in length. The left side of figure 3.48 shows the measurement principle. A current pulse is applied, at the end of the pulse the current and voltage is measured. The measurement is valid for the SoC at the end of the pulse. After one positive pulse its negative counterpart is applied. Due to this alternation of pulses the SoC stays the same after each charge/discharge cycle. The result is the large signal response of the battery. If several pulses are applied these measurement points can be combined and give a current-overvoltage curve that represents the non-linearity of the battery. This curve can then be fitted with the parallel equivalent circuits derived in the previous section 3.4.1. The benefit of this method is that the heat generated inside the cell for short pulses below ten seconds is negligible. For longer pulses, the measurements need to be compensated by the temperature change. The equations for deviations caused by constant current introduced in section 3.2.5.3 can serve as a starting point. The equations in that section give the deviation in impedance, which need to be converted into a voltage deviation.

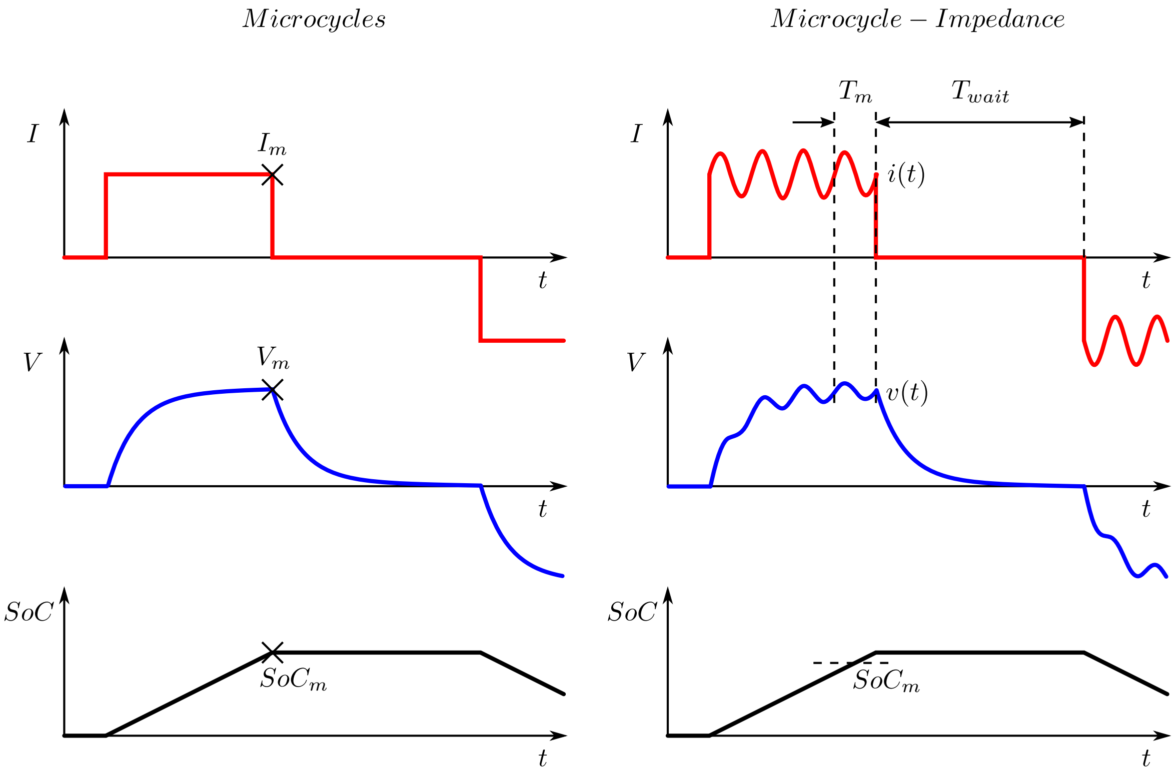

Figure 3.48: Comparison of two different methods to measure the non-linearity of impedance.

### 3.4.2.3 Microcycle-Impedance

The Microcycle-Impedance method is similar to the Microcycle method. The current pulse is superpositioned with a sinusoidal current signal causing the battery to respond with a sinusoidal change of the battery voltage with the same frequency. Karden et al. [59] used a similar method on lead-acid batteries in order to avoid artefacts caused by constant charging and discharging but not for determining Butler-Volmer parameters. He called them minicycles. Dumm in [36] used a similar method and applied pulses with a smaller length and therefore called them Microcycles. At the beginning, the current pulse causes a response of the battery voltage similar to an exponential function, which then turns into a rather linear change. Only the last period of the sinusoidal signal, before the pulse is turned off, is evaluated. This is done because a linear drift is easier to compensate as the initial exponential drift and that transients at the beginning would distort the impedance measurement [45]. The result is the small signal impedance at different magnitudes of the current pulse.

Here, the heat generated inside the cell for short pulses below ten seconds is negligible. For longer pulses, the measurements can be compensated by the equations developed in section 3.2.5.3. The data derived is split into the real and imaginary part as opposed to only the modulus giving this method an advantage over the Microcycle method. Because of this advantage, this method has been applied to determine the non-linearity of a cell in the next section 3.4.3. The detailed analysis of the data is also explained in that section.

#### 3.4.2.4 Harmonics

A sinusoidal signal of a certain frequency applied to a function that is not linear, e.g. an exponential function, causes the response to have the original frequency and several harmonics of that frequency. Harmonics are frequencies of an integer multiple of a base frequency. In this case the base frequency is the applied measurement frequency. Diard et al. [33; 34], Kiel et al. [63] and Kiel [62] showed how and at which magnitudes voltage harmonics are generated by a sinusoidal current. Kiel et al. considered it as an indication of a too high current excitation and suggested that the amplitude of the harmonics could be monitored in order to control the excitation current amplitude. But he did not give any further analysis which harmonic that should be, which threshold corresponds to which measurement deviation or which threshold should be taken. Both authors proposed to use the harmonics of the electrochemical system's response in order to correct the impedance measurements to a linear system. Diard et al. showed this with experimental data on a redox electrochemical system for which the influence of the non-linearity was very strong and whose measurement deviations were in the range of several percent (5 % to 50 %).

From the analytical derivation of the harmonics, it could be possible to determine the parameters of the underlying Butler-Volmer equation. For the case of an underlying constant current, Kiel et al. [63] simplified the Butler-Volmer equation to the Tafel equation, and with the help of a Taylor series expansion, derived the theoretical magnitudes of every harmonic. The mathematical trick of using a Taylor expansion comes with the cost that the expansion has to be done for every constant current applied. The Taylor expansion only fits the data well for values in close vicinity of the operation point at which the expansion was done. For the case of no underlying constant current, he simplified the Butler-Volmer equation to the sinus-hyperbolicus function assuming that $\alpha$ is always 0.5. Diard et al. [33] did something similar by assuming $\alpha = 0.5$ and by using a Maclaurin series. In both cases, only the value of $i_0$ can be varied. This simplification reduces the general applicability of this equation, since $\alpha$ is pinned to a fixed value of 0.5.

Equation 3.132 shows the general equation for any harmonic current $i_n$ caused by a sinusoidal voltage used in a Butler-Volmer equation. For the detailed derivation of this equation refer to appendix D.1.

$$\begin{aligned} \mathrm{F}\{i_n(t)\} = (-j)^n \cdot 2i_0 \cdot e^{\frac{(1-\alpha)zFV_{dc}}{RT}} \cdot \mathcal{I}_n\left(\frac{(1-\alpha)zF\hat{V}_m}{RT}\right) \\ - (-j)^n \cdot 2i_0 \cdot e^{\frac{-\alpha zFV_{dc}}{RT}} \cdot \mathcal{I}_n\left(\frac{-\alpha zF\hat{V}_m}{RT}\right) \end{aligned} \tag{3.132}$$

Figure 3.49 shows an example of this equation for specific values up to the 5th harmonic and compares it with values obtained from a simulation.

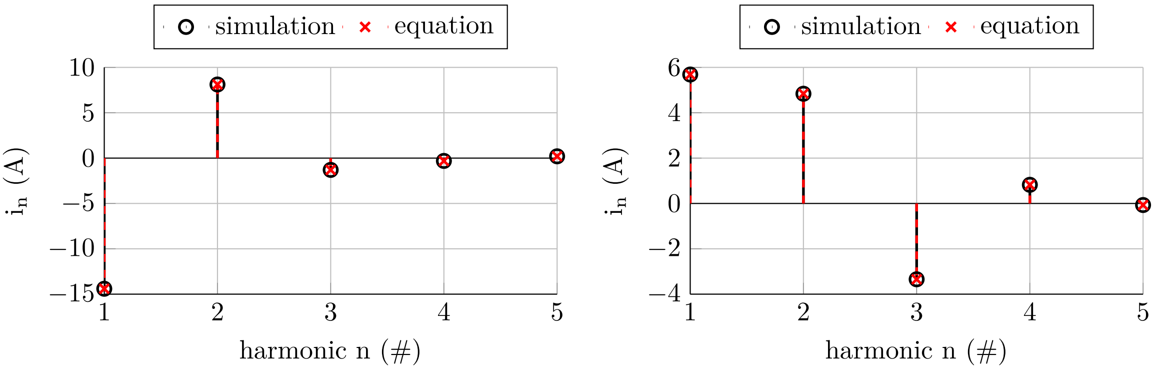

(a) Real part.

(b) Imaginary part.

Figure 3.49: Fundamental and harmonics of the current created by a sinusoidal voltage applied to a Butler-Volmer equation ($V_{dc} = 0.1V$, $\hat{V}_m = 0.1\,\mathrm{V}$, $i_0 = 0.5 + 2\mathrm{i}\,\mathrm{A}$, $\alpha = 0.65 + j0.45$). The values for $V_{dc}$, $\hat{V}_m$ were intentionally chosen large, in order to obtain large values for the harmonics.

It is valid for any voltage deflection of the battery from its OCV caused by a constant current. However, it assumes that the excitation is potentiostatic. For a galvanostatic excitation, the constant overvoltage $V_{dc}$, caused by the constant current, or the amplitude of the sinusoidal voltage $\hat{V}_m$, caused by a sinusoidal current, need to be pre-determined. An iterative solution process or a lookup table in which all overvoltages are mapped to a current can give this information. Kiel et al. [63] and Kiel's [62] equations directly use a galvanostatic excitation.

The linearization effect caused by two charge transfer reactions in series and discussed in section 3.4.1 and any other ohmic resistance only needs to be taken into account for the fundamental frequency. They do not affect the harmonics, since any linear part only causes the fundamental frequency of the response to be higher but not the harmonics.

The following two paragraphs discusses the applicability of the harmonics to identify:

1. the parameters of the Butler-Volmer equation.
2. a too high excitation current.

Can the harmonics be used to identify the parameters of the Butler-Volmer equation, namely $i_0$ and $\alpha$? For determining two unknowns, two independent equations are needed. The equations for two harmonics could be used for this purpose. In order to know which harmonics would be the best ones to use, all considerations are made for potentiostatic excitation, which can, once proven possible, transferred to galvanostatic excitation.

The theoretical considerations are done in the first step for the case when there is no constant voltage $V_{dc}$ present and in the second step if there is a constant voltage $V_{dc}$ present. For the case when there is no constant voltage present: The modified Bessel function of the first kind $\mathcal{I}_n$ is for even order numbers of $n$ an even function and for odd order numbers of $n$ an odd function. Or in mathematical terms: $\mathcal{I}_n(-x) = \mathcal{I}_n(x)$ for $n = 0,2,4,...$ and $\mathcal{I}_n(-x) = -\mathcal{I}_n(x)$ for $x_n = 1,3,5,....$ Equation 3.132 shows that the two summands can be added for odd order numbers but need to be subtracted for even order numbers. This becomes especially harmful the closer $\alpha$ is to the value 0.5. Then, the two summands cancel each other out for even order numbers. Because of this only the third and the fifth harmonic can be used. This is theoretically possible, but in a real application the result of the fifth harmonic is very small and will be subject to a lot of noise. Figure 3.50a shows the ratio of $\mathcal{I}_1(x)/\mathcal{I}_5(x)$. Depending on

the argument, 3.50a shows the amplification factor which need to be used to convert a value measured at the fifth harmonic to the fundamental. Also, any kind of noise would be amplified with the same factor. Because of this, the results derived from the fifth harmonic will most likely be unusable.
For the case when there is a constant voltage present. One summand of the equation 3.132 can be neglected since the value of its exponential function becomes very small. Because of this, it becomes possible to use the second and the third harmonic. However, as will be shown in section 4.1, the additional drift which is caused by an underlying constant voltage (or constant current for galvanostatic excitation) causes harmonics as well. These are much larger than the ones caused by the non-linearity of the Butler-Volmer equation making this approach also highly erroneous.
Although there is no formal inverse function for the modified Bessel function of the first kind $\mathcal{I}_n(x)$, it can be inverted for only positive or negative values of $x$ with a lookup table, meaning that for every value of $\mathcal{I}_n(x)$ there is only one $x$ which results to that value (appendix C.5 shows examples of $\mathcal{I}_n(x)$). For both cases, measurements without constant overvoltage or with constant overvoltage, the resulting equation for $\alpha$ is a transcendental equation, which does not have a closed form solution and would need to be solved by an iterative process.
To summarize, in most cases and at least for on-line applications, the noise at the fifth harmonic will be too large to derive any reasonable result. A drift causes additional harmonics, which make the simplification with the Tafel equation impossible. Even if these effects would not exist, the calculation would involve an iterative process using a lookup table. For those reasons the identification is theoretically possible but extremely difficult to apply in practice.

How applicable is the usage of the harmonics to identify a too high excitation current? This seems to be an interesting approach, since equation 3.132 shows that the fundamental and the harmonics are calculated in a similar way. Ratios between the fundamental and the harmonics could be used, making the exact identification of the parameteres unnecessary. To answer this question, only the Butler-Volmer equation is considered without any additional linear components. This allows the determination of the impact of the Butler-Volmer equation to the fundamental without the other linear components. All the considerations are made for potentiostatic excitation, which can, once proven possible, transferred to galvanostatic excitation. Equation D.7 shows the ratio for measurements without constant voltage. Equation D.9 shows the ratio for measurements with positive constant voltage for which the second term of equation 3.132 has been neglected, since for a positive constant voltage the factor $e^{\frac{(1-\alpha)zFV_{dc}}{RT}}$ becomes large and the factor $e^{\frac{-\alpha zFV_{dc}}{RT}}$ becomes small. For the reasons given above, for measurements without constant voltage, the third harmonic should be used and for measurements with constant voltage, the second harmonic should be used. For a detailed derivation of equations 3.133 and 3.133 please refer to appendix D.2.

$$\frac{\mathrm{F}\{i_{n=1}(t)\}}{\mathrm{F}\{i_{n=3}(t)\}} = \frac{-j}{(-j)^3} \cdot \left[ \frac{\mathcal{I}_1\left(\frac{(1-\alpha)zF\hat{V}_m}{RT}\right) - \mathcal{I}_1\left(\frac{-\alpha zFV_{dc}}{RT}\right)}{\mathcal{I}_3\left(\frac{(1-\alpha)zF\hat{V}_m}{RT}\right) - \mathcal{I}_3\left(\frac{-\alpha zFV_{dc}}{RT}\right)} \right] \tag{3.133}$$

$$\frac{\mathrm{F}\{i_{n=1}(t)\}}{\mathrm{F}\{i_{n=2}(t)\}} = \frac{-j}{(-j)^2} \cdot \frac{\mathcal{I}_1\left(\frac{(1-\alpha)zF\hat{V}_m}{RT}\right)}{\mathcal{I}_2\left(\frac{(1-\alpha)zF\hat{V}_m}{RT}\right)} \tag{3.134}$$

Equation D.7 already shows that without the knowledge of $\alpha$ no factor between the third harmonic and the fundamental frequency can be stated. Figure 3.50b shows the ratio of $\mathcal{I}_1(x)/\mathcal{I}_2(x)$.

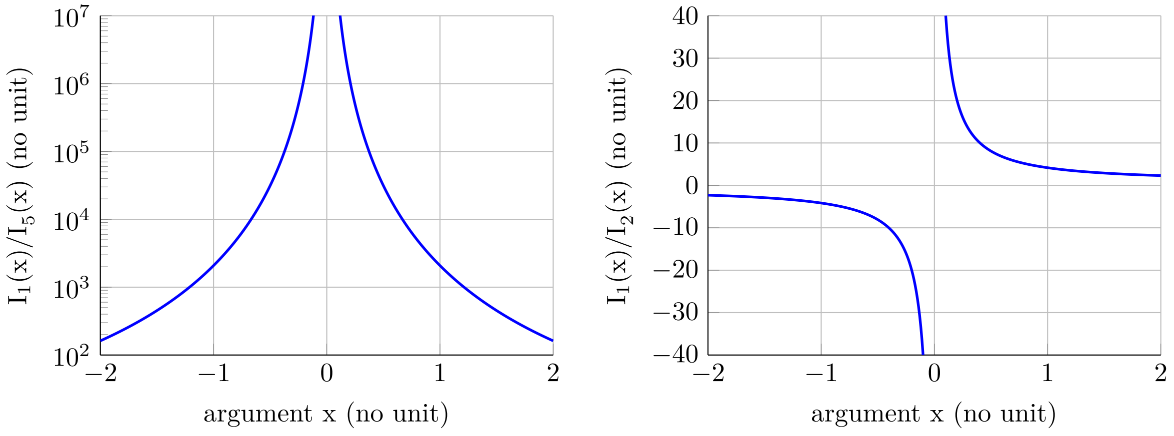

(a) $\mathcal{I}_1(x)/\mathcal{I}_5(x)$ (b) $\mathcal{I}_1(x)/\mathcal{I}_2(x)$

Figure 3.50: Ratios of the modified Bessel function of the first kind $\mathcal{I}_n(x)$. The argument $\frac{-\alpha z F \hat{V}_m}{RT}$ with $\alpha = 0.5$ would have a value of around 0.1 when $\hat{V}_m = 10\,\mathrm{mV}$ (minimum shown here) and 2.0 when $\hat{V}_m = 100\,\mathrm{mV}$ (maximum shown here).

Unfortunately, there is no constant factor between them, which would make it possible to conclude from the harmonic with any argument in the modified Bessel function of the first kind $\mathcal{I}_n(x)$ to the fundamental with the same argument in $\mathcal{I}_1(x)$. This makes it necessary to know the value of the argument. The same is true for any other ratios of the modified Bessel function of the first kind.

To know the argument it is necessary to know $\alpha$. If $\alpha$ would be known, the ratio of $\mathcal{I}_1(x)/\mathcal{I}_n(x)$ could be determined and by multiplying it with $-j/(-j)^n$ the factor between the harmonic value and the fundamental value could be determined without ever calculating the exchange current $i_0$. Calculating $\alpha$ poses the problems already discussed in the paragraph above, which discussed the possibility of identifying the Butler-Volmer parameters. But if $\alpha$ would be known, determining $i_0$ would be possible as well and instead of calculating the non-linear impact on the fundamental, the measurement deviation caused by the Butler-Volmer non-linearity could be directly calculated according to the equations introduced in the next two sections 3.4.4 and 3.4.6. The problem of identifying a too high excitation current by evaluating the harmonics of the measurement is therefore the same as the problem to identify the parameters by evaluating the harmonics. The answer to the question whether it is possible to identify a too high excitation current is therefore also the same: It is theoretically possible but extremely difficult to apply in practice.

### 3.4.3 Magnitude of Non-linearity

The raw measurements shown in this section were carried out during the supervision of the Master Thesis of Dumm [36]. They were only partly included in his thesis. The raw measurements were evaluated and fitted again in order to include them in this thesis.

Among the four different ways to measure non-linearity introduced in section 3.4.2 the Microcycle-Impedance was identified to be the best. The impact on temperature increase can be kept to a minimum due to the short apply time of the pulses and it does not rely on very noise free and extremely accurate sensors as the method using harmonics does. Compared to the Microcycles method, it also gives information on the real and imaginary part. Since this whole chapter is always dealing with both parts and revealed more insights because to this separation, this way is continued for measuring the impedance non-linearity.

Typically the Butler-Volmer equation is only defined for the real part. Since the charge transfer resistance $R_{ct}$ in parallel to the double layer capacitance $C_{dl}$ is a variable resistance (see figure 3.51).

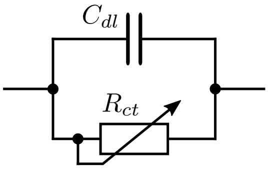

Figure 3.51: Theoretical model of the non-linearity of the charge transfer resistance $R_{ct}$ and the double layer capacity $C_{dl}$.

The capacitance $C_{dl}$ is considered to be independent from the current magnitude applied. However, for the imaginary part a similar effect as for the real part, i.e. a decrease in resistance with increasing current, was measured. Figure 3.54b and A.1.5b show this effect. Some capacitances are known to be voltage dependent, e.g. the capacitance of tantal capacitors. But for a li-ion battery the voltage change across the double layer capacitor $C_{dl}$ during an EIS measurement is too small to be relevant. Throughout this chapter the equation for real and imaginary part were the same. Only the parameters which need to be applied are different. In an attempt to stick to similar equations, the same modified Butler-Volmer equation 3.131 is used for the real and for the imaginary part. Fitting the imaginary measurements with the same Butler-Volmer equation was often possible. Figure 3.54b shows one data set for which the fitted data was not able to retrace the measurement data at high currents. In this case, due to the low imaginary overvoltage, the argument in the exponent does not become large enough when the value of $\alpha$ is in the range of 0.05 and 0.95. If larger values in the argument of the exponential function in equation 3.131 are be possible, the equation would also be able to fit the measured data very well.

The measurements were taken as described in section 3.4.2.3. The battery cell under test was placed in a liquid cooled copper block with a cylindrical opening, which was just large enough to accomodate the cylindrical battery cell. Thermal grease was additionally applied to improve the heat conductivity from the cell casing to the copper block. The thermal conductivity from the jelly roll to the casing of the cell cannot be improved and can be seen as the weakest link in the cooling chain. Because of this, a temperature change within the cell could not be entirely avoided during a Microcycle-Impedance pulse. In order to avoid the impact of a temperature increase from a precedent measurement pulse, large waiting times (see figure 3.48) between pulses were used.

To fit the measurement with the parallel equivalent circuit. First the ohmic resistance $R_{\Omega}$ was removed from the real part of the measured impedance. The data then represents the small signal impedance, real and imaginary part, at different magnitudes of the pulse current for the parallel equivalent circuit. Figure 3.52 shows how this piecewise small signal impedance values can be multiplied with the current step magnitudes in order to obtain the respective voltage values of a large signal response. Equation 3.136 and equation 3.137 respectively show the calculation of the voltage values for negative current and positive current. Please note that the obtained voltage values have a real and an imaginary part.

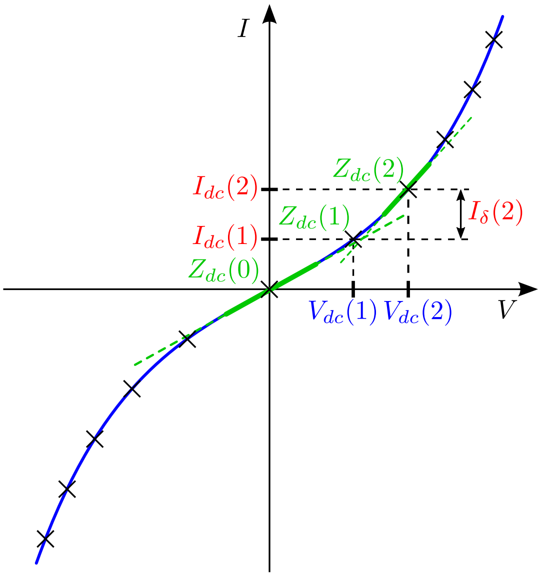

Figure 3.52: Piecewise current over voltage curve reconstruction with the knowledge of the impedance over current.

$$V_{dc}(0) = 0 \tag{3.135}$$

$$V_{dc}(x) = V_{dc}(x-1) + \underbrace{(I_{dc}(x) - I_{dc}(x-1))}_{=I_\delta(x)} \cdot \frac{1}{2}\left[Z_{dc}(x) + Z_{dc}(x-1)\right] \text{ for } x = 1..n \tag{3.136}$$

$$V_{dc}(x) = V_{dc}(x+1) + \underbrace{(I_{dc}(x) - I_{dc}(x+1))}_{=I_\delta(x)} \cdot \frac{1}{2}\left[Z_{dc}(x) + Z_{dc}(x+1)\right] \text{ for } x = -1..-n \tag{3.137}$$

These real and imaginary voltage curves are then fitted with the equation for the parallel equivalent circuit 3.131.
Table 3.3 shows the fitting results of measurements at different measurement frequencies taken at the same temperature $\vartheta = 25\,°\mathrm{C}$. A frequency with a higher non-linearity than another one produces lower values for the exchange current $i_0$ and higher values for the linear resistance $r$. The charge transfer coefficient $\alpha$ is an indicator for the symmetry of the resistance. A value of $\alpha$ between 0.5 and 1 indicates that the cell shows lower resistance during discharging than during charging. This is the case for the real part of the 10 mHz measurement. A value between 0 and 0.5 indicates that a cell shows lower resistances during charging than discharging. This is the case for the real part of the 1 kHz measurement. In the fitting process the value of $\alpha$ was limited to values between 0.05 and 0.95 in order to avoid unreasonable values. The more $\alpha$ deviates from 0.5, the more unsymmetric is the impedance. This reduces the range around 0 V in which the Butler-Volmer equation can be considered linear.

From only the fitting values, it is hard to tell which frequency is more non-linear. For example, the real part of the 10 mHz measurement has a very low value for $r$, indicating a very linear behavior, but also a very low value for $i_0$, indicating a non-linear behavior. The deviation of $\alpha$ from 0.5 makes an assessment even more difficult. For the real part of the 10 Hz measurement the values are the exact opposite: high $r$, high $i_0$ and $\alpha$ very close to 0.5. The values for the imaginary part do not show any trend in any direction making any assessment of the non-linearity impossible. Section 3.4.4 assesses the impact of those values to the deviation of the impedance measurement. Since the deviation to the impedance measurement is the most interesting indicator, this value can also be used as a proxy for assessing quantitatively in one value the non-linearity of a Butler-Volmer curve.

| | frequency | $R_\Omega$ (m$\Omega$) | $i_0$ (A) | $\alpha$ | $r$ (m$\Omega$) | $r^2$ |
|---|---|---|---|---|---|---|
| $Z_{real}$ | 10 mHz | 16.2 | 0.27 | 0.71 | 28 | 0.9996 |
| | 100 mHz | 16.2 | 1.15 | 0.68 | 28 | 1.0000 |
| | 1 Hz | 16.2 | 0.33 | 0.35 | 10 | 1.0000 |
| | 10 Hz | 16.2 | 2.88 | 0.47 | 116 | 0.9998 |
| | 100 Hz | 16.2 | 6.40 | 0.41 | 129 | 0.9989 |
| | 1 kHz | 0.0 | 0.05 | 0.28 | 16 | 0.9999 |
| $Z_{imag}$ | 10 mHz | 0.0 | -0.09 | 0.70 | -13 | 0.9991 |
| | 100 mHz | 0.0 | -7.41 | 0.95 | -23 | 0.9978 |
| | 1 Hz | 0.0 | -17.97 | 0.05 | -10 | 0.9968 |
| | 10 Hz | 0.0 | -9.30 | 0.45 | -7 | 0.9995 |
| | 100 Hz | 0.0 | -8.78 | 0.42 | -24 | 0.9996 |
| | 1 kHz | 0.0 | 29.76 | 0.05 | 21 | 0.9992 |

Table 3.3: Selected Microcycle-Impedance non-linearity measurements of the real and imaginary part fitted with the modified Butler-Volmer equation of 3.131. Parameter dependency on frequency. Raw measurements taken by [36].

Figure 3.53 shows the two measurements at 10 mHz and 10 Hz. The real part does not show the effect of the additional ohmic resistance $R_\Omega$ in series with the equivalent parallel circuit. Adding $R_\Omega$ would further linearize the curve. Especially the curve of the 10 mHz measurement shows the non-symmetry of the impedance for positive and negative currents. The same 2 A current needs 45 mV overvoltage in the charging direction and only $-40$ mV overvoltage in the discharging direction.

Table 3.4 shows the measurements at different temperatures with the measurement frequency 1 Hz. There is a clear trend for the real part and imaginary part of $i_0$ to increase with increasing temperature. The imaginary part of $r$ shows a clear trend to decrease with increasing temperature. The real part only shows a weak tendency in this direction. Both values, $i_0$ and $r$ indicate a more linear behaviour with increasing temperature. The real part of the $\alpha$ values are in a similar range. For all the measurements, the charge transfer coefficient $\alpha$ has a value below 0.5 indicating that the cell shows less resistance in charging direction than in discharging direction at 1 Hz regardless of the temperature.

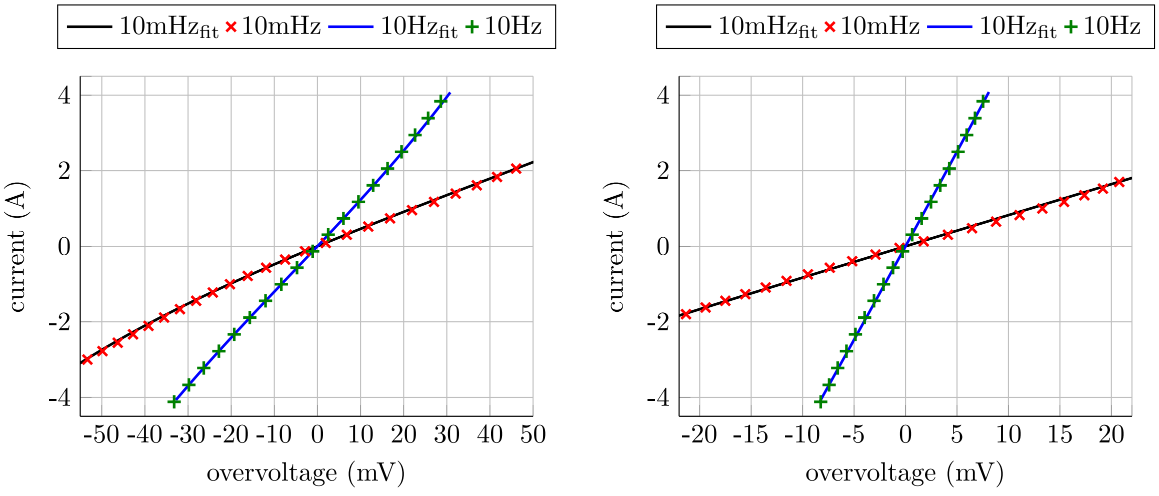

(a) Real part.

(b) Imaginary part.

Figure 3.53: Impedance non-linearity dependency on frequency of a full cell. (cylindrical LFP cell A.1, $\vartheta = 25\,°\mathrm{C}$, $SoC = 50\,\%$). For reasons of clarity only a subset of the measured points is shown. Raw measurements taken by [36].

| | temperature | $R_\Omega$ (m$\Omega$) | $i_0$ (A) | $\alpha$ | $r$ (m$\Omega$) | $r^2$ |
|---|---|---|---|---|---|---|
| $Z_{real}$ | 10 °C | 17.5 | 0.02 | 0.40 | 27 | 0.9985 |
| | 20 °C | 16.4 | 0.13 | 0.38 | 14 | 1.0000 |
| | 25 °C | 16.2 | 0.33 | 0.35 | 10 | 1.0000 |
| | 30 °C | 15.9 | 1.71 | 0.41 | 10 | 1.0000 |
| | 40 °C | 14.9 | 6.26 | 0.35 | 12 | 0.9995 |
| $Z_{imag}$ | 10 °C | 0.0 | -6.13 | 0.47 | -190 | 0.9918 |
| | 20 °C | 0.0 | -14.01 | 0.27 | -27 | 0.9907 |
| | 25 °C | 0.0 | -17.97 | 0.05 | -10 | 0.9968 |
| | 30 °C | 0.0 | -23.25 | 0.05 | -8 | 0.9838 |
| | 40 °C | 0.0 | -27.67 | 0.05 | -3 | 0.9669 |

Table 3.4: Selected Microcycle-Impedance non-linearity measurements of the real and imaginary part fitted with the modified Butler-Volmer equation of 3.131. Parameter dependency on temperature. Raw measurements taken by [36].

Figure 3.54 shows the two measurements at 10 °C and 25 °C. As expected, the impedance of the 10 °C measurement is higher than the impedance of the 25 °C measurement. The fitted curve for the imaginary part for the 25 °C measurement does not really fit the measurement data for high currents. The fitting process could not further change the parameter $\alpha$ to smaller values, since it already reached 0.05 which was set as the lower bound for this value. The low imaginary overvoltage makes it difficult to obtain high values in the argument of the exponential function. This makes it difficult to adequately bend the fitted curve in order to represent the measured data. This difficulty was found also at 30 °C and 40 °C, raising the question whether a further modified equation of the Butler-Volmer equation should be applied for the imaginary part.

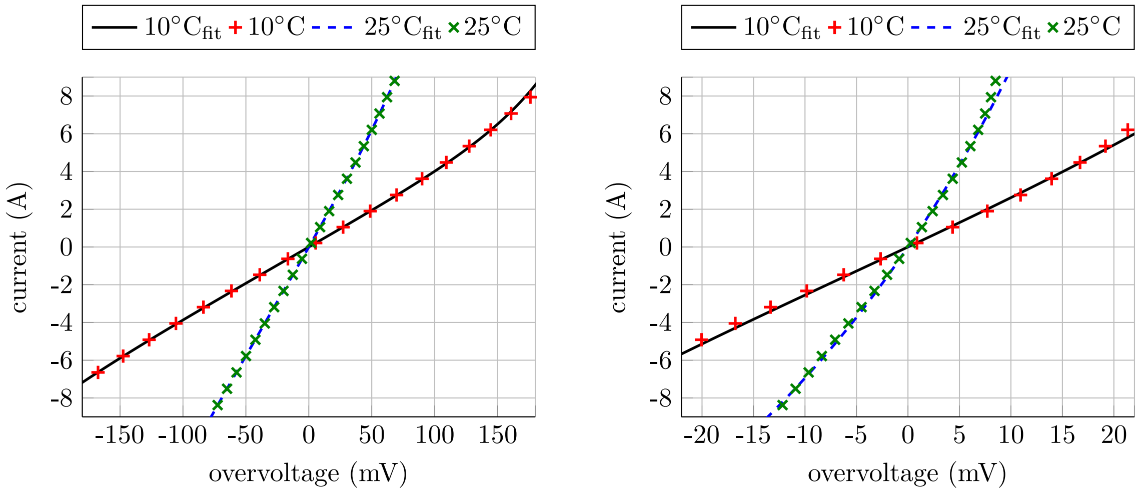

(a) Real part.

(b) Imaginary part.

Figure 3.54: Impedance non-linearity dependence on temperature of a full cell Lithium-Ion battery cell. (cylindrical LFP cell A.1, $f_m = 1\,\text{Hz}$, $SoC = 50\,\%$). For reasons of clarity only a subset of the measurement points are shown. Raw measurements taken by [36].

The LFP cell used showes very low dependency of the impedance over SoC. The same is true for its non-linearity over SoC. The table with the fitted parameters and a figure with 10 % and 90 % SoC is shown in the appendix A.1.

### 3.4.4 Impedance Measurement Deviation Caused by Single-sine Measurement

Appendix D.3 derives equation 3.138 - the Fourier transformation of the measured current assuming a potentiostatic excitation. A potentiostatic excitation during the impedance measurement is first assumed, since the Butler-Volmer equation cannot be analytically converted into a closed form that would give the voltage for a certain current.

$$\begin{aligned}\mathrm{F}\{i_m(t)\} = &-j\frac{2i_0}{T_m}\cdot T_m \cdot \mathcal{I}_1\left(\frac{(1-\alpha)zF\hat{V}_m}{RT}\right)\\ &+j\frac{2i_0}{T_m}\cdot T_m \cdot \mathcal{I}_1\left(\frac{-\alpha zF\hat{V}_m}{RT}\right)\\ &-j\frac{\hat{V}_m}{r}\end{aligned} \tag{3.138}$$

with the Fourier transformed current response, the conductance and the deviation of the conductance is:

$$Y_m = \frac{\mathrm{F}\{i_m(t)\}}{-j\hat{V}_m} \tag{3.139}$$

$$Y_m = \frac{2i_0}{\hat{V}_m}\cdot\left(\mathcal{I}_1\left(\frac{(1-\alpha)zF\hat{V}_m}{RT}\right) - \mathcal{I}_1\left(\frac{-\alpha zF\hat{V}_m}{RT}\right)\right) + \frac{1}{r} \tag{3.140}$$

$Z_0^{'}$ is the impedance value if there is no deflection of the Open-Circuit-Voltage, i.e. $\hat{V}_m = 0$. In this case the two modified Bessel functions of the first kind $\mathcal{I}_1$ go towards zero, but at the same time the fraction $i_0/\hat{V}_m$ goes towards infinity. Therefore the limit of the expression when $\hat{V}_m$ goes towards zero yields the value $Z_0^{'}$. This value can be used as the reference impedance in equation 3.143 for the measurement deviation.

$$Z_0^{'} = \lim_{\hat{V}_m\to 0} {Y_m}^{-1} \tag{3.141}$$

$$e_Z = \frac{|Z_e|}{Z_0^{'} + R_\Omega} = \frac{|{Y_m}^{-1} - Z_0^{'}|}{Z_0^{'} + R_\Omega} \tag{3.142}$$

$$e_Z = \frac{1}{Z_0^{'} + R_\Omega}\cdot\left[\left[\frac{2i_0}{\hat{V}_m}\cdot\left(\mathcal{I}_1\left(\frac{(1-\alpha)zF\hat{V}_m}{RT}\right) - \mathcal{I}_1\left(\frac{-\alpha zF\hat{V}_m}{RT}\right)\right) + \frac{1}{r}\right]^{-1} - Z_0^{'}\right] \tag{3.143}$$

In order to avoid an unintentional shift in SoC during the EIS measurement a galvanostatic excitation is usually used for batteries. The voltage drop over the non-linear resistance in the parallel equivalent circuit is equal to the voltage drop over the whole parallel circuit $r||Z_{NL}$. The resistance of that circuit is equal to $Z_0^{'}$ when no current is flowing. Under the assumption that the difference between $Z_0^{'}$, when no current is flowing, and the parallel circuit $r||Z_{NL}$, when current is flowing, is rather small, it can be approximated for the whole range with $Z_0^{'}$. Therefore $\hat{V}_m$ is replaced by $\hat{I}_m \cdot Z_0^{'}$ in equation 3.144 for the measurement deviation of the impedance:

$$e_Z \approx \frac{1}{Z_0^{'} + R_\Omega}\cdot\left|\left[\frac{2i_0}{\hat{I}_m Z_0^{'}}\cdot\left(\mathcal{I}_1\left(\frac{(1-\alpha)zF\hat{I}_m Z_0^{'}}{RT}\right) + \mathcal{I}_1\left(\frac{\alpha zF\hat{I}_m Z_0^{'}}{RT}\right)\right) + \frac{1}{r}\right]^{-1} - Z_0^{'}\right| \tag{3.144}$$

The measurement deviation shown here is dependent on the modified Bessel function of the first kind. In appendix C.5, several examples can be seen for this function. The general shape of the function as exponentially increasing with increasing argument fits with the curves published by Diard et al. in [33]. He derived his curves with a Taylor series expansion at the operation point.

The impedance measurement deviation $e_Z$ is dependent on the battery specific parameters $i_0$, $\alpha$, $r$ and on the measurement current amplitude $\hat{I}_m$. The additional parameter $R_\Omega$ decreases the deviation, but only for the real part. $e_Z$ is inversely proportional to the value of $i_0$. The larger that value, the lower the measurement deviation.

Dependence on $\hat{I}_m$ is more difficult to see, since it is also present in the exponential argument. Figure 3.55a shows this dependence. The measurement deviation increases quickly with increasing measurement current amplitudes. When no constant current is present, the deviation is the same for values of $\alpha$ symmetrical to 0.5, like $\alpha = 0.2$ and $\alpha = 0.8$. Figure 3.55b shows how the impedance measurement deviation is dependent on $\alpha$. It is lowest at 0.5 and increases the further it deviates from that value towards 0 or 1. Both figures show that the impact of $\hat{I}_m$ is stronger than the impact of $\alpha$.

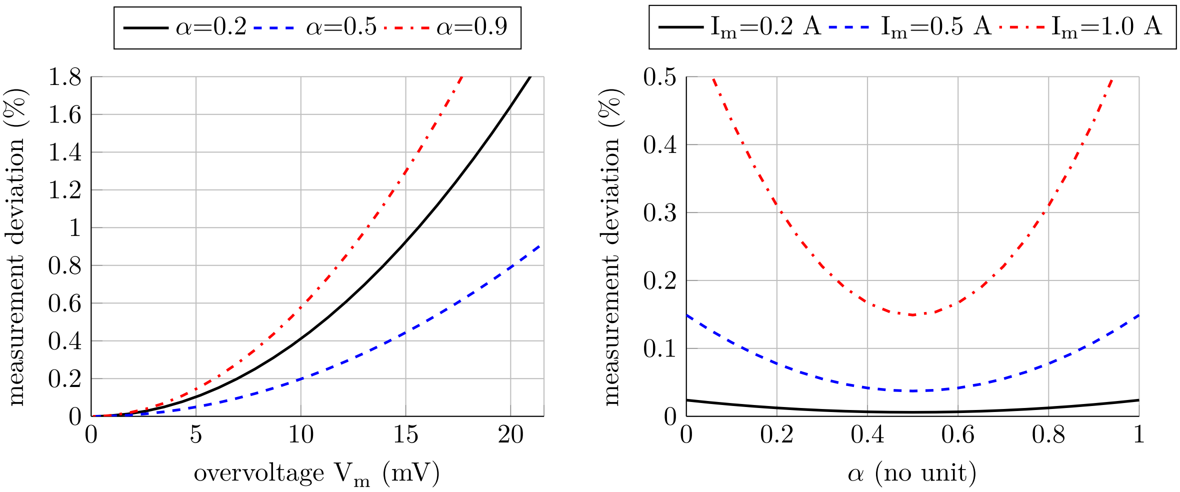

(a) Measurement deviation depending on the overvoltage $\hat{V}_m = Z_0^{'} \cdot \hat{I}_m$. Here, the measurement current amplitude $\hat{I}_m$ is proportional to overvoltage and is taking values from 0 to 3 CA with $Z_0^{'} = 7.2\,\mathrm{m\Omega}$.

(b) Measurement deviation depending on the parameter $\alpha$ and on the measurement current amplitude $\hat{I}_m$ causing the overvoltage $\hat{V}_m = Z_0^{'} \cdot \hat{I}_m$ with $Z_0^{'} = 7.2\,\mathrm{m\Omega}$.

Figure 3.55: Measurement deviation caused by the non-linearity of a battery cell (synthetic data with the parameters $i_0 = 1\,\mathrm{A}$, $R_\Omega = 0\,\mathrm{m\Omega}$, $r = 10\,\mathrm{m\Omega}$).

Figure 3.56a and 3.56b show the measurement deviation introduced by impedance non-linearity for different measurement frequencies. The measurement deviation of the real part increases with decreasing frequency and increasing current. Excitation current amplitudes of 3 CA cause a deviation of over 5 % for a 10 mHz measurement. Only when staying below 0.5 CA the deviation stays below the defined 0.1 % threshold over the whole frequency range.

The deviation of the imaginary part does not follow such a strict rule. The deviation of the 100 mHz measurement rises much quicker than the deviation of the 10 mHz measurement. In general, the deviation caused by large measurement currents is smaller for the imaginary part than for the real part of the impedance.

Figure 3.56c and 3.56d show the measurement deviation introduced by impedance non-linearity for different temperatures at a measurement frequency of 1 Hz. Although not entirely consistent, the deviation of both the real and the imaginary part increases with increasing current and in general also with decreasing temperature.

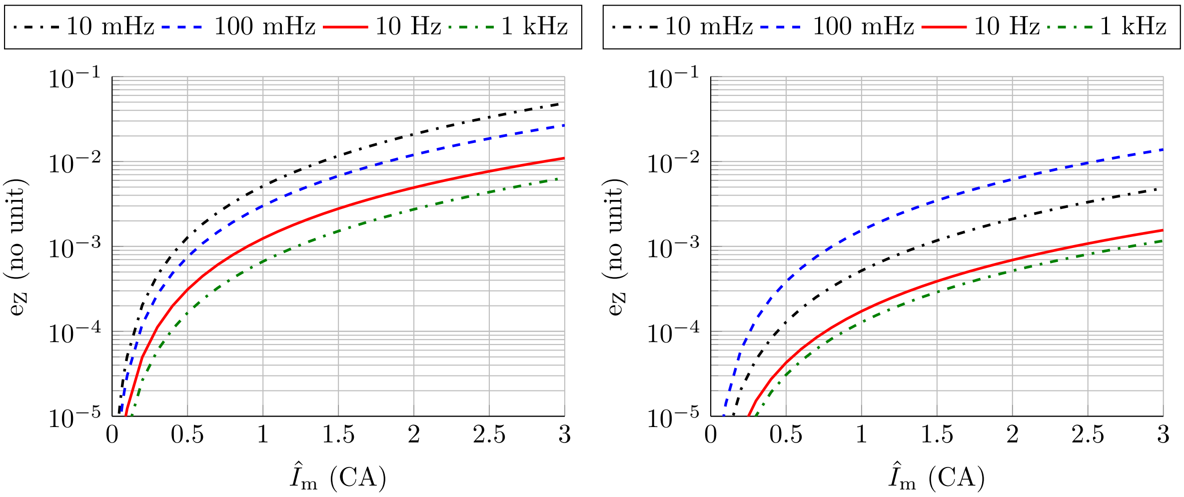

(a) Impedance real part deviation depending on the measurement frequency ($\vartheta = 25\,°C$).

(b) Impedance imaginary part deviation depending on the measurement frequency ($\vartheta = 25\,°C$).

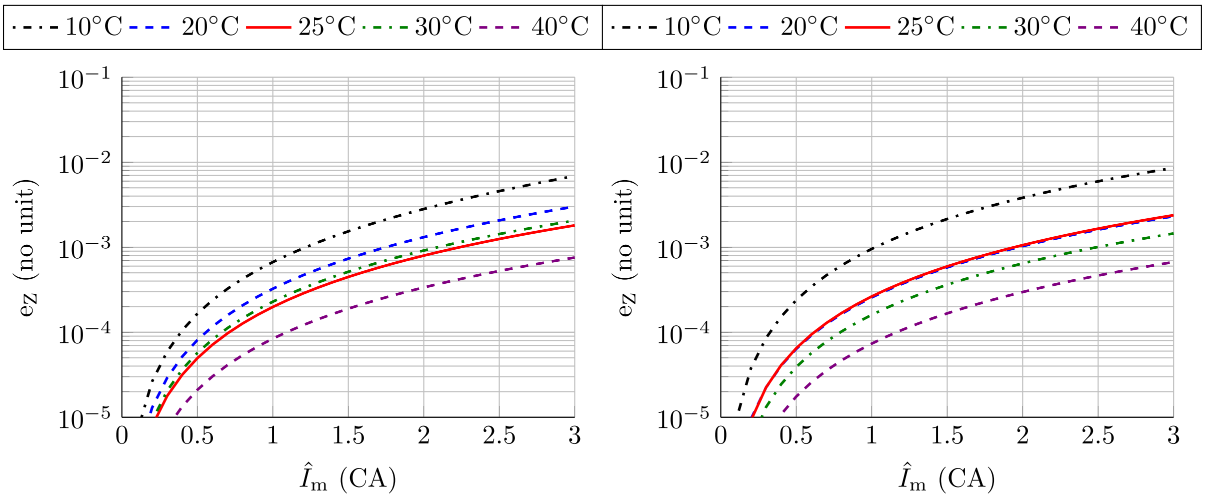

(c) Impedance real part deviation depending on the temperature ($f_m = 1\,Hz$).

(d) Impedance imaginary part deviation depending on the temperature ($f_m = 1\,Hz$).

Figure 3.56: Measurement deviation caused by the impedance non-linearity of a battery cell (cylindrical LFP-cell A.1, $SoC_{start} = 50\,\%$).

### 3.4.5 Impedance Measurement Deviation Caused by Multi-sine Measurement

For a multi-sine measurement, the other measurement frequencies deviate the cell from the equilibrium voltage. A simple closed algebraic equation for the deviation introduced is impossible to give, since the excitation currents at other frequencies as the currently evaluated measurement frequency change the operating point on the Butler-Volmer curve in a non-predictable way. However, when the Butler-Volmer curve is symmetrical, i.e. $\alpha = 0.5$, the deviation caused by the deflection to the positive side and to the negative side cancel each other out. Equation 3.145 would apply in this case. Refer to appendix D.4 for a detailed derivation of this equation.

$$e_Z \approx \frac{1}{Z_0' + R_\Omega} \cdot \left| \left[ \frac{2i_0}{\hat{I}_m Z_0'} \cdot \Sigma_{n=1}^{N} \left( 2j \cos\left(\frac{\pi}{2} \cdot x_n\right) \cdot \mathcal{I}_{x_n} \left( \frac{0.5zF\hat{I}_m Z_0'}{RT} \right) \right) + \frac{1}{r} \right]^{-1} - Z_0' \right| \tag{3.145}$$

$x_n$ is the ratio of the measurement frequency evaluated $f_m$ to another measurement frequency $f_n$ also applied in the same multi-sine signal ($x_n = \frac{f_m}{f_n}$). The simplification in equation 3.145 shows that for even multiples of the measurement frequencies, no deviations are caused for the measurement frequency. However, it is unavoidable that lower frequencies cause a measurement deviation and it is unavoidable that in a multi-sine measurement signal, some frequencies will be lower than others. Also, for values of $\alpha$ in close vicinity of 0.5 or low excitation currents, this equation could still be valid. The exact limits of its applicability would need to be determined by simulations since they depend on the parameters of the multi-sine signal, such as its amplitudes, frequencies and phases.

### 3.4.6 Measurement Deviation from Impedance Non-linearity Caused by Constant Current

Appendix D.5 derives in detail equation 3.146 - the current response of for a potentiostatic excitation where a constant current $V_{dc}$ is present.

$$\begin{aligned} \mathrm{F}\{i_m(t)\} = & -j \cdot 2i_0 \cdot e^{\frac{(1-\alpha)zFV_{dc}}{RT}} \cdot \mathcal{I}_1 \left( \frac{(1-\alpha)zF\hat{V}_m}{RT} \right) \\ & + j \cdot 2i_0 \cdot e^{\frac{-\alpha zFV_{dc}}{RT}} \cdot \mathcal{I}_1 \left( \frac{-\alpha zF\hat{V}_m}{RT} \right) \\ & - j \frac{\hat{V}_m}{r} \end{aligned} \tag{3.146}$$

Equation 3.146 shows that the factor $e^{\frac{(1-\alpha)zFV_{dc}}{RT}}$ and $e^{\frac{-\alpha zFV_{dc}}{RT}}$ introduced by the constant current can be considered as a modification of the exchange current $i_0$. This modification factor is dependent on the battery parameters $\alpha$, $z$ and on the overvoltage caused by the constant current $V_{dc}$. The only unknown factor is the impedance causing the constant overvoltage at a certain constant charge/discharge current. This value is equal to the heat generating rate for a constant current $HGR_{dc}$ from section 3.2.5, since the overvoltage is generating exactly the amount of irreversible heat. Figure 3.57a shows the dependency of this factor on the overvoltage $V_{dc} = HGR_{dc} \cdot I_{dc}$. The factor is not dependent on $i_0$ itself.

With equation 3.139 and equation 3.142, the deviation caused by impedance non-linearity when during the impedance measurement the battery is charged or discharged with a constant current becomes:

$$e_Z = \frac{1}{Z_0^{'} + R_\Omega} \cdot \left[ \left[ \frac{2}{\hat{I}_m Z_0^{'}} \cdot \left( i_0 \cdot e^{\frac{(1-\alpha)zF \cdot HGR_{dc} I_{dc}}{RT}} \cdot \mathcal{I}_1 \left( \frac{(1-\alpha)zF\hat{I}_m Z_0^{'}}{RT} \right) + i_0 \cdot e^{\frac{-\alpha zFHGR_{dc} I_{dc}}{RT}} \cdot \mathcal{I}_1 \left( \frac{\alpha zF\hat{I}_m Z_0^{'}}{RT} \right) \right) + \frac{1}{r} \right]^{-1} - Z_0^{'} \right] \tag{3.147}$$

$Z_0^{'}$ in this case is the small signal impedance when the constant voltage displacement $V_{dc}$ and the sinusoidal voltage excitation $\hat{V}_m$ goes to zero. The term $e^{\frac{(1-\alpha)zFV_{dc}}{RT}}$ is most relevant for positive currents and voltages, since for negative current and voltages the term becomes very small. For the same reason the term $e^{\frac{-\alpha zFV_{dc}}{RT}}$ is most relevant for for negative current and voltages. A high value for the charge transfer coefficient $\alpha$ indicates that the reactions are occurring quicker for the negative side and the overvoltage needed to achieve the same current is lower compared to the positive side. This also affects the linearity of the curve. Although the curve is steeper, for high values of $\alpha$, it is less linear on the negative side, whereas it is less steep but more linear on the positive side.

Figure 3.57b shows the dependency of the impedance deviation $e_Z$ on the constant overvoltage $V_{dc} = HGR_{dc} \cdot I_{dc}$ caused by a constant current. The lower the parameter $\alpha$ is, the higher is the measurement deviation caused by a positive constant current since the Butler-Volmer curve is less linear on the positive side. The opposite is the case for high values of $\alpha$. The reason why the deviation curve for $\alpha = 0.5$ increases with increasing constant overvoltage is that the constant overvoltage causes the operation point to deflect and at that point the Butler-Volmer equation is no longer symmetrical.

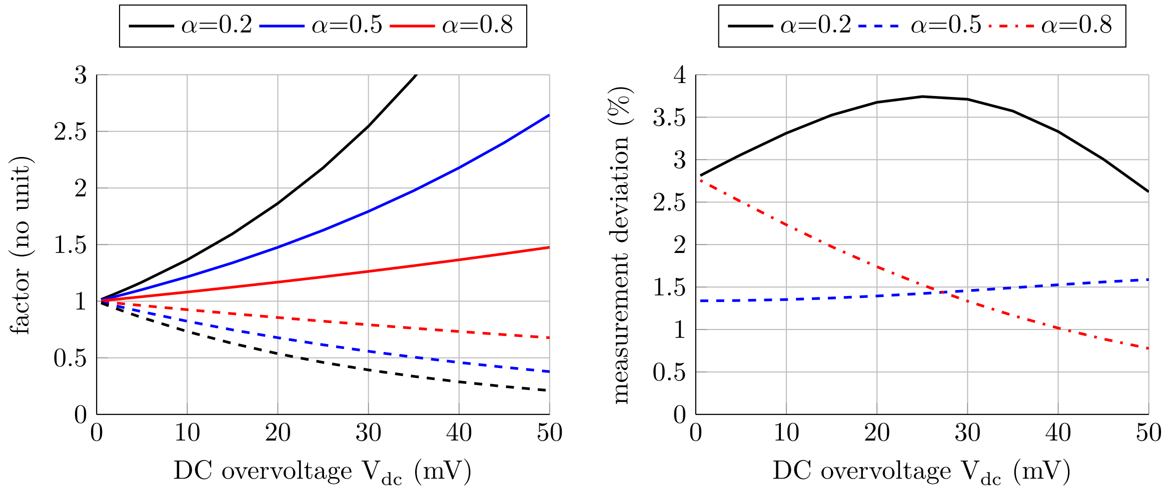

(a) $i_0$ modifying factor depending on $\alpha$ and overvoltage $V_{dc}$. Solid lines show $e^{\frac{(1-\alpha)zFV_{dc}}{RT}}$, dashed lines show $e^{\frac{-\alpha zFV_{dc}}{RT}}$.

(b) Measurement deviation caused by the non-linearity of a battery cell depending on $\alpha$ and overvoltage $V_{dc}$ ($\hat{I}_m = 0.5\,\mathrm{A}$, $i_0 = 1\,\mathrm{A}$, $R_\Omega = 0\,\mathrm{m\Omega}$, $r = 10\,\mathrm{m\Omega}$).

Figure 3.57: $i_0$ modifying factor and impedance measurement deviation depending on the magnitude of a constant positive overvoltage $V_{dc} = HGR_{dc} \cdot I_{dc}$ ($I_{dc} = 0$ to $1\,\mathrm{CA}$, $HGR_{dc} = 50\,\mathrm{m\Omega}$).

Figure 3.58a shows the impedance real part deviation over the underlying constant current $I_{dc}$ for several frequencies. A look at table 3.3 explains the differences between the curves. The reason for the 10 Hz curve being different and crossing 10 mHz and 100 mHz while $I_{dc}$ increases can be seen in figure

3.57b. $\alpha$ is for the 10 Hz curve close to 0.5, whereas the other two are close to 0.7. Over the increasing constant current $I_{dc}$, the measurement deviation of the curve with $\alpha = 0.5$ overtakes the one with the higher $\alpha$. The 1 kHz curve has a low $\alpha$ and no ohmic resistance part $R_{\Omega}$, which would lead to high deviations. Its exchange current density, however, is very small, which leads to the opposite effect. Since $\alpha$ is in the exponent of the modifying factor of $i_0$, it becomes more important the higher the constant current $I_{dc}$ is.

Table 3.3 can also explain the impedance deviation of the imaginary part in figure 3.58b. The low measurement deviation of 10 mHz is mainly caused by the low exchange current density $i_0$. The high deviation of 100 mHz and 1 kHz is due to the extreme values of $\alpha$ which are either at the lower or the upper set bound. Although in opposite extremes, the effective $HGR_{dc}$ for the imaginary part is much lower as for the real part. Therefore the curve never leaves the left part of the figure 3.57b where also higher values of $\alpha$ cause higher deviations than a value of $\alpha$ close to 0.5. This is why the 100 mHz curve, with $\alpha = 0.95$, has a much higher measurement deviation than the 10 Hz curve with $\alpha = 0.45$. The $HGR_{dc}$ for the imaginary part was calculated by the same extrapolation method introduced in section 3.2.5.2 for $Z_{real}$ and then compensated by the imaginary deviation caused by the OCV change as describe in section 3.3.2.2.

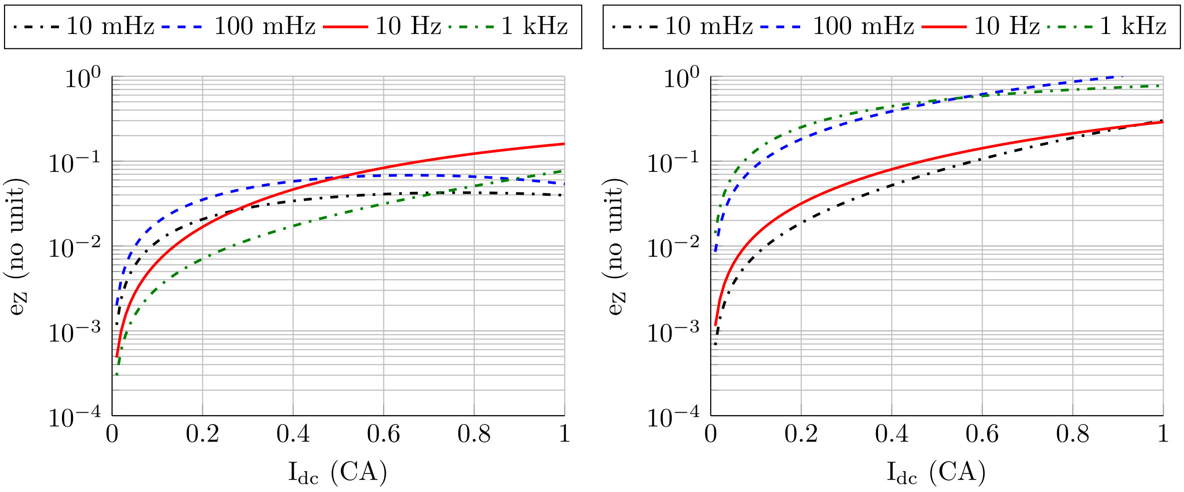

(a) Impedance real part deviation.

(b) Impedance imaginary part deviation.

Figure 3.58: Measurement deviation caused by the non-linearity of a battery cell depending on the measurement frequency (cylindrical LFP-cell A.1, $SoC_{start} = 50\,\%$, $\vartheta = 25\,°\mathrm{C}$, $\hat{I}_m = 0.5\,\mathrm{CA}$).

**Section Conclusion**

*This section discussed the problem of approximating the two electrode/electrolyte interfaces of commercial lithium-ion cells with one Butler-Volmer equation. It introduced an equivalent circuit of a non-linear resistance following the Butler-Volmer equation and an ohmic resistance in parallel as an approximation for two Butler-Volmer equations in series.*

*There are four different measurement methods for impedance non-linearity. The charge/discharge method has difficulties to compensate for the temperature influence at high current amplitudes and takes several hours, if not days, for low current amplitudes. The Microcycle method can only determine the absolute value of the non-linearity and does not separate it into real and imaginary parts. The Microcycle-Impedance method overcomes this shortcoming and was used for non-linearity measurements. The last method uses the harmonics acquired during an impedance measurement to determine the Butler-Volmer equation parameters or to identify a too high excitation. This method would require a low-noise environment with extremely accurate voltage and current sensors making it very difficult to apply in practice.*

*The non-symmetry and non-linearity is particularly pronounced for the imaginary impedance. This is aggravated by the absence of additional ohmic resistances, which exist for the real part. The measurement deviation introduced by impedance non-linearity is particularly large for low frequencies and low temperatures. An additional constant current increases the deviation significantly by displacing the operation point on the Butler-Volmer curve. The value of* $\alpha$ *in combination with the direction of the constant current is particularly critical in this case.*

## 3.5 Comparison of Measurement Deviation Sources

The equation for the measurement deviation derived in this chapter often assumed worst case conditions. The heat generated inside a cell, in section 3.2, assumed that there is no cooling of the battery cell during the time the excitation or the additional constant current was applied.

The impedance non-linearity, in section 3.4, simplified the overvoltage with $\hat{I}_m \cdot Z_0^{'}$ where $Z_0^{'}$ is the impedance without any deviation from non-linearity. The large signal resistance over a resistance described by a Butler-Volmer equation would result in a smaller value for $Z_0$ and therefore in a smaller overvoltage as the one assumed with this simplification. This simplification therefore overestimates the measurement deviation.

In reality the deviations are able to compensate each other. The temperature introduced by impedance heating could be partly compensated by entropy heating. A positive deviation introduced by impedance non-linearity could be partly compensated by a change in SoC. Due to the worst case estimations, the summation of all the deviations is invalid. When combining the deviations only their absolute values can be added and the result of it can only be considered a worst case estimation. Equation 3.148 describes the worst case measurement deviation caused by the excitation current of the impedance measurement and an additional constant current:

$$
\begin{aligned}
e_Z = \quad & \underbrace{\left| \frac{1}{Z_0} \frac{T_m}{2\pi} \frac{\Delta Z}{\Delta SoC} \bigg|_{T,\Delta SoC} \cdot \frac{\hat{I}_m}{C_{el}} \right|}_{\substack{\text{Deviation from sinusoidal measurement current} \\ \text{and SoC dependency of impedance (equation 3.25).}}} + \underbrace{\left| \frac{1}{Z_0} \frac{T_m}{2} \frac{\Delta Z}{\Delta SoC} \bigg|_{T,\Delta SoC} \cdot \left[ 1 - \frac{j}{2\pi} \right] \cdot \frac{I_{dc}}{C_{el}} \right|}_{\substack{\text{Deviation from constant current and SoC} \\ \text{dependency of impedance (equation 3.46).}}} + \\
+ \quad & \underbrace{\left| \frac{Z_\Theta}{Z_0} \cdot \left[ \mathcal{I}_0 \left( \frac{HGR_e}{C_{th}} \frac{\hat{I}_m \cdot T_m}{2\pi \cdot \Theta} \right) - \mathcal{I}_2 \left( \frac{HGR_e}{C_{th}} \frac{\hat{I}_m \cdot T_m}{2\pi \cdot \Theta} \right) - 1 \right] \right|}_{\substack{\text{Deviation from alternating temperature change caused by the entropy heating of the sinusoidal} \\ \text{measurement current and temperature dependency of impedance (equation 3.74).}}} + \\
+ \quad & \underbrace{\left| \frac{Z_\Theta}{Z_0} \cdot \left[ \mathcal{I}_0 \left( \frac{HGR_{fm}}{C_{th}} \cdot \frac{\hat{I}_m{}^2 \cdot T_m}{8\pi \cdot \Theta} \right) - j \cdot \mathcal{I}_1 \left( \frac{HGR_{fm}}{C_{th}} \cdot \frac{\hat{I}_m{}^2 \cdot T_m}{8\pi \cdot \Theta} \right) - 1 \right] \right|}_{\substack{\text{Deviation from alternating temperature change caused by impedance heating of the sinusoidal} \\ \text{measurement current and temperature dependency of impedance (equation 3.90).}}} + \\
+ \quad & \underbrace{\left| \frac{Z_\Theta}{Z_0} \cdot \left[ \frac{e^{\frac{\Delta T(t)}{\Delta t} \frac{T_m}{\Theta}} - 1}{\frac{\Delta T(t)}{\Delta t} \frac{T_m}{\Theta}} - \frac{\frac{\Delta T(t)}{\Delta t} \frac{T_m}{\Theta} \cdot \left( e^{\frac{\Delta T(t)}{\Delta t} \frac{T_m}{\Theta}} - 1 \right)}{\left( \frac{\Delta T(t)}{\Delta t} \frac{T_m}{\Theta} \right)^2 + 16\pi^2} + j \cdot \frac{4\pi \left( 1 - e^{\frac{\Delta T(t)}{\Delta t} \frac{T_m}{\Theta}} \right)}{\left( \frac{\Delta T(t)}{\Delta t} \frac{T_m}{\Theta} \right)^2 + 16\pi^2} - 1 \right] \right|}_{\substack{\text{Deviation from the temperature dependency of the impedance and the constant change of temperature} \\ \text{caused by entropy heating or impedance heating of a constant current or the constant} \\ \text{temperature increase caused by a sinusoidal current (equation 3.105).}}} + \\
+ \quad & \underbrace{\Bigg| \frac{1}{Z_0^{'}} \cdot \Bigg[ \Bigg[ \frac{2}{\hat{I}_m (Z_0^{'} - R_\Omega)} \cdot \Bigg( i_0 \cdot e^{\frac{(1-\alpha)zF \cdot HGR_{dc} \cdot I_{dc}}{RT}} \cdot \mathcal{I}_1 \left( \frac{(1-\alpha)zF \cdot (Z_0^{'} - R_\Omega) \cdot \hat{I}_m}{RT} \right) +}_{\text{Deviation from impedance non-linearity (equation 3.147).}} \\
& \overbrace{+ i_0 \cdot e^{\frac{-\alpha zF \cdot HGR_{dc} \cdot I_{dc}}{RT}} \cdot \mathcal{I}_1 \left( \frac{\alpha zF \cdot (Z_0^{'} - R_\Omega) \cdot \hat{I}_m}{RT} \right) \Bigg) + \frac{1}{r} \Bigg]^{-1} - (Z_0^{'} - R_\Omega) \Bigg] \Bigg|}
\end{aligned}
\qquad (3.148)
$$

The term $\frac{\Delta T(t)}{\Delta t}$ is defined as:

$$
\frac{\Delta T(t)}{\Delta t} = \frac{HGR_e}{C_{th}} \cdot I_{dc} + \frac{HGR_{dc}}{C_{th}} \cdot I_{dc}{}^2 + \frac{HGR_{fm}}{C_{th} \cdot 2} \cdot \hat{I}_m{}^2 \qquad (3.149)
$$

The combination of the different measurement deviations does not take into account any cross dependencies of the different sources. The impedance non-linearity would actually cause the overvoltage to be smaller than assumed in the equation for the measurement deviation caused by temperature change from impedance heating. The changing SoC would also cause all the other parameters, like entropy, impedance, impedance non-linearity used in the other equations, to change. These cross-dependencies could turn out to increase or decrease the deviation estimated without considering these cross-dependencies. Their impact would be rather small and less significant than other simplifications already done in this chapter. Therefore, they are only mentioned here but not further considered.

Equation 3.148 contains natural constants, such as the Faraday constant $F$, the gas constant $R$ and some battery cell specific constants such as the thermal capacity $C_{th}$ and the electrical capacity $C_{el}$ (constant over the time of the impedance measurement). It also contains a lot of battery cell specific variables. Table 3.5 shows these variables and reveals that most of these variables can be derived from the impedance $Z$.
Besides the impedance, only the entropy $\Delta S$, the exchange current $i_0$ and the charge transfer coefficient $\alpha$ are needed. These values are dependent on the measurement frequency $f_m$, the State-of-Charge $SoC$ and the cell temperature $\vartheta_{cell}$ over which they would need to be characterized. The two parameters for the impedance measurement which can be freely chosen are the excitation amplitude $\hat{I}_m$ and the measurement frequency, or its inverse value the measurement period $T_m$.

| battery cell variable | description | derived from | dependent on | | |
|---|---|---|---|---|---|
| | | | $f_m$ | $SoC$ | $\vartheta_{cell}$ |
| $Z_0$ | impedance with no measurement deviation | $Z$ | X | X | X |
| $Z_\Theta$ | temperature dependent part of the impedance $Z_\Theta = Z_0 - Z_{\not\Theta}$. | $Z$ | X | X | |
| $\Theta$ | exponential parameter for the temperature dependency of the impedance | $Z$ | X | X | |
| $HGR_{fm}$ | heat generation rate of impedance heating at the measurement frequency $HGR_{fm} = Z_{real}\left[f_m\right]$. | $Z$ | X | X | X |
| $HGR_{dc}$ | heat generation rate of impedance heating for constant current $HGR_{dc} = \Sigma_{k=1}^{N} Z_{real}\left[k \cdot (\frac{I_{dc}}{C_{el}})^{-1}\right] \cdot \left(\frac{4 \cdot I_{dc}}{k \cdot \pi \cdot \sqrt{2}}\right)^2$. | $Z$ | X | X | X |
| $R_\Omega$ | purely ohmic resistance of the impedance | $Z$ | X | X | X |
| $HGR_e$ | entropic heat generation rate $HGR_e = \Delta S \frac{T}{z\,F}$ | $\Delta S$ | | X | X |
| $i_0$ | exchange current | $i_0$ | X | X | X |
| $\alpha$ | charge transfer coefficient | $\alpha$ | X | X | X |

Table 3.5: Battery cell specific variables (1st column), their description (2nd column), from which battery cell parameter they can be derived (3rd column) and from which parameters the variable is dependent on (4th to 6th column).

Unfortunately, equation 3.148 cannot be solved to the excitation amplitude $\hat{I}_m$. But certain scenarios can be shown to get a better understanding of what sources for measurement deviation introduced in this chapter are the most relevant ones. Figure 3.59 shows the deviation components caused by a sinusoidal measurement. The dominant measurement deviation for imaginary and real part is mainly the deviation from impedance non-linearity. For low frequencies, however, the other parts start to be important as well. For the 10 mHz measurement the SoC change during the measurement causes a significant deviation for the real part and a larger deviation than the impedance non-linearity for the imaginary part.

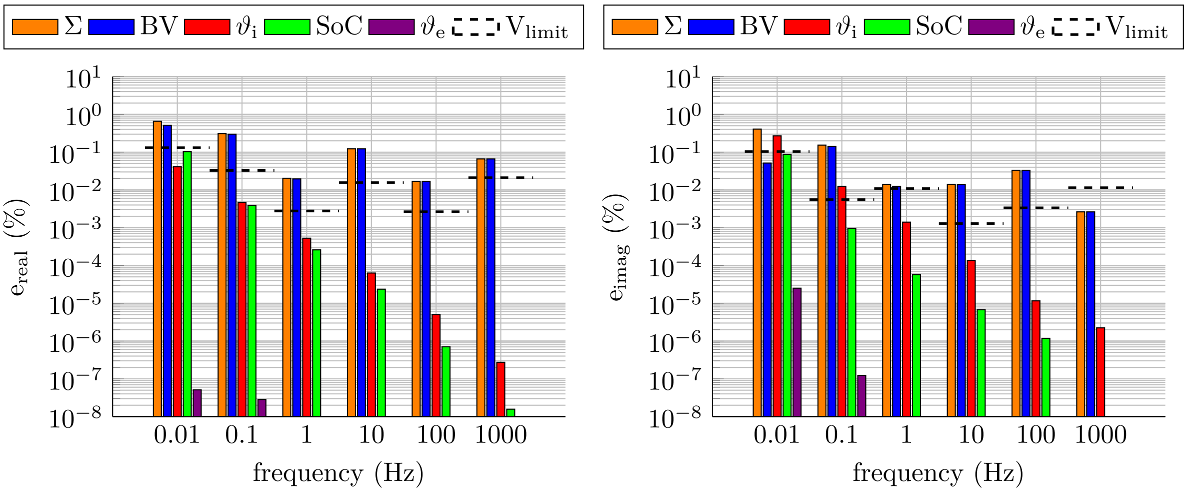

(a) Impedance real part.

(b) Impedance imaginary part.

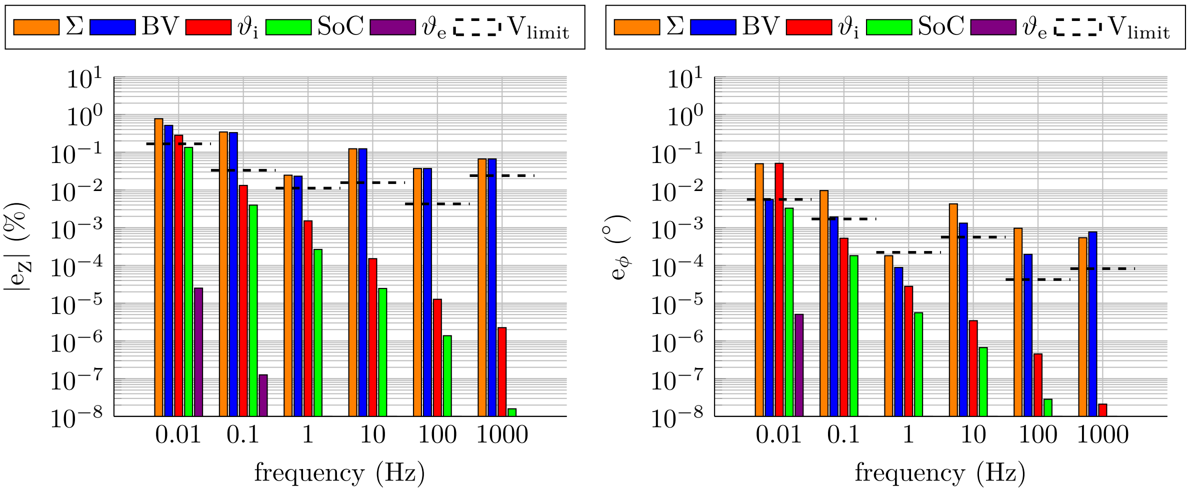

(c) Impedance modulus.

(d) Impedance phase.

Figure 3.59: Impedance measurement deviation components depending on measurement frequency $f_m$. 'Σ': sum of all components, 'BV': deviation from impedance non-linearity, '$\vartheta_i$': deviation from temperature increase by impedance heating, 'SoC': deviation from State-of-Charge change, '$\vartheta_e$': deviation from temperature increase by entropy heating, '$V_{limit}$': deviation limit from 10 mV-Criterion (cylindrical LFP-cell A.1, $SoC_{start} = 50\,\%$, $\vartheta = 25\,°\mathrm{C}$, $\hat{I}_m = 1\,\mathrm{CA}$).

The measurement deviation introduced by impedance heating is especially large for the imaginary part of the 10 mHz measurement. The deviation from entropy heating does not have a significant contribution irrelevant from the measurement frequency, neither for the real nor the imaginary part.

Kiel et al. [63] attributed the impedance change at low frequencies to the change of the charge transfer resistance at high excitation amplitudes. Here the imaginary measurement deviation at low frequencies at even a moderate current excitation amplitude of 1 CA is mainly caused by temperature increase. Kiel et al. used Lead-Acid-Batteries, whereas here an LFP li-ion battery cell was used. Nevertheless, the contribution of heat on the imaginary part of the impedance at low frequencies should be considered as a possible source of impedance measurement deviation also for other battery chemistries and battery types as the one used here.

Since the real part is much larger than the imaginary part, the modulus deviation is mainly governed by the deviations in the real part. Only the temperature increase due to impedance heating contributes noticeably for the 10 mHz measurement to the imaginary part. For the phase deviation it is even the main contributor for the 10 mHz measurement. In the case shown, the deviation does not get close to the 1 ° threshold. This is mainly due to the fact that it is measured in absolute values and not in relative terms. The 10 mHz measurement also shows that the main cause of the phase deviation is a measurement deviation in the imaginary part.
There is no error in the sum for figure 3.59d where the total phase deviation is smaller than the phase deviation from impedance heating. It is not the direct sum of the single phase deviations of each source. The sum of the phase deviation is the phase of the sum of the real and imaginary part subtracted from the phase of the impedance without deviation.

Figure 3.60 shows the measurement deviation for a measurement frequency of 1 Hz and an excitation amplitude of 3 CA. It is mainly the impedance non-linearity that dominates the measurement deviation over all temperatures.

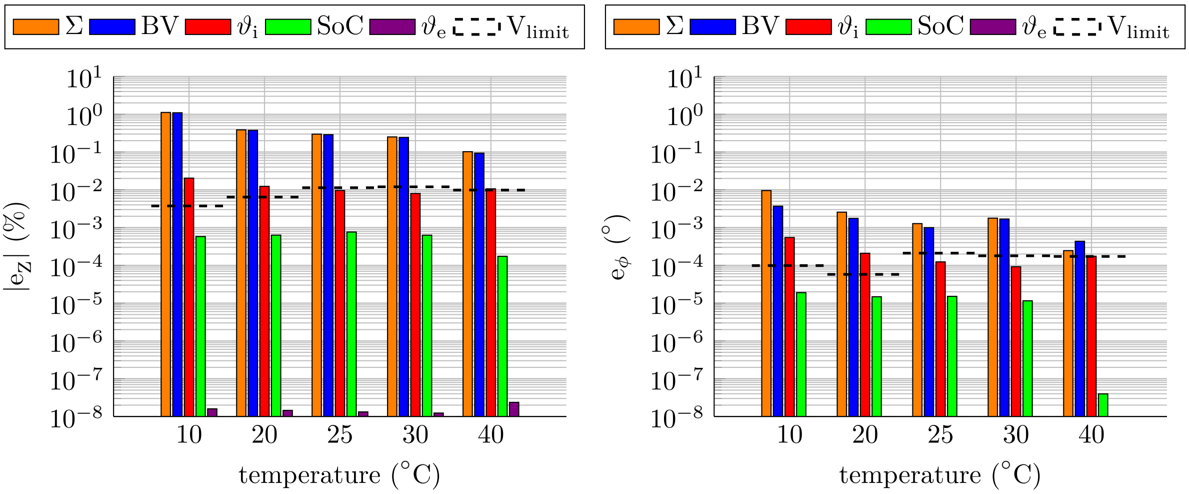

(a) Impedance modulus.

(b) Impedance phase.

Figure 3.60: Impedance measurement deviation depending on cell temperature $\vartheta_{cell}$. 'Σ': sum of all components, 'BV': deviation from impedance non-linearity, '$\vartheta_i$': deviation from temperature increase by impedance heating, 'SoC': deviation from State-of-Charge change, '$\vartheta_e$': deviation from temperature increase by entropy heating, '$V_{limit}$': deviation limit from 10 mV-Criterion (cylindrical LFP-cell A.1, $SoC_{start} = 50\,\%$, $f_m = 1\,\text{Hz}$, $\hat{I}_m = 3\,\text{CA}$).

The scenario shown in this figure as well as in the previous figure 3.59 show that despite large excitation amplitudes of 1 CA and 3 CA the total deviation stays below the 1 % and 1 ° threshold. The deviation caused when following the 10 mV-Criterion, which says that the voltage response amplitude should not be higher than 10 mV is indicated in both figures by the black dashed line. These values are often by several decades below the 1 % and 1 ° threshold. This shows that for this kind of battery cell, the 10 mV-Criterion is too restrictive when setting the excitation amplitude.

Figure 3.61 shows the measurement deviation caused with an underlying constant charge current of 1 CA. The deviation is compared to the impedance value at no constant current. The measurement deviation components are grouped into the deviations caused by the sinusoidal excitation current ('SIN'), the constant current ('DC') and the impedance non-linearity ('BV'). The impedance non-linearity was not grouped into the first two categories since its contribution to the measurement deviation cannot be clearly separated into these two parts.

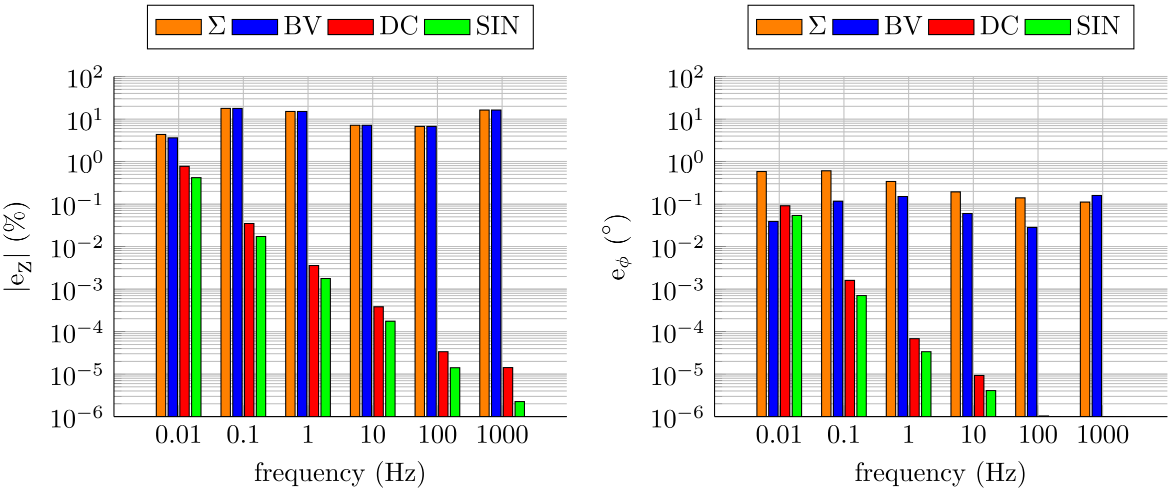

(a) Impedance modulus.

(b) Impedance phase.

Figure 3.61: Impedance measurement deviation depending on measurement frequency $f_m$ with underlying constant current when comparing the measurement to a measurement at no underlying constant current. 'Σ': sum of all components, 'BV': deviation from impedance non-linearity, 'DC': deviation from constant current, 'SIN': deviation from sinusoidal excitation current (cylindrical LFP-cell A.1, $SoC_{start} = 50\,\%$, $\vartheta = 25\,°\mathrm{C}$, $\hat{I}_m = 1\,\mathrm{CA}$, $I_{dc} = 0.5\,\mathrm{CA}$).

Equation 3.148 shows that the constant current creates a factor that increases the deviation of the sinusoidal excitation current. The modulus deviation caused with an underlying constant charge current can be well above 10 % and is almost entirely governed by impedance non-linearity. It also affects both real and imaginary part in similar ways as can be seen by the fact that the modulus deviation increases significantly but the phase deviation stays small.

These large deviations only occur when the measured impedance is compared to the impedance value at no constant current. When the impedance measurement is compared to a measurement at the same constant current and therefore the same shift on the Butler-Volmer curve but with an infinitesimal small excitation amplitude, the introduced deviation is only slightly higher than for the cases with no constant current shown in figure 3.59 and 3.60.

**Chapter Conclusion**

*This chapter introduced a methodology to determine the systematic impedance measurement deviation caused by the battery under test itself. It derived an equation with which the deviation can be estimated before the impedance measurement is taken. The deviation estimation is based on previous measurement results of impedance, entropy and impedance non-linearity described by an introduced modified Butler-Volmer equation. By setting a desired deviation limit, with this equation, the maximum excitation current for electrochemical impedance spectroscopy can be determined.*

*The distinction between ohmic heat and reaction heat is unnecessary when deriving the irreversible heat generation rate from impedance measurements. The irreversible heat generated can be derived from the impedance measurements down to very low frequencies and even to the constant charge/discharge case. A change in Open-Circuit-Voltage was identified as having an impact on the impedance imaginary part but is independent on the amplitude of the excitation current. The impedance non-linearity was shown to be also present for the imaginary part. The mathematical description of this non-linearity would need further research as neither the traditional nor a modified Butler-Volmer equation does perfectly fit the measured data.*

*The biggest contributor to the total deviation of an electrochemical impedance spectroscopy measurement is for most conditions, the impedance non-linearity, followed by the temperature change from impedance heating, followed by the State-of-Charge change and, least important, the temperature change from entropy heating. The* 10 mV-*Criterion was shown to be too restrictive to limit the excitation current for the battery cell used. This might be similar for other lithium-ion battery cells. This finding opens up the possibility of higher excitation currents, which would come with the benefit of less noise in the impedance measurement.*

# 4 On-line Electrochemical Impedance Spectroscopy Measurements

**Abstract**

*On-line Electrochemical impedance spectroscopy means that the battery can stay in the location of operation. Batteries are often in operation and only have little downtime. Therefore measurements should be done during operation or charging. Alternatively, measurements should at least be done right after the usage, a time in which the battery is not charged or discharged but the terminal voltage is still in relaxation. These conditions cause drifts in the voltage measurement, which introduce high measurement deviations into the calculated impedance. These deviations can be suppressed or corrected by various drift correction methods on the voltage readings.*

*On-line implementation of an electrochemical impedance spectroscopy system should make use of already existing components in the battery system in order to save cost. Analog amplifiers are expensive and must be built specifically for the task. The widespread use of power electronic circuits ensures that around a battery in operation there is often a power electronic circuit that charges it, balances the capacity of the single cells, or stabilizes the voltage of the battery to a fixed value. These power electronic circuits can operate as switched-mode amplifiers to generate the desired excitation current for the on-line electrochemical impedance spectroscopy measurement. Switched-mode excitation causes narrowband distortions, which alias over the sampling rate to the measurement frequency bandwidth. These distortions can be avoided by selecting only distortion-free measurement frequencies.*

*The voltage and current sensors of these devices as well as the voltage readers of the battery monitors inside the battery management system could be used to record the measurement signals. However, these sensors and converters have a parasitic behavior. The parasitic current shunt inductance can cause measurement deviations for the real and the imaginary part at high frequencies above the intercept frequency.*

Figure 4.1 shows the different parts necessary for an on-line EIS implementation of the excitation with a switched-mode amplifier. First, the stimulus signal is generated on a micro-controller or read out from a non-volatile memory. By controlling the power electronic switches of the amplifier the desired stimulus frequency is modulated on a carrier signal frequency. It then passes through a low pass filter in order to attenuate the switching frequency before it stimulates the battery. An ADC converts voltage and current into a discrete series of measurements. They are then transferred to a processor, where the data is analyzed, compensated and transformed into the frequency-domain. The ratio of voltage and current in the frequency-domain is the desired complex impedance.

The aspects that can introduce measurement deviations and are of particular interest for an on-line EIS measurement are covered in this chapter. This chapter is organized in the reverse way as the described process. Section 4.1 covers various ways of compensating, suppressing and correcting the drift, which might be present in the voltage readings and the resulting impedance. Section 4.2 of this chapter

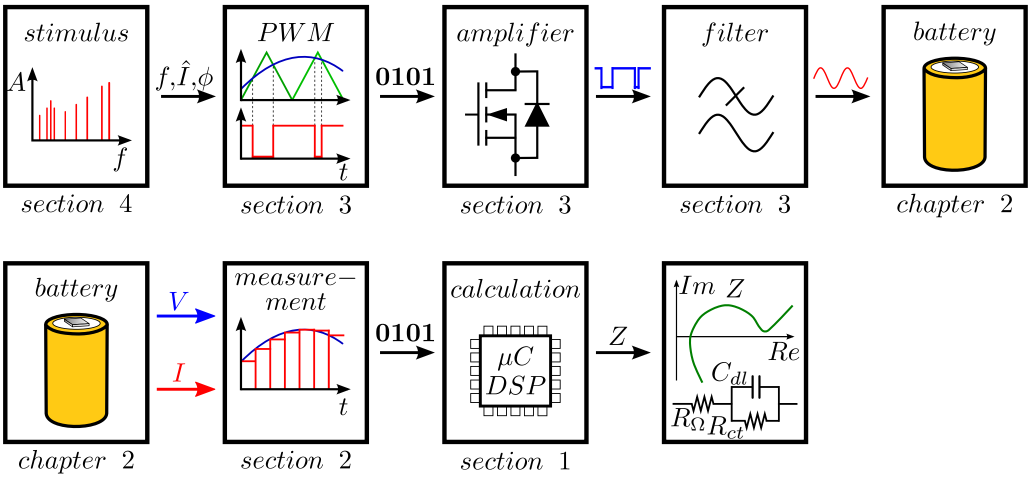

Figure 4.1: Sequence for switched-mode EIS excitation.

discusses influence of the parasitic current shunt inductance on the impedance measurement. Section 4.3 deals with the distortions introduced by the switched-mode amplifier. Baseband harmonics can introduce measurement deviations directly. The switching frequency and sideband harmonics introduce measurement deviations over their aliases. It also shows methods to reduce these distortions. These distortions stay relevant in the last section 4.4 about a distortion-free frequency grid on which the measurement frequencies can be placed during the stimulus design process.

## 4.1 Drift Correction

The word drift is often used in different contexts, which can lead to confusion. In general, a drift describes the effect, that the system under test is non-stationary. Drifts can be grouped into three categories:

1. **Voltage drift**: The voltage at the end of an EIS measurement is not the same as at the beginning.
2. **Short term drifts in the state of the battery**: The state of the battery at the end of the measurement period is not the same as the state at the beginning of the measurement period. These kind of drifts cause the battery to be non-stationary and were covered in chapter 3.
3. **Long term drifts in the state of the battery**: These are changes in the state of the battery which take several hours or days. They are so slow, that during the EIS measurement, the state of the battery can be considered stationary. Kindermann et al. reported such a drift in [64], when he reported a still changing impedance of his li-ion batteries after several hours of relaxation. These kind of drifts are not covered in this thesis.

The voltage drift is the main aspect covered in this section. They can cause such high measurement deviations, that the measured impedance can become completely useless. According to the development of the voltage during the impedance measurement this chapter categorizes two different drift types: linear and exponential. These two types can have different reasons why they occur:

1. **Linear voltage drift**: The battery has been charged or discharged during the measurement and the OCV at the end of the measurement period is different from the one at the beginning of the measurement period. The change in OCV can come from a change in SoC or a change in temperature.
2. **Exponential voltage drift**: The battery was recently charged or discharged and the OCV is in relaxation. This leads to an exponential drift, since the battery is approaching a final steady value.

Steps, due to load changes, and logarithmic-like drifts that occur at the beginning of charging or discharging processes, although relevant for the real application, are left out in this section.

Figure 4.2 gives an overview of five different drift correction types and at what point in the data analysis they are employed. One of them, the drift correction in the frequency-domain is a new method. The five methods are:

1. Time-domain drift correction
2. Windowing
3. Frequency-domain drift correction
4. Time-course interpolation
5. Z-domain drift correction via Z-Hit

Time-domain drift correction and windowing are applied on the time-domain measurement data, whereas frequency-domain drift correction acts on the already Fourier-transformed voltage measurement. Time course interpolation and Z-domain drift correction performs its correction on the final impedance data. Time course interpolation does not correct voltage drifts but drifts in the state of the electrochemical system under study. Z-domain drift correction corrects both, voltage drifts and drifts

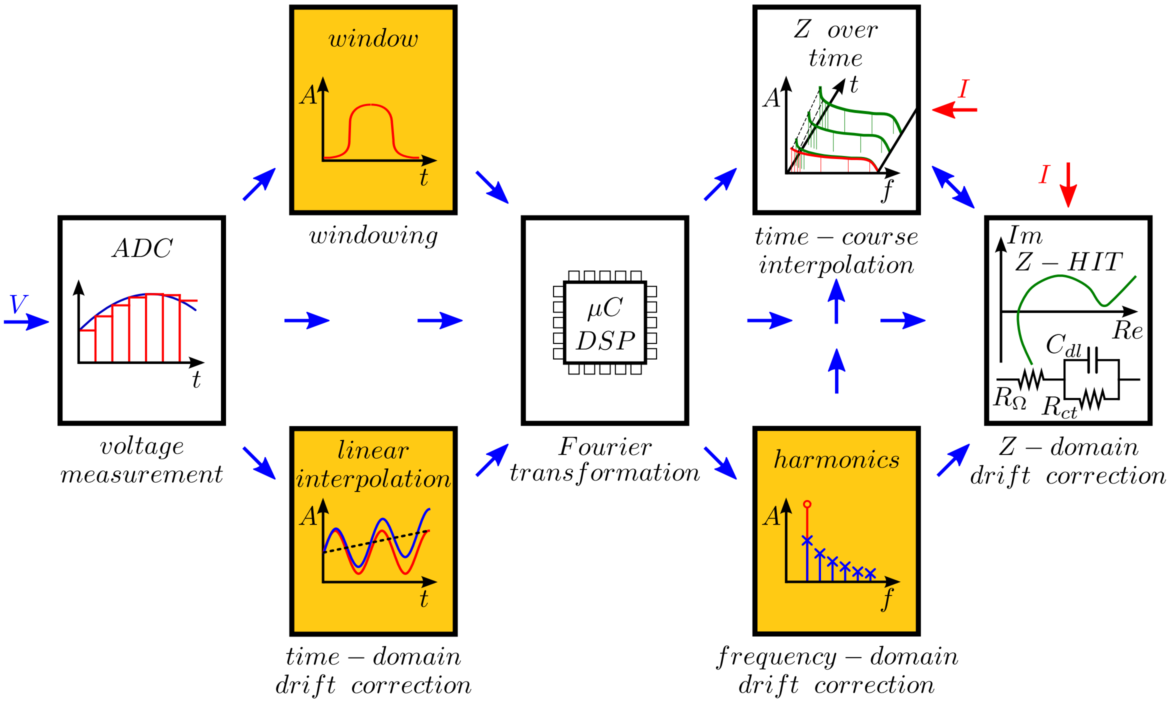

Figure 4.2: Overview over the different drift compensation methods.

in the state of the electrochemical system. The first three methods correct only a voltage drift and cannot be combined with each other. The time-course interpolation and Z-domain drift correction can be additionally applied independent from each other and the first three. The last two methods are not the focus of this section, but are introduced briefly in the next two paragraphs.

Some electrochemical systems are not stationary and their state changes over time, since their components deteriorate or their reactants change during operation. This becomes critical if the change is significant during the time of one sinus-sweep measurement. If the impedance spectra is recorded with several consecutive sinus-sweep measurements in order to observe the evolution of the impedance change, none of the spectra gives a ‘snapshot’ picture of the state of the electrochemical system at a particular point in time. The time-course interpolation is able to correct the spectra in order to obtain a ‘snapshot’ spectra. The method relies on several consecutive measurements. Due to the observed evolution of the impedance for every measurement frequency the governing function how the impedance changes over time can be determined. With that knowledge, the impedance at any time instant can be interpolated. Usually the time instant chosen is the one when the high frequencies were measured during the sinus-sweep measurement. Since they are performed so quickly they can be considered instantaneous and do not have to be interpolated. Stoynov [115; 116] introduced that method. Savova-Stoynov and Stoynov [101] further elaborated how to design experiments for tracking changes in a non-stationary system. Schiller et al. [103] used that method to track the change in impedance of a fuel cell that changed rapidly during carbon monoxide poisoning.

Ehm et al. described the Z-domain correction via Z-HIT in [38; 39]. The name Z-HIT stands for impedance (Z), because it is applied to impedance, and Hilbert tranform (HIT), because it uses the Hilbert transform. Impedance spectra often form a two-pole transfer function, which shows an interrelation between phase and modulus. The Hilbert transform is the logarithmic version of the

Kramers-Kronig relationship [71; 72]. The Hilbert transform and the Kramers-Kronig relationship can be used to detect deviations from minimal-phase characteristics and verify whether the impedance spectra represents a system that fulfills the conditions of stability, causality, linearity and continuity [1]. However, the integration for both methods has to be done from negative infinity to infinity. The Z-HIT method operates on a finite bandwidth. The method relies on equation 4.1 [38; 39] in which the impedance modulus is reconstructed from the impedance phase.

$$ln\left|H(\omega_0)\right| \approx \underbrace{\frac{2}{\pi}\cdot\int_{\omega_{max}}^{\omega_0}\varphi(\omega)\mathrm{d}\,ln\omega}_{integration} + \underbrace{\frac{\pi}{6}\cdot\left.\frac{\mathrm{d}\,\varphi(\omega)}{\mathrm{d}\,ln\omega}\right|_{\omega_0}}_{derivation} + \underbrace{const.}_{adjustment} \tag{4.1}$$

The equation consists of three summands. The first one is the integration of the phase over the logarithmic frequency from the maximum measured frequency $\omega_{max}$ to $\omega_0$, the frequency at which the curve should be reconstructed. The second summand is the derivative of the phase at $\omega_0$. The last one is a constant value. The reconstructed modulus without this value is, in ideal cases, parallel to the measured modulus. By fitting the reconstructed modulus onto the measured modulus, this constant value is determined. The application of the Z-HIT method raises two main questions. On the one hand it focuses on generating a system with minimal-phase characteristic. It remains unclear whether the corrected system is the best representation of the measured system. On the other hand it relies heavily on the phase measurement. Section 3.3 showed that for lower frequencies, the imaginary part of the impedance carries a measurement deviation due to the Open-Circuit-Voltage change. For low frequencies this significantly changes the phase of the measured impedance. The Z-HIT correction is typically done for low frequencies, since these frequencies particularly suffer from drifts. It is unclear if the Z-HIT method corrects the imaginary impedance deviation shown in section 3.3 or if it would use the wrong phase in order to calculate a wrong modulus.
Wagner and Schulze applied this method alongside the time-domain drift compensation and the time-course interpolation in [123] for a fuel cell under carbon monoxide poisoning.

### 4.1.1 Time-Domain Drift Correction

This method directly uses the time-domain measurements. To correct a given measurement time it records, the initial voltage $y(k_0)$ waits a measurement period $N_{Tm}$ and records the voltage $y(k_0+N_{Tm})$. If no drift would be present, these two voltages are the same. If they are different, the method assumes a linear progression between these two voltages. To rectify any existing drift, it applies equation 4.2 to the stored voltage measurements at every sample $y(k_0+k)$ in order to arrive at a corrected voltage $y_c(k_0+k)$. An adjusted drift is applied after every measurement period. In this way this method can also correct drifts, which can be approximated by a series of linear drifts. However, this is more and more difficult the smaller the measurement frequency is. Schiller et al. [102] and Kiel [62] described this method.

$$y_c(k_0+k) = y(k_0+k) - \frac{y\left(k_0+N_{Tm}\right)-y(k_0)}{N_{Tm}}\cdot k \tag{4.2}$$

Figure 4.3 shows an example of this method with synthetic data. The measurement data $y_m$ with an amplitude of one has a drift $y_{drift}$ with a slope of 1 over the measurement period $T_m$. This drift causes the imaginary part of the measurement $Y_m$ to be less than half of the actual signal $Y_{sin}$. If the measurement is compensated by the linear drift compensation, the correct value is recovered.

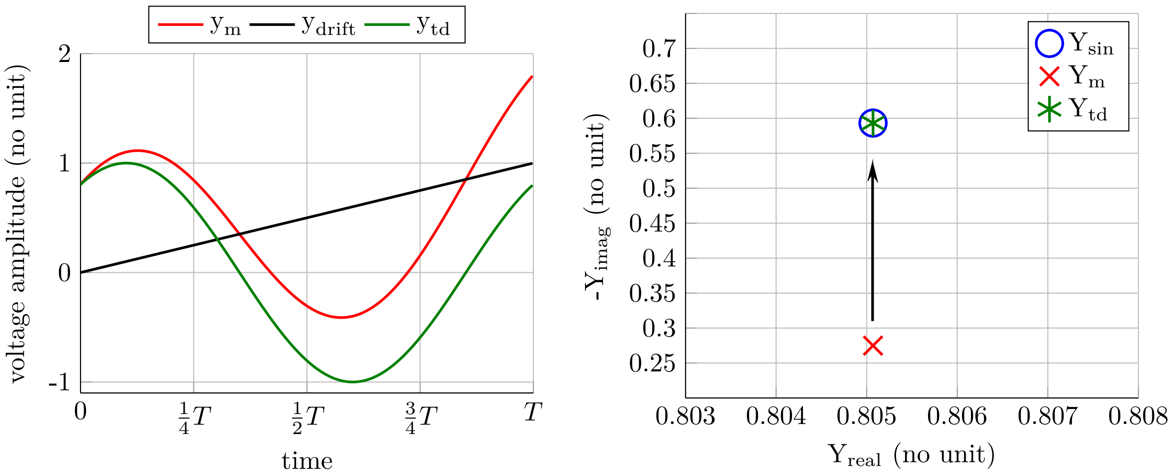

(a) Time-domain representation of a linear drift with time-domain correction.

(b) Complex plane representation of time-domain correction of a linear drift.

Figure 4.3: Time-domain and complex plane representation of a linear drift correction in time-domain (synthetic data).

### 4.1.2 Drift Measurement Deviation Suppression by Windowing

The effect of a drift is similar to the one of spectral leakage. The measurement is not periodic over the measurement time and therefore causes a measurement deviation for all evaluated frequencies. Because of this similarity, the remedy 'windowing' also works for drift measurement deviations. A window forces the beginning and the end of a measurement sequence to zero. Several proposed windows exist in the literature. The ones considered here, are the Box window, the Kaiser window, which uses the modified bessel function of the first kind $\mathcal{I}$ with a fixed value for $\alpha_{Kaiser}$ of 3 (equation 4.3). And three windows based on the cosinus function with different complexity: the Hamming window (equation 4.4), the Blackman-Nuttal window (equation 4.5) and the Flat-Top window (equation 4.6).

$$w_K(k) = \frac{\mathcal{I}_0\left(\pi\alpha\sqrt{1-(\frac{2k}{N-1}-1)^2}\right)}{\mathcal{I}_0(\pi\alpha)} \tag{4.3}$$

$$w_H(k) = a_0 - a_1 \cdot \cos\left(\frac{2\pi k}{N-1}\right)$$
$$\text{with } a_0 = 0.54,\ a_1 = 0.46 \tag{4.4}$$

$$w_{BN}(k) = a_0 - a_1 \cdot \cos\left(\frac{2\pi k}{N-1}\right) + a_2 \cdot \cos\left(\frac{4\pi k}{N-1}\right) - a_3 \cdot \cos\left(\frac{6\pi k}{N-1}\right)$$
$$\text{with } a_0 = 0.3636,\ a_1 = 0.4892,\ a_2 = 0.1366,\ a_3 = 0.01064 \tag{4.5}$$

$$w_{FT}(k) = a_0 - a_1 \cdot \cos\left(\frac{2\pi k}{N-1}\right) + a_2 \cdot \cos\left(\frac{4\pi k}{N-1}\right) - a_3 \cdot \cos\left(\frac{6\pi k}{N-1}\right) + a_4 \cdot \cos\left(\frac{8\pi k}{N-1}\right)$$
$$\text{with } a_0 = 1.0,\ a_1 = 1.93,\ a_2 = 1.29,\ a_3 = 0.388,\ a_4 = 0.028 \tag{4.6}$$

Figure 4.4 shows the trade-off that is made when using a window function. The window reduces the frequency resolution of the measurement.

A minimum number of measurement periods $w_x$ can be defined, which is necessary for the window not to suppress the actual measurement frequency. It can be identified in figure 4.4 at the point at which

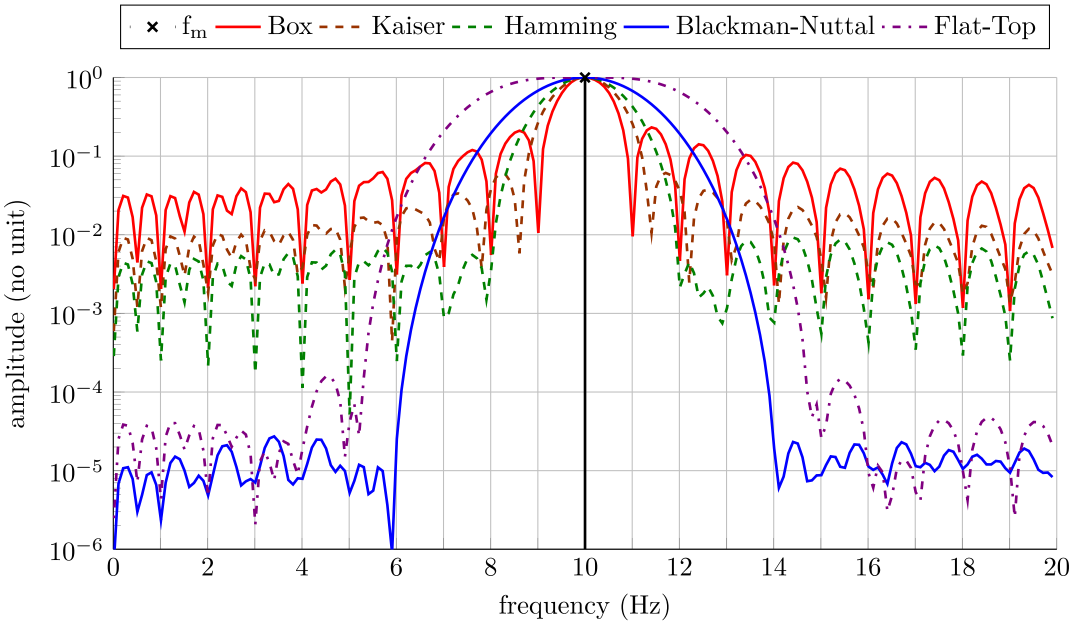

Figure 4.4: Comparison of the frequency response of the Box, Kaiser, Hamming, Blackman-Nuttal and the Flat-Top window in combination with a DFT ($f_m = 10\,\mathrm{Hz}$, $T_a = 10 \cdot T_m$).

the window changes from the passband to the stopband. It is $w_x \approx 1$ for the Box window, $w_x \approx 1.5$ for the Kaiser window (although 2 periods are necessary in this case to avoid spectral leakage), $w_x \approx 2$ for the Hamming window, $w_x \approx 4$ for the Blackman-Nuttal window and $w_x \approx 5$ for the Flat-Top window.

The benefit of windowing compared to the time-domain drift correction is that the single measurements do not have to be stored until the end of the period in order to window them. Every new incoming measurement is directly multiplied by its respective factor of the window and then transferred to the Fourier transformation. Afterwards it can be discarded.

Figure 4.5 shows an example of this method with a similar synthetic data as in figure 4.3 for the time-domain drift correction. The same drift is stretched out over 10 periods in order to comply with the minimum number of measurement periods for every applied window. The figure 4.5a shows the measurement signal multiplied with the Blackman-Nuttal window. The multiplication causes the signal to go to zero at the beginning and at the end of the measurement time. Because of this, the method does not really compensate the measurement deviation; it rather suppresses it. Figure 4.5b includes all the introduced windows. Only the Blackman-Nuttal and the Flat-Top window can suppress the measurement deviation from the drift sufficiently. The Kaiser and the Hamming window are still away from the actual value. The threshold applied for this assessment is again the 0.1% and 0.1° deviation limit introduced in chapter 3. It seems that the suppression below $10^{-4}$ of the Blackman-Nuttal and the Flat-Top window is necessary in order to comply with this threshold.

### 4.1.3 Drift Correction in the Frequency-Domain

Each of the two methods introduced in the previous sections had one significant shortcoming. The drift correction in the time-domain needed to store the data during one entire measurement period, before it could apply the correction and start with the Fourier transformation. The windowing method

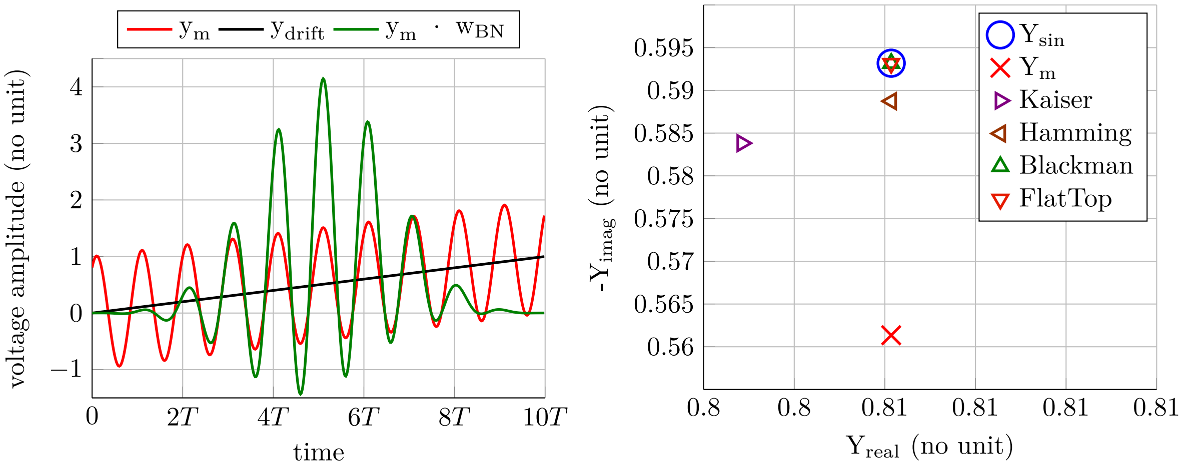

(a) Time-domain representation of a linear drift containing 10 periods. $y_m \cdot \omega_{BN}$ is the same signal windowed by a Blackman-Nuttal window.

(b) Complex plane representation of a linear drift measurement deviation suppression by windowing.

Figure 4.5: Time-domain and complex plane representation of a linear drift suppression by windowing (synthetic data).

required a minimum number of measurement periods. The more effective the window was to suppress the measurement deviation caused by a drift the more periods it required. The drift correction in the frequency-domain can overcome both of these shortcomings. It does not need to store measurement data and it only requires one period of the measurement frequency.

A drift of a voltage or current signal can be interpreted as a simple superposition of the drift signal and the sinusoidal response to the excitation signal. Transformed into the frequency-domain, the same superposition of the two signals still takes place (see equations 4.7).

$$\mathcal{F}\left\{y_{drift} + y_{sin}\right\} = Y_{drift} + Y_{sin} \tag{4.7}$$

The Fourier transformation of the pristine response of the actual measurement signal $Y_{sin}$ only appears at the measurement frequency itself. The Fourier transformation of the drift signal $Y_{drift}$ also appears at other frequencies. Its Fourier transformed signal can be separated into its real and imaginary part, whose calculation can be done separately (see equation 4.8 to 4.10).

$$c_n = \frac{2}{T}\int_0^T y_{drift} \cdot e^{-j2\pi\frac{n}{T}t}\mathrm{d}t = a_n - jb_n \tag{4.8}$$

$$a_n = \frac{2}{T}\int_0^T y_{drift} \cdot cos\left(2\pi\frac{n}{T}t\right)\mathrm{d}t \tag{4.9}$$

$$b_n = \frac{2}{T}\int_0^T y_{drift} \cdot sin\left(2\pi\frac{n}{T}t\right)\mathrm{d}t \tag{4.10}$$

The idea of the frequency-domain drift correction is that the Fourier transformed measurement signal is compensated by the part that was caused by the drift signal. This results in the pristine response of the impedance. The difficulty is that only both signal can be measured at the measurement frequency. By calculating various harmonic values of the real part $a_n$ and imaginary part $b_n$ and knowing their dependency on each other, the drift value at the measurement frequency $a_1$ and $b_1$ can be estimated. The next sections show these dependencies between the harmonics for a linear and an exponential drift.

To a apply the method in practice, it needs some additional Fourier transformations on harmonics of the measurement frequency running at the same time as the Fourier transformations of the measurement frequency. Like the windowing, the time-domain data does not need to be stored. Like the time-domain drift correction, it can be applied even when only one period is measured. A similar method was patented by Petrescu et al. [86; 87], presented by Diard and Petrescu [35] and is used in EIS meters from Bio-logic Instruments [13]. This uses two additional Fourier transformations, one to the left of the measurement frequency and one to the right. It takes the average of both and assumes that this is the contribution of the drift at the measurement frequency. It therefore corrects the measurement frequency by this value. This method is applied separately for the imaginary part and for the real part of the impedance. This approach does not completely coincide with the analysis given in the next two section, neither for the linear drift, nor for the exponential drift. Measuring half the measurement frequency means that the measurement time has to be twice as long, which is unnecessary when analyzing the dependencies of the harmonics as done in the next two sections.

#### 4.1.3.1 Linear Drift

A linear drift $A \cdot t + B$ has actually two parameters $A$ and $B$. However, when transforming the drift into the frequency-domain, the constant part $B$ disappears. Therefore a linear drift can be considered as a one parameter function $A \cdot t$.

The real part fundamental $a_1$ and harmonics $a_n$ of the linear drift is Fourier transformed separately (see equation 4.13) from the imaginary part fundamental $b_1$ and harmonics $b_n$ (see equation 4.17).

$$y_{drift} = A \cdot t \tag{4.11}$$

$$a_n = \frac{2}{T_m} \int_0^{T_m} A \cdot t \cdot cos\left(2\pi \frac{n}{T_m} t\right) \mathrm{d}t \tag{4.12}$$

$$= \frac{2A}{T_m} \int_0^{T_m} t \cdot cos\left(2\pi \frac{n}{T_m} t\right) \mathrm{d}t \tag{4.13}$$

Starting with the real part, the integral for the slope of equation 4.13 is solved by using lemma C.13, but ends up to be zero (see equation 4.14)

$$a_n = \frac{2A}{T} \left[ \frac{cos\left(2\pi \frac{n}{T} t\right)}{\left(2\pi \frac{n}{T}\right)^2} + \frac{t \cdot sin\left(2\pi \frac{n}{T} t\right)}{2\pi \frac{n}{T}} \right]_0^T$$

$$a_n = \frac{2A}{T} \left[ \underbrace{\frac{cos\left(2\pi n\right)}{\left(2\pi \frac{n}{T}\right)^2}}_{=\frac{1}{\left(2\pi \frac{n}{T}\right)^2}} - \underbrace{\frac{cos\left(0\right)}{\left(2\pi \frac{n}{T}\right)^2}}_{=\frac{1}{\left(2\pi \frac{n}{T}\right)^2}} \right] + \frac{2A}{T} \left[ \underbrace{\frac{T \cdot sin\left(2\pi n\right)}{2\pi \frac{n}{T}}}_{=0} - \underbrace{\frac{2A}{T} \frac{0 \cdot sin\left(0\right)}{2\pi \frac{n}{T}}}_{=0} \right] \tag{4.14}$$

$$a_n = 0 \tag{4.15}$$

With this information we can state the

**$\mathbf{a_{lin,n}}$-rule for calculating the fundamental real part at the measurement frequency:**

The real part of a linear drift is 0 (see equation 4.16). The real part at the measurement frequency $a_1$

does not need to be corrected.

$$a_{lin,n} = a_1 \tag{4.16}$$

Continuing with the imaginary part, the integral for the slope can be solved by using lemma C.12. Compared to the real part, the imaginary part is not zero.

$$\begin{aligned}
y_{drift} &= A \cdot t \\
b_n &= \frac{-2}{T_m} \int_0^{T_m} A \cdot t \cdot \sin\left(2\pi \frac{n}{T_m} t\right) \mathrm{d}t \\
&= \frac{-2A}{T_m} \int_0^{T_m} t \cdot \sin\left(2\pi \frac{n}{T_m} t\right) \mathrm{d}t \qquad (4.17) \\
b_n &= \frac{-2A}{T_m} \left[ \frac{sin\left(2\pi \frac{n}{T_m} t\right)}{\left(2\pi \frac{n}{T_m}\right)^2} - \frac{t \cdot \cos\left(2\pi \frac{n}{T_m} t\right)}{2\pi \frac{n}{T_m}} \right]_0^{T_m} \\
b_n &= \frac{-2A}{T_m} \left[ \underbrace{\frac{\sin(2\pi n)}{\left(2\pi \frac{n}{T_m}\right)^2}}_{=0} - \underbrace{\frac{\sin(0)}{\left(2\pi \frac{n}{T_m}\right)^2}}_{=0} \right] - \frac{-2A}{T_m} \left[ \underbrace{\frac{T_m \cdot \cos(2\pi n)}{2\pi \frac{n}{T_m}}}_{=\frac{T_m \cdot \cos(2\pi n)}{2\pi \frac{n}{T_m}}} - \underbrace{\frac{0 \cdot \cos(0)}{2\pi \frac{n}{T_m}}}_{=0} \right] \\
b_n &= \frac{2A}{T_m} \cdot \frac{T_m \cdot \overbrace{\cos(2\pi n)}^{=1}}{2\pi \frac{n}{T_m}} \qquad (4.18) \\
b_n &= \frac{AT_m}{\pi} \cdot \frac{1}{n} \qquad (4.19)
\end{aligned}$$

The $k = 2^x$-harmonics of the imaginary part form a geometric series, where the value of one series element is equal to the sum of all series elements which follow. As any geometric series, the sum over all its elements has a finite value (see equation 4.20).

$$\sum_{k=0}^{\infty} p_0 q^k = \frac{p_0}{1-q} \qquad \text{with } p_0 = \frac{AT}{\pi}, \quad q = \frac{1}{2}, \quad k = 2, 4, 8, 16, 32, ... \tag{4.20}$$

The value of the harmonic at every point in the series is always the sum of the remaining elements. Two rules can be stated for the imaginary part:

1. **$\mathbf{b_{lin,\Sigma N}}$-rule for calculating the fundamental imaginary part at the measurement frequency:**
   The real imaginary part over $k = 2^x$ forms a geometric series. The fundamental imaginary part $b_1$ is corrected by the sum of $N$ series elements and the last element is added twice (see equation 4.21).

$$b_{lin,\Sigma N} = b_1 - \sum_{n=1}^{N} b_{2^n} + b_{2^N} \tag{4.21}$$

2. **$\mathbf{b_{lin,n}}$-rule for calculating the fundamental imaginary part at the measurement frequency:**
   The values of the harmonics for the imaginary part decrease with higher harmonic numbers in a $\frac{1}{n}$ way. The fundamental imaginary part $b_1$ is corrected by the $n^{th}$ harmonic by multiplying its value by $n$ (see equation 4.22).

$$b_{lin,n} = b_1 - n \cdot b_n \tag{4.22}$$

Figure 4.6a shows that for a linear drift the deviation of the real part is constant for all harmonics and almost zero. Figure 4.6b shows a simple "Division-by-2" pattern for the imaginary part of the linear drift for $k = 2^x$ harmonics. The progress of the Fourier summation of the imaginary part reveals another interesting possibility. The $k = 2^x$ harmonics arrive at half the period at half their final value. On the other hand, all the $k = 2^x$ harmonics arrive at the same value at half the period. This allows to perform the Fourier transformation for the first half of the period for one harmonic and for the other half for another harmonic. The summation, carried out during the Fourier transformation for the other harmonic would start again from zero after the first half. Since the real part is always zero, it does not have to be calculated at all.

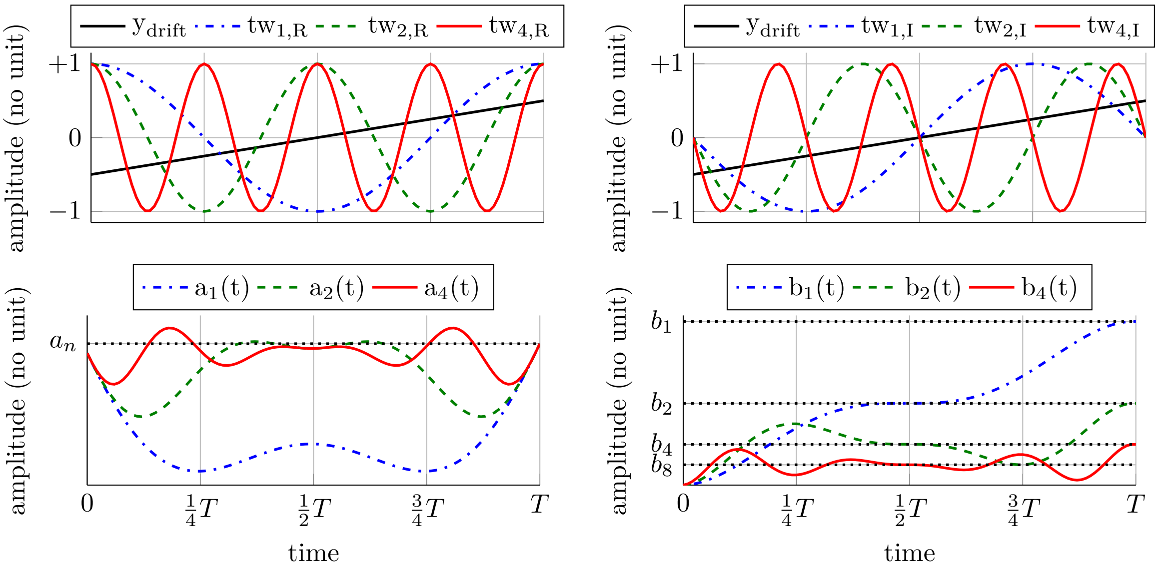

(a) Real part.

(b) Imaginary part.

Figure 4.6: Harmonics calculation of the real and imaginary part for a linear drift (synthetic data).

The two rules, $b_{lin,\Sigma N}$ and $b_{lin,n}$, are applied to synthetic data in order to show their applicability. Figure 4.7a shows a linear drift $y_{drift}$, which distorts the impedance measurement $Y_m$ as shown in figure 4.7b. Equation 4.23 shows the $b_{lin,\Sigma N}$-rule for calculating $Y_{lin\Sigma 64}$. Equation 4.24 shows the $b_{lin,n}$-rule for calculating $Y_{lin4}$.

$$Y_{lin\Sigma 64} = Y_m - j\left[\sum_{n=1}^{6} b_{2^n} + b_{64}\right] \tag{4.23}$$

$$Y_{lin4} = Y_m - j \cdot 4 \cdot b_4 \tag{4.24}$$

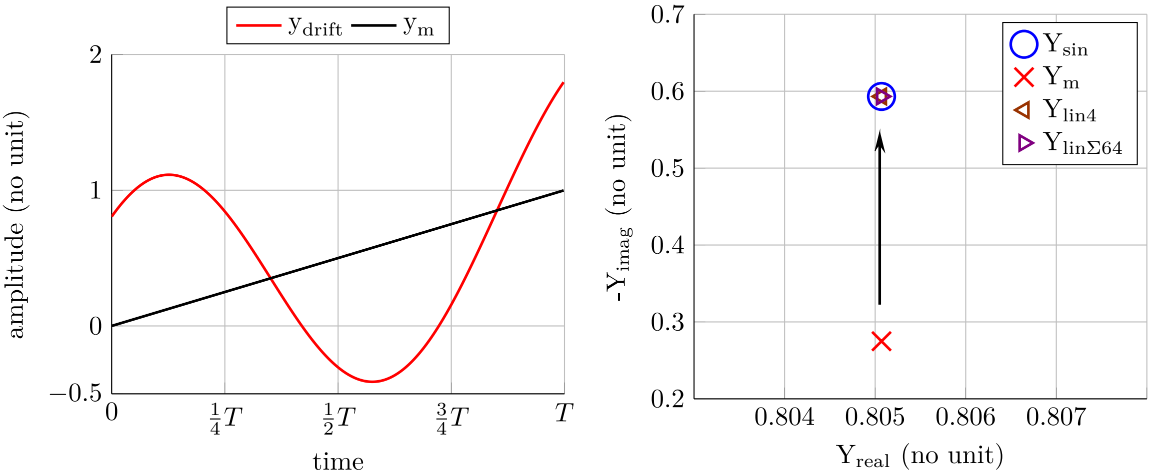

(a) Time-domain representation of a linear drift.

(b) Complex plane correction of a linear drift.

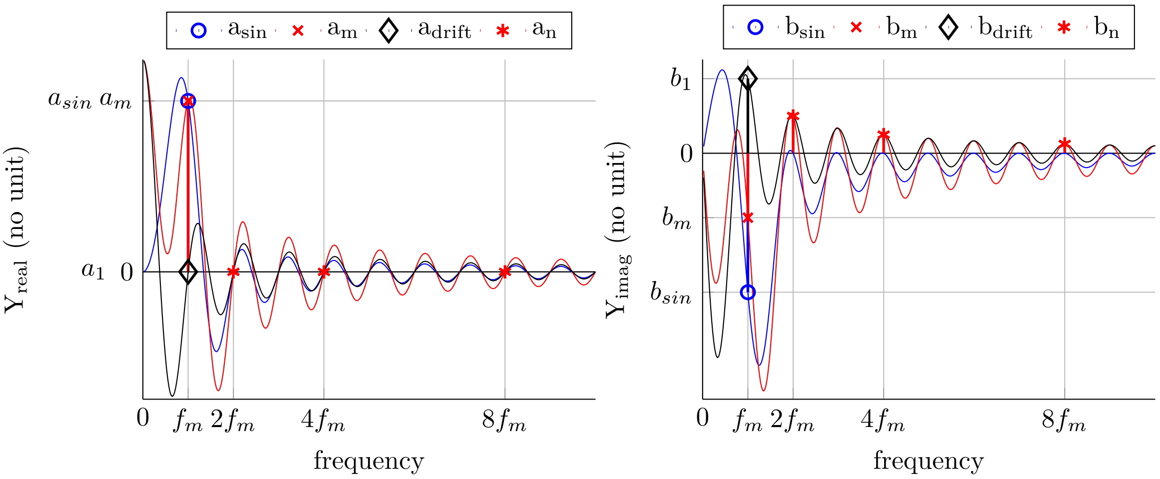

(c) Frequency-domain of the real part of a linear drift.

(d) Frequency-domain of the imaginary part of a linear drift.

Figure 4.7: Time-domain, complex plane and frequency-domain representation of a linear drift correction in the frequency-domain (synthetic data).

Figure 4.7b shows two corrections of a measurement distorted by a drift $Y_m$. The first one $Y_{lin\Sigma 64}$ was done with equation 4.23 using harmonics up to the 64th. The second one $Y_{lin4}$ was done with equation 4.24. Both methods compensate the drift deviation on synthetic data. Equation 4.23 uses several higher harmonics. This comes with the benefit, that it creates a mean over several measurement values. However, higher harmonics are small compared to the fundamental. They are used with high multiplication factors. These factors also amplify the noise which is measured with the harmonics. When equation 4.24 is used with the lowest harmonic possible the associated noise is hardly amplified. Figure 4.7c and 4.7d show the real and imaginary part in the frequency-domain if the measurement is evaluated for a continuous frequency range from 0 Hz to $10 \cdot f_m$. Please note that except for integer multiples of the measurement frequency, spectral leakage occurs.

#### 4.1.3.2 Exponential Drift

The exponential drift is considered as a two parameter function $A \cdot e^{-\frac{1}{\tau} \cdot t}$ with the factor $A$ and the exponential time parameter $\tau$. As for the linear drift, the Fourier transformation is done separately for the real part fundamental and harmonics $a_n$ (see equation 4.25), and for the imaginary part fundamental and harmonics $b_n$ (see equation 4.32).

Lemma C.15 solves the integral 4.25 for the real part to equation 4.26.

$$
\begin{align}
y_{drift} &= A \cdot e^{-\frac{1}{\tau}\cdot t} \notag \\
a_n &= \frac{2A}{T_m} \int_0^{T_m} e^{-\frac{1}{\tau}\cdot t} \cdot cos\left(2\pi \frac{n}{T_m} t\right) \mathrm{d}t \tag{4.25} \\
a_n &= \frac{2A}{T_m} \left[ \frac{e^{-\frac{1}{\tau}\cdot t}\left(-\frac{1}{\tau} \cdot cos\left(2\pi \frac{n}{T_m} t\right) + 2\pi \frac{n}{T_m} \cdot sin\left(2\pi \frac{n}{T_m} t\right)\right)}{\frac{1}{\tau^2} + \left(2\pi \frac{n}{T_m}\right)^2} \right]_0^{T_m} \notag \\
a_n &= \frac{2A}{T_m} \left[ \frac{-\frac{1}{\tau}}{\frac{1}{\tau^2} + \left(2\pi \frac{n}{T_m}\right)^2} \left( e^{-\frac{T_m}{\tau}} \cdot \underbrace{cos\left(2\pi n\right)}_{=1} - e^{-\frac{0}{\tau}\cdot} \underbrace{e^0 \cdot cos\left(0\right)}_{=1} \right) \right] \notag \\
&+ \frac{2A}{T_m} \left[ \frac{2\pi \frac{n}{T_m}}{\frac{1}{\tau^2} + \left(2\pi \frac{n}{T_m}\right)^2} \left( e^{-\frac{T_m}{\tau}} \cdot \underbrace{sin\left(2\pi n\right)}_{=0} - e^{-\frac{0}{\tau}\cdot} \underbrace{e^0 \cdot sin\left(0\right)}_{=0} \right) \right] \notag \\
a_n &= 2A \frac{\frac{1}{\tau}}{\frac{T_m}{\tau^2} + 4\pi^2 \frac{1}{T_m} n^2} \left(1 - e^{-\frac{T_m}{\tau}}\right) \tag{4.26}
\end{align}
$$

Substituting the terms in equation 4.26 with
$p_a = 2A\left(1 - e^{-\frac{T_m}{\tau}}\right)$, $q = \frac{T_m}{\tau^2}$, $r = 4\pi^2 \frac{1}{T_m}$
yields a simplified equation for the harmonics:

$$
a_n = \frac{p_a}{q + rn^2} \tag{4.27}
$$

The harmonic of any number $n_1$ can then be put into relation to another harmonic of any other number $n_2$:

$$
\begin{align}
\frac{a_{n1}}{a_{n2}} &= \frac{\frac{p_a}{q+rn_1^2}}{\frac{p_a}{q+rn_2^2}} \notag \\
\frac{a_{n1}}{a_{n2}} &= \frac{q}{q+rn_1^2} + \frac{rn_2^2}{q+rn_1^2} \notag \\
\frac{a_{n1}}{a_{n2}} &= \frac{1}{1+\frac{r}{q}n_1^2} + \frac{\frac{r}{q}n_2^2}{1+\frac{r}{q}n_1^2} \tag{4.28}
\end{align}
$$

$$
\begin{align}
\frac{a_{n1}}{a_{n2}} \cdot \left(1 + \frac{r}{q}n_1^2\right) &= 1 + \frac{r}{q}n_2^2 \notag \\
\frac{a_{n1}}{a_{n2}} + \frac{a_{n1}}{a_{n2}} \cdot \frac{r}{q}n_1^2 - \frac{r}{q}n_2^2 &= 1 \notag \\
\frac{r}{q} &= \frac{1 - \frac{a_{n1}}{a_{n2}}}{\frac{a_{n1}}{a_{n2}}n_1^2 - n_2^2} \tag{4.29}
\end{align}
$$

**$a_{expn1/n2}$-rule for calculating the fundamental real part at the measurement frequency:**
The relationship between two harmonics is determined by calculating the term $\frac{r}{q}$ with equation 4.30. The index $\frac{n_1}{n_2}$ is used to indicate with which harmonics this term was calculated. Once determined,

the real part at the measurement frequency is calculated with equation 4.31. It is similar to equation 4.28 with $n_1 = 1$. The index $expn_1/n_2$ is used to indicate based on which harmonics the term $\frac{r}{q}$ was calculated. For equation 4.31 one of the harmonics $a_{n1}$, $a_{n2}$ for calculating $\frac{r}{q}$ or any other harmonic can be used. It is best to use the highest harmonic which is free of systematic measurement deviations in order to keep the amplification of potentially present noise as low as possible.

$$\frac{r}{q}_{\frac{n1}{n2}} = \frac{1 - \frac{a_{n1}}{a_{n2}}}{\frac{a_{n1}}{a_{n2}} n_1^2 - n_2^2} \tag{4.30}$$

$$a_{expn1/n2} = \left( \frac{1}{1 + \frac{r}{q}_{\frac{n1}{n2}}} + \frac{\frac{r}{q}_{\frac{n1}{n2}} n_x^2}{1 + \frac{r}{q}_{\frac{n1}{n2}}} \right) \cdot a_{nx} \tag{4.31}$$

For the imaginary part, lemma C.14 solves its integral 4.32 to equation 4.33.

$$\begin{aligned} y_{drift} &= A \cdot e^{-\frac{1}{\tau} \cdot t} \\ b_n &= \frac{2A}{T_m} \int_0^{T_m} e^{-\frac{1}{\tau} \cdot t} \cdot sin\left(2\pi \frac{n}{T_m} t\right) \mathrm{d}t \end{aligned} \tag{4.32}$$

$$\begin{aligned} b_n &= \frac{2A}{T_m} \left[ \frac{e^{-\frac{1}{\tau} \cdot t} \left( -\frac{1}{\tau} \cdot sin\left(2\pi \frac{n}{T_m} t\right) - 2\pi \frac{n}{T_m} \cdot cos\left(2\pi \frac{n}{T_m} t\right)\right)}{\frac{1}{\tau^2} + \left(2\pi \frac{n}{T_m}\right)^2} \right]_0^{T_m} \\ b_n &= \frac{2A}{T_m} \left[ \frac{-\frac{1}{\tau}}{\frac{1}{\tau^2} + \left(2\pi \frac{n}{T_m}\right)^2} \left( e^{-\frac{T_m}{\tau}} \cdot \underbrace{sin\left(2\pi n\right)}_{=0} - e^{-\frac{0}{\tau}} \cdot \underbrace{e^0 \cdot sin\left(0\right)}_{=0} \right) \right] \\ &- \frac{2A}{T_m} \left[ \frac{2\pi \frac{n}{T_m}}{\frac{1}{\tau^2} + \left(2\pi \frac{n}{T_m}\right)^2} \left( e^{-\frac{T_m}{\tau}} \cdot \underbrace{cos\left(2\pi n\right)}_{=1} - e^{-\frac{0}{\tau}} \cdot \underbrace{e^0 \cdot cos\left(0\right)}_{=1} \right) \right] \\ b_n &= 2A \frac{2\pi \frac{n}{T_m}}{\frac{T_m}{\tau^2} + 4\pi^2 \frac{1}{T_m} n^2} \left(1 - e^{-\frac{T_m}{\tau}}\right) \end{aligned} \tag{4.33}$$

Substituting the terms in equation 4.26 with
$p_b = \frac{4\pi A}{T_m}\left(1 - e^{-\frac{T_m}{\tau}}\right), \qquad q = \frac{T_m}{\tau^2}, \qquad r = 4\pi^2 \frac{1}{T_m}$
yields a simplified equation for the harmonics:

$$b_n = \frac{p_b \cdot n}{q + rn^2} \tag{4.34}$$

The harmonics can then be put into relation to each other:

$$
\begin{aligned}
\frac{b_{n1}}{b_{n2}} &= \frac{\frac{p_b \cdot n_1}{q+rn_1^2}}{\frac{p_b \cdot n_2}{q+rn_2^2}} = \frac{n_1}{n_2} \cdot \frac{q+rn_2^2}{q+rn_1^2} \\
\frac{b_{n1}}{b_{n2}} &= \frac{n_1}{n_2} \cdot \left( \frac{q}{q+rn_1^2} + \frac{rn_2^2}{q+rn_1^2} \right) \\
\frac{b_{n1}}{b_{n2}} &= \frac{\frac{n_1}{n_2}}{1+\frac{r}{q}n_1^2} + \frac{\frac{r}{q}n_2 n_1}{1+\frac{r}{q}n_1^2} \qquad (4.35) \\
\frac{b_{n1}}{b_{n2}} \cdot \left(1+\frac{r}{q}n_1^2\right) &= \frac{n_1}{n_2} + \frac{r}{q}n_2 n_1 \\
\frac{b_{n1}}{b_{n2}} + \frac{b_{n1}}{b_{n2}} \cdot \frac{r}{q}n_1^2 - \frac{r}{q}n_1 n_2 &= \frac{n_1}{n_2} \\
\frac{r}{q} &= \frac{\frac{n_1}{n_2} - \frac{b_{n1}}{b_{n2}}}{\frac{b_{n1}}{b_{n2}}n_1^2 - n_1 n_2} \qquad (4.36)
\end{aligned}
$$

**$\mathbf{b_{expn1/n2}}$-rule for calculating the fundamental imaginary part at the measurement frequency:**

The process is the same for the imaginary part as for the real part with the **$\mathbf{a_{expn1/n2}}$**-rule. The relationship between two harmonics is determined by calculating the term $\frac{r}{q}$ with equation 4.37. The index $\frac{n_1}{n_2}$ is used to indicate with which harmonics this term was calculated. Once determined, the imaginary part at the measurement frequency is calculated with equation 4.38. It is similar to equation 4.35 with $n_1 = 1$. The index $expn_1/n_2$ is used to indicate based on which harmonics the term $\frac{r}{q}$ was calculated. For equation 4.38 one of the harmonics $a_{n1}$ or $a_{n2}$ for calculating $\frac{r}{q}$ or any other harmonic can be used. It is best to use the highest harmonic which is free of systematic measurement deviations to keep the amplification of the potentially present noise as low as possible.

$$
\frac{r}{q}_{\frac{n_1}{n_2}} = \frac{\frac{n_1}{n_2} - \frac{b_{n1}}{b_{n2}}}{\frac{b_{n1}}{b_{n2}}n_1^2 - n_1 n_2} \tag{4.37}
$$

$$
b_{expn1/n2} = \left( \frac{\frac{1}{n_x}}{1+\frac{r}{q}_{\frac{n_1}{n_2}}} + \frac{\frac{r}{q}_{\frac{n_1}{n_2}} n_x}{1+\frac{r}{q}_{\frac{n_1}{n_2}}} \right) \cdot b_{nx} \tag{4.38}
$$

Figure 4.8a shows that the deviation of the real part is not constant for an exponential drift as it is for a linear drift. It decreases fast with higher harmonics due to the $n^2$ term in equation 4.26. In this example $a_4$ is already very close to zero. Figure 4.8b does not show the simple ‘Division-by-2’ pattern figure 4.6b shows for the linear drift. The value of the harmonics for the imaginary part decreases much slower than for the real part.

By using the $a_{expn1/n2}$-rule and $b_{expn1/n2}$-rule the combined measurement of the voltage response and the drift during an EIS measurement $Y_m$ is corrected by using equation 4.39

$$
Y_{expn1/n2} = Y_m - \left(a_{expn1/n2} - jb_{expn1/n2}\right) \tag{4.39}
$$

Two approaches were used one with $n_1 = 2$ and $n_2 = 4$, labeled $Y_{exp2/4}$ and one with $n_1 = 4$ and $n_2 = 8$, labeled $Y_{exp4/8}$. The results of these two approaches can be seen in figure 4.9b. Both are applied on the synthetic signal distorted by an exponential drift $Y_m$. The exponential correction works for both approaches. Figure 4.9c and 4.9d show the real and imaginary part in the frequency-domain if

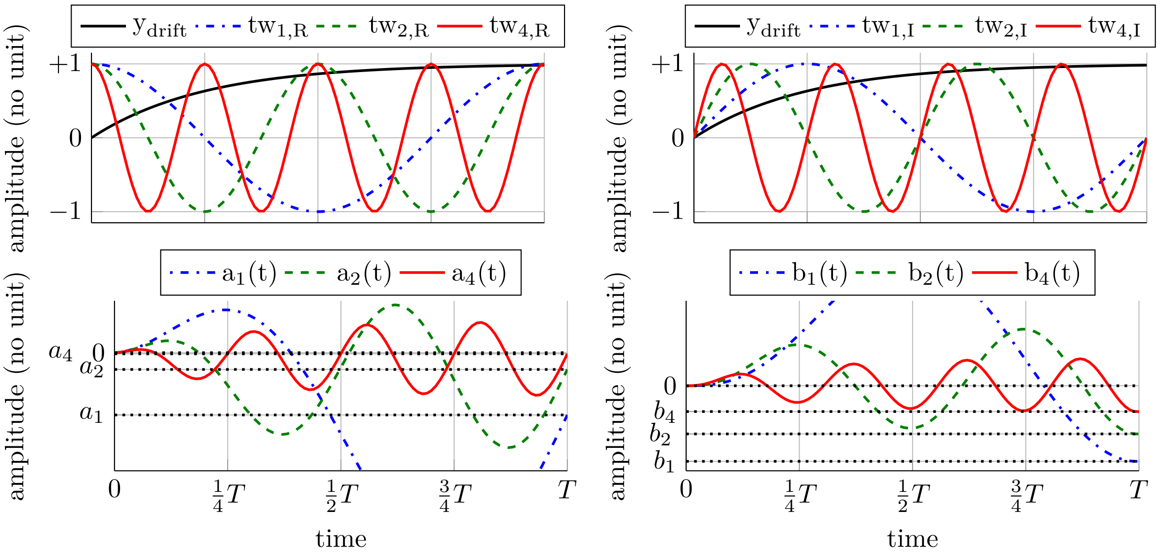

(a) Real part.

(b) Imaginary part.

Figure 4.8: Harmonics calculation of the real and imaginary part for an exponential drift (synthetic data).

the measurement is evaluated for a continuous frequency range from 0 Hz to $10 \cdot f_m$. Except for integer multiples of the measurement frequency, a spectral leakage deviation occurs for the other frequencies. For the correction, various harmonics can be used in order to correct the measurement. The higher the order of the harmonic, the stronger measurement noise is amplified.

The exponential drift correction in the frequency-domain incorporates the linear drift correction in the frequency-domain. A linear drift can be seen as an exponential drift with a very large time constant $\tau$ compared to the measurement period $T_m$. When substituting the exponential function with a Taylor series expansion, which is stopped after the linear element ($1^{\text{st}}$ derivative), equation 4.13 and 4.17 turn into equation 4.25 and 4.32. Only the linear slope $A$ changes to the value $-\frac{A}{\tau}$.

### 4.1.4 Comparison of Correction Methods

The application of the three methods introduced so far is mutually exclusive. Determining the effectiveness of the three methods is therefore of interest. Figure 4.10a and table 4.1 show the method applied to a sinusoidal frequency with 2 measurement periods distorted by a linear drift. The linear drift correction in the frequency-domain $Y_{fdlin4}$, the linear drift correction in the time-domain $Y_{td}$ and the exponential drift correction in the frequency-domain $Y_{fdexp2/4}$ are all able to correct that measurement deviation. The Blackman-Nuttal window $Y_{wBN}$ does not work properly since the minimum number of measurement periods $w_x$ is not met. For the same drift with a measurement of 4 periods the Blackman-Nuttal window is able to suppress the drift measurement deviation sufficiently. The Hamming window $Y_{wH}$ does work but has an insufficient suppression.
The method proposed by Petrescu et al. [86; 87] was applied by evaluating the measurement data at half the measurement frequency and one and a half the measurement frequency. Due to the size of the frequency bins the Fourier transformation cannot be performed at frequencies which are closer to the measurement frequency. This is only possible if the more periods are measured, which is unpractical since it extends the total measurement time. Figure 4.10a and table 4.1 show that this method

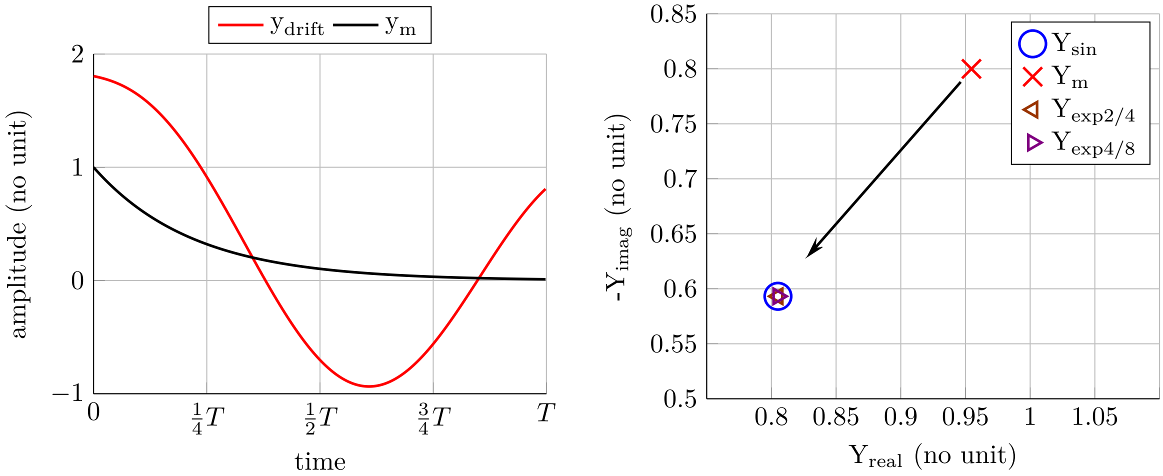

(a) Time-domain representation of an exponential drift.

(b) Complex plane correction of an exponential drift.

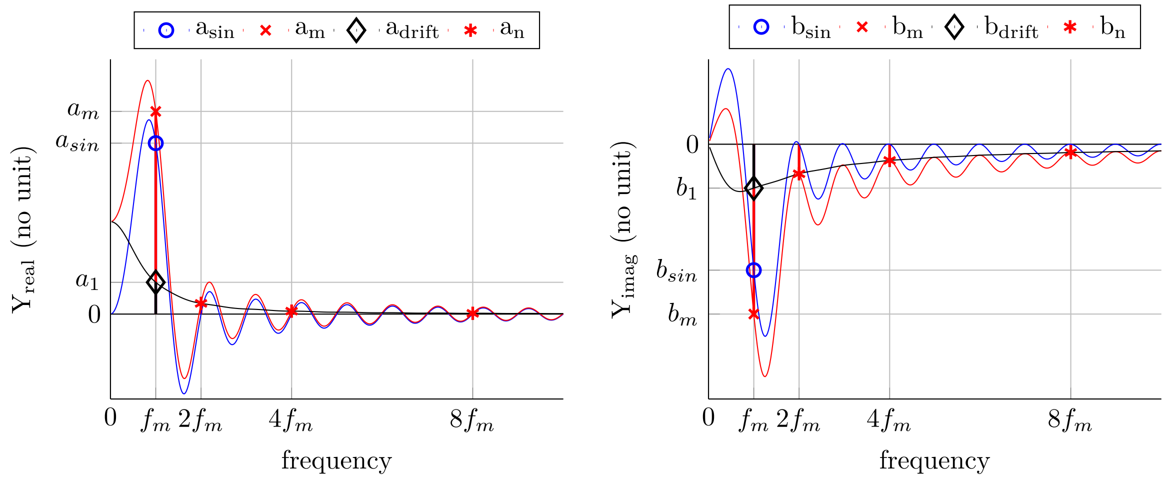

(c) Frequency-domain of the real part of an exponential drift.

(d) Frequency-domain of the imaginary part of an exponential drift.

Figure 4.9: Time-domain, complex plane and frequency-domain representation of an exponential drift correction in the frequency-domain (synthetic data).

overcompensates the imaginary drift deviation (see $Y_{fdPetrescu}$-value). Section 4.1.3.1 showed that the imaginary part for a linear drift shows a $\frac{1}{n}$ relationship. Assuming that the imaginary part at half the measurement frequency has a value of 6. In this case the imaginary part at the measurement frequency which is double that frequency has a value of 3 and the imaginary part at one and a half the measurement frequency is triple that frequency has a value of 2. Petrescu's method now takes the average of 6 and 2 and corrects the imaginary part wrongly at the measurement frequency by 4. Figure 4.10a shows this overcompensation by a factor of 4/3 of the actual deviation.

Figure 4.10b and table 4.2 show the same comparison for an exponential drift with 2 periods. The linear drift correction in the frequency-domain $Y_{fdlin4}$ and the linear drift correction in the time-domain $Y_{td}$ only correct the imaginary part of the impedance. Both methods overcompensate the imaginary drift measurement deviation, since the applied rules from both methods, are not suitable for an exponential drift. If the measurement is taken over more periods the correction of the imaginary part becomes better. Due to the additional periods, the linear drift correction in the time-domain $Y_{td}$ as well as in the frequency-domain $Y_{fdlin4}$ would be then able to approximate the exponential drift by several linear

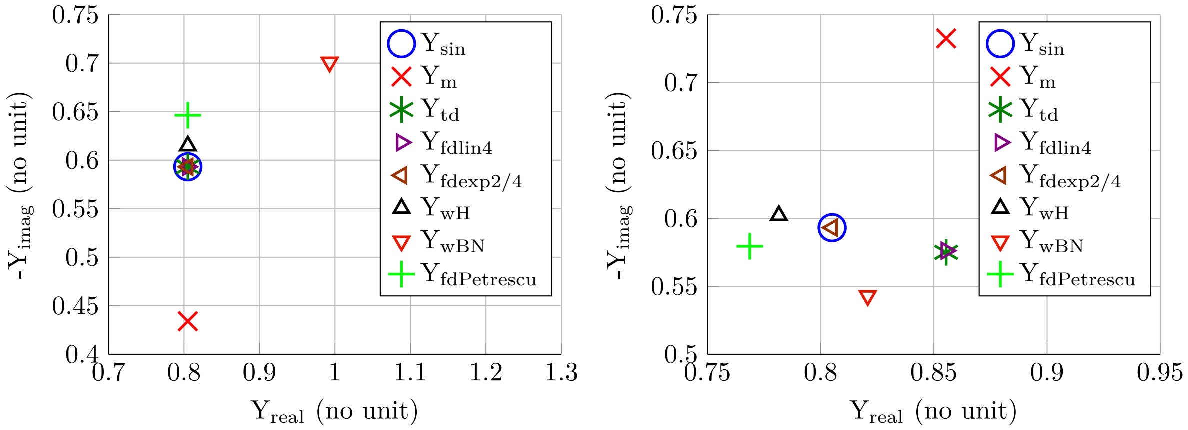

(a) Correction comparison of a linear drift containing 2 periods (signal from figure 4.9a with a linear drift stretched out over 2 periods).

(b) Correction comparison of an exponential drift containing 2 periods (signal from figure 4.9a with the exponential drift stretched out over 2 periods).

Figure 4.10: Correction comparison of an exponential drift (synthetic data).

ones, significantly improving the correction of the imaginary part. However, the real part would still not be corrected as these two methods are not operating on the real part.

The exponential drift correction in the frequency-domain $Y_{fdexp2/4}$ is able to correct the imaginary and the real measurement deviation. Both window functions do make the measurement better but do not suppress the entire deviation. As for the linear drift, Petrescu's method improves the measurement but overcompensates it and leaves it with a quite high measurement deviation.

| $Y_c$ | $Y_{sin} - Y_c$ | | | $Y_m - Y_c$ | | |
|---|---|---|---|---|---|---|
| | $\Delta Y_{real}$ | $\Delta Y_{imag}$ | $\Delta Y$ | $\Delta Y_{real}$ | $\Delta Y_{imag}$ | $\Delta Y$ |
| $Y_{td}$ | 0.0000 | 0.0000 | 0.0000 | 0.0000 | 0.1591 | 0.1591 |
| $Y_{fdlin4}$ | 0.0000 | 0.0000 | 0.0000 | 0.0000 | 0.1591 | 0.1591 |
| $Y_{fdexp2/4}$ | 0.0000 | 0.0000 | 0.0000 | 0.0000 | 0.1591 | 0.1591 |
| $Y_{wH}$ | 0.0000 | 0.0216 | 0.0216 | 0.0000 | 0.1808 | 0.1808 |
| $Y_{wBN}$ | -0.1879 | 0.1077 | 0.2166 | -0.1879 | 0.2668 | 0.3264 |
| $Y_{fdPetrescu}$ | 0.0000 | 0.0531 | 0.0531 | 0.0000 | 0.2122 | 0.2122 |

Table 4.1: Numerical data for the correction comparison of a linear drift from figure 4.10a (corrected signal $Y_c$, $\Delta Y = \sqrt{\Delta Y_{real}^2 + \Delta Y_{imag}^2}$).

| $Y_c$ | $Y_{sin} - Y_c$ | | | $Y_m - Y_c$ | | |
|---|---|---|---|---|---|---|
| | $\Delta Y_{real}$ | $\Delta Y_{imag}$ | $\Delta Y$ | $\Delta Y_{real}$ | $\Delta Y_{imag}$ | $\Delta Y$ |
| $Y_{td}$ | -0.0504 | -0.0182 | 0.0535 | 0.0000 | -0.1574 | 0.1574 |
| $Y_{fdlin4}$ | -0.0504 | -0.0169 | 0.0531 | 0.0000 | -0.1562 | 0.1562 |
| $Y_{fdexp2/4}$ | 0.0000 | 0.0000 | 0.0000 | 0.0504 | -0.1392 | 0.1481 |
| $Y_{wH}$ | 0.0235 | 0.0089 | 0.0251 | 0.0739 | -0.1303 | 0.1498 |
| $Y_{wBN}$ | -0.0157 | -0.0501 | 0.0525 | 0.0346 | -0.1894 | 0.1925 |
| $Y_{fdPetrescu}$ | 0.0364 | -0.0137 | 0.0389 | 0.0867 | -0.1530 | 0.1759 |

Table 4.2: Numerical data for the correction comparison of an exponential drift from figure 4.10b (corrected signal $Y_c$, $\Delta Y = \sqrt{\Delta Y_{real}^2 + \Delta Y_{imag}^2}$).

Up to now only the correction for one signal at one frequency was compared. The impedance is a ratio of two signals, taken at several frequencies. Figure 4.11 shows a sinus-sweep measurement performed with a cylindrical Lithium Nickel Cobalt Aluminum Oxide ($\text{LiNiCoAlO}_2$) (NCA) cell and the Bio-Logic SP300 [14] with an additional constant discharging current of 1 A. Because of this constant current, the voltage experienced a drift.

The $Z_{ref}$ curve was measured immediately afterwards with the same settings except the constant discharge current. The current and voltage were measured additionally with a high resolution data acquisition system (DEWEsoft®). The DFT on the externally measured data resulted in the impedance $Z_m$, for which almost every frequency is distorted. The Bio-Logic SP300 measured $Z_{bio}$ without the drift correction box checked in their software. The better shape of the curve suggests that some kind of correction mechanisms are still applied by the instrument. However, once the sinus-sweep measurement enters frequencies below 1 Hz the impedance values remain wrongly at the local minima. The time-domain drift correction $Z_{td}$ is able to redraw the diffusion branch but the curve is not smooth and 'jumps' from one frequency to the other. Lastly, the frequency-domain exponential drift correction $Z_{fdexp2/4}$ is able to correct the measurement deviations. But also for this method some 'jumps' are visible.

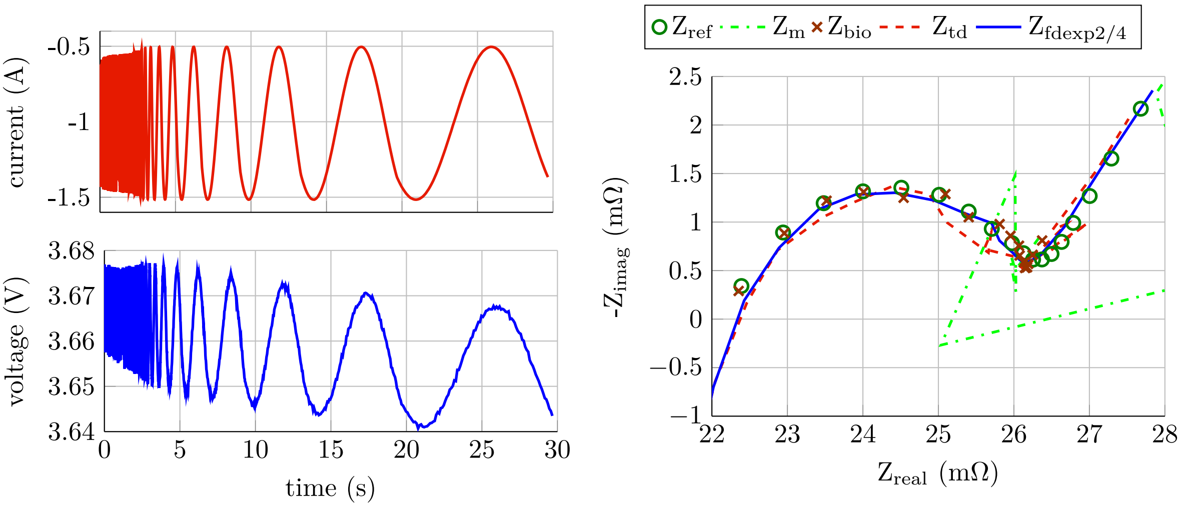

(a) Current (top) and voltage (bottom).

(b) Nyquist plot.

Figure 4.11: Comparison of different correction methods on a EIS sinus-sweep measurement (cylindrical NCA cell A.4).

**Section Conclusion**

*This section discussed various ways of correcting a drift in an electrochemical impedance spectroscopy measurement. It focused on voltage drifts and not on drifts in the state of the battery. For the voltage drift it compared three methods: time-domain correction, windowing and frequency-domain correction. It introduced a new method in the frequency-domain. this method takes advantage of the information that can be derived from harmonics of the measurement frequency. For linear and exponential drifts, there are fixed relationships between the real and imaginary part of the fundamental frequency and its harmonics. For a linear drift, evaluating one harmonic is sufficient, because a linear drift has only one variable: the slope. For an exponential drift two harmonics are necessary, since an exponential drift* $y = A \cdot e^{-t/\tau}$ *has two variables: the time constant in the exponent and the constant factor before the exponent. Using a peculiarity, the computational effort of the linear drift correction can be reduced to a quarter of a full Fourier transformation: only the imaginary part has to be evaluated until half the frequency and can then be multiplied by two. The variables themselves, although possible, do not need to be calculated. Only the ratios between the harmonics are important. When applying the exponential drift rules, it already incorporates the linear drift rules, making it therefore unnecessary to identify which kind of drift is present.*

*This method has an advantage especially for on-line electrochemical impedance spectroscopy, where the calculations are done on an embedded controller for which fast memory is scarce. Compared to the linear time-domain drift correction, the embedded controller does not need to store all the measurement data in order to correct it at the end of half the measurement period. It is applicable to a single period impedance measurement and therefore still keeps the time benefit compared to the windowing method for which it is mandatory to record several periods of the measurement frequency.*

## 4.2 Impedance Measurement Deviation Caused by the Parasitic Current Shunt Inductance

Most commercial impedance meters measure the current over a shunt resistance. The voltage drop over the shunt resistance is linear to the current that flows through it. This is an inexpensive way to measure the current. Because of this, an on-line EIS meter would most likely use a shunt resistance to measure current. This section shows how and by which value an measurement deviation is introduced by the parasitic inductance of the current shunt of an impedance meter.

Like all electric and electronic components, shunt resistors have a parasitic behavior. The parasitic behavior that is most dominant for a shunt resistance is its inductance. This becomes most relevant for high frequencies, where the battery can be simplified by an equivalent circuit of the ohmic resistance $R_\Omega$ and the inductance $L_{bat}$. The shunt resistor can be seen as the actual ohmic resistance $R_{sh}$ in series with a parasitic inductance $L_{sh}$. Figure 4.12 shows the simplified equivalent circuits and formula symbols used in this section.

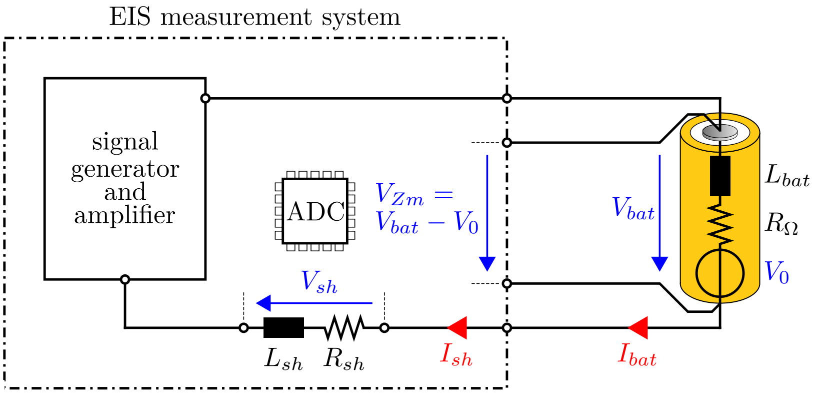

Figure 4.12: Simplified schematic of a EIS meter and simplified equivalent circuit of a battery.

The voltage drop over the shunt is

$$V_{sh} = I_{sh} \cdot (R_{sh} + j \cdot 2\pi f_m \cdot L_{sh})$$

Shunts are usually calibrated with their DC resistance. A constant current is forced through the resistor and the voltage is measured. An amplification factor $G_{sh} = \frac{1}{R_{sh}}$ is determined in this way and stored in the impedance meter. The measured current therefore becomes:

$$I_m = G_{sh} \cdot V_{sh} = \frac{1}{R_{sh}} \cdot V_{sh}$$
$$I_m = I_{sh} \cdot \left(1 + j \cdot 2\pi f_m \cdot \frac{L_{sh}}{R_{sh}}\right)$$

The impedance measurement in galvanostatic mode is performed by driving a current through the battery and measuring the voltage response. In this case the actual current $I_{sh}$, not the measured current $I_m$, flows through the battery:

$$V_{Zm} = I_{sh} \cdot Z_m$$
$$V_{Zm} = I_{sh} \cdot (R_\Omega + j \cdot 2\pi f_m \cdot L_{bat})$$

The impedance is calculated by dividing the voltage response through the current measured over the shunt:

$$Z_m = \frac{V_{Zm}}{I_m} = \frac{V_{Zm,real} + jV_{Zm,imag}}{I_{sh,real} + jI_{sh,imag}} = \frac{I_{sh} \cdot R_\Omega + jI_{sh} \cdot 2\pi f_m \cdot L_{bat}}{I_{sh} + jI_{sh} \cdot 2\pi f_m \cdot \frac{L_{sh}}{R_{sh}}}$$

$$Z_m = \frac{(R_\Omega + j \cdot 2\pi f_m \cdot L_{bat}) \cdot \left(1 - j2\pi f_m \cdot \frac{L_{sh}}{R_{sh}}\right)}{1 + 4\pi^2 {f_m}^2 \cdot \frac{L_{sh}^2}{R_{sh}^2}}$$

$$Z_m = \underbrace{\frac{R_\Omega + 4\pi^2 {f_m}^2 \cdot L_{bat} \cdot \frac{L_{sh}}{R_{sh}}}{1 + 4\pi^2 {f_m}^2 \cdot \frac{L_{sh}^2}{R_{sh}^2}}}_{Z_{m,real}} + j \underbrace{\frac{2\pi f_m \cdot \left(L_{bat} - R_\Omega \cdot \frac{L_{sh}}{R_{sh}}\right)}{1 + 4\pi^2 {f_m}^2 \cdot \frac{L_{sh}^2}{R_{sh}^2}}}_{Z_{m,imag}} \tag{4.40}$$

In equation 4.40 $I_{sh}$ disappears and only battery and shunt variables remain. Equation 4.40 shows that the real part of the measured impedance increases at higher frequencies and moves towards $\frac{L_{bat}}{L_{sh}} \cdot R_{sh}$. It increases more rapidly the larger the ratio $\frac{L_{bat}}{R_\Omega}$ is compared to the ratio $\frac{L_{sh}}{R_{sh}}$. The imaginary part of the measured impedance decreases with higher frequencies and moves towards zero. The measured impedance is positive, if $\frac{L_{bat}}{R_\Omega} > \frac{L_{sh}}{R_{sh}}$, is negative, if $\frac{L_{bat}}{R_\Omega} < \frac{L_{sh}}{R_{sh}}$, and zero, if $\frac{L_{bat}}{R_\Omega} = \frac{L_{sh}}{R_{sh}}$ independent from the measurement frequency.

For the relative deviation, the dependencies on frequency are again different. Figure 4.13 shows the measurement deviation for the real and the imaginary part for the battery parameters of a cylindrical LFP cell (A.1) and various values of $\frac{L_{sh}}{R_{sh}}$.

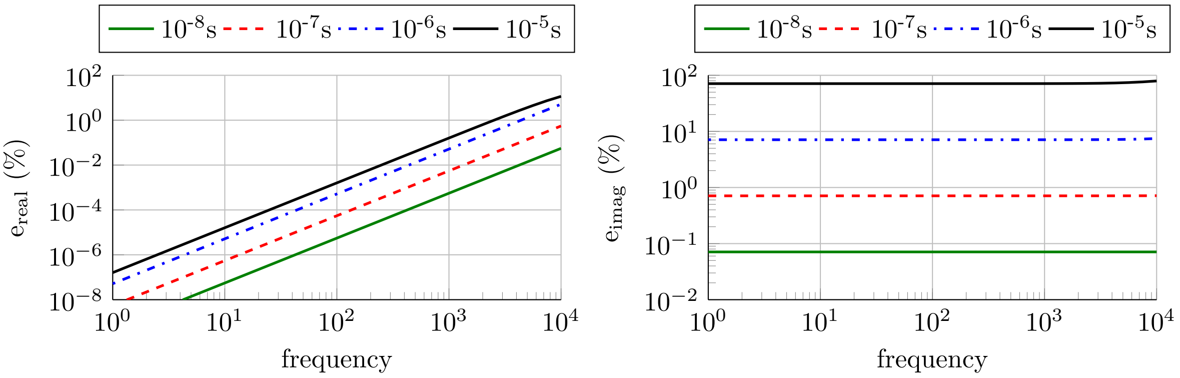

(a) Real part.

(b) Imaginary part.

Figure 4.13: Measurement deviation from parasitic shunt impedance for different values of $\frac{L_{sh}}{R_{sh}}$ (battery values from cylindrical LFP cell A.1, $R_\Omega = 16.2\,\mathrm{m\Omega}$, $L_{bat} = 228\,\mathrm{nH}$).

Figure 4.13 shows that the shunt inductance not only affects the imaginary part, but also the real part with increasing frequency. This should be the explanation for the peculiarity that is often seen for the high frequency part of the Nyquist plot. The Nyquist curve ‘twists’ counter-clockwise for higher frequencies. This effect is often referred to as skin effect [56]. Skin effect describes the effect that at high frequencies the current is displaced from the center of a conductor to its surface. However, this effect usually only becomes relevant for frequencies above 10 kHz. Figure 4.14 shows the Nyquist plot of an LFP cell (A.1). At 10 kHz, the ‘twist’ is already noticeable.

The ratio $\frac{L_{sh}}{R_{sh}}$ can be identified by fitting the measurement data, assuming a fixed value for $R_\Omega$ and $L_{bat}$. Figure 4.14 shows the results of the identification process. The minimum real impedance over the spectrum was used as $R_\Omega$ and the battery inductance was calculated from the imaginary part at 50 kHz by $L = \frac{Z_{imag}}{\omega}$. When fitting the real part of equation 4.40 to the measurement data from 3.5 to 25 kHz, the $\frac{L_{sh}}{R_{sh}}$ ratio was identified to be $2.0 \cdot 10^{-6}$ s, which is a value in a reasonable range and reconfirmed by similar values obtained by this fitting process with other battery cell impedances measured with the same current range. With these values the 'twist' can be redrawn with only the equation 4.40, the identified ratio $\frac{L_{sh}}{R_{sh}}$ and the fixed battery parameters $R_\Omega$ and $L_{bat}$. For very high frequencies above 25 kHz, the imaginary part increases in a way equation 4.40 cannot represent. In this frequency range, other parasitic effects in the impedance meter could become relevant or it could be an actual imaginary impedance change of the battery cell.

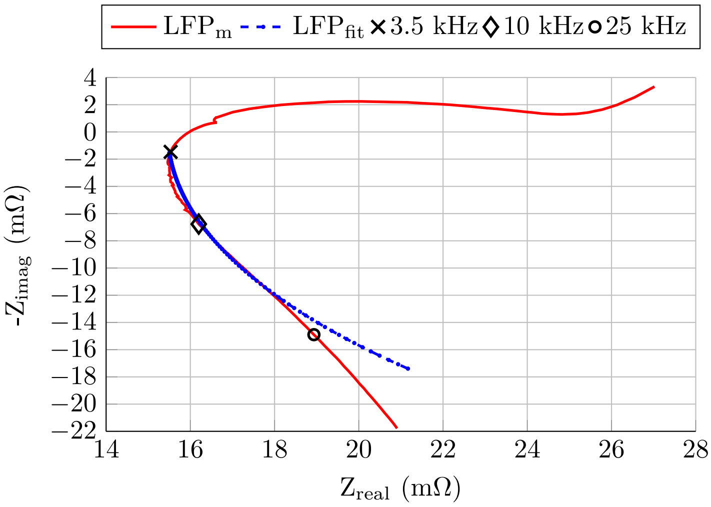

Figure 4.14: Nyquist curve 'twists' counter-clockwise for higher measurement frequencies explained by the parasitic shunt inductance. EIS measurements and fit with equation 4.40 (cylindrical LFP cell A.1, $f_m = 100$ mHz to 50 kHz).

### Section Conclusion

*The measurement deviation introduced by the parasitic inductance of the shunt resistor was derived. The measurement deviation is not only imaginary, but it also affects the real part for higher frequencies. It increases the measured real part and makes the Nyquist curve 'twist' counterclockwise for high frequencies. This explains this peculiarity of the Nyquist plot, often referred to as skin effect.*

## 4.3 Narrowband Distortions Caused by Switched-mode Excitation

### 4.3.1 Harmonics Caused by Switched-mode Excitation

The content of this section has been published in parts in [65].

The most simplest form of a switched-mode amplifier is a half bridge with a low pass filter as shown in figure 4.15. A half bridge is sufficient since the battery can be charged and discharged by switching between the supply voltage $V_{dc}$ higher than the battery voltage and the negative terminal of the battery. This topology can be found in any bidirectional vehicle charger and could therefore serve as a low-cost implementation.

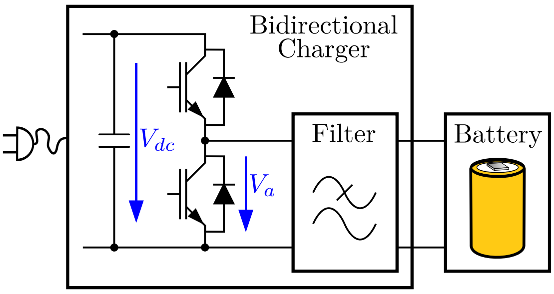

Figure 4.15: Half Bridge for switched mode excitation.

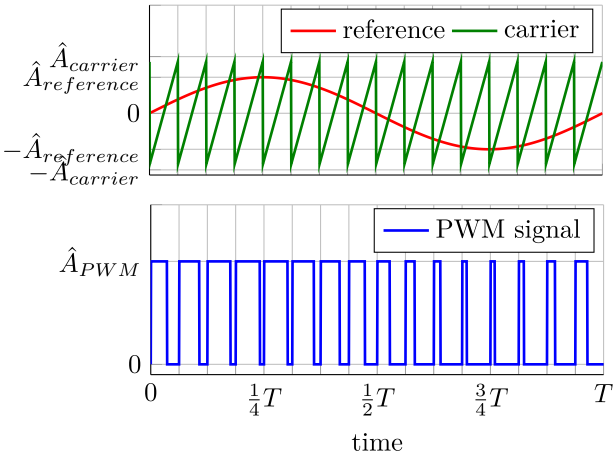

Figure 4.16: Pulse width modulation process with a sawtooth triangle carrier and a sinusoidal reference signal ($M$= 0.7, synthetic data).

In a switched mode amplifier the desired measurement frequency $f_m$ is not directly generated, but modulated onto a carrier frequency $f_c$, which is the switching frequency of the amplifier. For the modulation process the measurement frequency becomes the modulated frequency. Figure 4.16 shows this process. A reference signal is compared to the sawtooth carrier signal. If the reference signal is larger than the carrier signal the pulse-width modulation (PWM) output signal is turned high, which turns on the upper switch of the half bridge. With the modulation process several other frequencies with different amplitudes are present at the output of a non-filtered switched-mode amplifier whose output voltage can be described as follows [50]:

$$\begin{aligned} v_a(t) = &\frac{C_{00}}{2} \\ &+ C_{01}\ e^{j\omega_m t+\theta_m} \\ &+ \sum_{n=2}^{\infty} C_{0n}\ e^{jn(\omega_m t+\theta_m)} \\ &+ \sum_{m=1}^{\infty} C_{m0}\ e^{jm(\omega_c t+\theta_c)} \end{aligned}$$

$$+\sum_{m=1}^{\infty}\sum_{\substack{n=-\infty\\(n\neq 0)}}^{\infty} C_{mn}\, e^{jn(\omega_m t+\theta_m)+jm(\omega_c t+\theta_c)} \tag{4.41}$$

Each line of equation 4.41 corresponds to the respective line of the following list of voltage components:

1. The DC offset
2. The fundamental modulated frequency $\omega_m$
3. Harmonics of the modulated frequency (with $n$ being the baseband harmonics index)
4. The carrier frequency $\omega_c$ and the harmonics of the carrier frequency (with $m$ being the carrier harmonics index)
5. Sidebands of the fundamental frequency around the carrier frequency and the harmonics of the carrier frequency (with $m$ being the carrier harmonics index and $n$ being the sideband harmonics index)

Figure 4.17 shows these components for a $\frac{\omega_c}{\omega_m}$ - ratio of 16 and a modulation index of $M = 0.10$. The modulation index is defined as the ration of the actual mean output voltage to the maximum possible output voltage $M = \frac{\overline{V_a}}{V_{dc}}$. This results in a THD value of 13.7 which means that the geometric sum of all harmonic amplitudes is 13.7 times higher than the amplitude of the measurement frequency (see equation 4.42).

$$THD = \frac{\sqrt{\sum_{n=2}^{\infty} C_{0n}^2 + \sum_{m=1}^{\infty}\sum_{n=-\infty}^{\infty} C_{mn}^2}}{C_{01}} \tag{4.42}$$

Although a high value, it is not surprising since the modulation index is very low with $M = 0.10$. Such a small modulation index is necessary due to the small current which is needed for an EIS measurement and the capability of delivering very high currents for a typical half bridge of a bidirectional vehicle charger.

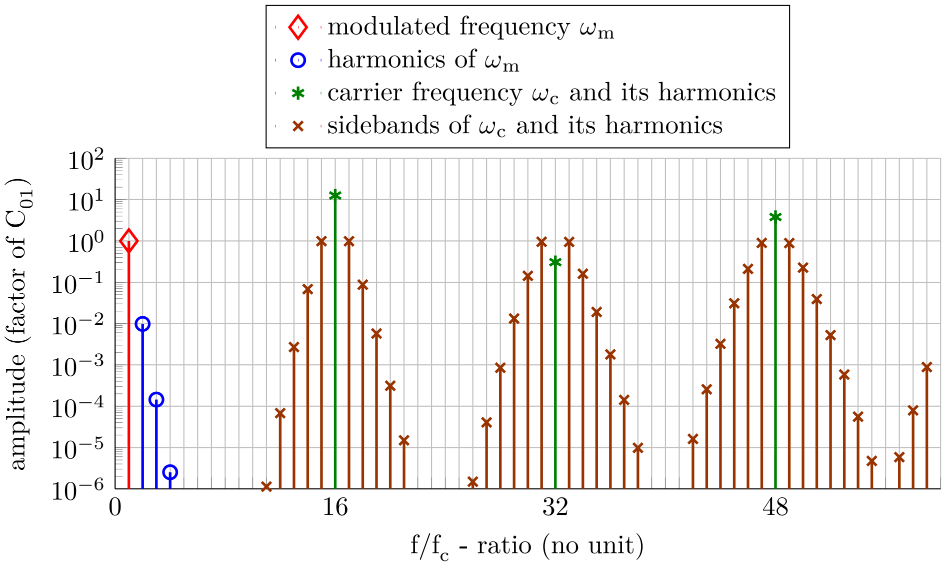

Figure 4.17: Fundamental, harmonics and sidebands of a sawtooth trailing edge pulse width modulation process ($\frac{\omega_c}{\omega_m} = 16$ and $M = 0.10$, synthetic data).

### 4.3.2 Impedance Measurement Deviation Caused by Narrowband Distortions

This section will provide an answer to the question why the narrowband distortions described in the previous section can cause deviations for an on-line impedance measurement and how critical this deviation is. Narrowband distortions become a source of measurement deviation when they are beyond the Nyquist theorem frequency of half the sampling frequency $f_s$. An ADC with a high horizontal resolution, i.e. a high sampling frequency, would solve this. However, for an EIS measurement an ADC with a high vertical resolution, i.e. a low number for the ‘voltage per bit’ resolution, is required due to the small voltage amplitudes. In the design of an ADC vertical and horizontal resolution can be traded against each other. In the case of a Sigma-Delta-ADC these two values can sometimes even be traded against each other by the final application engineer. In an on-line EIS system the sampling frequency will most likely be just a few factors above the highest measurement frequency because of the desire of a high vertical resolution and because higher resolution costs more. Because of this, the sampling frequency $f_s$ would only be 2 to 10 times higher than the maximum measurement frequency. The same is true for the switching frequency. High switching frequencies are most beneficial if the control loop is also very fast. High switching frequencies also increase the losses inside the electronic switch which increases the effort to cool it. Fast control loops and effective cooling systems are costly and therefore the switching frequency is kept rather low at around 5 to 20 times the maximum measurement frequency. When they are sampled they fold back into the measurement frequency range. If they fall to one of the bins of a measurement frequency they superposition with the actual signal at that frequency. What makes this case worse is that the harmonics have a different phase than the measurement frequency. Every harmonic can have a different one. Although every single phase can be determined by equations derived in the next sections, for now, they are considered random from $-\pi$ to $+\pi$, since the deviation in this section is determined in general and not for a particular harmonic.

This aliasing effect happens for the current and the voltage. Figure 4.18a shows this case for the voltage response. It shows the actual voltage response $V_{Z0\,f_m}$ at the measurement frequency (here 1 kHz), the voltage response at the harmonic frequency $V_{Z0\,f_h}$ (here 16 kHz), which cannot be resolved as shown in the figure since the sampling frequency only measures at the blue crosses ($f_s = 5\,\text{kSPS}$). The resulting voltage measurement $V_{Zm}$ is the result of this superposition. Figure 4.18b shows this in the complex plane. The harmonic evaluated at the measurement frequency $V_{Z0}{}^{a}_{f_h}$ is like an additional phasor which displaces the actual voltage response $V_{Z0\,f_m}$ to a measured voltage response $V_{Zm}$ which is distorted in modulus and phase.

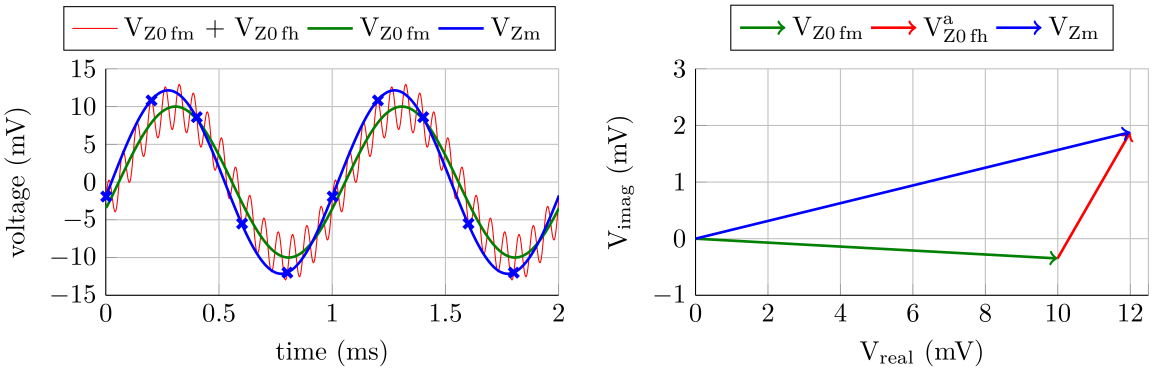

(a) Time-domain representation.

(b) Complex plane representation.

Figure 4.18: Aliasing of an impedance response from a frequency $f_h$ higher than the Nyquist theorem to the measurement frequency $f_m$ (synthetic data).

The result is not only the weighted average of two impedance responses at different frequencies. It is even more distorted by the difference in phase of the current at the measurement frequency and the current at the harmonic frequency (see equation 4.43).

$$Z_m = \frac{\mathbf{V_{Z0}}_{f_m} + \mathbf{V_{Z0}}_{f_h}}{\mathbf{I_m}_{f_m} + \mathbf{I_m}_{f_h}} = \frac{\hat{V}_{Z0\,f_m} \cdot e^{j\phi_{V\,f_m}} + \hat{V}_{Z0\,f_h} \cdot e^{j\phi_{V\,f_h}}}{\hat{I}_{m\,f_m} \cdot e^{j\phi_{I\,f_m}} + \hat{I}_{m\,f_h} \cdot e^{j\phi_{I\,f_h}}} \tag{4.43}$$

In order to assess the necessary attenuation for a modulus deviation below 0.1 % and a phase deviation below 0.1 °, equations 4.44 and 4.47 are used.

$$\begin{aligned}
\phi_{Z_m} &= \tan\left(\frac{V_{imag}}{V_{real}}\right) - \tan\left(\frac{I_{imag}}{I_{real}}\right) \\
\phi_{Z_m} &= \tan\left(\frac{\overbrace{\hat{V}_{Z0\,f_m} \cdot \sin(\phi_{V\,f_m}) + \hat{V}_{Z0\,f_h} \cdot \sin(\phi_{V\,f_h})}^{V_{imag}}}{\underbrace{\hat{V}_{Z0\,f_m} \cdot \cos(\phi_{V\,f_m}) + \hat{V}_{Z0\,f_h} \cdot \cos(\phi_{V\,f_h})}_{V_{real}}}\right) \\
&\qquad - \tan\left(\frac{\overbrace{\hat{I}_{m\,f_m} \cdot \sin(\phi_{I\,f_m}) + \hat{I}_{m\,f_h} \cdot \sin(\phi_{I\,f_h})}^{I_{imag}}}{\underbrace{\hat{I}_{m\,f_m} \cdot \cos(\phi_{I\,f_m}) + \hat{I}_{m\,f_h} \cdot \cos(\phi_{I\,f_h})}_{I_{real}}}\right)
\end{aligned} \tag{4.44}$$

$$|Z_m| = \frac{\sqrt{V_{real}^2 + V_{imag}^2}}{\sqrt{I_{real}^2 + I_{imag}^2}} \tag{4.45}$$

$$\begin{aligned}
\sqrt{V_{real}^2 + V_{imag}^2} &= \Big(\hat{V}_{Z0}{}^2_{f_m} \underbrace{\cos^2(\phi_{V\,f_m})}_{=\frac{1}{2}(1+\cos\phi_{V\,f_m})\text{ with C.5}} + \hat{V}_{Z0}{}^2_{f_h} \underbrace{\cos^2(\phi_{V\,f_h})}_{=\frac{1}{2}(1+\cos\phi_{V\,f_h})\text{ with C.5}} \\
&+ 2\hat{V}_{Z0\,f_m}\hat{V}_{Z0\,f_h} \cdot \underbrace{\cos(\phi_{V\,f_m}) \cdot \cos(\phi_{V\,f_h})}_{\cos(\phi_{V\,f_m}+\phi_{V\,f_h})+\sin(\phi_{V\,f_m})\cdot\sin(\phi_{V\,f_h})\text{ with C.2}} \\
&+ \hat{V}_{Z0}{}^2_{f_m} \underbrace{\sin^2(\phi_{V\,f_m})}_{=\frac{1}{2}(1-\cos\phi_{V\,f_m})\text{ with C.4}} + \hat{V}_{Z0}{}^2_{f_h} \underbrace{\sin^2(\phi_{V\,f_h})}_{=\frac{1}{2}(1-\cos\phi_{V\,f_h})\text{ with C.4}} \\
&+ 2\hat{V}_{Z0\,f_m}\hat{V}_{Z0\,f_h} \cdot \underbrace{\sin(\phi_{V\,f_m}) \cdot \sin(\phi_{V\,f_h})}_{-\cos(\phi_{V\,f_m}+\phi_{V\,f_h})-\cos(\phi_{V\,f_m})\cdot\cos(\phi_{V\,f_h})\text{ with C.2}} \Big)^{\frac{1}{2}} \\
&= \Big(\frac{1}{2}\hat{V}_{Z0}{}^2_{f_m} + \frac{1}{2}\hat{V}_{Z0}{}^2_{f_h} + \frac{1}{2}\hat{V}_{Z0}{}^2_{f_m} + \frac{1}{2}\hat{V}_{Z0}{}^2_{f_h} \\
&+ 2\hat{V}_{Z0\,f_m}\hat{V}_{Z0\,f_h} \cdot \underbrace{[\sin(\phi_{V\,f_m}) \cdot \sin(\phi_{V\,f_h}) - \cos(\phi_{V\,f_m}) \cdot \cos(\phi_{V\,f_h})]}_{=-\cos(\phi_{V\,f_m}+\phi_{V\,f_h})}\Big)^{\frac{1}{2}}
\end{aligned} \tag{4.46}$$

Deriving $\sqrt{I_{real}^2 + I_{imag}^2}$ is done in the same way as deriving $\sqrt{V_{real}^2 + V_{imag}^2}$.

$$|Z_m| = \sqrt{\frac{(\hat{V}_{Z0\,f_m})^2 + (\hat{V}_{Z0\,f_h})^2 - 2\hat{V}_{Z0\,f_m}\hat{V}_{Z0\,f_h} \cdot cos(\overbrace{\phi_{V\,f_m} + \phi_{V\,f_h}}^{2\cdot\phi_{I\,f_m}+\phi_{Z\,f_m}+\phi_{f\,h}+\phi_{Z\,f_h}})}{(\hat{I}_{m\,f_m})^2 + (\hat{I}_{m\,f_h})^2 - 2\hat{I}_{m\,f_m}\hat{I}_{m\,f_h} \cdot cos(\underbrace{\phi_{I\,f_m} + \phi_{I\,f_h}}_{2\cdot\phi_{I\,f_m}+\phi_{f\,h}})}} \tag{4.47}$$

Since these equations are too complex and have too many variables, the phases are set to typical values of a li-ion battery cell and the impedance moduli are normalized and set to the same value:

$$\phi_{Z0f_m} = -10\,^\circ \tag{4.48}$$

$$\phi_{Z0f_h} = 30\,^\circ \tag{4.49}$$

$$|Z_{0f_m}| = 1\,\Omega \tag{4.50}$$

$$|Z_{0f_h}| = 1\,\Omega \tag{4.51}$$

$$\phi_{If_m} = 0\,^\circ \tag{4.52}$$

$$\hat{I}_{mf_m} = 1\,\mathrm{A} \tag{4.53}$$

The variables that are left are the random phase $\phi_{fh}$ and the ratio of the magnitude of the current at the harmonic frequency to the one at the measurement frequency $A_{fh}$.

$$\phi_{fh} = \phi_{If_h} \tag{4.54}$$

$$A_{fh} = \frac{\hat{I}_{mf_h}}{\hat{I}_{mf_m}} \tag{4.55}$$

Figure 4.19a and 4.19b show the modulus and the phase deviation respectively dependent on these two variables. The maximum and the minimum are not around 0 ° or 180 ° plus or minus the impedance phases, because at these angles the voltage and the current would increase or decrease both simultaneously. A simultaneous change of both, voltage and current, does not change the impedance modulus. The phase deviation threshold of 0.1 ° is met with an attenuation $A_{f_h}$ of around $2 \cdot 10^{-3}$ for any value of the phase $\phi_{fh}$. When the harmonic is over ten times as high as in figure 4.17 of section 4.3.1, the attenuation of this harmonic would need to be around 74 dB in order to not cause any deviation higher than the defined threshold. With that attenuation $A_{fh}$ also the modulus deviation threshold of 0.1 % is met for any value of the phase $\phi_{fh}$.

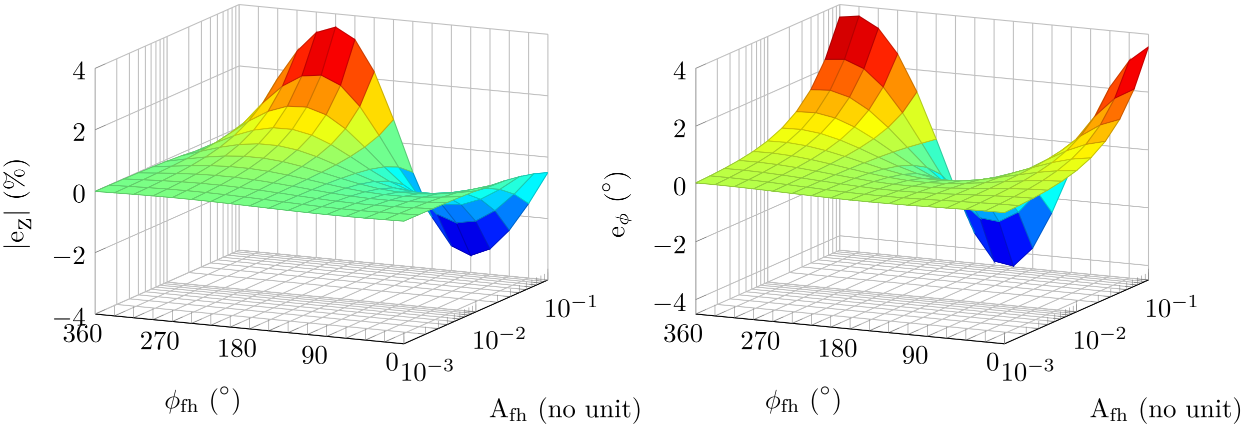

(a) Modulus deviation.

(b) Phase deviation.

Figure 4.19: Modulus and phase deviation of the measurement frequency according to equation 4.47 and 4.44 depending on the phase $\phi_{fh}$ and modulus $A_{fh}$ of the higher frequency harmonic $f_h$ (synthetic data).

### 4.3.3 Topologies for On-line Electrochemical Impedance Spectroscopy Implementation

The content of this section has been published in parts in [65] and [67] and was developed during the supervision of the Master Thesis of Riebel [95].

In a real-world application, a battery is often surrounded by power electronic circuits as shown in figure 4.20. A charger charges the battery if the user deems the SoC too low. Manufacturing tolerances and different operating conditions like different ambient temperatures cause the batteries to age differently and also to show different self-discharge rates. A balancing circuitry helps to keep the battery cells at the same SoC. In its most basic form, the balancing circuitry consists of a switch and a resistor. A lot of devices need a fixed voltage. DC/DC converters stabilize the voltage of a battery which otherwise would change with its SoC.

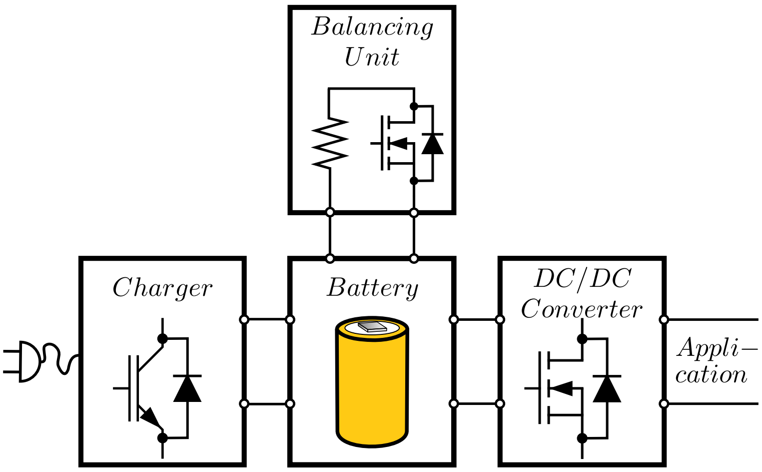

Figure 4.20: Topologies for stimulus generation: ‘Battery Charger Topology’, ‘Balancing Unit Topology’ and ‘DC Supply Topology’.

All these power electronic components can generate the stimulus current for an impedance spectroscopy on the battery cells. Due to the applied switching process none of these topologies generate a perfect sinusoidal current, but generate additional harmonics which vary in magnitude and phase. Additionally, these components come with DC-link capacitors, inductors and output capacitors which attenuate the harmonics but also the measurement frequency.

According to the characteristic harmonics and the effective filter, the different implementation approaches are separated into three categories and named according to the device which is used: ‘Battery Charger Topology’, ‘Balancing Unit Topology’ and ‘DC Supply Topology’.

The Battery Charger Topology and the DC Supply Topology can benefit from the fact that around a hundred cells are connected in series. The excitation current for these batteries only has to be generated once on the whole pack level and then passes through all the cells in series. For safety reasons the battery management system always measures the cell voltage of each individual cell in series and the pack current. With the excitation current and the voltage response the complex impedance can be calculated. Cells in parallel have to be considered as one large cell.

The maximum frequency measured should be 1 kHz for large format batteries used in battery packs, above that frequency the battery behaves purely inductive and not much information can be derived from the measurement. The switching frequency of most high voltage inverters is around 4 to 8 kHz. The Insulated Gate Bipolar Transistors (IGBTs) used in these inverters can be switched at a much higher frequency when they are operated below their rated current [110]. Since usually only a fraction of the rated current of the power converters and chargers is needed for an EIS measurement it can be assumed that the switching frequency could be set well above 10 kHz at limited current.

The disadvantages of this kind of amplifier are similar to the comparison of switched mode power supplys (SMPSs) to linear regulators. Just as a SMPS, the switched-mode amplifier is much more efficient as its linear counterpart at the cost of a higher output current ripple and a lower output voltage accuracy. At a first glance this low accuracy seems to make this type of implementation undesirable. For a continuous measurement of the battery impedance, very accurate measurements have to be achieved, since changes in the battery impedance occur very slowly. For on-line EIS being a valuable instrument these changes have to be identified at a very early stage. The introduction of Class D amplifiers in audio applications show that switched-mode amplifiers can be at the same time efficient and highly accurate. But the way they operate and especially the disturbance they generate has to be well understood in order to use it for EIS.

Knowledge of the effective filter is important when designing the EIS system in order to make sure that the measurement frequencies can pass through but harmonics which occur due to the switching process are attenuated as much as possible. A detailed knowledge of the generated harmonics allows to estimate how much the battery will heat up and therefore change its temperature during the measurement. This is necessary in order to assess the validity of the EIS measurement.

#### 4.3.3.1 Charger Topology

The battery in this topology is at the output of an AC/DC converter. This converter first rectifies the alternating voltage of the grid to a constant DC-link voltage at its input and then converts the DC-link voltage down to the voltage of the battery with a buck converter at its output. In order to perform EIS with no constant current, the output stage has to be bidirectional and therefore consist of a half-bridge as shown in figure 4.21.

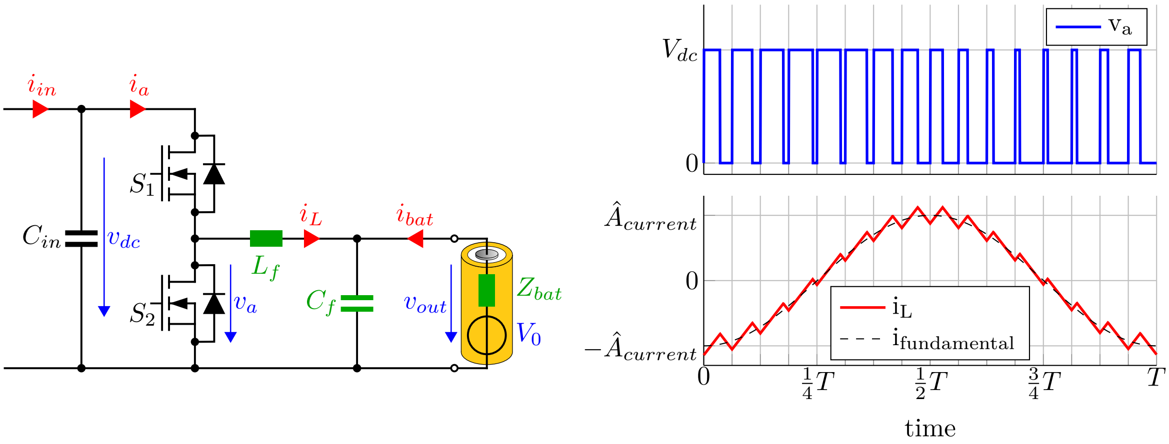

(a) Schematic.

(b) Voltage and current (synthetic data).

Figure 4.21: Battery Charger Topology.

The input stage of the AC/DC converter has to be bidirectional, by replacing the rectifying diodes with switches, or the DC-link capacitor has to be large enough to accommodate the energy that comes from the battery during the discharging half-sine wave. Depernet et al. [31], Nguyen et al. [81] and Koch and Jossen [65] published tests using that topology.

The desired measurement frequency is modulated onto a carrier frequency with the switches of the output half-bridge. Afterwards, an output filter smooths the generated pulse train signal. In its simplest form it consists only of the output choke. Koch et al. has shown in [68] that due to the intrinsic inductive behavior of every battery cell, it is best to use an LC-Filter in order to attenuate frequencies outside the measurement frequency band.

The amplitude of each of the components can be determined either by simulation or analytically. The analytical method gives a better insight into the interdependencies of the magnitudes of the harmonics to the modulation index $M$, the DC-link voltage and modulation method; and was therefore used. The method of the Double Fourier Integral is used to calculate the amplitude of these harmonic frequencies with algebraic equations. It was first presented by Black [15], applied to power electronic converters by Bowes et al. [19] and extensively explained by Holmes and Lipo in [50] and Holmes and McGrath in [51]. With this method, equation 4.56 to 4.60 for a regular sampled sawtooth trailing edge PWM process can be derived, which show the dependence of the harmonics on $V_{dc}$, the modulated frequency $\omega_m$, the carrier frequency $\omega_c$ and the modulation index $M$.

From Holmes et al. [50]:

$$C_{00} = \frac{V_{dc}}{2} \tag{4.56}$$

$$C_{01} = \frac{V_{dc}}{2} M \tag{4.57}$$

$$C_{0n} = \frac{V_{dc}}{\pi} \frac{\mathcal{J}_n\left(n\frac{\omega_m}{\omega_c}\pi M\right)}{n\frac{\omega_m}{\omega_c}} \cdot \left[\sin\left(n\frac{\pi}{2}\right) - j\cos\left(n\frac{\pi}{2}\right)\right] \tag{4.58}$$

$$C_{m0} = j\frac{V_{dc}}{m\pi}\left[\cos\left(m\pi\right) - \mathcal{J}_0\left(m\pi M\right)\right] \tag{4.59}$$

$$C_{mn} = \frac{V_{dc}}{\pi} \frac{\mathcal{J}_n\left(\left[m + n\frac{\omega_m}{\omega_c}\right]\pi M\right)}{\left[m + n\frac{\omega_m}{\omega_c}\right]} \cdot \left[\sin\left(n\frac{\pi}{2}\right) - j\cos\left(n\frac{\pi}{2}\right)\right] \tag{4.60}$$

With $\mathcal{J}_x$ being the $x^{th}$ Bessel function, $m$ the carrier harmonics index and $n$ the baseband and sideband harmonics index. For this calculation a $V_{dc}$ with a double output voltage was assumed. The influence of a different DC-link voltage will be further discussed in section 4.3.4. Table 4.3 compares the theoretical values and the experimental values of the total harmonic distortion and of single frequency magnitudes.

Figure 4.22 shows the time and frequency-domain signals of a Battery Charger Topology with a LC-Filter consisting of a 46 $\mu$H choke and a 135 $\mu$F foil capacitor ($f_{3\,\mathrm{dB}} = 2\,\mathrm{kHz}$). The stack used consisted of three cells (cylindrical LCO cell A.3) totaling to an Open-Circuit-Voltage of around $V_{OCV} = 11.5\,\mathrm{V}$. The DC-link voltage $V_{dc}$ was at double the Open-Circuit-Voltage of the stack. For figure 4.22 and table 4.3 the unfiltered signals before the LC-Filter were used in order to measure substantial distortions. For the impedance calculation in figure 4.23 and table 4.4 the filtered signals after the LC-Filter were used.

The experimentally obtained distortion of the half-bridge output voltage is slightly higher than the theoretical values, which is due to the idealized feedback control for the theoretical values. The theoretical battery voltage response disturbance corresponds well with the measured battery current disturbance. But the measured battery voltage disturbance is much higher. This is due to the inductive behavior of the battery at high frequencies and the measured noise that becomes quite significant, since the measured voltage amplitudes are in the range of a few mV.

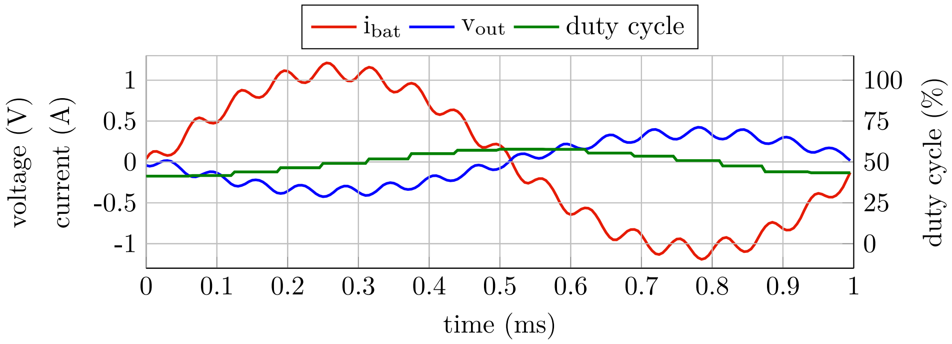

(a) Time-domain signals of $i_{bat}$, $v_{out}$ (without the battery OCV $V_0$) and the corresponding duty cycle (on-time of switch S1 divided by the switching period).

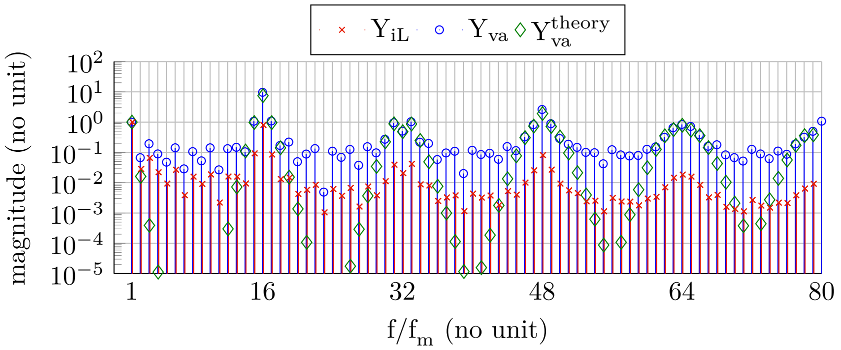

(b) Amplitude spectrum of the unfiltered signals $i_L$, $v_a$ and the theoretical values for $v_a$, normalized to the amplitude of the measurement frequency $C_{01}$.

Figure 4.22: Time-domain and frequency-domain signals for the Battery Charger Topology ($f_m = 1\,\text{kHz}$, $f_c = 16\,\text{kHz}$, measured signals except for $Y_{va}^{theory}$).

| Signal | $THD$ | $HD_2$ | $HD_3$ | $HD_{16}$ | $HD_{32}$ | $HD_{64}$ |
|---|---|---|---|---|---|---|
| $v_{a,\,theory}$ | 8.3817 | 0.0161 | 0.0004 | 7.4966 | 0.4828 | 0.7879 |
| $v_a$ | 10.5343 | 0.0670 | 0.1932 | 9.6601 | 0.5050 | 0.8383 |
| $i_L$ | 0.8264 | 0.0285 | 0.0660 | 0.8027 | 0.0207 | 0.0185 |
| $i_{bat}$ | 0.1079 | 0.0204 | 0.0226 | 0.1005 | 0.0014 | 0.0003 |
| $v_{out,\,theory}$ | 0.1003 | 0.0183 | 0.0002 | 0.0967 | 0.0015 | 0.0006 |
| $v_{out}$ | 0.1984 | 0.0240 | 0.0188 | 0.1914 | 0.0044 | 0.0009 |

Table 4.3: Comparison of the total harmonic distortion and selective normalized harmonic frequency magnitudes for the Battery Charger Topology (values as factors of the measurement frequency amplitude $C_{01}$, measured values except for the ones with index ‘theory’).

Figure 4.23 shows the Nyquist plot of the impedance of three LCO cells (A.3) obtained in the Battery Charger Topology with two successive measurements compared to a measurement taken with the EISmeter $Z_{ref}$, a commercially available impedance meter. Table 4.4 shows the deviation of the impedance measurements.

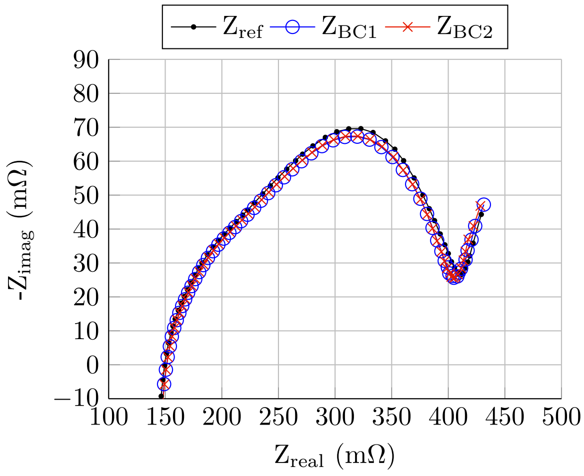

Figure 4.23: Measured Impedance with the Battery Charger Topology ($\hat{I}_m = 200\,\text{mA}$, $f_m = 10\,\text{mHz}$ to $2\,\text{kHz}$, $f_c = 64\,\text{kHz}$) compared to a reference measurement with the EISmeter (1 % accuracy modulus, 1 ° accuracy phase).

| | Modulus | Phase | Impedance | |
|---|---|---|---|---|
| | *max* | *max* | *max* | *mean* |
| | $\left(\left\lvert\frac{\Delta\lvert Z\rvert}{\lvert Z\rvert}\right\rvert\right)$ | $(\lvert\Delta\phi_Z\rvert)$ | $\left(\frac{\lvert\Delta Z\rvert}{\lvert Z\rvert}\right)$ | $\left(\frac{\lvert\Delta Z\rvert}{\lvert Z\rvert}\right)$ |
| | [in %] | [in °] | [in %] | [in %] |
| $(Z_{BC1}, Z_{ref})$ | 2.9282 | 2.2474 | 4.0537 | 2.0233 |
| $(Z_{BC2}, Z_{ref})$ | 3.1007 | 2.1977 | 4.0260 | 2.1496 |
| $(Z_{BC1}, Z_{BC2})$ | 0.7123 | 0.0604 | 0.7124 | 0.2012 |

Table 4.4: Deviation of two successive EIS measurements $Z_{BC1/2}$ measured with the Battery Charger Topology and the reference EIS measurement $Z_{ref}$ (for the first line: $\left\lvert\frac{\Delta\lvert Z\rvert}{\lvert Z\rvert}\right\rvert = \frac{\lvert Z_{ref}\rvert - \lvert Z_{BC1}\rvert}{\lvert Z_{ref}\rvert}$, $\lvert\Delta\phi_Z\rvert = \lvert\phi_{Zref} - \phi_{ZBC1}\rvert$, $\frac{\lvert\Delta Z\rvert}{\lvert Z\rvert} = \frac{\lvert Z_{ref} - Z_{BC1}\rvert}{\lvert Z_{ref}\rvert}$, for the other lines the same logic applies).

### 4.3.3.2 Balancing Unit Topology

Figure 4.24 shows a balancing resistor and a switch, which were originally intended to equilibrate the SoC of the cells in a stack. In this topology, they generate the excitation current.

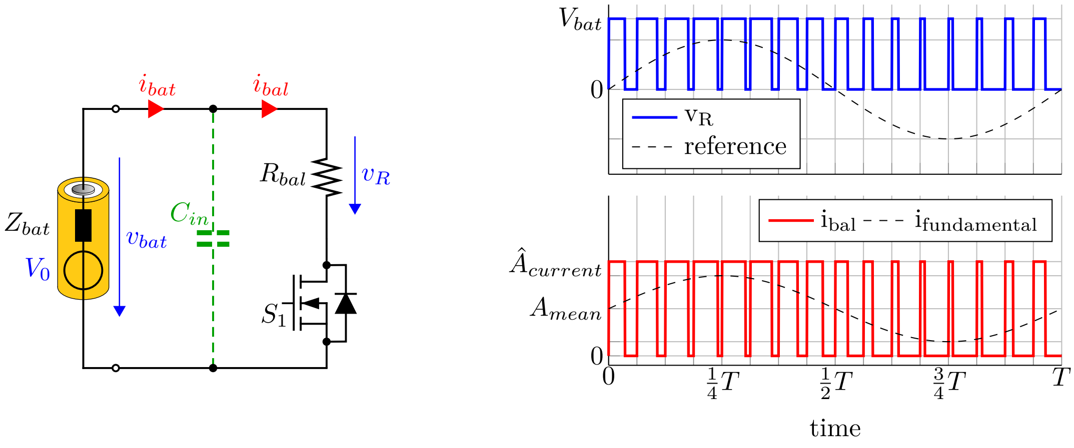

(a) Schematic.

(b) Voltage and current (synthetic data).

Figure 4.24: Balancing Unit Topology.

Since there is usually no filter in place, the battery current is completely pulsed. In the case that the battery is buffered with a capacitor, this would have a filtering effect. The excitation can only occur with a DC-offset, since the balancing resistor can only discharge the battery. Due to this DC-offset, the SoC of the batteries changes after each measurement. There is either the possibility to operate the switch directly with the desired measurement frequency as shown in Figure 4.25 or to modulate the measurement frequency onto a higher carrier frequency as shown in Figure 4.26. The non-modulated signal can be represented as superposition of an infinite series of sinusoidal signals. The mathematical expression of this series can be stated as [6; 55]:

$$V_a = V_{dc}\,\frac{4}{\pi}\sum_{k=1}^{\infty}\frac{\sin\left((2k-1)\omega_m t\right)}{2k-1} \tag{4.61}$$

The harmonics for a modulated signal can be derived from the Double Fourier Integral as done in appendix E.3 by replacing the DC-link voltage $V_{dc}$ with the battery current $I_{bat} = V_{bat}/R_{bal}$:

$$\begin{aligned} i_{bal}(t) = {} & \frac{C_{00}}{2} \\ & + \sum_{n=1}^{2} C_{0n}\; e^{jn(\omega_m t+\theta_m)} \\ & + \sum_{m=1}^{\infty} C_{m0}\; e^{jm(\omega_c t+\theta_c)} \\ & + \sum_{m=1}^{\infty}\sum_{\substack{n=-\infty \\ (n\neq 0)}}^{\infty} C_{mn}\; e^{jn(\omega_m t+\theta_m)+jm(\omega_c t+\theta_c)} \end{aligned} \tag{4.62}$$

$$C_{00} = 2I_{dc} \tag{4.63}$$

$$C_{0n} = \frac{V_{bat}}{R_{bal}}\frac{1}{\left[n\frac{\omega_m}{\omega_c}\right]\pi}\mathcal{J}_n\left(n\frac{\omega_m}{\omega_c}\pi M'\right)\cdot\left[\sin\left(n\frac{\pi}{2}\right) - j\cos\left(n\frac{\pi}{2}\right)\right] \tag{4.64}$$

$$C_{m0} = \frac{V_{bat}}{R_{bal}}\frac{1}{m\pi}\cdot\sin\left(2m\frac{I_{dc}}{I_{bal}}\pi\right) + j\frac{V_{bat}}{R_{bal}}\frac{1}{m\pi}\left(\cos\left(2m\frac{I_{dc}}{I_{bal}}\pi\right) - \mathcal{J}_0\left(m\pi M'\right)\right) \tag{4.65}$$

$$C_{mn} = \frac{V_{bat}}{R_{bal}}\frac{1}{\pi\left[m+n\frac{\omega_m}{\omega_c}\right]}\mathcal{J}_n\left(\pi M'\left[m+n\frac{\omega_m}{\omega_c}\right]\right)\left[\sin\left(n\frac{\pi}{2}\right) - j\cos\left(n\frac{\pi}{2}\right)\right] \tag{4.66}$$

Table 4.5 and table 4.6 compare the theoretical values with the experimental values. The experimentally obtained distortion of the battery current $i_{bat}$ compares well with the theoretical values for both the non-modulated and the modulated signal. For both, the distortion of the battery voltage response is also significantly higher. This again is due to the inductive behavior of the battery at high frequencies and the measured noise.

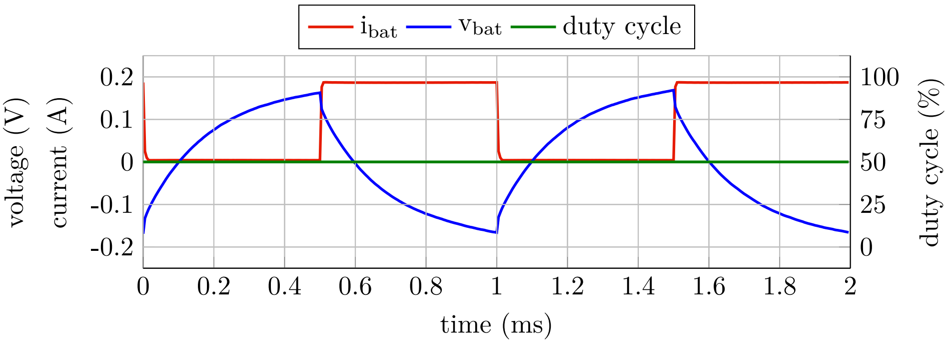

(a) Time-domain signals of $i_{bat}$, $v_{bat}$ (without the battery OCV $V_0$) when excitation current is unmodulated.

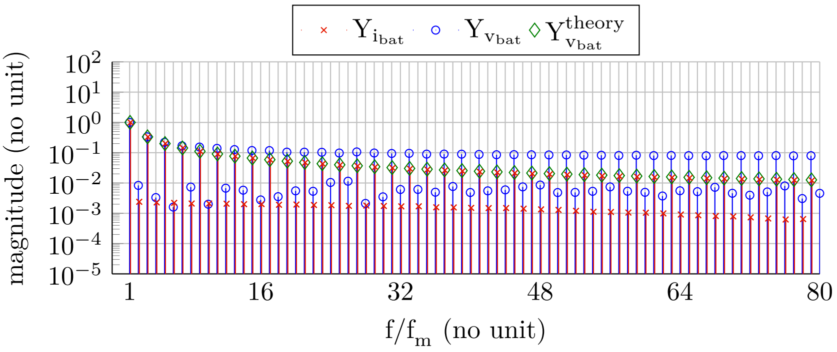

(b) Amplitude spectrum of $i_{bat}$, $v_R$ and theoretical values for $v_R$ normalized to the amplitude of the measurement frequency.

Figure 4.25: Time-domain and frequency-domain signals for the Balancing Unit Topology with a non-modulated duty cycle of 50 % ($f_m$ = 500 Hz, $f_c$ = 8 kHz, measured signals except for $Y_{v_{bat}}^{theory}$).

| | $THD$ | $HD_2$ | $HD_3$ | $HD_{16}$ | $HD_{32}$ | $HD_{64}$ |
|---|---|---|---|---|---|---|
| $i_{bat,\ theory}$ | 0.4834 | 0.0000 | 0.3333 | 0.0000 | 0.0000 | 0.0000 |
| $i_{bat}$ | 0.4767 | 0.0024 | 0.3339 | 0.0020 | 0.0017 | 0.0009 |
| $v_{bat}$ | 0.7236 | 0.0083 | 0.3341 | 0.0028 | 0.0061 | 0.0055 |

Table 4.5: Comparison of the total harmonic distortion and selective normalized harmonic frequency magnitudes of a non-modulated measurement frequency signal in the Balancing Unit Topology (values as factors of the measurement frequency amplitude, $f_m$ = 500 Hz, $f_c$ = 8 kHz, measured values except for the ones with index ‘theory’).

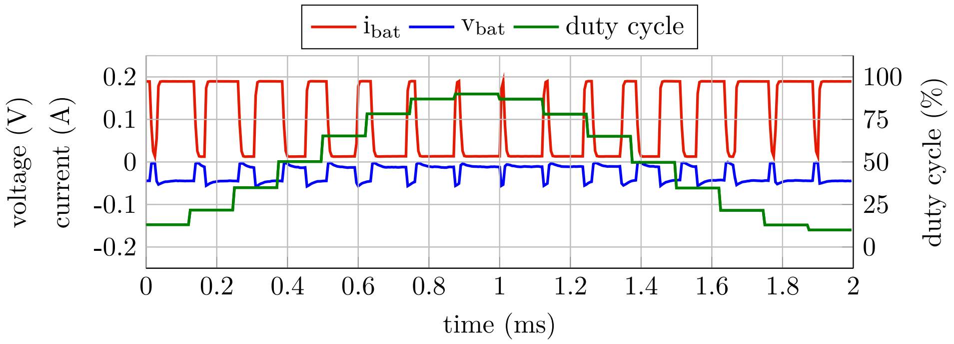

(a) Time-domain signals of $i_{bat}$, $v_{bat}$ (without the battery OCV $V_0$) and the corresponding duty cycle (on-time of switch S1 divided by the switching period).

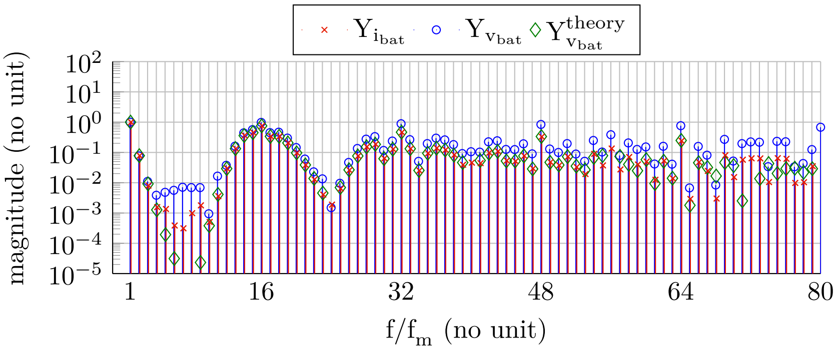

(b) Amplitude spectrum of $i_{bat}$, $v_R$ and theoretical values for $v_R$ normalized to the amplitude of the measurement frequency.

Figure 4.26: Time-domain and frequency-domain signals for the Balancing Unit Topology with a modulated duty cycle ($f_m = 500\,\mathrm{Hz}$, $f_c = 8\,\mathrm{kHz}$, measured signals except for $Y_{v_{bat}}^{theory}$).

| | $THD$ | $HD_2$ | $HD_3$ | $HD_{16}$ | $HD_{32}$ | $HD_{64}$ |
|---|---|---|---|---|---|---|
| $i_{bat,\,theory}$ | 1.3930 | 0.0781 | 0.0092 | 0.7544 | 0.4665 | 0.2490 |
| $i_{bat}$ | 1.3784 | 0.0630 | 0.0717 | 0.7637 | 0.4670 | 0.2456 |
| $v_{bat}$ | 3.8944 | 0.0661 | 0.0865 | 1.4062 | 1.4090 | 1.3162 |

Table 4.6: Total harmonic distortion and selective normalized harmonic frequency magnitudes of a modulated measurement frequency signal in the Balancing Unit Topology (values as factors of the measurement frequency amplitude, $f_m = 500\,\mathrm{Hz}$, $f_c = 8\,\mathrm{kHz}$, measured values except for the ones with index ‘theory’).

Figure 4.27 shows the Nyquist plot of three successive impedance measurements of three LCO cells in series (see appendix A.3) obtained in the Balancing Unit Topology. Three cells in series and treating them as a single cell would not make sense in a real balancing circuit. Also the used measurement current is not in the range of a typical balancing circuit. However, in order to make the measurements comparable with the ones in the Battery Charger Topology and Battery DC-Source Topology the same stack and the same current magnitude was also used for this topology. Section 4.3.3.4 compares the three circuits with each other. Due to the inherent discharge, the SoC changed by 2 % during each measurement. For this reason, the measurements are not compared in a table.

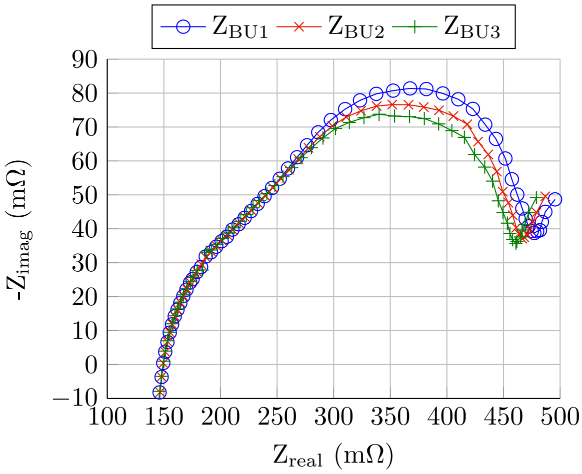

Figure 4.27: Measured Impedance with the Balancing Unit Topology ($\hat{I}_m = 200\,\text{mA}$, $f_m = 10\,\text{mHz}$ to $2\,\text{kHz}$, $f_c = 64\,\text{kHz}$).

#### 4.3.3.3 DC-Supply Topology

Most electronic equipment requires a very stable voltage source over the whole SoC range of the battery. In these cases, the battery supplies a DC/DC converter, which generates a stabilized voltage as shown in figure 4.28a. In order to perform EIS with no DC-offset, the DC/DC converter has to be bidirectional and therefore consist of a half-bridge. In the case of a DC/AC voltage supply a half-bridge is already necessary to produce the alternating current. In the case of a three phase DC/AC converter, the three half-bridges allow to cancel certain harmonics, which leads to a shift of the harmonic frequencies towards higher frequencies by a factor of three. Since the DC/AC converters are based on a similar hardware as the bidirectional DC/DC converter, only the latter is discussed in this section. Howey et al. [52] used this topology in his experiments.

In the Battery Charger Topology of figure 4.21, the current through the battery is continuous. When the current $I_L$ is positive, it increases when the switch S1 is turned on. Besides some higher frequency currents that are attenuated by the filter capacitor $C_f$, the same current runs through the battery. If the switch S1 is turned off, the current freewheels over the diode of S2 and in that way still runs through the battery. The same is the case when $I_L$ is negative and the switch S2 is turned on and off. Therefore a continuous current through the battery is secured.
In the case of the DC Supply Topology of figure 4.28 there is no continuous current through the battery. The current of the battery is interrupted once the switch S1 is turned off. Although the current freewheels over the diode of S2, if S1 is turned off, it only continues to supply the output of the converter. Once S1 is turned on again, the instantaneous current $i_L$, which runs through the

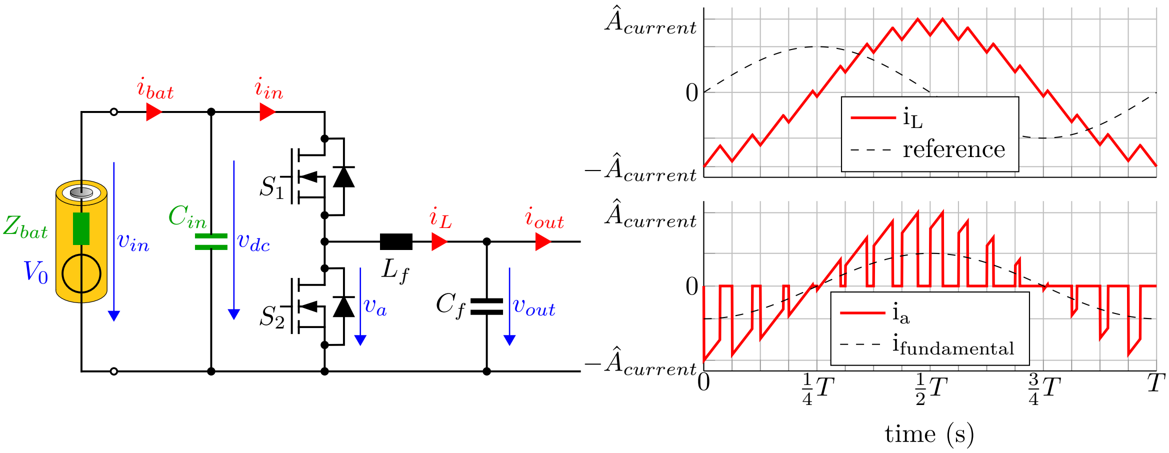

(a) Schematic.

(b) Reference signal, inductor current $i_L$, input current $i_{in}$ and its fundamental (synthetic data).

Figure 4.28: DC Supply Topology.

inductor $L_f$, is drawn from the battery. For the battery, the converter acts as a current source or load that supplies or draws in every switching period the current, which has been set by the PWM controller. Therefore, the current that is supplied and drawn from the battery is a pulsed sinusoidal current, which is chopped into time slices of the switching period. The combination of the capacitor $C_{in}$ and the inner impedance of the battery $Z_{bat}$ act as a filter for the pulsed current and smoothen its shape.
Figure 4.29 shows the current of a three cell stack (cylindrical LCO cell A.3) with a 2 mF input capacitor. The pulsed current as well as the pulsed voltage response of the battery can still be seen.

To calculate the harmonics in the case of a Battery Charger Topology of section 4.3.3.1, it was assumed that the DC-link voltage $V_{dc}$ is turned on and off. In order to calculate the harmonics, which are generated on the input of a DC/DC converter as in the DC Supply Topology, the sinusoidal current that is controlled through the inductance $L_f$ is switched on and off. By replacing the DC-link voltage in the Double Fourier Integral with a sinusoidal current, the generated harmonics can be analytically determined with (for details see appendix E.4):

$$\begin{aligned} i_{in}(t) = {} & \frac{C_{00}}{2} \\ & + \sum_{n=1}^{2} C_{0n}\ e^{jn(\omega_m t+\theta_m)} \\ & + \sum_{m=1}^{\infty} C_{m0}\ e^{jm(\omega_c t+\theta_c)} \\ & + \sum_{m=1}^{\infty} \sum_{\substack{n=-\infty \\ (n\neq 0)}}^{\infty} C_{mn}\ e^{jn(\omega_m t+\theta_m)+jm(\omega_c t+\theta_c)} \end{aligned} \tag{4.67}$$

$$C_{00} = \frac{A_A}{2} \cdot M \tag{4.68}$$

$$C_{01} = \frac{A_A}{2} \tag{4.69}$$

$$C_{02} = \frac{A_A}{4} \cdot M \tag{4.70}$$

$$C_{m0} = \frac{A_A}{m\pi} \mathcal{J}_1(m\pi M) \tag{4.71}$$

$$C_{m(n=-1 \text{ or } +1)} = \frac{A_A}{2\pi m} \left[\sin(m\pi) - j\left(\mathcal{J}_0(m\pi M) - \mathcal{J}_2(m\pi M) - \cos(m\pi)\right)\right] \tag{4.72}$$

$$C_{mn} = -j\frac{A_A}{2\pi m}\left[j^{n+1}\mathcal{J}_{n+1}(m\pi M) + j^{n-1}\mathcal{J}_{n-1}(m\pi M)\right] \qquad \text{for } n \neq -1,\, n \neq 1 \tag{4.73}$$

With $A_A = \frac{M \cdot V_{dc}}{|Z_{load}|}$ being the amplitude of the sinusoidal modulated frequency. Please note that $C_{01}$ is the amplitude of the measurement frequency used for the EIS measurement of the battery. It is only half of the amplitude of the modulated frequency. For these equations, a continuous control circuit was assumed. This usually does not lead to baseband harmonics. However, in this case, there is still a quite high amplitude at the baseband harmonic $C_{02}$.

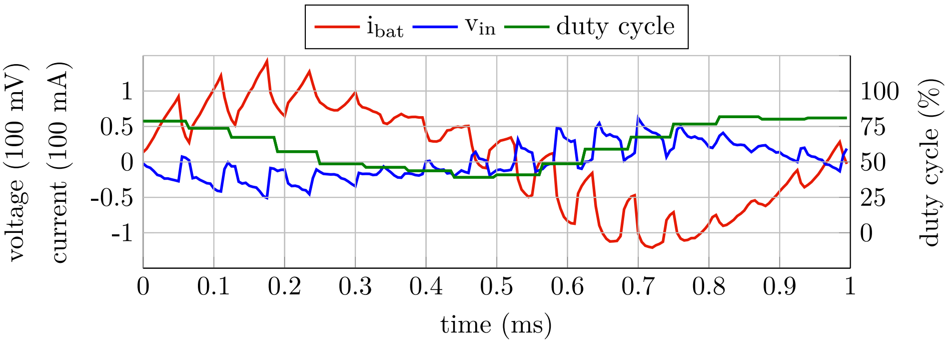

(a) Time-domain signals of $i_{bat}$, $v_{in}$ (without the battery OCV $V_0$) and the corresponding duty cycle (on-time of switch S1 divided by the switching period).

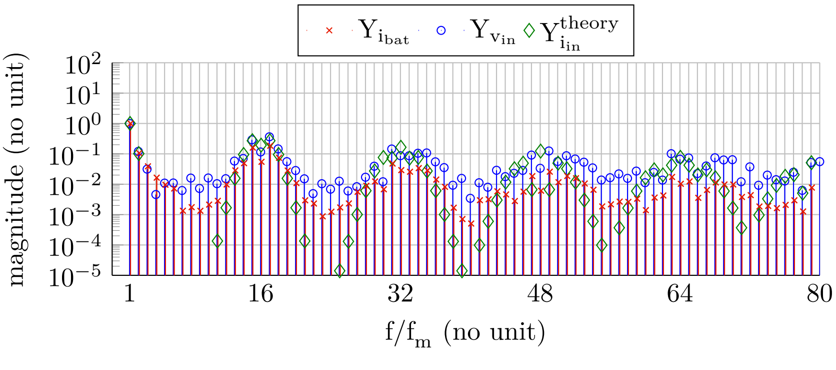

(b) Amplitude spectrum of the filtered signals $i_{bat}$, $v_{in}$ and theoretical values for $i_{in}$ normalized to the amplitude of the measurement frequency $C_{01}$.

Figure 4.29: Time-domain and frequency-domain signals of the battery current $i_{bat}$ and the battery response voltage $v_{in}$ for the DC Supply Topology with 2 mF input capacitor ($f_m = 1\,\text{kHz}$, $f_c = 16\,\text{kHz}$, measured signals except for $Y_{i_{in}}^{theory}$).

Table 4.7 compares the theoretical values with the experimental values. The experimentally obtained distortions of the battery current $i_{bat}$ compare acceptable with the theoretical values. As for the previous topologies, the distortion of the battery voltage response is significantly higher, here as well. This is caused by the inductive behavior of the battery at high frequencies and the measured noise.

| | $THD$ | $HD_2$ | $HD_3$ | $HD_{16}$ | $HD_{32}$ | $HD_{64}$ |
|---|---|---|---|---|---|---|
| $i_{bat,theory}$ | 0.5695 | 0.1017 | 0.0000 | 0.1933 | 0.1647 | 0.0768 |
| $i_{bat}$ | 0.3091 | 0.1058 | 0.0389 | 0.0548 | 0.0291 | 0.0103 |
| $v_{bat}$ | 0.6703 | 0.1208 | 0.0314 | 0.1154 | 0.0869 | 0.0668 |

Table 4.7: Comparison of the total harmonic distortion and selective normalized harmonic frequency magnitudes for the DC Supply Topology (values as factors of the measurement frequency amplitude, $f_m = 1\,\mathrm{kHz}$, $f_c = 16\,\mathrm{kHz}$, measured values except for the ones with index 'theory').

Figure 4.30 shows the Nyquist plot of the impedance of three cells in series (cylindrical LCO cell A.3) obtained in the DC Supply Topology with two successive measurements compared to a measurement taken with the EISmeter. Although the Nyquist plots look very close together table 4.8 shows similar deviations of the impedance measurement as for the Battery Charger Topology. This is because the impedances of every single frequency are compared to each other. The single measurement points deviate from each other but are still on the same Nyquist plot. This gives the impression that the deviation is small.

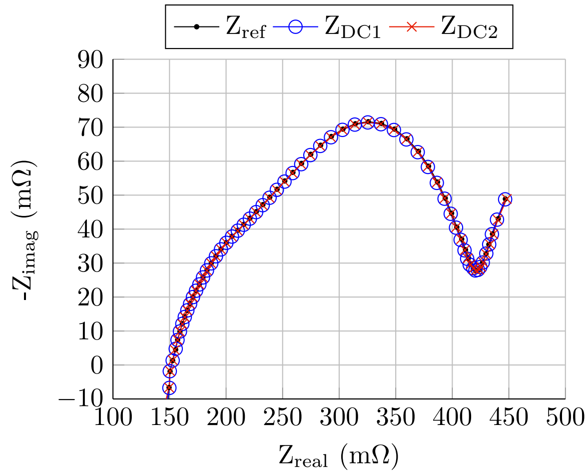

Figure 4.30: Measured Impedance with the DC Supply Topology ($\hat{I}_m = 200\,\mathrm{mA}$, $f_m = 10\,\mathrm{mHz}$ to $2\,\mathrm{kHz}$, $f_c = 64\,\mathrm{kHz}$) compared to a reference measurement with the EISmeter (1 % accuracy modulus, 1 ° accuracy phase).

| | Modulus | Phase | Impedance | |
|---|---|---|---|---|
| | *max* | *max* | *max* | *mean* |
| | $\left(\left\lvert\frac{\Delta\lvert Z\rvert}{\lvert Z\rvert}\right\rvert\right)$ | $(\lvert\Delta\phi_Z\rvert)$ | $\left(\frac{\lvert\Delta Z\rvert}{\lvert Z\rvert}\right)$ | $\left(\frac{\lvert\Delta Z\rvert}{\lvert Z\rvert}\right)$ |
| | [in %] | [in °] | [in %] | [in %] |
| $Z_{DC1}, Z_{ref}$ | 3.5971 | 4.6650 | 8.1642 | 2.6747 |
| $Z_{DC2}, Z_{ref}$ | 3.6117 | 4.2014 | 7.3340 | 2.6493 |
| $Z_{DC1}, Z_{DC2}$ | 0.5103 | 0.4636 | 0.9248 | 0.0826 |

Table 4.8: Deviation of two successive EIS measurements $Z_{DC1/2}$ measured with the DC Supply Topology and the reference EIS measurement $Z_{ref}$ (for the first line: $\left\lvert\frac{\Delta\lvert Z\rvert}{\lvert Z\rvert}\right\rvert = \frac{\lvert Z_{ref}\rvert - \lvert Z_{DC1}\rvert}{\lvert Z_{ref}\rvert}$, $\lvert\Delta\phi_Z\rvert = \lvert\phi_{Zref} - \phi_{ZDC1}\rvert$, $\frac{\lvert\Delta Z\rvert}{\lvert Z\rvert} = \frac{\lvert Z_{ref} - Z_{DC1}\rvert}{\lvert Z_{ref}\rvert}$, for the other lines the same logic applies).

#### 4.3.3.4 Comparison

All of the different implementation approaches come with advantages and disadvantages. The Battery Charger Topology has the most pristine current generation, due to the LC-filter; that forms in combination with the battery inductance, a filter of third order. The DC Supply Topology only forms a filter of second order with its input capacitor and the battery inductance. However, it only has to filter a chopped sinusoidal current, which has much lower harmonics as the chopped DC-link voltage of the Battery Charger Topology. Therefore these topologies almost have similar values. The worst distortion values of the excitation signal has the Balancing Unit Topology since there is no filter in place.

A problematic disadvantage of the Battery Charger Topology and the DC Supply Topology is that if the current is not measured by the BMS, it has to be measured by the charger or DC/DC converter. In that case, the current and voltage need to be transferred and synchronized during the measurement. The Balancing Unit Topology measures current and voltage in one place.

Additionally, the Balancing Unit Topology can generate a different excitation current for each battery cell. It can be optimized according to the current state of the battery cell. The other two topologies only can create one current for the whole stack that will stimulate all the cells equally.

The most important disadvantage of the Balancing Unit Topology is that the excitation current is limited to the balancing current, which is usually not larger than 100 mA. Battery cells and paralleled cells, with combined capacity of more than 10 Ah, often have an inner resistance of less than 10 mΩ and therefore the battery voltage response amplitude is only 1 mV, which requires a very accurate voltage measurement. The Battery Charger Topology and the DC Supply Topology do not have that limitation since they are usually designed for much higher currents.

All topologies suffer from the fact that the components are often unidirectional and only become bidirectional if they are specifically designed for this purpose, with the exception of the Balancing Unit Topology, which is not capable of charging the cell. This disadvantage can be overcome if the charger can communicate with the BMS, which controls the balancing unit. In that case the battery charger can compensate the discharge, which is caused by the balancing unit.

### 4.3.4 Distortion Reduction by Adjusting the DC-link Voltage

The content of this section has been published in parts in [65].

Keeping the DC-link voltage $V_{dc}$ at double the battery voltage provides symmetrical conditions, but it is unnecessary. The required excitation current only needs to provide a voltage response amplitude of a few mV per battery cell. Instead of decreasing the modulation index, the DC-link voltage could also be lowered, making the upper switch of the half-bridge operate at higher duty cycles. This method can be applied to the Battery Charger Topology and the Battery DC-Supply Topology. In this section only the Battery Charger Topology is analyzed in detail. All equations, figures and tables therefore only apply to the Battery Charger Topology and the schematic in figure 4.21. $V_{bat}$ instead of $V_0$ is used for the battery voltage which includes the overvoltages over the complex impedance. From the equations 4.56, 4.57, 4.58, 4.59 and 4.60 only the equations 4.56 and 4.59 need to be adjusted to equation 4.74 and 4.75, since they are the only ones that are affected. Equation 4.74 shows the desired result: The static DC output of the half-bridge is equal to the battery voltage (in equation 4.41 the DC value is only half the value of $C_{00}$). Equation 4.75 describes how the carrier frequency and its harmonics are affected by this change. The amplitude as well as the phase of $C_{m0}$ changes with $\frac{V_{bat}}{V_{dc}}$.

$$C_{00} = 2V_{bat} \tag{4.74}$$

$$\begin{aligned} C_{m0} = {} & \frac{V_{dc}}{m\pi}\left[\sin\left(2\frac{V_{bat}}{V_{dc}}m\pi\right)\right] + j\frac{V_{dc}}{m\pi} \\ & \cdot \left[\cos\left(2\frac{V_{bat}}{V_{dc}}m\pi\right) - \mathcal{J}_0\left(m\pi M\right)\right] \end{aligned} \tag{4.75}$$

The modulation index describes how much the voltage of the measurement frequency varies as a factor of the maximum possible variation and therefore needs to be adjusted with decreasing DC-link voltage. For reasons of clarity, this has not been done. The modulation index is simply limited depending on $V_{dc}$ as in equation 4.76. For the calculation of the harmonics at decreased $V_{dc}$ with equations 4.74, 4.58, 4.75 and 4.60, the same modulation index, if the output could be varied between zero Volt and half of $V_{dc}$, needs to be used.

$$M_{max} = \frac{V_{dc}}{V_{bat}} - 1 \tag{4.76}$$

As an additional benefit, with decreased DC-link voltage, the electronic switches of the half-bridge can be rated at lower blocking voltages. However, the necessary modulation index for the highest battery impedance value, the attenuation of the filter over the whole measurement frequency range, a voltage reserve for dynamic changes of the feedback control system and the minimum off-time of the electronic switches constitute a lower limit for the DC-link voltage.

The overall distortion factor is reduced by a decreased DC-link voltage as shown in figure 4.31. Once the DC-link voltage is chosen, the only way to change the signal amplitude is to alter the modulation index, since usually the DC-link voltage is stabilized with large capacitors that make dynamic changes difficult. Changing the modulation index has great implications on the harmonic distortions. For example, the DC-link voltage is set to be $V_{dc} = 1.2 \cdot V_{bat}$ where a signal of $0.04 \cdot V_{bat}$ can be generated at a THD of around 3. If now a signal of $0.01 \cdot V_{bat}$ needs to be generated, a total harmonic distortion of around 12 occurs. If the DC-link voltage would have been set to $V_{dc} = 1.1 \cdot V_{bat}$, only a THD of 4 would occur. It is therefore beneficial if the output amplitude and the modulation index change as little as possible. This becomes especially important if the DC-link voltage is already very small, since further reductions of the modulation index make the distortions increase very sharply.

Changing the amplitude is necessary due to the changing complex impedance of the battery depending on the frequency as well as the different attenuation of the output low-pass filter. For a li-ion battery at $V_{OCV} = 3\,\mathrm{V}$, generating a signal of $0.04 \cdot V_{bat}$ would generate a 120 mV signal per cell when only a 10 mV signal is needed. Even with taking the attenuation of the low-pass filter into account, this constitutes the upper limit of the signal generated, since Voltage drops over the IGBT switches and resistances that are not part of the battery are tried to be kept as low as possible to increase efficiency. A signal of $0.0025 \cdot V_{bat}$ for a li-ion battery at $V_{OCV} = 4.2\,\mathrm{V}$ would generate a 10.5 mV signal and could be considered as the lower limit of the output amplitude.

To verify the theoretical values, tests were performed on a small stack of three cells in series (cylindrical LCO cell A.3). Each of the cell was at $V_{OCV} = 3.8\,\mathrm{V}$. This corresponds to an SoC of around 50 %.

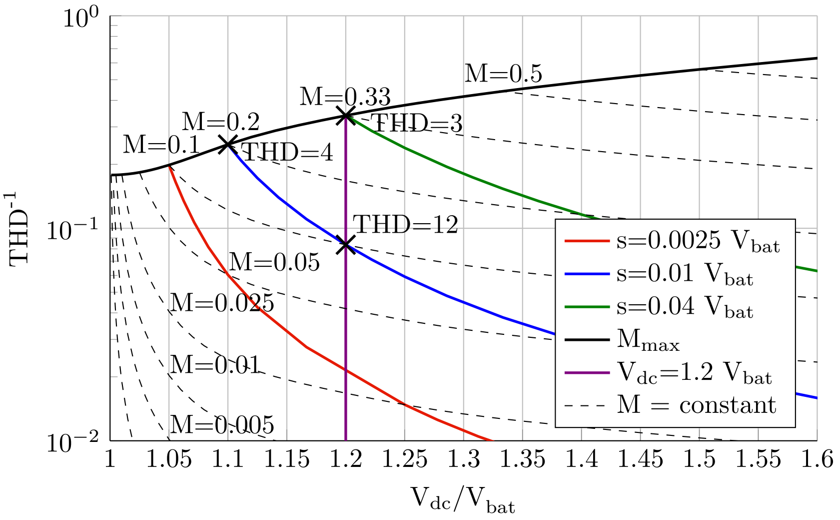

Figure 4.31: Total harmonic distortion depending on the DC-link voltage factor $\frac{V_{dc}}{V_{bat}}$ and signal amplitude $s$.

The DC-link voltage was set to double the stack voltage ($3 \cdot 3.8\,\mathrm{V} \cdot 2 = 22.8\,\mathrm{V}$) and to 1.2 times the stack voltage ($3 \cdot 3.8\,\mathrm{V} \cdot 1.2 = 13.7\,\mathrm{V}$) to test its influence on the generated harmonics.

Table 4.9 shows the theoretical values and experimental results for the total harmonic distortion and the amplitude of the carrier frequency $C_{10}$. Figure 4.32 shows the time-domain and frequency-domain plots of the generated voltages and currents as well as the duty cycle and the used LC-Filter characteristic.

| | | $V_{dc} = 2 \cdot V_{bat}$ | | $V_{dc} = 1.2 \cdot V_{bat}$ | |
|---|---|---|---|---|---|
| | | theory | experiment | theory | experiment |
| $v_a$ | THD (no unit) | 9.29 | 11.8 | 2.50 | 4.92 |
| | $C_{10}$ (no unit) | 8.43 | 11.1 | 1.54 | 3.22 |
| $i_{bat}$ | THD (no unit) | 0.136 | 0.112 | 0.029 | 0.056 |
| | $C_{10}$ (no unit) | 0.136 | 0.110 | 0.025 | 0.031 |

Table 4.9: Comparison of THD and the amplitude of the carrier frequency $C_{10}$ for the Battery Charger Topology switched output voltage $v_a$ and battery current $i_{bat}$ (signal amplitude $s = 1\,\mathrm{A}$).

The amplitude of the carrier frequency is over a third smaller with the lower DC-link voltage (3.22 to 11.1). The THD is with 4.92 over two times lower than the THD of 11.8, for the DC-link voltage at twice the battery stack voltage. Compared to the theoretical values, the experimental results for the output voltage $V_a$ are all higher especially for the case when $V_{dc} = 1.2 \cdot V_{bat}$. This could be due to additional disturbances created by the feedback control loop. In the time-domain, it can be clearly seen that the current and also the voltage response of the battery is much smoother for $V_{dc} = 1.2 \cdot V_{bat}$. Further reductions of the DC-link voltage are not possible since the electronic switch $S1$ already operates close to 100 % duty cycle (see figure 4.32b). With a battery stack of several hundred volts, total stack voltage further reductions are possible since the voltage drop over the switches and the ohmic resistance of the choke and cables will stay the same.

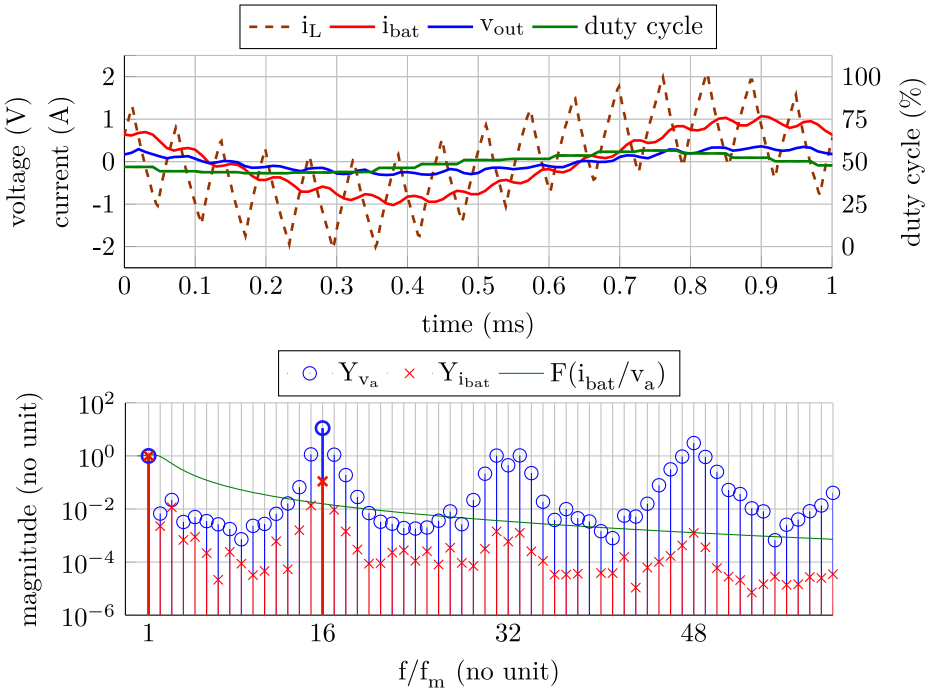

(a) $V_{dc} = 2 \cdot V_{bat}$.

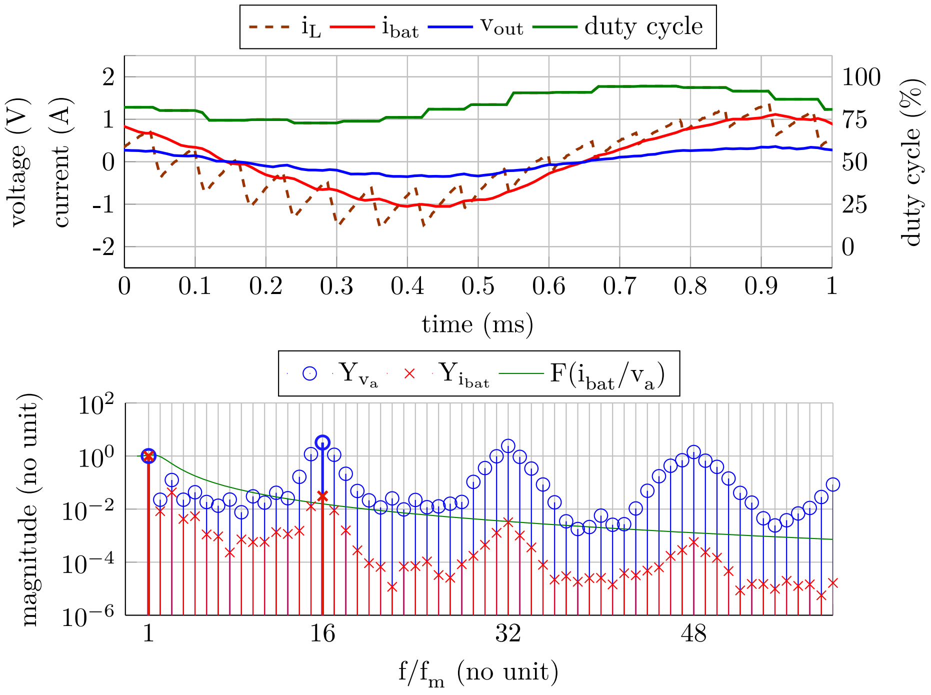

(b) $V_{dc} = 1.2 \cdot V_{bat}$.

Figure 4.32: Time-domain waveforms of the inductor current $i_L$, the battery current $i_{bat}$, the output voltage $v_{out}$ and the duty cycle of the Battery Charger Topology. Spectrum of the switched output voltage $v_a$ (measured values), the battery current $i_{bat}$ after the LC-filter (measured values) and the used filter (theoretical values) at different DC-link voltages $V_{dc}$. The amplitude of the measurement frequency at 1 kHz is normalized to 1.

**Section Conclusion**

*A cost effective implementation of on-line electrochemical impedance spectroscopy would use already existing components. Depending on the place of the battery and the power electronic circuit used, different topologies for on-line electrochemical impedance spectroscopy are created. They differ in the harmonics they generated and in the filter that attenuates these harmonic frequencies. All topologies are capable of generating accurate impedance spectra. There is no implementation that is superior to the other. It is up to the application engineer to decide which is the best approach for his specific application and his capability to change the hardware and software of the components involved.*

*All topologies create some kind of switched-mode excitation. The associated distortions with this excitation can cause deviations in the impedance measurement. Therefore, the distortions need to be reduced. A cost-effective way to reduce the distortions is the reduction of the DC-link voltage.*

## 4.4 Distortion-free Frequency Grid

Stimulus design for system identification is a wide research topic [88], especially for broadband signals, which contain several frequencies and there are several possibilities for optimization. The phase of the single frequency components can be optimized [20; 49; 108] or only frequencies measured with the highest information content [99; 100]. Some of them are only applicable to batteries with limitations as, for example, the suggestion to increase the stimulus amplitude for frequencies of interest [88; 100]. As shown in chapter 3 of this thesis, for li-ion batteries, this can cause systematic measurement deviations.

Usually, it is assumed that the frequencies can all be measured on a continuous spectrum. Geerardyn et al. showed in [47] that for a multi-sine signal, a quasi-logarithmic frequency grid consisting of multiples of the lowest frequency should be used. This reduces the measurement time and avoids spectral leakage at the same time.

In the scope of this thesis, [66] was published. It presents an approach to avoid narrowband distortions, which alias to the measurement bandwidth. It uses a computational intensive algorithm to determine the best frequencies to measure the impedance in order to avoid these narrowband distortions. This section tries to extend on the idea of the avoidance of narrowband distortions by introducing a frequency grid with permissible frequencies, which are free from narrowband distortions. It gives a recommendation on the minimum measurement time for frequencies on this grid. Minimum measurement times are necessary to avoid narrowband disturbances, as measurement bins of the Fourier transformation increase in size with decreasing measurement time.

### 4.4.1 Process to Define Distortion-Free Grid

Figure 4.33 shows the principle of the proposed distortion-free frequency grid. The idea is to select the ratio between the sampling frequency $f_s$ and the carrier frequency $f_c$ in such a way that the aliased harmonics of the carrier frequency repeat themselves in a deterministic way with $f_{rep}$. Since it is unavoidable that some aliased harmonics fall very close to 0 Hz, a harmonic $m_{CH}$ is defined for which the distortion is small enough to be considered to be zero. This harmonic is made to fall exactly to zero. In this way a safe lower frequency bandwidth is created in which the measurement frequencies can be selected freely. Above this safe lower frequency bandwidth a frequency grid with the spacing $f_{grid}$ is defined which is distortion-free. The finer this frequency grid is made the longer the necessary measurement time becomes. The steps needed to create the whole distortion-free frequency grid are:

1. Define the carrier harmonics $m_{CH}$ whose magnitude is small enough not to create undesired distortions.
2. Define $p$ in order to define the ratio between the sampling frequency $f_s$ and the carrier frequency $f_c$ with equation 4.77.
3. The aliased carrier harmonic frequencies will repeat themselves with $f_{rep}$ (equation 4.78) from 0 Hz to $\frac{1}{2}f_s$.
4. Define the sideband harmonic $n_{SB}$ whose magnitude is small enough not to create undesired distortions.
5. A safe lower frequency band is defined up the frequency $f_{m,safemax}$ according to equation 4.82.

6. Select the granularity of the grid by selection $q$ which defines the possible measurement frequencies above the safe lower frequency bandwith according to equation 4.84.
7. Apply the measurement frequency for the apply time $T_a$ to make the frequency bin narrow enough to avoid carrier and sideband harmonics which might be right next to the measurement frequency (see equation 4.91).

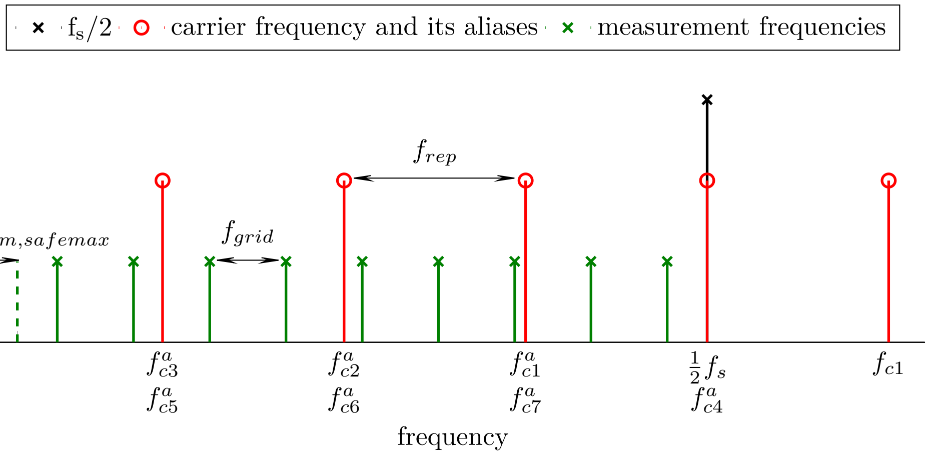

Figure 4.33: Principle of the distortion-free frequency grid.

### 4.4.2 Repetition of Carrier Harmonics

Depernet et al. used in [31] the output of a DC/DC converter to implement a on-line EIS measurement system on a lead-acid battery. He selected the sampling rate $f_s$ to exactly be the switching frequency $f_c$ of his DC/DC converter. With this selection, the alias of the switching frequency falls exactly to 0 Hz, a frequency he did not want to measure. However, the sidebands of the switching frequency are exactly on the measurement frequency. He used the Battery Charger Topology and also claimed that he sufficiently suppressed the sidebands of the switching frequency.
Section 4.3.3.3 showed that for the DC Supply topology, it is not the switching frequency that has the highest amplitude, but its two first sidebands $C_{1,1}$ and $C_{1,-1}$ to the left and to the right. If the selection of $f_s = f_c$ would be made, the most significant harmonics would distort the measurement. Both first sidebands of the switching frequency will fall to the measurement frequency, since the sideband on the negative side of 0 Hz will mirror to the positive side. Even worse, all the harmonics of the switching frequency will also fall to 0 Hz. Their sidebands $C_{x,1}$ and $C_{x,-1}$ will distort the measurement frequency as well. Even if the measurement frequency is changed the distortions will exactly follow the measurement frequency, since the first sidebands are always the modulated frequency apart from the switching frequency and its harmonics. Therefore, this is not a advisable setting for on-line EIS. Nevertheless, it is a very likely setting to be chosen. Controllers and similar control systems often incorporate a module for PWM control and a module with an ADC. They often run on a single clock, which can be divided, but not by uneven numbers. Often this ratio is limited to a $2^x$ value. If the ADC clock is set to any $2^x$-ratio of the PWM clock, the switching frequency falls to 0 Hz again. This makes it likely for others to use the setting of Depernet et al. as well.

In order to avoid that the carrier frequency, its harmonics or their sidebands fall to the frequency bin of the measurement frequency, they need to alias to the measurement frequency bandwidth in a foreseeable way. For on-line EIS this should also be quick and simple, and should not need long computations as used in [66]. The harmonics should fall to the measurement bandwidth in such a way that there is either no or only a small increase in measurement time per measurement frequency. When harmonics are present in close proximity of the measurement frequency, an increase in the number of recorded periods is necessary in order to make the frequency bin of the Fourier transformation smaller. For example, a Fourier transformation at 10 Hz with only one measurement period will be distorted by all the aliased frequency harmonics from 0 Hz to 20 Hz.

One of the infinite series of carrier harmonics will unavoidably fall to 0 Hz. Equation 4.77 shows at what combination of the carrier or switching frequency $f_c$ and the sampling rate $f_s$ this will happen for the carrier harmonic index $m_{CH}$:

$$f_s = \frac{f_c \cdot m_{CH}}{p} \qquad \text{with } GCD(\,p\,, m_{CH}\,) = 1 \qquad (\textbf{G}\text{reatest } \textbf{C}\text{ommon } \textbf{D}\text{enominator}) \tag{4.77}$$

In this case the ${m_{CH}}^{th}$ harmonic of the switching frequency $f_c$ falls to 0 Hz. $p$ is a integer number which does not have a common divisor with $m_{CH}$ except 1. The selection of $m_{CH}$ should be based on an assessment of the harmonics and the filters in place. It should be chosen with the assumption that at the ${m_{CH}}^{th}$ carrier harmonic and above all the harmonics are small enough to be irrelevant. The aliased measurement frequencies repeat themselves on a grid equally spaced between 0 Hz and $\frac{f_s}{2}$ with the frequency spacing:

$$f_{rep} = \frac{f_s}{m_{CH}} \tag{4.78}$$

Figure 4.34 shows this for $m_{CH} = 3$. The switching frequency $f_{c1}$ is mirrored over $\frac{f_s}{2}$ to the measurement frequency band to $f_{c1}^a$. The second harmonic of the switching frequency $f_{c2}$ is aliased to $f_{c2}^a$ and finally the third one $f_{c3}$ is aliased to 0 Hz.

The benefit of selecting a small value for $m_{CH}$ is that between 0 Hz and $\frac{f_s}{m_{CH}}$, there never is an alias of a carrier harmonic. This safe lower frequency band is the larger, the smaller $m_{CH}$ is.

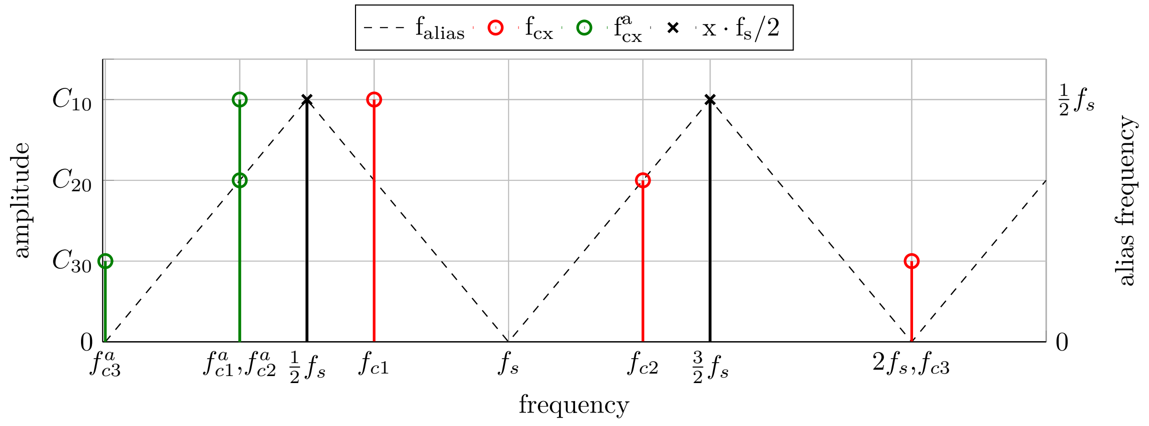

Figure 4.34: Repetition of the switching frequency harmonics when the sampling frequency is set according to equation 4.77 ($m_{CH} = 3$, $p = 2$, synthetic data).

Equation 4.79 gives the aliasing frequency $f_h^a$ dependent on the sampling rate $f_s$ and the harmonic frequency $f_h$. This definition is unusual, but it comes with the benefit that the mathematical rules of the modular arithmetic can be used.

$$f_h^a = \begin{cases} f_h \mod f_s & k \cdot \frac{f_s}{2} \leq f_h < (k+1) \cdot \frac{f_s}{2} \quad \text{for } k = 0,2,4,6,8,... \\ \underbrace{\underbrace{\frac{f_s}{2} - \left(f_h - \frac{f_s}{2}\right)}_{-f_h+f_s} \mod f_s}_{-f_h \mod f_s} & k \cdot \frac{f_s}{2} \leq f_h < (k+1) \cdot \frac{f_s}{2} \quad \text{for } k = 1,3,5,7,9,... \end{cases} \tag{4.79}$$

The mathematical proof for equation 4.77 is given by the use of modular arithmetic. This is possible, since the frequency grid proposed in this section is based on fraction of the switching frequency $f_c$. When multiplying the modular arithmetic formulas by the denominator of that fraction and dividing the formulas by the switching frequency $f_c$, all the numbers become integer values and the normal rules of modular arithmetic can be applied. In the second case of equation 4.79, the constant part $+f_s$ can be deleted, because the modulo is taken over exactly this value. For the first case of equation 4.79, the ${m_{CH}}^{th}$ switching frequency harmonic falls to 0 Hz when the integer number $m$, the carrier harmonics index, fulfills the following equation:

$$\begin{aligned} & & (m \cdot f_c) \mod f_s \overset{!}{=} 0 \\ \Rightarrow & \quad (m \cdot f_c) & \mod \left(\frac{f_c \cdot m_{CH}}{p}\right) \overset{!}{=} 0 \\ \Rightarrow & & m \cdot p \mod m_{CH} \overset{!}{=} 0 \end{aligned} \tag{4.80}$$

Equation 4.80 was multiplied by $p$ and divided by $f_c$ in order to arrive at integer numbers. Equation 4.80 only becomes 0 if $m = m_{CH}$ because $GCD(p,m_{CH}) = 1$.
For the second case of equation 4.79 the following equation needs to become 0 for an integer number of $m$:

$$-m \cdot p \mod m_{CH} \overset{!}{=} 0 \tag{4.81}$$

Equation 4.81 also only becomes 0 if $m = m_{CH}$ because $GCD(p, m_{CH}) = 1$.

By having only the ${m_{CH}}^{th}$ carrier harmonic fall to 0 Hz instead of the first one, this shifts the effective harmonics that are causing measurement deviations to higher frequencies. Perfect Butterworth filters, as they are used in power electronics, are almost impossible to apply with a battery. The extremely low resistance of the battery requires very large capacitors and very low inductors. In these non-ideal Butterworth filters, the frequencies for which the attenuation per decade fits to the order of the Butterworth filter are shifted towards higher frequencies [68]. By setting the sampling frequency according to equation 4.77, this shortcoming of the filter can be avoided. The ${m_{CH}}^{th}$ switching frequency harmonic is also much lower than the first one, even without filter attenuation. Anti-aliasing filter before the ADCs are another solution, but can introduce an additional measurement deviation if the one for the current and the one for the voltage do not have exactly the same transfer characteristics. The additional electronics for the Anti-aliasing filter, especially accurate ones, are costly and cannot be assumed to be present in an on-line EIS system.

### 4.4.3 Safe Lower Frequency Bandwidth

The frequency grid for the carrier frequency and its harmonics creates a safe lower frequency bandwidth, where no distortions can be found. This is beneficial, because due to the often-used logarithmic spacing, most measured frequencies are in the lower frequency range.
The only harmonics that can enter the frequencies below $f_{rep}$ are the sidebands. The sidebands are, by the measurement frequency, apart from the aliased carrier frequency or its harmonics $f^a_{cx}$. This reduces the size of this safe frequency bandwidth by the number of sidebands $(n_{SB} - 1)$ to avoid times the measurement frequency $f_m$. To effectively suppress the distortions in a Fourier transformation, windows other than the Box window can be applied. Section 4.1.2 already introduced several windows, with their characteristic minimum number of measurement periods $w_x$. If measured by a factor of $\frac{T_a}{T_m}$ longer than the minimum number of measurement periods, the frequency bin width reduces by this factor. With these considerations, a maximum measurement frequency for the safe lower frequency bandwidth can be defined by:

$$\begin{aligned} f^a_{c1} - (n_{SB} - 1) \cdot f_{m,safemax} &= \left(\frac{T_a}{T_m} w_x + 1\right) \cdot f_{m,safemax} \\ \Rightarrow \quad f_{m,safemax} &= \frac{f^a_{c1}}{\frac{T_a}{T_m} w_x + n_{SB}} = \frac{f_s}{m_{CH} \cdot (\frac{T_a}{T_m} w_x + n_{SB})} \end{aligned} \tag{4.82}$$

Figure 4.35 shows this for $n_{SB} = 4$ and a Blackman-Nuttal window for which $w_x = 4$.

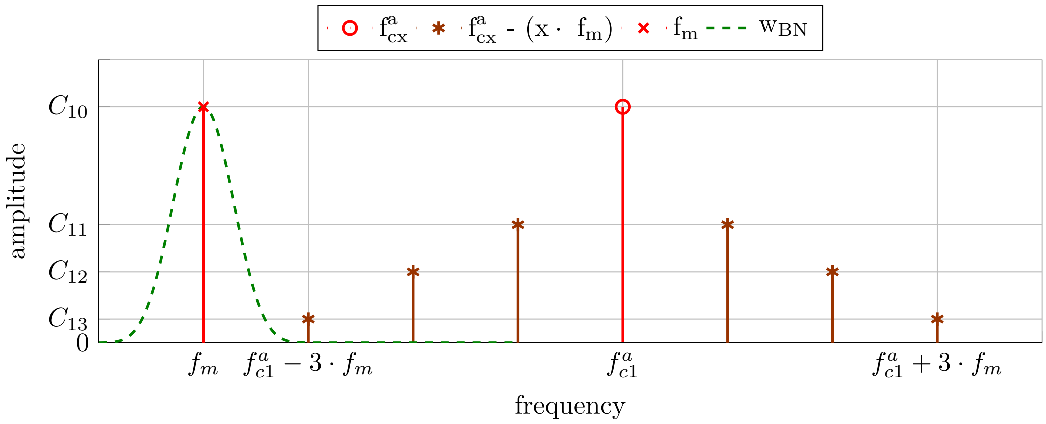

Figure 4.35: Safe lower frequency bandwidth illustration with a Blackman-Nuttal window ($n_{SB} = 4$, synthetic data).

### 4.4.4 Frequency Grid

Not all measurement frequencies can be put into the safe lower frequency bandwidth. High switching and sampling frequencies come with higher costs. Especially for on-line EIS systems, these costs need to be limited.
All measurement frequencies higher than $f_{m,safemax}$ should be set on a grid following equation 4.83

and 4.84:

$$f_m = k \cdot f_{grid} \qquad \text{with } k \in \mathbb{N} \tag{4.83}$$

$$f_{grid} = \frac{f_s}{q} \qquad \text{with } GCD(\,q\,,\, m_{CH}\,) = 1 \qquad (\textbf{G}\text{reatest } \textbf{C}\text{ommon } \textbf{D}\text{enominator}) \tag{4.84}$$

The measurement frequencies on this grid must avoid the harmonics generated by the switching process. If inequation 4.85 becomes true, one of the alias of the switching frequency harmonics or their sidebands fall to the measurement frequency. It needs to be verified that for no combination of the carrier harmonic index $m$ and the sideband harmonic index $n$ this inequation becomes true, except for the designed case of $m = m_{CH}$ and $n = 1$. Equation 4.85 was multiplied by $p \cdot q$ and divided by $f_c$ in order to arrive at integer numbers.

$$\left(\pm m \cdot f_c \pm n \cdot \frac{1}{q} \cdot \overbrace{\frac{f_c \cdot m_{CH}}{p}}^{f_s}\right) \mod \left(\overbrace{\frac{f_c \cdot m_{CH}}{p}}^{f_s}\right) \overset{!}{\neq} \frac{1}{q} \cdot \overbrace{\frac{f_c \cdot m_{CH}}{p}}^{f_s}$$

$$\Rightarrow \qquad (\pm m \cdot p \cdot q \pm n \cdot m_{CH}) \mod (m_{CH} \cdot q) \overset{!}{\neq} m_{CH}$$

$$\Rightarrow \begin{cases} (+m \cdot p \cdot q \pm n \cdot m_{CH}) \mod (m_{CH} \cdot q) \overset{!}{\neq} m_{CH} \\ \qquad k \cdot \frac{m_{CH}}{2} \leq m < (k+1) \cdot \frac{m_{CH}}{2} \quad \text{for } k = 0,2,4,6,8,... \\ (-m \cdot p \cdot q \pm n \cdot m_{CH}) \mod (m_{CH} \cdot q) \overset{!}{\neq} m_{CH} \\ \qquad k \cdot \frac{m_{CH}}{2} \leq m < (k+1) \cdot \frac{m_{CH}}{2} \quad \text{for } k = 1,3,5,7,9,... \end{cases} \tag{4.85}$$

The case separation in equation 4.85 is strictly not correct. In order to determine whether the harmonic frequency $f_h$ falls into case 1 or case 2, also $n$ needs to be considered. The sideband harmonics index $n$ is not considered in order to arrive at a general proof of the proposed frequency grid. If it would be considered, the equation would need to be distinguished case by case, which is only possible in a simulation. By neglecting the right side, the first and the second case of equation 4.85 need to be applied to more values of $n$ than necessary. Since the proof should be made that inequation 4.85 is not true (except for the combination $m = m_{CH}$ and $n = 1$), increasing the amount of possible cases will not lead to a wrong conclusion.
The two summands are evaluated separately by applying the general modular arithmetic equation:

$$a + b \mod c = (a \mod c + b \mod c) \mod c \tag{4.86}$$

The separate evaluation of both summands, allows to determine all possible remainders of the two summands. These are theleast residue systems with which, in a second step, the sum of the two summands can be solved. The least residue system $\Psi_m$ of the left side of equation 4.85 is shown for both cases by 4.87 and the least residue system of the right side $\Psi_n$ by 4.88.

$$\Psi_m = \left[0,\, p,\, 2\,p,\, 3\,p,\, ...,\, \frac{m_{CH}}{2}\,p\right] \tag{4.87}$$

$$\Psi_n = [0,\, m_{CH},\, 2\,m_{CH},\, 3\,m_{CH},\, ...,\, (q-1)\,m_{CH}] \tag{4.88}$$

The carrier harmonics repeat themselves after $\frac{m_{CH}}{2} \cdot p$ and take values in steps of $p$. They do not repeat themselves by $m_{CH} \cdot p$ because after $\frac{m_{CH}}{2}$ the second part of equation 4.85 applies. The sideband harmonics repeat themselves after $(q-1) \cdot m_{CH}$ and take values in steps of $m_{CH}$. Now the summation of both can be evaluated. The first solution, when equation 4.85 becomes true is when $m = m_{CH}$ and $n = 1$. This is the case that was designed to happen.

There are two cases which need to be considered for evaluating whether another solution might occur. The first is when $m_{CH}$ is even and an integer number of repetition frequencies $f_{rep}$ falls between 0 Hz and $\frac{1}{2} f_s$. The second is when $m_{CH}$ is odd and the gap between the carrier harmonic closest to $\frac{1}{2} f_s$ and $\frac{1}{2} f_s$ is $\frac{1}{2} f_{rep}$.

For the first case a solution might occur if the left side of the summand results in a value of exactly $\left(\frac{m_{CH}}{2} - r\right) \cdot p$ and the right side becomes $r \cdot p \pm m_{CH}$, for which $r$ is a integer from 1 to $\frac{m_{CH}}{2}$. Since $p$ and $m_{CH}$ do not have a common divisor, this can only happen if $n = qp \pm 1$. In this case the right side would take a value of $m_{CH} qp \pm m_{CH}$, or after the modulo applied $p \pm m_{CH}$. As the least residue system of the right side 4.88 shows us, this can never happen since $m_{CH}$ and $p$ do not have a common divisor and therefore $n$ would need to become $q \cdot m_{CH}$.

For the second case, when $m_{CH}$ is odd, the carrier harmonics could fall to a value at which they only need $\frac{p}{2}$ before they reach $\frac{m_{CH}}{2} \cdot p$, at which they would repeat themselves. In this case the right side only needs to become a value of $\frac{p}{2} \pm m_{CH}$. Here again, this can never happen since $p$ and $m_{CH}$ do not have a common divisor.

This means that on the frequency grid the number of avoided sidebands is infinite except for the designed case of $m = m_{CH}$ and $n = 1$.

The frequency gap $f_{gap}$ is the minimum gap any measurement frequency has to its own aliased sidebands and to the carrier harmonics if it follows equation 4.83. Equation 4.89 shows that it is dependent on $f_{grid}$. The finer the grid the smaller this gap becomes. The frequency bins of the measurement need to be adjusted according to $f_{grid}$. In order for the bin to change from the passband to the stopband within this frequency gap, a minimum number of periods must be measured according to equation 4.90.

$$f_{gap} = \frac{f_{rep}}{q} = \frac{f_s}{m_{CH} \cdot q} = \frac{f_{grid}}{m_{CH}} = \frac{f_m}{m_{CH} \cdot k} \tag{4.89}$$

$$\begin{aligned} \frac{T_m}{T_a} w_x \cdot f_m = f_{gap} &= \frac{f_m}{m_{CH} \cdot k} \\ \frac{T_a}{T_m} &= m_{CH} \cdot w_x \cdot k \end{aligned} \tag{4.90}$$

$$\begin{aligned} \frac{T_m}{T_a} w_x \cdot f_m = f_{gap} &= \frac{f_{grid}}{m_{CH}} \\ \frac{T_a}{T_m} &= \frac{m_{CH} \cdot w_x}{f_{grid}} \end{aligned} \tag{4.91}$$

Equation 4.91 shows that once a frequency grid is chosen and only $k$ is modified the measurement time for all measurement frequencies on the grid stays the same. However, the frequency grid can be switched during a sinus-sweep measurement. The lowest time is needed if $k$ is always kept at 1. If $k$ is kept constant, the number of measurement periods for all measurement frequencies stays the same.

If the measurement frequencies are not on the grid, harmonics distort the measurement. This can be seen by the experiment of Howey et al. in [52]. He used an electric motor controller in the DC Supply Topology to perform an EIS on a li-ion battery stack. He used pseudo random noise as a stimulus signal. Pseudo random noise is a broadband signal, which stimulates in a certain bandwidth all the frequencies. The sidebands of the carrier harmonics are therefore also all the frequencies of that bandwidth. His measurements show a funnel-like increase of the measurement deviation towards higher frequencies. Even without the exact knowledge of his switching frequency or sampling rate, it can still be assumed that these deviations come from distortions of the aliased harmonics.

### 4.4.5 Example for the Distortion-Free Frequency Grid

Figure 4.36 shows an example with synthetic data for a measurement frequency on a distortion-free frequency grid for a Battery Charger Topology with a predefined switching frequency $f_c = 4\,\text{kHz}$. The process introduced in section 4.4.1 is now applied to this example with specific values:

1. $m_{CH} = 10$.
2. For $p = 9$ the sampling rate is set to $f_s = 4444\,\text{SPS}$.
3. This leads to a repetition frequency of $f_{rep} = 444.4\,\text{Hz}$.
4. $n_{SB} = 5$.
5. The safe lower frequency bandwidth for a maximum apply time of the measurement frequency of one period and using the Blackman-Nuttal window goes from 0 Hz to $f_{m,safemax} = 49.38\,\text{Hz}$.
6. For $q = 19$ the measurement frequency grid $f_{grid}$ becomes 233.9 Hz.
7. The gap to possible harmonics of the carrier frequency and its sidebands is $f_{gap} = 23.39\,\text{Hz}$. Therefore, the measurement frequency $f_m = 233.9\,\text{Hz}$ needs to be measured with $w_x \cdot m_{CH} = 40$ periods when using a Blackman-Nuttal window.

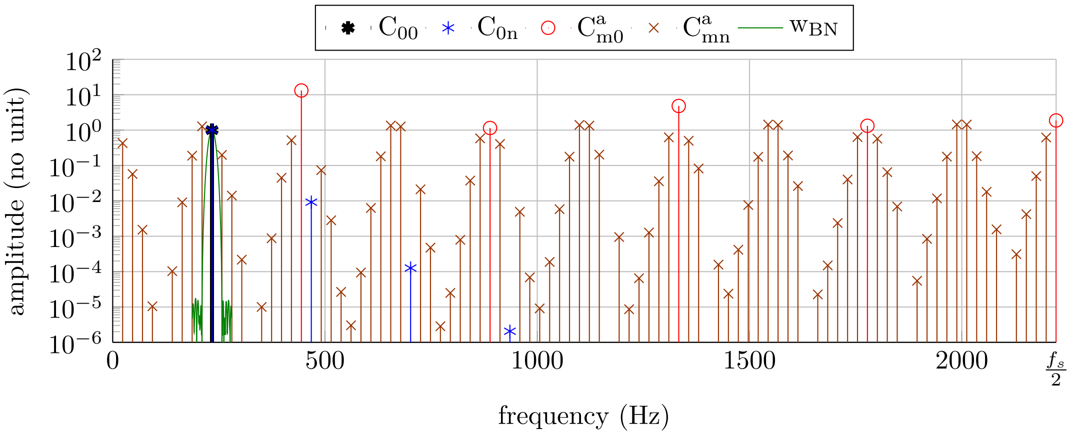

Figure 4.36: Example of a measurement frequency on the frequency grid with a Blackman-Nuttal window and harmonics from the Battery Charger Topology ($f_c = 4\,\text{kHz}$, $m_{CH} = 10$, $p = 9$, $q = 19$, $f_s = 4444\,\text{SPS}$, $f_m = 233.9\,\text{Hz}$). The Blackman-Nuttal window is only represented from $0.8 f_m$ to $1.2 f_m$ (synthetic data).

Due to the linear scale of the x-axis, the safe lower frequency bandwidth is difficult to see. When the measurement frequency is placed in this frequency bandwidth, the sidebands in figure 4.36 look different, since they are dependent on the measurement frequency $f_m$.

**Section Conclusion**

*This section introduced a frequency grid, which prevents narrowband distortions caused by the switching process of a switched-mode amplifier. With the suggested frequency grid, the effective harmonics that cause measurement deviations can be shifted to such high frequencies that they become irrelevant. A safe lower frequency bandwidth was defined in which the measurement frequencies can be chosen freely. For higher frequencies, the measurement frequencies need to be placed on a frequency grid, which is defined by fractions of the sampling frequency.*

**Chapter Conclusion**

*Voltage drifts during the measurement cause high deviations in the impedance measurement. Various ways to correct, suppress and compensate these drifts were presented. A new method based on the Fourier transformed measurement signals was introduced.*

*The parasitic inductance of the current shunt causes the increase in impedance real part or counterclockwise ‘twist’ of the Nyquist plot for higher frequencies. The parasitic inductance of the current should be calibrated and its introduced measurement deviation corrected.*

*In order to save cost, already existing power electronic circuits should be used for an on-line electrochemical impedance spectroscopy measurement. These switched-mode amplifiers can be grouped into three categories: ’Battery Charger Topology’, ’Balancing Unit Topology’ and ’DC Supply Topology’. They differ in terms of their generated harmonics and the effective filter. These harmnonics can be reduced by adjusting the DC-link voltage and can be avoided by selecting measurement frequencies on a distortion-free measurement grid.*

# 5 Conclusion

The impedance that is measured by electrochemical impedance spectroscopy is only valid if the analyzed system fulfills the Linear-Time-Invariant condition. Batteries are inherently non-linear and time-variant. The impedance that is measured for them is therefore prone to several systematic deviations. This thesis described the four most common ones: the change (1) of the State-of-Charge, (2) of the cell temperature and (3) of the Open-Circuit-Voltage as well as (4) the non-linearity of the impedance towards the applied current. An equation was developed with which the deviation of an impedance measurement can be estimated based on previous characterizations of the same battery cell. These characterizations are mainly based on previous impedance measurements. Since the equation is not based on an iterative calculation or other computation intensive calculations, it can be implemented into the embedded controller of an on-line electrochemical impedance spectroscopy system.

Measurement deviations caused by drift and narrowband distortions especially occur for electrochemical impedance spectroscopy measurements on batteries, which are in their real-world application. A new way of compensating voltage drifts in the frequency-domain was presented. It is especially interesting for on-line applications, since the measurement data does not need to be stored before the drift correction is applied. Neither does it increase the measurement time. The generation of harmonics of three different on-line electrochemical impedance spectroscopy topologies was derived by algebraic equations. The knowledge of their magnitude can help to estimate the measurement deviation introduced by them when they are aliased into the measurement frequency bandwidth. Additionally, a distortion-free frequency grid was proposed, which is capable of avoiding all harmonics of a relevant magnitude.

The 10 mV-Criterion for lithium-ion batteries has been disproven. Another explanation for the skin effect in the Nyquist plot was found.
The 10 mV-Criterion states that the maximum amplitude of the voltage response during an electrochemical impedance spectroscopy measurement should not surpass 10 mV. This thesis showed that for the lithium-ion battery used and for all measurement frequencies and conditions applied, the 10 mV-Criterion was too restrictive for a maximum measurement deviation threshold of 1 % for the modulus and 1 ° for the phase. Although not universally transferable, it shows that this battery cell had a very linear behavior, and other lithium-ion battery cells might have as well.
The term skin effect is often used, when in the Nyquist plot, the real part of the impedance increases for frequencies below the x-axis in the Nyquist plot. For these higher frequencies the Nyquist curve looks like, as it ‘twists’ counter-clockwise. In this thesis, this effect was attributed to the parasitic inductance of the current shunt. The inductance does not only affect the imaginary part, it also affects the real part for high frequencies.

The perfect on-line electrochemical impedance spectroscopy system would be quick, cheap, accurate and requiring little computation. Achieving all four goals at the same time is impossible. The engineer who designs such a system needs to balance all of these four parameters. The more measurement periods are taken, the smaller the frequency bin becomes and the more narrowband distortions and voltage drifts could be avoided. If measurement time has to be quick, this is not an option. But then voltage drift corrections have to be done by computation and narrowband distortions might deteriorate the accuracy of the measurement. A sophisticated analog circuit with an anti-aliasing filter and an analog-to-digital converter with high vertical resolution would make the system very accurate and reduce narrowband distortions but it would also make it very expensive. A calibration of the current shunt, not only with a DC but also with an AC signal, would make it possible to compensate the measurement deviation introduced by the parasitic shunt inductance. But calibration is undesired in any manufacturing plant, since it involves valuable manufacturing time and equipment.

The extensive explanation of how and to what extent measurement deviations occur for an electrochemical impedance spectroscopy measurement on lithium-ion batteries, as presented in this thesis, could serve for designing reliable on-line impedance meters and their control. But it should not stop there. Once implemented on-line, impedance measurements will serve for state estimations. These are complex algorithms for which the measurements serve as inputs. But the output of such a state estimation can only be as good as the input. With the calculation of the actual state, e.g. State-of-Charge, the deviation boundaries which come with it should also be estimated from the quality of the measurements on the basis of which it is calculated.

A complete description of the measurement deviations for an impedance measurement should also include measurement noise, i.e. random measurement deviations. With a complete understanding of how noise on current and voltage affect the reliability of the impedance measurement, an informed choice could be made regarding the type of analog-to-digital converter and its resolution. The confidence interval for which the measurement is correct could be determined and handed down to state estimation algorithms to calculate the confidence interval of their state estimation.

Some questions are left unanswered by this thesis. In chapter 3, section 3.4.3, the non-linearity of the imaginary part of the impedance was fitted with the same modified Butler-Volmer equation as the real part. During the fitting process the value of the charge transfer coefficient $\alpha$ arrived at the lower or higher bounds of 0.05 or 0.95 for some data sets. This raises the question whether the imaginary part does follow the same equation or should not rather be fitted to a further modified version of the Butler-Volmer equation.

Section 3.4.6, on the measurement deviation caused by impedance non-linearity, introduced an exchange current modifying factor in the equation for determining the measurement deviation when a constant current is applied. For the imaginary part, the DC overvoltage was determined in the same way as for the real part minus the linear correction shown in section 3.3. Whether this approach is correct is unconfirmed. This imaginary overvoltage was not confirmed by an other experiment as it was done for the real part with the heat generation experiment in section 3.2.3.

Section 3.3 showed that for lower frequencies, the imaginary part of the impedance carries a systematic measurement deviation due to the Open-Circuit-Voltage change. For low frequencies this significantly changes the phase of the measured impedance. The Z-HIT method introduced in section 4.1 uses the phase in order to reconstruct a modulus with which the measured modulus is corrected. This is typically done for low frequencies, since these frequencies particularly suffer from drifts. It is unclear if the Z-HIT method corrects the imaginary impedance deviation shown in section 3.3 or if it would use the wrong phase in order to calculate an equally wrong modulus. In this case it would not correct the measurement but introduce an additional systematic measurement deviation.

In order to make on-line electrochemical impedance spectroscopy a reality, more work needs to be done on the application of such additional information. Some work has already been done, especially for the determination of aging [118] or the sensor-less temperature measurement [69; 93; 105; 114]. But still more applications are needed. The ones already published need to become more robust towards other effects that might be wrongly interpreted.

The strength of electrochemical impedance spectroscopy is also its weakness. A lot of changes in the battery affect the impedance spectra, often even on a broad range of measurement frequencies. To single out the effect that could have caused one change, other effects need to be held constant. For on-line electrochemical impedance spectroscopy in its real-life application this is impossible. Another way is to fully understand how and by what value all possible effects change the impedance spectra. This comprehensive knowledge still does not exist and further research needs to done in this area.

# References

[1] P. Agarwal, M. E. Orazem, and L. H. Garcia–Rubio. “Application of Measurement Models to Impedance Spectroscopy: III . Evaluation of Consistency with the Kramers–Kronig Relations”. In: *Journal of The Electrochemical Society* 142.12 (1995), pp. 4159–4168. DOI: `10.1149/1.2048479` (cit. on p. 109).

[2] S. Al Hallaj, J. Prakash, and J. R. Selman. “Characterization of commercial Li-ion batteries using electrochemical–calorimetric measurements”. In: *Journal of Power Sources* 87.1–2 (2000), pp. 186–194. ISSN: 0378-7753. DOI: `10.1016/S0378-7753(99)00472-3` (cit. on p. 42).

[3] D. Andre, M. Meiler, K. Steiner, H. Walz, T. Soczka-Guth, and D. U. Sauer. “Characterization of high-power lithium-ion batteries by electrochemical impedance spectroscopy. II: Modelling”. In: *Journal of Power Sources* 196.12 (2011), pp. 5349–5356. ISSN: 0378-7753. DOI: `10.1016/j.jpowsour.2010.07.071` (cit. on p. 43).

[4] *APR18650M1A Datasheet.* April 2009 (cit. on p. 194).

[5] *APR18650M1A Material Safety Datasheet* (cit. on p. 194).

[6] G. B. Arfken and H. J. Weber. *Mathematical methods for physicists.* 6th ed. Boston: Elsevier, 2005. ISBN: 0-12-088584-0 (cit. on p. 138).

[7] T. M. Bandhauer, S. Garimella, and T. F. Fuller. “A Critical Review of Thermal Issues in Lithium-Ion Batteries”. In: *Journal of The Electrochemical Society* 158.3 (2011), R1–R25. DOI: `10.1149/1.3515880` (cit. on p. 42).

[8] A. J. Bard and L. R. Faulkner. *Electrochemical methods: Fundamentals and applications.* 2nd ed. New York: Wiley, 2001. ISBN: 978-0-471-04372-0 (cit. on pp. 10, 11, 77).

[9] E. Barsoukov and J. R. Macdonald. *Impedance spectroscopy: Theory, experiment, and applications.* Second edition. 2005. ISBN: 0-471-64749-7 (cit. on pp. 3, 16).

[10] E. Barsoukov, S. H. Ryu, and Lee H. “A novel impedance spectrometer based on carrier function Laplace-transform of the response to arbitrary excitation”. In: *Journal of Electroanalytical Chemistry* 536.1–2 (2002), pp. 109–122. ISSN: 1572-6657. DOI: `10.1016/S0022-0728(02)01209-3` (cit. on pp. 14, 15, 58).

[11] F. Barth, P. Mühlbauer, F. Nikol, and K. Wörle. *Mathematische Formeln und Definitionen.* 8th edition. Bayerischer Schulbuch Verlag GmbH, 2004. ISBN: 3-7627-3272-8 (cit. on p. 207).

[12] P. M. Biesheuvel, D. Brogioli, and Hamelers, H. V. M. “Negative Joule Heating in Ion-Exchange Membranes”. In: *ArXiv e-prints* (2014) (cit. on p. 80).

[13] *Bio-logic - Application note 17* (cit. on p. 113).

[14] *Bio-logic-SP2xx-300 Product Specifications* (cit. on pp. 26, 123).

[15] H. S. Black. *Modulation theory.* Bell Telephone Laboratories series. Van Nostrand, 1953 (cit. on p. 135).

[16] H. Blanke, O. Bohlen, S. Buller, De Doncker, R. W., B. Fricke, A. Hammouche, D. Linzen, Marc Thele, and Dirk Uwe Sauer. "Impedance measurements on lead–acid batteries for state-of-charge, state-of-health and cranking capability prognosis in electric and hybrid electric vehicles". In: *Journal of Power Sources* 144.2 (2005), pp. 418–425. ISSN: 0378-7753. DOI: `10.1016/j.jpowsour.2004.10.028` (cit. on p. 3).

[17] O. Bohlen, S. Buller, De Doncker, R. W., M. Gelbke, and R. Naumann. "Impedance based battery diagnosis for automotive applications". In: *Power Electronics Specialists Conference, 2004. PESC 04. 2004 IEEE 35th Annual.* Vol. 4. 2004, 2792–2797 Vol.4. DOI: `10.1109/PESC.2004.1355275` (cit. on p. 3).

[18] L. Bortels, B. Van den Bossche, J. Deconinck, S. Vandeputte, and A. Hubin. "Analytical solution for the steady-state diffusion and migration involving multiple reaction ions Application to the identification of Butler-Volmer kinetic parameters for the ferri-/ferrocyanide redox couple". In: *Journal of Electroanalytical Chemistry* 429.1–2 (1997), pp. 139–155. ISSN: 1572-6657. DOI: `10.1016/S0022-0728(96)05014-0` (cit. on p. 11).

[19] S. R. Bowes and B. M. Bird. "Novel approach to the analysis and synthesis of modulation processes in power convertors". In: *Electrical Engineers, Proceedings of the Institution of* 122.5 (1975), pp. 507–513. ISSN: 0020-3270. DOI: `10.1049/piee.1975.0141` (cit. on p. 135).

[20] S. Boyd. "Multitone signals with low crest factor". In: *IEEE Transactions on Circuits and Systems* 33.10 (1986), pp. 1018–1022. ISSN: 0098-4094. DOI: `10.1109/TCS.1986.1085837` (cit. on pp. 34, 150).

[21] S. Buller. *Impedance based simulation models for energy storage devices in advanced automotive power systems.* Vol. Bd. 31. Aachener Beiträge des ISEA. Aachen: Shaker, 2003. ISBN: 3-8322-1225-6 (cit. on p. 17).

[22] P. Büschel, U. Tröltzsch, and O. Kanoun. "Calculation of the distribution of relaxation times for characterization of the dynamic battery behavior". In: *Systems, Signals and Devices (SSD), 2012 9th International Multi-Conference on.* 2012, pp. 1–3. DOI: `10.1109/SSD.2012.6198129` (cit. on p. 3).

[23] P. Büschel, U. Tröltzsch, and O. Kanoun. "Use of stochastic methods for robust parameter extraction from impedance spectra". In: *Electrochimica Acta* 56.23 (2011), pp. 8069–8077. ISSN: 0013-4686. DOI: `10.1016/j.electacta.2011.01.047` (cit. on p. 3).

[24] J. F. Chicharo and Kilani, M. T. "A sliding Goertzel algorithm". In: *Signal Processing* 52.3 (1996), pp. 283–297. ISSN: 0165-1684. DOI: `10.1016/0165-1684(96)00066-7` (cit. on p. 20).

[25] H. Cho, M. s. Kim, D. b. Kim, and J. u. Kim. "R2$^2$SDF FFT Implementation with Coefficient Memory Reduction Scheme". In: *Conference Proceedings of IEEE Vehicular Technology Conference.* 2006, pp. 1–4. DOI: `10.1109/VTCF.2006.321` (cit. on p. 19).

[26] J. P. Christophersen, C. G. Motloch, J. L. Morrison, and W. Albrecht. "Method and Apparatus for In-situ Characterization of Energy Storage and Energy Conversion Devices". US20070257681A1. May 4, 2006 (cit. on p. 3).

[27] J. P. Christophersen, C. G. Motloch, J. L. Morrison, I. B. Donnellan, and W. H. Morrison. "Impedance Noise Identification for State-of-Health Prognostics". In: *Proceedings of the 43rd Power Sources Conference.* 2008 (cit. on p. 3).

[28] F. Ciucci and C. Chen. "Analysis of Electrochemical Impedance Spectroscopy Data Using the Distribution of Relaxation Times: A Bayesian and Hierarchical Bayesian Approach". In: *Electrochimica Acta* 167 (2015), pp. 439–454. ISSN: 0013-4686. DOI: `10.1016/j.electacta.2015.03.123` (cit. on p. 3).

[29] A. Cuadras and O. Kanoun. "SoC Li-ion battery monitoring with impedance spectroscopy". In: *Systems, Signals and Devices, 2009. SSD '09. 6th International Multi-Conference on.* 2009, pp. 1–5. DOI: `10.1109/SSD.2009.4956761` (cit. on p. 3).

[30] C. Daniel and J. O. Besenhard. *Handbook of battery materials.* 2nd, completely rev. and enlarged ed. Weinheim: Wiley-VCH Verlag, 2011. ISBN: 978-3-527-32695-2 (cit. on p. 12).

[31] D. Depernet, O. Ba, and A. Berthon. "Online impedance spectroscopy of lead acid batteries for storage management of a standalone power plant". In: *Journal of Power Sources* 219 (2012), pp. 65–74. ISSN: 03787753. DOI: `10.1016/j.jpowsour.2012.07.053` (cit. on pp. 3, 135, 151).

[32] J.-P. Diard, B. Le Gorrec, and C. Montella. "Deviation from the polarization resistance due to non-linearity I - theoretical formulation". In: *Journal of Electroanalytical Chemistry* 432.1–2 (1997), pp. 27–39. ISSN: 1572-6657. DOI: `10.1016/S0022-0728(97)00213-1` (cit. on p. 77).

[33] J.-P. Diard, B. Le Gorrec, and C. Montella. "Deviation of the polarization resistance due to non-linearity II. Application to electrochemical reactions". In: *Journal of Electroanalytical Chemistry* 432.1–2 (1997), pp. 41–52. ISSN: 1572-6657. DOI: `10.1016/S0022-0728(97)00234-9` (cit. on pp. 83, 92).

[34] J.-P. Diard, B. Le Gorrec, and C. Montella. "Impedance measurement errors due to non-linearities—I. Low frequency impedance measurements". In: *Electrochimica Acta* 39.4 (1994), pp. 539–546. ISSN: 0013-4686. DOI: `10.1016/0013-4686(94)80098-7` (cit. on pp. 77, 83).

[35] J.-P. Diard and B. Petrescu. "Méthode de Compensation de Dérive lors d'une Mesure d'Impédance Electrochimique". In: *20éme Forum sur les Impédances Electrochimiques, Paris, 17 Décembre 2007.* Paris, 2007 (cit. on p. 113).

[36] P. Dumm. *Impedance Non-Linearity of Lithium-Ion Battery Cells: A Comparison of Measurement Methods.* Master Thesis. Technische Universität München, 2014 (cit. on pp. 82, 86, 89, 90, 196).

[37] A. Eddahech, O. Briat, and J.-M. Vinassa. "Thermal characterization of a high-power lithium-ion battery: Potentiometric and calorimetric measurement of entropy changes". In: *Energy* 61 (2013), pp. 432–439. ISSN: 0360-5442. DOI: `10.1016/j.energy.2013.09.028` (cit. on p. 43).

[38] W. Ehm, H. Göhr, R. Kaus, B. Röseler, and C. A. Schiller. "The evaluation of electrochemical impedance spectra using a modified logarithmic Hilbert transform". In: *ACH - Models in Chemistry* 137.2-3 (2000), pp. 145–157 (cit. on pp. 108, 109).

[39] W. Ehm, R. Kaus, C. A. Schiller, and W. Strunz. "Z - HIT - A Simple Relation Between Impedance Modulus and Phase Angle Providing a New Way to the Validation of Electrochemical Impedance Spectra". In: *New trends in electrochemical impedance spectroscopy (EIS) and electrochemical noise analysis (ENA).* Ed. by F. Mansfeld, F. Huet, and O. R. Mattos. Vol. v. 2000-24. Proceedings. Pennington and NJ: Electrochemical Society, 2001. ISBN: 9781566772914 (cit. on pp. 108, 109).

[40] *EIS-meter Product Specifications* (cit. on p. 26).

[41] A. Farmann, W. Waag, and Sauer D.U. “Application-specific electrical characterization of high power batteries with lithium titanate anodes for electric vehicles”. In: *Energy* 112 (2016), pp. 294–306. ISSN: 0360-5442. DOI: `10.1016/j.energy.2016.06.088` (cit. on pp. 79, 81).

[42] M. Fleckenstein, S. Fischer, O. Bohlen, and B. Bäker. “Thermal Impedance Spectroscopy - A method for the thermal characterization of high power battery cells”. In: *Journal of Power Sources* 223 (2013), pp. 259–267. ISSN: 0378-7753. DOI: `10.1016/j.jpowsour.2012.07.144` (cit. on p. 58).

[43] M. Gaberscek, R. Dominko, and J. Jamnik. “The meaning of impedance measurements of LiFePO4 cathodes: A linearity study”. In: *Journal of Power Sources* 174.2 (2007), pp. 944–948. ISSN: 0378-7753. DOI: `10.1016/j.jpowsour.2007.06.205` (cit. on p. 81).

[44] C. Gabrielli, F. Huet, M. Keddam, and J. F. Lizee. “Measurement time versus accuracy trade-off analyzed for electrochemical impedance measurements by means of sine, white noise and step signals”. In: *Journal of Electroanalytical Chemistry and Interfacial Electrochemistry* 138.1 (1982), pp. 201–208. ISSN: 0022-0728. DOI: `10.1016/0022-0728(82)87141-6` (cit. on pp. 14, 17).

[45] C. Gabrielli, M. Keddam, and J.-F. Lizzee. “On an impedance measurement error arising for fast swept sinusoidal excitation”. In: *Journal of Electroanalytical Chemistry and Interfacial Electrochemistry* 163.1–2 (1984), pp. 419–427. ISSN: 0022-0728. DOI: `10.1016/S0022-0728(84)80071-6` (cit. on p. 82).

[46] J. Geder, R. Arunachala, S. Jairam, and A. Jossen. “Thermal Behavior of Aged Lithium-Ion Batteries: Calorimetric Observations”. In: *IEEE Green Energy and Systems Conference.* November 9, 2015 (cit. on p. 51).

[47] E. Geerardyn, Y. Rolain, and J. Schoukens. “Design of Quasi-Logarithmic Multisine Excitations for Robust Broad Frequency Band Measurements”. In: *Instrumentation and Measurement, IEEE Transactions on* 62.5 (2013), pp. 1364–1372. ISSN: 0018-9456. DOI: `10.1109/TIM.2012.2232474` (cit. on p. 150).

[48] G. Goertzel. “An Algorithm for the Evaluation of Finite Trigonometric Series”. In: *The American Mathematical Monthly* 65.1 (1958), pp. 34–35 (cit. on pp. 20, 174).

[49] P. Guillaume, J. Schoukens, R. Pintelon, and I. Kollar. “Crest-factor minimization using nonlinear Chebyshev approximation methods”. In: *IEEE Transactions on Instrumentation and Measurement* 40.6 (1991), pp. 982–989. DOI: `10.1109/19.119778` (cit. on pp. 34, 150).

[50] D. G. Holmes and T. A. Lipo. *Pulse width modulation for power converters: Principles and practice.* Hoboken: Wiley-Interscience, op. 2003. ISBN: 9780471208143 (cit. on pp. 128, 135, 173, 209, 210, 221, 222, 224).

[51] D. G. Holmes and B. P. McGrath. “Opportunities for harmonic cancellation with carrier-based PWM for a two-level and multilevel cascaded inverters”. In: *Industry Applications, IEEE Transactions on* 37.2 (2001), pp. 574–582. ISSN: 0093-9994. DOI: `10.1109/28.913724` (cit. on p. 135).

[52] D. Howey, P. Mitcheson, V. Yufit, G. Offer, and N. Brandon. “On-line measurement of battery impedance using motor controller excitation”. In: *Vehicular Technology, IEEE Transactions on* PP.99 (2013). ISSN: 0018-9545. DOI: `10.1109/TVT.2013.2293597` (cit. on pp. 3, 20, 141, 156).

[53] *ICR18650-30B Specification.* Feb. 2010 (cit. on p. 199).

[54] E. Jacobsen and R. Lyons. “The Sliding DFT”. In: *Signal Processing Magazine, IEEE* 20.2 (2003), pp. 74–80 (cit. on p. 20).

[55] A. J. Jerri. *The Gibbs Phenomenon in Fourier Analysis, Splines and Wavelet Approximations.* Vol. 446. Mathematics and Its Applications. Boston and MA: Springer US, 1998. ISBN: 978-1-4419-4800-7 (cit. on p. 138).

[56] A. Jossen. “Fundamentals of battery dynamics”. In: *Journal of Power Sources* 154.2 (2006), pp. 530–538. ISSN: 0378-7753. DOI: `10.1016/j.jpowsour.2005.10.041` (cit. on pp. 9–11, 126).

[57] A. Jossen and W. Weydanz. *Moderne Akkumulatoren richtig einsetzen: 36 Tabellen.* 1. Aufl. Neusäß: Ubooks, 2006. ISBN: 3-939359-11-4 (cit. on p. 7).

[58] O. Kanoun and U. Troltzsch. “Application of Parameter Extraction Techniques for Impedance Spectroscopy”. In: *2005 IEEE Instrumentationand Measurement Technology Conference Proceedings.* Vol. 3. 2005, pp. 2281–2286. DOI: `10.1109/IMTC.2005.1604583` (cit. on p. 3).

[59] E. Karden, S. Buller, and De Doncker, R. W. “A method for measurement and interpretation of impedance spectra for industrial batteries”. In: *Journal of Power Sources* 85.1 (2000), pp. 72–78. ISSN: 0378-7753. DOI: `10.1016/S0378-7753(99)00385-7` (cit. on p. 82).

[60] Kazuhiko T., Masahiro I., Kazuo T., Junichi Y., and Shigeto O. “Quick testing of batteries in lithium-ion battery packs with impedance-measuring technology”. In: *Journal of Power Sources* 128.1 (2004), pp. 67–75. ISSN: 0378-7753. DOI: `10.1016/j.jpowsour.2003.09.045` (cit. on pp. 1, 3).

[61] P. Keil and A. Jossen. “Charging protocols for lithium-ion batteries and their impact on cycle life—An experimental study with different 18650 high-power cells”. In: *Journal of Energy Storage* 6 (2016), pp. 125–141. ISSN: 2352-152X. DOI: `10.1016/j.est.2016.02.005` (cit. on p. 2).

[62] M. Kiel. “Impedanzspektroskopie an Batterien unter besonderer Berücksichtigung von Batteriesensoren für den Feldeinsatz”. PhD thesis. RWTH, Aachen, Germany, 4. April 2013 (cit. on pp. 83, 84, 109).

[63] M. Kiel, D. U. Sauer, P. Turpin, M. Naveed, and E. Favre. “Validation of single frequency Z measurement for standby battery state of health determination”. In: *INTELEC 2008 - 2008 IEEE 30th International Telecommunications Energy Conference.* 2008, pp. 1–7. DOI: `10.1109/INTLEC.2008.4664020` (cit. on pp. 3, 9, 15, 83, 84, 100).

[64] F. M. Kindermann, A. Noel, S. V. Erhard, and A. Jossen. “Long-term equalization effects in Li-ion batteries due to local state of charge inhomogeneities and their impact on impedance measurements”. In: *Electrochimica Acta* 185 (2015), pp. 107–116. ISSN: 0013-4686. DOI: `10.1016/j.electacta.2015.10.108` (cit. on pp. 4, 107).

[65] R. Koch and A. Jossen. “Impedance Spectroscopy for Battery Monitoring with Switched Mode Amplifiers”. In: *Proceedings of the 16th International Power Electronics and Motion Control Conference and Exposition, (PEMC).* 2014, pp. 496–501. DOI: `10.1109/EPEPEMC.2014.6980542` (cit. on pp. 4, 128, 133, 135, 145).

[66] R. Koch and A. Jossen. “Speed Optimized Multisine Stimuli for Electrochemical Impedance Spectroscopy with a Switched Mode Excitation”. In: *Proceedings of the IEEE Vehicle Power and Propulsion Conference (VPPC).* 2014, pp. 1–6. DOI: `10.1109/VPPC.2014.7007135` (cit. on pp. 150, 152).

[67] R. Koch and A. Jossen. “Temperature Measurement of Large Format Pouch Cells with Impedance Spectroscopy”. In: *Conference Proceedings of the 28th International Electric Vehicle Symposium and Exhibition.* 2015 (cit. on pp. 3, 133).

[68] R. Koch, R. Kuhn, I. Zilberman, and A. Jossen. “Electrochemical Impedance Spectroscopy for Online Battery Monitoring - Power Electronics Control”. In: *Proceedings of the 16th European Conference on Power Electronics and Applications, EPE’14-ECCE Europe.* 2014, pp. 1–10 (cit. on pp. 135, 153).

[69] R. Koch, C. Riebel, and A. Jossen. “On-line Electrochemical Impedance Spectroscopy Implementation for Telecommunication Power Supplies”. In: *Proceedings of the IEEE 37th International Telecommunications Energy Conference, INTELEC 2015.* 2015, pp. 1–6 (cit. on pp. 3, 15, 161).

[70] R. Koch, C. Vergote, P. Osswald, A. Jossen, and R. Kuhn. “Direct and Indirect Measurement of Reversible and Irreversible Heat in Lithium-Ion Batteries”. In: *65th Annual Meeting of the International Society of Electrochemistry* (cit. on pp. 12, 13).

[71] H. A. Kramers. “Theory of dispersion in the X-ray region”. In: *Phys. Z.* 30 (1929) (cit. on p. 109).

[72] R. d. L. Kronig. “On the Theory of Dispersion of X-Rays”. In: *J. Opt. Soc. Am.* 12.6 (1926), pp. 547–557. DOI: `10.1364/JOSA.12.000547` (cit. on p. 109).

[73] D. Linden and T. B. Reddy. *Handbook of batteries.* 3rd ed. McGraw-Hill handbooks. New York: McGraw-Hill, 2002. ISBN: 0-07-135978-8 (cit. on p. 43).

[74] R. G. Lyons. *Understanding digital signal processing.* Reading and Mass: Addison Wesley Pub. Co., 1997. ISBN: 0-201-63467-8 (cit. on p. 19).

[75] P. Mauracher and E. Karden. “Dynamic modelling of lead/acid batteries using impedance spectroscopy for parameter identification”. In: *Journal of Power Sources* 67.1–2 (1997), pp. 69–84. ISSN: 0378-7753. DOI: `10.1016/S0378-7753(97)02498-1` (cit. on p. 3).

[76] N. W. Mc Lachlan. *Bessel functions for engineers.* 2nd edition. Oxford University Press, 1961 (cit. on pp. 209–212).

[77] K. A. Murashko, A. V. Mityakov, V. Y. Mityakov, S. Z. Sapozhnikov, J. Jokiniemi, and J. Pyrhönen. “Determination of the entropy change profile of a cylindrical lithium-ion battery by heat flux measurements”. In: *Journal of Power Sources* 330 (2016), pp. 61–69. ISSN: 0378-7753. DOI: `10.1016/j.jpowsour.2016.08.130` (cit. on p. 13).

[78] *NCR18650 Datasheet.* 2012 (cit. on p. 201).

[79] N. Nevaranta, S. Derammelaere, J. Parkkinen, B. Vervisch, T. Lindh, K. Stockman, M. Niemelä, O. Pyrhönen, and J. Pyrhönen. “Online Identification of a Mechanical System in Frequency Domain Using Sliding DFT”. In: *IEEE Transactions on Industrial Electronics* 63.9 (2016), pp. 5712–5723. ISSN: 0278-0046. DOI: `10.1109/TIE.2016.2574303` (cit. on p. 21).

[80] J. S. Newman and K. E. Thomas-Alyea. *Electrochemical systems.* 3rd ed. Hoboken and N.J: J. Wiley, 2004. ISBN: 0-471-47756-7 (cit. on pp. 9, 10, 179).

[81] T. T. Nguyen, V. L. Tran, and W. Choi. “Development of the intelligent charger with battery State-Of-Health estimation using online impedance spectroscopy”. In: *Proceedings of the IEEE 23rd International Symposium on Industrial Electronics (ISIE).* 2014, pp. 454–458. DOI: `10.1109/ISIE.2014.6864656` (cit. on p. 135).

[82] N. Nieto, L. Díaz, J. Gastelurrutia, I. Alava, F. Blanco, J. Carlos Ramos, and A. Rivas. “Thermal Modeling of Large Format Lithium-Ion Cells”. In: *Journal of The Electrochemical Society* 160.2 (2013), A212–A217. DOI: `10.1149/2.042302jes` (cit. on pp. 42, 62).

[83] D. M. Onchis and P. Rajmic. “Generalized Goertzel algorithm for computing the natural frequencies of cantilever beams”. In: *Signal Processing* 96, Part A (2014), pp. 45–50. ISSN: 0165-1684. DOI: `10.1016/j.sigpro.2013.07.026` (cit. on p. 20).

[84] P. J. Osswald, M. del Rosario, J. Garche, A. Jossen, and H. E. Hoster. “Fast and Accurate Measurement of Entropy Profiles of Commercial Lithium-Ion Cells”. In: *Electrochimica Acta* 177 (2015), pp. 270–276. ISSN: 0013-4686. DOI: `10.1016/j.electacta.2015.01.191` (cit. on pp. 12, 13, 42).

[85] L. Papula. *Mathematische Formelsammlung für Ingenieure und Naturwissenschaftler*. 11., vol. [6]. Berlin: Springer Vieweg, 2014. ISBN: 978-3-8348-1913-0 (cit. on p. 208).

[86] B. Petrescu, J.-P. Petit, and J.-C. Poignet. “Method of Determining the Impedance of an Electrochemical System”. US 7,253,631 B2. 2007 (cit. on pp. 113, 120).

[87] B. Petrescu, J.-P. Petit, and J.-C. Poignet. “Procede de Determination de l’Independance d’un Systeme Electrochimique”. FR 02 08897. 2004 (cit. on pp. 113, 120).

[88] R. Pintelon and J. Schoukens. *System identification: A frequency domain approach*. 2nd ed. Hoboken et al.: Wiley and IEEE Press, 2012. ISBN: 978-0-470-64037-1 (cit. on pp. 18, 150).

[89] G. L. Plett. “Extended Kalman filtering for battery management systems of LiPB-based 5HEV6 battery packs: Part 1. Background”. In: *Journal of Power Sources* 134.2 (2004), pp. 252–261. ISSN: 0378-7753. DOI: `10.1016/j.jpowsour.2004.02.031` (cit. on p. 3).

[90] G. L. Plett. “Extended Kalman filtering for battery management systems of LiPB-based 5HEV6 battery packs: Part 2. Modeling and identification”. In: *Journal of Power Sources* 134.2 (2004), pp. 262–276. ISSN: 0378-7753. DOI: `10.1016/j.jpowsour.2004.02.032` (cit. on p. 3).

[91] G. L. Plett. “Extended Kalman filtering for battery management systems of LiPB-based 5HEV6 battery packs: Part 3. State and parameter estimation”. In: *Journal of Power Sources* 134.2 (2004), pp. 277–292. ISSN: 0378-7753. DOI: `10.1016/j.jpowsour.2004.02.033` (cit. on p. 3).

[92] F. Qureshi and O. Gustafsson. “Analysis of twiddle factor memory complexity of radix-2i pipelined FFTs”. In: *Conference Record of the 43rd Asilomar Conference on Signals, Systems and Computers*. 2009, pp. 217–220. DOI: `10.1109/ACSSC.2009.5470121` (cit. on p. 19).

[93] L. H. J. Raijmakers, D. L. Danilov, J. P. M. van Lammeren, M. J. G. Lammers, and P. H. L. Notten. “Sensorless battery temperature measurements based on electrochemical impedance spectroscopy”. In: *Journal of Power Sources* 247 (2014), pp. 539–544. ISSN: 0378-7753. DOI: `10.1016/j.jpowsour.2013.09.005` (cit. on pp. 3, 15, 161).

[94] Y. Reynier, R. Yazami, and B. Fultz. “The entropy and enthalpy of lithium intercalation into graphite”. In: *Journal of Power Sources* 119–121 (2003), pp. 850–855. ISSN: 0378-7753. DOI: `10.1016/S0378-7753(03)00285-4` (cit. on p. 12).

[95] C. Riebel. *Generation of Harmonics of Switched Mode Excitation for Online Electrochemical Impedance Spectroscopy: Master Thesis*. Master Thesis. Technische Universität München, 2015 (cit. on p. 133).

[96] A. G. Ritchie. “Recent developments and likely advances in lithium rechargeable batteries”. In: *Journal of Power Sources* 136.2 (2004), pp. 285–289. ISSN: 0378-7753. DOI: `10.1016/j.jpowsour.2004.03.013` (cit. on p. 1).

[97] RWTH Aachen. “Skript und Uebung, Aerodynamik, WW10/11”. In: (2010) (cit. on p. 231).

[98] M. Safari and C. Delacourt. “Modeling of a Commercial Graphite/LiFePO4 Cell”. In: *Journal of The Electrochemical Society* 158.5 (2011), A562. ISSN: 00134651. DOI: `10.1149/1.3567007` (cit. on p. 77).

[99] B. Sanchez, C. R. Rojas, G. Vandersteen, R. Bragos, and J. Schoukens. “On the calculation of the D-optimal multisine excitation power spectrum for broadband impedance spectroscopy measurements”. In: *Measurement Science and Technology* 23.8 (2012), p. 085702. ISSN: 0957-0233. DOI: `10.1088/0957-0233/23/8/085702` (cit. on p. 150).

[100] B. Sanchez, G. Vandersteen, R. Bragos, and J. Schoukens. “Optimal multisine excitation design for broadband electrical impedance spectroscopy”. In: *Measurement Science and Technology* 22.11 (2011), p. 115601 (cit. on pp. 18, 34, 150).

[101] B. Savova-Stoynovm and Z. Stoynov. “Four-dimensional estimation of the instantaneous impedance”. In: *Electrochimica Acta* 37.12 (1992), pp. 2353–2355. ISSN: 0013-4686. DOI: `10.1016/0013-4686(92)85131-4` (cit. on p. 108).

[102] C. A. Schiller, F. Richter, E. Gulzow, and N. Wagner. “Relaxation impedance as a model for the deactivation mechanism of fuel cells due to carbon monoxide poisoning”. In: *Phys. Chem. Chem. Phys.* 3.11 (2001), pp. 2113–2116. DOI: `10.1039/B007674K` (cit. on p. 109).

[103] C. A. Schiller, F. Richter, E. Gulzow, and N. Wagner. “Validation and evaluation of electrochemical impedance spectra of systems with states that change with time”. In: *Phys. Chem. Chem. Phys.* 3.3 (2001), pp. 374–378. DOI: `10.1039/B007678N` (cit. on p. 108).

[104] Schmidt J.P., Manka D., Klotz D., and Ivers-Tiffée E. “Investigation of the thermal properties of a Li-ion pouch-cell by electrothermal impedance spectroscopy”. In: *Journal of Power Sources* 196.19 (2011), pp. 8140–8146. ISSN: 0378-7753. DOI: `10.1016/j.jpowsour.2011.05.047` (cit. on p. 58).

[105] J. P. Schmidt, S. Arnold, A. Loges, D. Werner, T. Wetzel, and E. Ivers-Tiffée. “Measurement of the internal cell temperature via impedance: Evaluation and application of a new method”. In: *Journal of Power Sources* 243 (2013), pp. 110–117. ISSN: 0378-7753. DOI: `10.1016/j.jpowsour.2013.06.013` (cit. on pp. 3, 15, 161).

[106] J. P. Schmidt, A. Weber, and E. Ivers-Tiffée. “A novel and precise measuring method for the entropy of lithium-ion cells: ΔS via electrothermal impedance spectroscopy”. In: *Electrochimica Acta* 137 (2014), pp. 311–319. ISSN: 0013-4686. DOI: `10.1016/j.electacta.2014.05.153` (cit. on pp. 12, 13).

[107] H. Schranzhofer, J. Bugajski, H. J. Santner, C. Korepp, K. C. Möller, J. O. Besenhard, M. Winter, and W. Sitte. “Electrochemical impedance spectroscopy study of the SEI formation on graphite and metal electrodes”. In: *Journal of Power Sources* 153.2 (2006), pp. 391–395. ISSN: 0378-7753. DOI: `10.1016/j.jpowsour.2005.05.034` (cit. on p. 3).

[108] M. Schroeder. “Synthesis of low-peak-factor signals and binary sequences with low autocorrelation (Corresp.)” In: *IEEE Transactions on Information Theory* 16.1 (1970), pp. 85–89. ISSN: 0018-9448. DOI: `10.1109/TIT.1970.1054411` (cit. on pp. 34, 150).

[109] B. Scrosati and J. Garche. “Lithium batteries: Status, prospects and future”. In: *Journal of Power Sources* 195.9 (2010), pp. 2419–2430. ISSN: 0378-7753. DOI: `10.1016/j.jpowsour.2009.11.048` (cit. on p. 1).

[110] K. Sheng, B. W. Williams, X. He, Z. Qian, and S. J. Finney. “Measurement of IGBT switching frequency limits”. In: *Proceedings of the 30th Annual IEEE Power Electronics Specialists Conference, PESC 99*. Vol. 1. 1999, 376–380 vol.1. DOI: `10.1109/PESC.1999.789031` (cit. on p. 134).

[111] *SLPB110255255H Material Safety Datasheet* (cit. on p. 203).

[112] *SLPB110255255H Specifications 60Ah* (cit. on p. 203).

[113] S. W. Smith. *The scientist and engineer’s guide to digital signal processing*. 2nd edition. San Diego (Calif.): California Technical Pub., 1999. ISBN: 0-9660176-7-6 (cit. on pp. 19, 20, 22).

[114] R. Srinivasan, B. G. Carkhuff, M. H. Butler, and A. C. Baisden. “Instantaneous measurement of the internal temperature in lithium-ion rechargeable cells”. In: *Electrochimica Acta* 56.17 (2011), pp. 6198–6204. ISSN: 0013-4686. DOI: `10.1016/j.electacta.2011.03.136` (cit. on pp. 3, 15, 161).

[115] Z. Stoynov. “Nonstationary impedance spectroscopy”. In: *Electrochimica Acta* 38.14 (1993), pp. 1919–1922. ISSN: 0013-4686. DOI: `10.1016/0013-4686(93)80315-Q` (cit. on p. 108).

[116] Z. Stoynov. “Rotating fourier transform—new mathematical basis for non-stationary impedance analysis”. In: *Electrochimica Acta* 37.12 (1992), pp. 2357–2359. ISSN: 0013-4686. DOI: `10.1016/0013-4686(92)85132-5` (cit. on p. 108).

[117] K. E. Thomas and J. Newman. “Heats of mixing and of entropy in porous insertion electrodes”. In: *Journal of Power Sources* 119–121 (2003), pp. 844–849. ISSN: 0378-7753. DOI: `10.1016/S0378-7753(03)00283-0` (cit. on p. 42).

[118] U. Tröltzsch, O. Kanoun, and H.-R. Tränkler. “Characterizing aging effects of lithium ion batteries by impedance spectroscopy”. In: *Electrochimica Acta* 51.8–9 (2006), pp. 1664–1672. ISSN: 0013-4686. DOI: `10.1016/j.electacta.2005.02.148` (cit. on pp. 3, 161).

[119] *UR18650SAX Datasheet*. Jan. 2012 (cit. on p. 197).

[120] *UR18650SAX Material Safety Datasheet*. Dec. 2008 (cit. on p. 197).

[121] C. Vergote. *Impedance based modelling of Lithium-ion batteries for heat generation estimation: Master Thesis*. Master Thesis. Technische Universität München, 2014 (cit. on pp. 49, 55).

[122] W. Waag, S. Käbitz, and D. U. Sauer. “Experimental investigation of the lithium-ion battery impedance characteristic at various conditions and aging states and its influence on the application”. In: *Applied Energy* 102 (2013), pp. 885–897. ISSN: 0306-2619. DOI: `10.1016/j.apenergy.2012.09.030` (cit. on pp. 3, 14).

[123] N. Wagner and M. Schulze. “Change of electrochemical impedance spectra during CO poisoning of the Pt and Pt–Ru anodes in a membrane fuel cell (PEFC)”. In: *Electrochimica Acta* 48.25–26 (2003), pp. 3899–3907. ISSN: 0013-4686. DOI: `10.1016/S0013-4686(03)00528-0` (cit. on p. 109).

[124] T. H. Wan, M. Saccoccio, C. Chen, and F. Ciucci. “Influence of the Discretization Methods on the Distribution of Relaxation Times Deconvolution: Implementing Radial Basis Functions with 5DRTtools6”. In: *Electrochimica Acta* 184 (2015), pp. 483–499. ISSN: 0013-4686. DOI: `10.1016/j.electacta.2015.09.097` (cit. on p. 3).

[125] G. N. Watson. *A treatise on the theory of Bessel functions*. 1st edition. Cambridge and New York: Cambridge University Press, 1922 (cit. on pp. 209, 210).

[126] Wei-Chou F. “Method of Measuring Remaining Capacity of a Storage Cell by Comparing Impedance Plot Characteristics”. US 5,241,275. 1993 (cit. on p. 3).

[127] Xiao M. and Choe S.-Y. “Theoretical and experimental analysis of heat generations of a pouch type LiMn2O4/carbon high power Li-polymer battery”. In: *Journal of Power Sources* 241 (2013), pp. 46–55. ISSN: 0378-7753. DOI: `10.1016/j.jpowsour.2013.04.062` (cit. on pp. 42, 65).

[128] R. Yazami and K. Maher. “Thermodynamics of Lithium-Ion Batteries”. In: *Lithium-ion batteries*. Ed. by G. Pistoia. Elsevier, 2014, pp. 567–604. ISBN: 978-0-444-59513-3 (cit. on p. 14).

[129] C. O. Yoon, Y. Barsukov, and J. H. Kim. *Laplace transform impedance spectrometer and its measurement method*. United States Patent US006502046B1, 2002 (cit. on p. 14).

# Glossary

**10 mV-Criterion** Criterion used to assess whether an excitation current is too large and caused the battery to respond in a non-linear way. The response is assumed to be sufficiently linear when the voltage amplitude did not surpass 10 mV.

**Aliasing** Aliasing is an effect that occurs when a signal is sampled and transformed into the frequency-domain, but the signal containes frequencies that were higher than half the sample frequency (Nyquist-Shannon sampling theorem).

**anode** Electrode to which the negative electrons move towards to and the positive li-ion move away from. In this thesis it refers to the negative electrode.

**Accelerated Rate Calorimeter** An adiabatic environment that makes sure that there is no heat exchange from the inside to the outside of its enclosed container.

**Arrhenius** The Arrhenius equation states the exponential temperature dependency of the rate constant.

**Blackman-Nuttal** The Blackman-Nuttal window is a windowing function for digital signal processing.

**Box** The Box window is a windowing function for digital signal processing.

**Butler-Volmer** The Butler-Volmer equation describes the electrochemical kinetics of an electrode. Named after J.A.V. Butler and M. Volmer.

**C-rate** Current amplitude in reference to the capacity of the battery cell. The unit used is CA. 1 CA equals the current to charge or discharge the battery by 100 % in one hour.

**cathode** Electrode to which the positive li-ion move towards to and the negative electrons move away from. In this thesis it refers to the positive electrode.

**Crest factor** The ratio of peak (amplitude) value to effective (root-mean-square) value of a signal.

**Double Fourier Integral** The Double Fourier Integral is a method to determine the harmonics generated by a switched-mode converter [50].

**drift** The term describes the effect when the voltage or the state of the battery at the end of the impedance measurement is not equal to the one at the beginning of the measurement. In this thesis mainly used for voltage drifts.

**duty cycle** Ratio between on and off state of a switch or high and low state of a signal, especially pulse signals. For the Charger Topology, the Balancing Unit Topology and the DC-Supply Topology it is the on-time of switch S1 divided by the switching period.

**enthalpy** Part of the Gibbs' free energy that is the internal energy and the product of pressure and volume.

**entropy** Part of the Gibbs' free energy that describes its dependency on temperature.

**entropy heating** Heat generated by an exothermal reaction or cold generated by an endothermal reaction.

**Flat-Top** The Flat-Top window is a windowing function for digital signal processing.

**Fourier transformation** Method to transform time-domain data into the frequency-domain. The method is based on summing up the the time-domain data multiplied with a reference phasor of the evaluated frequency.

**galvanostatic** Excitation mode of the EIS for which a current perturbation is generated and the voltage response is observed.

**Gibbs' free energy** Gibbs free energy of a system is the energy available to perform work.

**Half-Bridge-converter** Power electronic converter consisting only of one half-bridge leg with two switches and a choke.

**Hamming** The Hamming window is a windowing function for digital signal processing.

**heat generation rate** Normalized amount of heat generated by the current. For entropy heating, it is linearly dependent on current (for the definition see equation 3.58). For impedance heating, it is dependent on the square of the current (for the definition see equation 3.77).

**impedance heating** Heat generated by all ways that can be explained by the impedance measurement. These are sources such as ohmic heating, reaction heating, etc.

**impedance non-linearity** Non-linearity of the impedance described by the Butler-Volmer equation and other effects caused directly by the impedance itself.

**inner resistance** The term 'inner resistance' is used in this thesis for all the equivalent circuit components, e.g. resistive, capacitive, inductive, inside the battery cell except the voltage source.

**intercept frequency** Intercept frequency with the x-Axis in the Nyquist plot. Frequency at which the imaginary part of the impedance becomes zero.

**Kaiser** The Kaiser window is a windowing function for digital signal processing. It has an adjustable parameter $\alpha$.

**least residue system** A set of integer values containing the smallest representative of all residue classes of a congruence relation.

**Linear-Time-Invariant** A system whose parameters do not change over time and the inputs affect the outputs only in a linear way is called a Linear-Time-Invariant System. These two properties allow the superposition of different inputs.

**Maclaurin series** The Maclaurin series is a Taylor series expansion at $x = 0$.

**Microcycle-Impedance** During the Microcycle-Impedance method, current pulses superpositioned with a sinusoidal current are applied in order to investigate the impedance non-linearity.

**Microcycle** Microcycles are current pulses in order to investigate the voltage drop they cause. They are used to investigate the impedance non-linearity.

**modulus** Absolute value of the impedance. $|Z| = \sqrt{{Z_{real}}^2 + {Z_{imag}}^2}$.

**multi-sine excitation** Excitation signal of a multi-sine measurement.

**multi-sine measurement** Impedance measurement for which several frequencies are applied at the same time.

**Goertzel** Algorithm, performing a frequency transformation, published in [48], named after Gerald Goertzel.

**potentiostatic** Excitation mode of the EIS for which a voltage perturbation is generated and the current response is observed.

**$r^2$** A measure of the quality of a fitted regression line. Measures how close the data points are to the regression line.

**single-sine measurement** Impedance measurement for which only a single frequency is applied.

**sinus-sweep measurement** Impedance measurement for which several single-sine measurements are applied one after another.

**SoC shift** Average change in SoC caused by a current signal. The average SoC shift is the average change in SoC, which was present throughout the time when the signal was applied. E.g. if a rectangular current signal charged a battery from 50 % to 60 % and back to 50 % SoC, the final SoC change was 0% but the SoC shift was 5 %.

**SoC sweep** Range of SoC a current signal caused a battery to move over. E.g. if a rectangular current signal charged a battery from 50 % to 60 % and back to 50 % SoC, the SoC sweep was 10 %.

**spectral leakage** Spectral leakage is an effect that occurs when not an integer number of periods of the evaluated frequency is used in a Fourier transformation.

**switched-mode** Switched-mode excitation means that the electronic switch that generates the excitation is operated in switching-mode compared to an analog continuous-mode.

**Tafel** The Tafel equation describes either only the anodic or the cathodic part of the Butler-Volmer equation.

**total harmonic distortion** Ratio of the geometric sum of all harmonics divided by the fundamental frequency: $THD = \frac{\sqrt{\Sigma_{n=2}^{\infty} harmonics_n}}{fundamental}$.

# Abbreviations

**ADC** analog-to-digital converter
**ARC** Accelerated Rate Calorimeter

**BMS** battery management system

**CPE** Constant Phase Element

**DFT** Discrete Fourier Transformation

**EIS** electrochemical impedance spectroscopy

**FFT** Fast Fourier Transform
**FIR** finite impulse response

**IGBT** Insulated Gate Bipolar Transistor
**IIR** infinite impulse response

**LCO** Lithium Cobalt Oxide ($LiCoO_2$)
**LFP** Lithium Iron Phosphate ($LiFePO_4$)
**li-ion** lithium-ion
**LMO** Lithium Manganese Oxide ($LiMn_2O_4$)
**LTI** Linear-Time-Invariant

**NCA** Lithium Nickel Cobalt Aluminum Oxide ($LiNiCoAlO_2$)
**NiMH** Nickel-Metal Hydride
**NMC** Lithium Nickel Manganese Cobalt Oxide ($Li(Ni_xMn_yCo_z)O_2$)

**OCV** Open-Circuit-Voltage

**PWM** pulse-width modulation

**SEI** Solid-Electrolyte-Interface
**SMPS** switched mode power supply
**SNR** signal-to-noise ratio
**SoC** State-of-Charge
**SoH** state-of-health
**SPS** samples per second

**THD** total harmonic distortion

**UPS** uninterruptible power supply

# Formula Symbols

$\alpha$ Charge transfer coefficient. $\alpha$ is used as the cathodic charge transfer coefficient in this thesis. The anodic one is $1-\alpha$. This is the same notation as used by Newman and Thomas-Alyea [80]. $[\alpha]$ = no unit

$C$ amplitude $C_{mn}$ of the $m^{\text{th}}$ carrier and $n^{\text{th}}$ sideband harmonic, $[C]$ = no unit

$C_{el}$ electrical capacity, $[C_{el}] = \mathrm{As}$

$C_{dl}$ double layer capacitor of the SEI-layer, $[C_{dl}] = \mathrm{F}$

$C_{th}$ thermal capacity, $[C_{th}] = \mathrm{Ws\,K^{-1}}$

$D$ duty cycle ratio, $D = \frac{t_{on}}{t_{on}+t_{off}}$, $[D]$ = no unit

$e_Z$ relative deviation of an electrochemical impedance measurement, $[e_Z]$ = no unit

$F$ Faraday constant, $F = 96\,485.3329\,\mathrm{As\,mol^{-1}}$

$f_c$ carrier frequency of a modulation process, equal to the switching frequency of a switched-mode amplifier, $[f_c] = \mathrm{Hz}$

$f_i$ intercept frequency, $[f_i] = \mathrm{Hz}$

$f_m$ measurement frequency or modulated frequency, $[f_m] = \mathrm{Hz}$

$f_{rep}$ repetition frequency of the aliased carrier harmonics, $[f_{rep}] = \mathrm{Hz}$

$f_s$ sampling rate or sampling frequency, $[f_s] = \mathrm{Hz}$

$G$ Gibb's free energy

$H$ enthalpy, $[H] = \mathrm{J\,mol^{-1}}$

$HGR$ heat generation rate of impedance heating

$HGR_{dc}$ heat generation rate of impedance heating caused by a direct current, $[HGR_e] = \mathrm{J\,A^{-2}\,s^{-1}}$

$HGR_e$ heat generation rate of entropy heating, $[HGR_e] = \mathrm{J\,A^{-1}\,s^{-1}}$

$HGR_{fm}$ heat generation rate of impedance heating cause by the measurement frequency, $[HGR_{fm}] = \mathrm{J\,A^{-2}\,s^{-1}}$

$\mathcal{I}$ modified bessel function of the first kind

$i_0$ exchange current, $[i_0] = \mathrm{A}$

$I_{dc}$ constant current, $[I_{dc}] = \mathrm{A}$

$i_m$ measurement current changing over time, $[i_m] = \mathrm{A}$

$I_m$ measurement current, $[I_m] = \mathrm{A}$

$\hat{I}_m$ amplitude of the measurement current, $[\hat{I}_m] = \mathrm{A}$

$\mathcal{J}$ bessel function of the first kind

$L_{bat}$ battery inductance, $[L_{bat}] = \mathrm{H}$

$m$ carrier harmonics index, $m \in \mathbb{N}_0$

$M$ modulation index, $M = 0...1$

$M'$ modified modulation index, $M' = 0...M'_{max}$, $M'_{max} < 1$ (see equation E.13 and equation E.35)

$m_{CH}$ first carrier harmonic which aliases to $0\,\mathrm{Hz}$, $m_{CH} \in \mathbb{N}$

$n$ baseband and sideband harmonics index, $n \in \mathbb{Z}$

$n_{SB}$ first sideband harmonic, which falls into the measurement frequency bin, $n_{SB} \in \mathbb{Z}$

$N_{Tm}$ number of samples for one period of the measurement frequency $N_{Tm} = \frac{f_s}{f_m}$

$\omega_c$ angular frequency of the carrier frequency $f_c$, $\omega_c = 2\pi f_c$, $[\omega_c] = \mathrm{Hz}$

$\omega_m$ angular frequency of the measurement or modulated frequency $f_m$, $\omega_m = 2\pi f_m$, $[\omega_m] = \mathrm{Hz}$

$p$ carrier harmonics divisor for defining the distortion-free grid, $p \in \mathbb{N}$, $GCD(p, m_{CH}) = 1$

$\phi_I$ current phase angle, $[\phi_I] = \mathrm{rad}$

$\phi_V$ voltage phase angle, $[\phi_V] = \mathrm{rad}$

$\phi_Z$ impedance phase angle, $[\phi_Z] = \mathrm{rad}$

$\phi_{Z0}$ impedance phase angle of the impedance without any measurement deviations, $[\phi_{Z0}] = \mathrm{rad}$

$q$ carrier harmonics divisor for defining the distortion-free grid, $q \in \mathbb{N}$, $GCD(q, m_{CH}) = 1$

$\dot{Q}$ heat flux, $[\dot{Q}] = \mathrm{J\,s^{-1}}$

$Q_{irr}$ irreversible heat, $[Q_{irr}] = \mathrm{J}$

$Q_{rev}$ reversible heat, $[Q_{rev}] = \mathrm{J}$

$r$ linear resistance in the equivalent circuit for a double Butler-Volmer non-linear circuit, r is a complex value, $[r] = \Omega$

$R$ gas constant, $R = 8.314\,459\,8\,\mathrm{J\,mol^{-1}\,K^{-1}}$

$R_{ct}$ charge transfer resistance of the SEI-layer, $[R_{ct}] = \Omega$

$R_\Omega$ purely ohmic resistance of the impedance, not subject to impedance non-linearity, it is the real part of the impedance at the intercept frequency $f_i$, $[R_\Omega] = \Omega$

$S$ entropy, $[S] = \mathrm{J\,mol^{-1}\,K^{-1}}$

$\sigma_W$ Warburg coefficient, $[\sigma_W] = \Omega\,\mathrm{s}^{0.5}$

$SoC$ State-of-Charge, $[SoC] = \%$, i.e. 0.0 to 1.0

$\Delta\overline{SoC}$ SoC shift, $[\Delta\overline{SoC}] = \%$, i.e. 0.0 to 1.0

$\Delta\widehat{SoC}$ SoC sweep, $[\Delta\widehat{SoC}] = \%$, i.e. 0.0 to 1.0

$T$ absolute temperature, $[T] = \mathrm{K}$

$T_m$ period of the measurement frequency, $T_m = f_m^{-1}$, $[T_m] = \mathrm{s}$

$T_{min}$ period of the lowest frequency in a multisine measurement, $[T_{min}] = \mathrm{s}$

$T_a$ applied time of a frequency for an impedance measurement, $[T_a] = \mathrm{s}$

$\tau_D$ time constant of the heat transfer from the coil to the casing of the cell, $[\tau_D] = \mathrm{s}$

$\vartheta$ temperature in °C beginning with 0 °C at 273.15 K, $[\vartheta] = {}^\circ\mathrm{C}$

$\Theta$ exponential parameter for the temperature dependency of the impedance, $[\Theta] = \mathrm{K}$

$\vartheta_{cell}$ temperature of the battery cell, $[\vartheta_{cell}] = {}^\circ\mathrm{C}$

$V_0$ equilibrium voltage, $[V_0] = \mathrm{V}$

$V_{dc}$ constant voltage, $[V_{dc}] = \mathrm{V}$

$v_e$ voltage signal of an electrochemical impedance measurement causing a measurement deviation based by the absolute impedance deviation $Z_e$, $[v_e] = \mathrm{V}$

$v_m$ measurement voltage changing over time, $[v_m] = \mathrm{V}$

$\hat{V}_m$ amplitude of the measurement voltage for potentiostatic excitation, $[\hat{V}_m] = \mathrm{V}$

$V_{OCV}$ Open-Circuit-Voltage, $[V_{OCV}] = \mathrm{V}$

$V_{Z0}$ voltage response of the impedance without any measurement deviations, $[V_{Z0}] = \mathrm{V}$

$\hat{V}_{Z0}$ amplitude of the voltage response of the impedance without any measurement deviations, $[\hat{V}_{Z0}] = \mathrm{V}$

$V_{Zm}$ voltage response of the measured impedance, $[V_{Zm}] = \mathrm{V}$

$\hat{V}_{Zm}$ amplitude of the voltage response of the measured impedance, $[\hat{V}_{Zm}] = \mathrm{V}$

$v_{BV}$ difference between electrode potential and the equilibrium potential for the Butler-Volmer equation $[v_{BV}] = \mathrm{V}$

$w_x$ minimum number of measurement periods, for which a window does not suppress the measurement frequency itself, $[w_x]$ = no unit

$Y_m$ measured conductance, $[Y_m] = \frac{1}{\Omega}$

$z$ Number of electrons exchanged in an electrochemical system, $[z]$ = no unit

$Z$ complex impedance value, $[Z] = \Omega$

$Z_0$ reference impedance without any measurement deviations assuming that the measurement could be done with $I_m = 0\,\mathrm{A}$ and instantly fast, $[Z_0] = \Omega$

$Z_0^{'}$ reference impedance without any measurement deviations and without the ohmic resistance $R_\Omega$, , $[Z_0^{'}] = \Omega$

$Z_e$ absolute deviation of an electrochemical impedance measurement, $[Z_e] = \Omega$

$Z_{imag}$ imaginary part of the impedance, $[Z_{imag}] = \Omega$

$Z_m$ measured impedance, $[Z_m] = \Omega$

$Z_{OCV}$ impedance deviation caused by OCV displacement, $[Z_{OCV}] = \Omega$

$Z_{OCV/SoC}$ impedance deviation caused by OCV displacement from a change in state-of-charge. This deviation is only imaginary, $[Z_{OCV/SoC}] = \Omega$

$Z_{OCV/\vartheta}$ impedance deviation caused by OCV displacement from entropy and a change in temperature. This deviation is only imaginary, $[Z_{OCV/\vartheta}] = \Omega$

$Z_{real}$ real part of the impedance, $[Z_{real}] = \Omega$

$Z_{th}$ thermal impedance, $[Z_{th}] = \frac{\mathrm{J}}{\mathrm{W}}$

$Z_{\not\Theta}$ temperature independent part of the impedance, $[Z_{\not\Theta}] = \Omega$

$Z_{\Theta}$ temperature dependent part of the impedance, $[Z_{\Theta}] = \Omega$

$Z_W$ Warburg impedance, $[Z_W] = \Omega$

# List of Figures

1.1 Graphical overview of the thesis. . . . . 5

2.1 Construction of a li-ion battery cell and its equivalent electrical circuit for the inner resistance. . . . . 8
2.2 Overpotential of charge transfer reaction following a Butler-Volmer equation. . . . . 11
2.3 $\Delta S$ measurement methods (cylindrical NMC-cell A.2, $\hat{I}_m = 3\,\mathrm{CA}$, $SoC_{start} = 50\,\%$, $f_m = 1\,\mathrm{mHz}$) . . . . . 12
2.4 Comparison of the results of the $\delta V/\delta T$ method and the $Q_{rev}$ method with $f_m = 1\,\mathrm{mHz}$ (cylindrical NMC-cell A.2). . . . . 13
2.5 Current pulse method versus electrochemical impedance spectroscopy. . . . . 15
2.6 Excitation Signals used for EIS measurements (synthetic data). . . . . 17
2.7 DFT principle. . . . . 19
2.8 Comparison of the frequency response of the DFT (DFT), the Goertzel algorithm (Goertzel), the sliding DFT (sDFT), the sliding Goertzel algorithm (sGoertzel) and the ‘power spectrum of the cross-correlation’ (PSX) used with a rectangular box window ( $f_m = 10\,\mathrm{Hz}$, $T_a = 10 \cdot T_m$ ). . . . . 21
2.9 Possible measurement deviations occurring by the Fourier transformation with DFT (synthetic data). . . . . 22

3.1 Possible sources of measurement deviation during an electrochemical impedance measurement. . . . . 26
3.2 Impedance dependency on SoC for cylindrical cells with different li-ion chemistries (LFP-cell A.1, NMC-cell A.2, LCO-cell A.3, NCA-cell A.4, $\vartheta = 25\,^\circ\mathrm{C}$, $f_m = 10\,\mathrm{mHz}$). . . 29
3.3 Changes of SoC and subsequent simulated changes in impedance and voltage response during an impedance measurement. (cylindrical LFP-cell A.1, $\hat{I}_m = 3.0\,\mathrm{CA}$, $SoC_{start} = 30\,\%$, $\vartheta = 25\,^\circ\mathrm{C}$, $f_m = 10\,\mathrm{mHz}$). . . . . 30
3.4 Measurement deviation caused by SoC change during impedance measurements with different excitation current magnitudes. (cylindrical cells A.1 to A.4, $SoC_{start} = 30\,\%$, $\vartheta = 25\,^\circ\mathrm{C}$, $f_m = 10\,\mathrm{mHz}$). . . . . 32
3.5 Measurement deviation caused by SoC change during impedance measurements at different SoCs. (cylindrical cells A.1 to A.4, $\hat{I}_m = 0.5\,\mathrm{CA}$, $\vartheta = 25\,^\circ\mathrm{C}$, $f_m = 10\,\mathrm{mHz}$). . . 33
3.6 Comparison of equation 3.25 with a linear impedance to SoC dependency to a simulation with an impedance resolution of 1 % (cylindrical LFP-cell A.1, $SoC_{start} = 30\,\%$, $\vartheta = 25\,^\circ\mathrm{C}$, $f_m = 10\,\mathrm{mHz}$). . . . . 34
3.7 Harmonics caused by a change in voltage response due to the SoC change during impedance measurements. (cylindrical LFP-cell A.1, $\hat{I}_m = 3\,\mathrm{CA}$, $SoC_{start} = 30\,\%$, $\vartheta = 25\,^\circ\mathrm{C}$, $f_m = 10\,\mathrm{mHz}$). . . . . 36

3.8 Introducing an additional current at half the measurement frequency eliminates the measurement deviation introduced by SoC change. Figure shows change in SoC and subsequent changes in impedance and voltage response during an impedance measurement (cylindrical LFP-cell A.1, $\hat{I}_{Tm} = 1\,\mathrm{CA}$, $\hat{I}_{2 \cdot Tm} = -1\,\mathrm{CA}$, $\varphi_{2 \cdot Tm} = 0\,°$, $SoC_{start} = 30\,\%$, $\vartheta = 25\,°\mathrm{C}$, $f_m = 10\,\mathrm{mHz}$). . . . . . . . . . . . . . . . . . . . . . . . . 36

3.9 Changes of SoC and subsequent changes in impedance and voltage response due to constant charging during an impedance measurement. (cylindrical LFP-cell A.1, $I_{dc} = \frac{3.0}{\pi}\mathrm{CA}$, $SoC_{start} = 30\,\%$, $\vartheta = 25\,°\mathrm{C}$, $f_m = 10\,\mathrm{mHz}$). The figure shows simulated values and only the effect of the constant current. $\Delta v_{bat}$ assumes a sinusoidal excitation current of 0.5 CA but only shows the effect of the impedance change caused by the constant current. The figure therefore omits for all waveforms the changing SoC effect of the sinusoidal excitation current. . . . . . . . . . . . . . . . . . . . . . . . . . . . . . . 38

3.10 Measurement deviation from SoCs change caused by constant current charging during impedance measurements. (LFP-cell A.1, NMC-cell A.2, LCO-cell A.3, NCA-cell A.4, $SoC_{start} = 30\,\%$, $\vartheta = 25\,°\mathrm{C}$, $f_m = 10\,\mathrm{mHz}$). . . . . . . . . . . . . . . . . . . . . . . . . 40

3.11 Measurement deviation caused by SoC change due to a constant charging current during the impedance measurement at different SoCs (LFP-cell A.1, NMC-cell A.2, LCO-cell A.3, NCA-cell A.4, constant current charge rate $= \frac{3}{\pi}\mathrm{CA}$, $SoC_{start} = 30\,\%$, $\vartheta = 25\,°\mathrm{C}$, $f_m = 10\,\mathrm{mHz}$). . . . . . . . . . . . . . . . . . . . . . . . . . . . . . . . . 40

3.12 Temperature dependency of the impedance at different measurement frequencies. (NMC pouch cell A.5, $SoC = 50\,\%$). . . . . . . . . . . . . . . . . . . . . . . . . . . . . . 43

3.13 Frequency dependency of the parameter $\Theta$ for the real and imaginary part of the impedance at $10\,\%$ and $50\,\%$ $SoC$ (NMC pouch cell A.5, fitting range $\vartheta = 15$ to $45\,°\mathrm{C}$). 45

3.14 Frequency dependency of the temperature independent part of the impedance $Z_{\not\vartheta}$ at 10% and 50% $SoC$ (NMC pouch cell A.5, fitting range $\vartheta = 15$ to $45°C$). . . . . . . . . 45

3.15 Simulated impedance change from entropy heating caused by the excitation current during the impedance measurement. The graphs show no transitory effect but show one period of a theoretically infinitely long applied excitation current (NMC pouch cell A.5, $SoC = 50\,\%$, $f_m = 10\,\mathrm{mHz}$). . . . . . . . . . . . . . . . . . . . . . . . . . . . 48

3.16 Maximum measurement deviation by temperature change from entropy heating caused by the excitation current dependent on the measurement frequency and C-rates (NMC pouch cell A.5, $SoC = 50\,\%$, $\vartheta = 25\,°\mathrm{C}$). . . . . . . . . . . . . . . . . . . . . . . . . 48

3.17 Measurement Setup. . . . . . . . . . . . . . . . . . . . . . . . . . . . . . . . . . . 50

3.18 Measurement Principle. . . . . . . . . . . . . . . . . . . . . . . . . . . . . . . . . 50

3.19 Heat generation rate for sinusoidal currents. measured by direct measurements in an ARC and indirect measurements by EIS (cylindrical LFP-cell A.1, $SoC = 50\,\%$, $\vartheta = 40\,°\mathrm{C}$, $\hat{I}_m = 3\,\mathrm{CA}$). . . . . . . . . . . . . . . . . . . . . . . . . . . . . . . . . 52

3.20 Proof of the consistency of the EIS measurement as an indicator for the heat generation rate for different SoCs, current amplitudes and temperatures (cylindrical LFP-cell A.1). 53

3.21 Simulated impedance change from the alternating part of the impedance heating caused by the excitation current during the impedance measurement (NMC pouch cell A.5, $SoC = 50\,\%$, $f_m = 10\,\mathrm{mHz}$). . . . . . . . . . . . . . . . . . . . . . . . . . . . 54

3.22 Measurement deviation by temperature change from impedance heating caused by the excitation current dependent on the measurement frequency and measurement current amplitude (NMC pouch cell A.5, $SoC = 50\,\%$). . . . . . . . . . . . . . . . . . . . . . . 55

3.23 Decomposition of pulse trains into their harmonic components (synthetic data). . . . . 56

3.24 Heat generation rate of a pulsed current measured by direct measurements in an ARC and indirect EIS measurements of $Z_{real}$ (cylindrical LFP-cell A.1, $SoC = 50\,\%$, $\vartheta = 40\,°C$, $\hat{I}_{pulse} = 3\,CA$, $D = 50\,\%$). . . . . 57

3.25 Principle of the temperature prediction during a constant charge/discharge event. . . . 58

3.26 $I_{cell}$ in this graph is a short current pulse in order to generate a heat pulse inside the cell. $\vartheta_{cell}$ is the temperature measured on the casing of the cell, which increases according to a $1^{st}$-order lag element. The phase delay $\tau_D$ is the time constant of this $1^{st}$-order lag element (synthetic data). . . . . 59

3.27 Determination of phase delay $\Delta\Phi$ due to heat transfer in the cell. . . . . 59

3.28 Determining the charge/discharge impedance heating by extrapolating the diffusion branch of the graph of the heat generation rate (cylindrical NMC-cell A.2, $SoC_{start} = 50\,\%$, $\vartheta = 40\,°C$, $\hat{I}_m = 1.27\,CA$). . . . . 60

3.29 Measured and estimated heat flux and temperature over SoC for a constant current charge event with 1 CA (cylindrical NMC-cell A.2). . . . . 61

3.30 Measured and estimated heat flux and temperature over SoC for a constant current discharge event with 1 CA (cylindrical NMC-cell A.2). . . . . 62

3.31 Impedance change caused by the constant part of the excitation current's impedance heating during the impedance measurement (NMC pouch cell A.5, $SoC = 50\,\%$, $f_m = 10\,mHz$). . . . . 64

3.32 Measurement deviation by temperature change from the constant part of the excitation current's impedance heating dependent on the measurement frequency and excitation current amplitude (NMC pouch cell A.5, $SoC = 50\,\%$). . . . . 65

3.33 The origin of the OCV displacement is a change in SoC in combination with the OCV curve of the cell. . . . . 66

3.34 Time-domain voltages during an EIS measurement of the pristine impedance response $V_{Z0}$, the displacement in open circuit voltage $V_{OCV}$ and the sum of the two $V_{Zm}$. Simulation in which the SoC sweeps from 50 % to around 76.5 % during the measurement making it possible to see the effect of the OCV displacement. ($\hat{I}_m = 3\,CA$, $SoC_{start} = 50\,\%$, $\vartheta = 25\,°C$, $f_m = 1\,mHz$). . . . . 67

3.35 OCV and Change of OCV for cylindrical cells with different li-ion chemistries (LFP-cell A.1, NMC-cell A.2, LCO-cell A.3, NCA-cell A.4, $\vartheta = 25\,°C$). . . . . 68

3.36 Harmonics of the real and imaginary part normalized to the amplitude of the fundamental for the combined response of the voltage drop over the impedance and the OCV change from figure 3.34b (cylindrical NMC-cell A.2, $\hat{I}_m = 3\,CA$, $SoC_{start} = 50\,\%$, $\vartheta = 25\,°C$, $f_m = 1\,mHz$). . . . . 69

3.37 Visualization of the superposition of the real Impedance voltage $V_{Z0}$, the impact of the change in Open-Circuit-Voltage $V_{OCV}$ and the resulting measured voltage $V_{Zm}$. . . 70

3.38 Measurement deviation due to the change in OCV during an impedance measurement. The figure shows the measured impedance $Z_m$, the deviation caused by OCV displacement determined by a simulation $Z_{OCV/sim}$ and by the linear estimation $Z_{OCV/SoC}$ according to equation 3.120 and the corrected impedance $Z_0$ (cylindrical NMC-cell A.2, $\hat{I}_m = 0.5\,CA$, $\vartheta = 25\,°C$, $f_m = 10\,mHz$). . . . . 72

3.39 Imaginary measurement deviations for EIS measurement frequencies from 1 mHz to 500 Hz (cylindrical NMC-cell A.2, $\hat{I}_m = 0.5\,CA$, $SoC_{start} = 50\,\%$, $\vartheta = 25\,°C$). . . . . 73

3.40 The origin of the OCV displacement is a change in temperature in combination with the entropy $\Delta S$ of the cell. . . . . . 73
3.41 Comparison between the entropy $\Delta S$ and the OCV difference to $\vartheta = 25\,°\mathrm{C}$ at $5\,°\mathrm{C}$, $15\,°\mathrm{C}$ and $35\,°\mathrm{C}$ (cylindrical NMC-cell A.2). . . . . . 74
3.42 Comparison of the measurement deviation introduced by SoC change $e_{OCV/SoC}$ and introduced by temperature change $e_{OCV/\vartheta}$ (cylindrical NMC-cell A.2, $\vartheta = 25\,°\mathrm{C}$). . . . 75
3.43 Two single Butler-Volmer equations, their series connection and the attempt to fit the series connection with a single Butler-Volmer equation. ($i_{0C} = 0.5$, $i_{0A} = 0.25$, $\alpha_C = 0.5$, $\alpha_A = 0.35$). . . . . . 78
3.44 Different options to approximate two in-series Butler-Volmer equations. . . . . . 78
3.45 Sum of two Butler-Volmer equations according to equation 3.128, fitted by a single Butler-Volmer equation, a serial and a parallel circuit ($i_{0C} = 0.5\,\mathrm{A}$, $i_{0A} = 0.25\,\mathrm{A}$, $\alpha_C = 0.5$, $\alpha_A = 0.35$). The fitting was done for the current interval from $-2.5\,\mathrm{A}$ to $2.5\,\mathrm{A}$. . . . . . 79
3.46 $\mathrm{r}^2$ value for the fitting of a double Butler-Volmer equation 3.128 with a single Butler-Volmer equation 3.129, with the serial circuit (equation 3.130) and with the parallel circuit (equation 3.131). . . . . . 80
3.47 Non-linearity for different SoCs measured with the charge/discharge method (cylindrical NMC-cell A.2). . . . . . 81
3.48 Comparison of two different methods to measure the non-linearity of impedance. . . . 82
3.49 Fundamental and harmonics of the current created by a sinusoidal voltage applied to a Butler-Volmer equation ($V_{dc} = 0.1V$, $\hat{V}_m = 0.1\,\mathrm{V}$, $i_0 = 0.5 + 2\mathrm{i}\,\mathrm{A}$, $\alpha = 0.65 + j0.45$). The values for $V_{dc}$, $\hat{V}_m$ were intentionally chosen large, in order to obtain large values for the harmonics. . . . . . 84
3.50 Ratios of the modified Bessel function of the first kind $\mathcal{I}_n(x)$. The argument $\frac{-\alpha z F \hat{V}_m}{RT}$ with $\alpha = 0.5$ would have a value of around 0.1 when $\hat{V}_m = 10\,\mathrm{mV}$ (minimum shown here) and 2.0 when $\hat{V}_m = 100\,\mathrm{mV}$ (maximum shown here). . . . . . 86
3.51 Theoretical model of the non-linearity of the charge transfer resistance $R_{ct}$ and the double layer capacity $C_{dl}$. . . . . . 87
3.52 Piecewise current over voltage curve reconstruction with the knowledge of the impedance over current. . . . . . 88
3.53 Impedance non-linearity dependency on frequency of a full cell. (cylindrical LFP cell A.1, $\vartheta = 25\,°\mathrm{C}$, $SoC = 50\,\%$). For reasons of clarity only a subset of the measured points is shown. Raw measurements taken by [36]. . . . . . 89
3.54 Impedance non-linearity dependence on temperature of a full cell Lithium-Ion battery cell. (cylindrical LFP cell A.1, $f_m = 1\,\mathrm{Hz}$, $SoC = 50\,\%$). For reasons of clarity only a subset of the measurement points are shown. Raw measurements taken by [36]. . . . . 90
3.55 Measurement deviation caused by the non-linearity of a battery cell (synthetic data with the parameters $i_0 = 1\,\mathrm{A}$, $R_\Omega = 0\,\mathrm{m\Omega}$, $r = 10\,\mathrm{m\Omega}$). . . . . . 92
3.56 Measurement deviation caused by the impedance non-linearity of a battery cell (cylindrical LFP-cell A.1, $SoC_{start} = 50\,\%$). . . . . . 93
3.57 $i_0$ modifying factor and impedance measurement deviation depending on the magnitude of a constant positive overvoltage $V_{dc} = HGR_{dc} \cdot I_{dc}$ ($I_{dc} = 0$ to $1\,\mathrm{CA}$, $HGR_{dc} = 50\,\mathrm{m\Omega}$). . . . . . 95

3.58 Measurement deviation caused by the non-linearity of a battery cell depending on the measurement frequency (cylindrical LFP-cell A.1, $SoC_{start} = 50\,\%$, $\vartheta = 25\,°\mathrm{C}$, $\hat{I}_m = 0.5\,\mathrm{CA}$). . . . . . 96

3.59 Impedance measurement deviation components depending on measurement frequency $f_m$. ‘$\Sigma$’: sum of all components, ‘BV’: deviation from impedance non-linearity, ‘$\vartheta_i$’: deviation from temperature increase by impedance heating, ‘SoC’: deviation from State-of-Charge change, ‘$\vartheta_e$’: deviation from temperature increase by entropy heating, ‘$V_{limit}$’: deviation limit from 10 mV-Criterion (cylindrical LFP-cell A.1, $SoC_{start} = 50\,\%$, $\vartheta = 25\,°\mathrm{C}$, $\hat{I}_m = 1\,\mathrm{CA}$). . . . . . 100

3.60 Impedance measurement deviation depending on cell temperature $\vartheta_{cell}$. ‘$\Sigma$’: sum of all components, ‘BV’: deviation from impedance non-linearity, ‘$\vartheta_i$’: deviation from temperature increase by impedance heating, ‘SoC’: deviation from State-of-Charge change, ‘$\vartheta_e$’: deviation from temperature increase by entropy heating, ‘$V_{limit}$’: deviation limit from 10 mV-Criterion (cylindrical LFP-cell A.1, $SoC_{start} = 50\,\%$, $f_m = 1\,\mathrm{Hz}$, $\hat{I}_m = 3\,\mathrm{CA}$). . . . . . 101

3.61 Impedance measurement deviation depending on measurement frequency $f_m$ with underlying constant current when comparing the measurement to a measurement at no underlying constant current. ‘$\Sigma$’: sum of all components, ‘BV’: deviation from impedance non-linearity, ‘DC’: deviation from constant current, ‘SIN’: deviation from sinusoidal excitation current (cylindrical LFP-cell A.1, $SoC_{start} = 50\,\%$, $\vartheta = 25\,°\mathrm{C}$, $\hat{I}_m = 1\,\mathrm{CA}$, $I_{dc} = 0.5\,\mathrm{CA}$). . . . . . 102

4.1 Sequence for switched-mode EIS excitation. . . . . . 106

4.2 Overview over the different drift compensation methods. . . . . . 108

4.3 Time-domain and complex plane representation of a linear drift correction in time-domain (synthetic data). . . . . . 110

4.4 Comparison of the frequency response of the Box, Kaiser, Hamming, Blackman-Nuttal and the Flat-Top window in combination with a DFT ($f_m = 10\,\mathrm{Hz}$, $T_a = 10 \cdot T_m$). . . . 111

4.5 Time-domain and complex plane representation of a linear drift suppression by windowing (synthetic data). . . . . . 112

4.6 Harmonics calculation of the real and imaginary part for a linear drift (synthetic data). 115

4.7 Time-domain, complex plane and frequency-domain representation of a linear drift correction in the frequency-domain (synthetic data). . . . . . 116

4.8 Harmonics calculation of the real and imaginary part for an exponential drift (synthetic data). . . . . . 120

4.9 Time-domain, complex plane and frequency-domain representation of an exponential drift correction in the frequency-domain (synthetic data). . . . . . 121

4.10 Correction comparison of an exponential drift (synthetic data). . . . . . 122

4.11 Comparison of different correction methods on a EIS sinus-sweep measurement (cylindrical NCA cell A.4). . . . . . 123

4.12 Simplified schematic of a EIS meter and simplified equivalent circuit of a battery. . . . 125

4.13 Measurement deviation from parasitic shunt impedance for different values of $\frac{L_{sh}}{R_{sh}}$ (battery values from cylindrical LFP cell A.1, $R_\Omega = 16.2\,\mathrm{m\Omega}$, $L_{bat} = 228\,\mathrm{nH}$). . . . . . 126

4.14 Nyquist curve ‘twists’ counter-clockwise for higher measurement frequencies explained by the parasitic shunt inductance. EIS measurements and fit with equation 4.40 (cylindrical LFP cell A.1, $f_m = 100\,\mathrm{mHz}$ to $50\,\mathrm{kHz}$). . . . . . 127

4.15 Half Bridge for switched mode excitation. . . . . . . . . . . . . . . . . . . . . . . . . . . 128
4.16 Pulse width modulation process with a sawtooth triangle carrier and a sinusoidal reference signal ($M$= 0.7, synthetic data). . . . . . . . . . . . . . . . . . . . . . . . . . 128
4.17 Fundamental, harmonics and sidebands of a sawtooth trailing edge pulse width modulation process ($\frac{\omega_c}{\omega_m} = 16$ and $M = 0.10$, synthetic data). . . . . . . . . . . . . . . . . . 129
4.18 Aliasing of an impedance response from a frequency $f_h$ higher than the Nyquist theorem to the measurement frequency $f_m$ (synthetic data). . . . . . . . . . . . . . . . . 130
4.19 Modulus and phase deviation of the measurement frequency according to equation 4.47 and 4.44 depending on the phase $\phi_{fh}$ and modulus $A_{fh}$ of the higher frequency harmonic $f_h$ (synthetic data). . . . . . . . . . . . . . . . . . . . . . . . . . . . . . . . . 132
4.20 Topologies for stimulus generation: 'Battery Charger Topology', 'Balancing Unit Topology' and 'DC Supply Topology'. . . . . . . . . . . . . . . . . . . . . . . . . . . . . . . . 133
4.21 Battery Charger Topology. . . . . . . . . . . . . . . . . . . . . . . . . . . . . . . . . . . 134
4.22 Time-domain and frequency-domain signals for the Battery Charger Topology ($f_m = 1\,\text{kHz}$, $f_c = 16\,\text{kHz}$, measured signals except for $Y_{va}^{theory}$). . . . . . . . . . . . . . . . . 136
4.23 Measured Impedance with the Battery Charger Topology ($\hat{I}_m = 200\,\text{mA}$, $f_m = 10\,\text{mHz}$ to $2\,\text{kHz}$, $f_c = 64\,\text{kHz}$) compared to a reference measurement with the EISmeter (1 % accuracy modulus, 1 ° accuracy phase). . . . . . . . . . . . . . . . . . . . . . . . . . . . 137
4.24 Balancing Unit Topology. . . . . . . . . . . . . . . . . . . . . . . . . . . . . . . . . . . . 137
4.25 Time-domain and frequency-domain signals for the Balancing Unit Topology with a non-modulated duty cycle of 50 % ($f_m = 500\,\text{Hz}$, $f_c = 8\,\text{kHz}$, measured signals except for $Y_{v_{bat}}^{theory}$). . . . . . . . . . . . . . . . . . . . . . . . . . . . . . . . . . . . . . . . 139
4.26 Time-domain and frequency-domain signals for the Balancing Unit Topology with a modulated duty cycle ($f_m = 500\,\text{Hz}$, $f_c = 8\,\text{kHz}$, measured signals except for $Y_{v_{bat}}^{theory}$). 140
4.27 Measured Impedance with the Balancing Unit Topology ($\hat{I}_m = 200\,\text{mA}$, $f_m = 10\,\text{mHz}$ to $2\,\text{kHz}$, $f_c = 64\,\text{kHz}$). . . . . . . . . . . . . . . . . . . . . . . . . . . . . . . . . 141
4.28 DC Supply Topology. . . . . . . . . . . . . . . . . . . . . . . . . . . . . . . . . . . . . . 142
4.29 Time-domain and frequency-domain signals of the battery current $i_{bat}$ and the battery response voltage $v_{in}$ for the DC Supply Topology with 2 mF input capacitor ($f_m = 1\,\text{kHz}$, $f_c = 16\,\text{kHz}$, measured signals except for $Y_{i_{in}}^{theory}$). . . . . . . . . . . . . . . . 143
4.30 Measured Impedance with the DC Supply Topology ($\hat{I}_m = 200\,\text{mA}$, $f_m = 10\,\text{mHz}$ to $2\,\text{kHz}$, $f_c = 64\,\text{kHz}$) compared to a reference measurement with the EISmeter (1 % accuracy modulus, 1 ° accuracy phase). . . . . . . . . . . . . . . . . . . . . . . . . . . . 144
4.31 Total harmonic distortion depending on the DC-link voltage factor $\frac{V_{dc}}{V_{bat}}$ and signal amplitude $s$. . . . . . . . . . . . . . . . . . . . . . . . . . . . . . . . . . . . . . . . . . 147
4.32 Time-domain waveforms of the inductor current $i_L$, the battery current $i_{bat}$, the output voltage $v_{out}$ and the duty cycle of the Battery Charger Topology. Spectrum of the switched output voltage $v_a$ (measured values), the battery current $i_{bat}$ after the LC-filter (measured values) and the used filter (theoretical values) at different DC-link voltages $V_{dc}$. The amplitude of the measurement frequency at 1 kHz is normalized to 1. 148
4.33 Principle of the distortion-free frequency grid. . . . . . . . . . . . . . . . . . . . . . . . 151
4.34 Repetition of the switching frequency harmonics when the sampling frequency is set according to equation 4.77 ($m_{CH} = 3$, $p = 2$, synthetic data). . . . . . . . . . . . . . . 152
4.35 Safe lower frequency bandwidth illustration with a Blackman-Nuttal window ($n_{SB} = 4$, synthetic data). . . . . . . . . . . . . . . . . . . . . . . . . . . . . . . . . . . . . . . . 154

4.36 Example of a measurement frequency on the frequency grid with a Blackman-Nuttal window and harmonics from the Battery Charger Topology ($f_c = 4\,\text{kHz}$, $m_{CH} = 10$, $p = 9$, $q = 19$, $f_s = 4444\,\text{SPS}$, $f_m = 233.9\,\text{Hz}$). The Blackman-Nuttal window is only represented from $0.8 f_m$ to $1.2 f_m$ (synthetic data). . . . . . . . . . . . . . . . . . . . . . 157

A.1.1 Photo of a cylindrical LFP cell from A123. . . . . . . . . . . . . . . . . . . . . . . . . . . 194
A.1.2 OCV over SoC of a cylindrical LFP cell from A123. . . . . . . . . . . . . . . . . . . . . . . 194
A.1.3 Impedance dependency on SoC and temperature. . . . . . . . . . . . . . . . . . . . . . . 195
A.1.4 $\Delta S$ over SoC. . . . . . . . . . . . . . . . . . . . . . . . . . . . . . . . . . . . . . . . . 195
A.1.5 Impedance non-linearity dependence on SoC ($\vartheta = 25\,°C$, $SoC = 50\,\%$). For reasons of clarity only a subset of the measured points is shown. Raw measurements taken by [36]. 196
A.2.1 Photo of a cylindrical NMC cell. . . . . . . . . . . . . . . . . . . . . . . . . . . . . . . . 197
A.2.2 OCV over SoC of a cylindrical NMC cell. . . . . . . . . . . . . . . . . . . . . . . . . . . . 197
A.2.3 Impedance dependency on SoC and temperature. . . . . . . . . . . . . . . . . . . . . . . 198
A.2.4 $\Delta S$ over SoC. . . . . . . . . . . . . . . . . . . . . . . . . . . . . . . . . . . . . . . . . 198
A.3.1 Photo of a cylindrical LiCoO cell. . . . . . . . . . . . . . . . . . . . . . . . . . . . . . . 199
A.3.2 OCV over SoC of a cylindrical LCO cell. . . . . . . . . . . . . . . . . . . . . . . . . . . . 199
A.3.3 Impedance dependency on SoC and temperature. . . . . . . . . . . . . . . . . . . . . . . 200
A.4.1 Photo of a cylindrical NCA cell. . . . . . . . . . . . . . . . . . . . . . . . . . . . . . . . 201
A.4.2 OCV over SoC of a cylindrical NCA cell. . . . . . . . . . . . . . . . . . . . . . . . . . . . 201
A.4.3 Impedance dependency on SoC and temperature. . . . . . . . . . . . . . . . . . . . . . . 202
A.5.1 Photo of an NMC pouch cell from DOW KOKAM. . . . . . . . . . . . . . . . . . . . . . . 203
A.5.2 OCV over SoC of an NMC pouch cell from DOW KOKAM. . . . . . . . . . . . . . . . . . 203
A.5.3 Impedance dependency on SoC and temperature. . . . . . . . . . . . . . . . . . . . . . . 204
A.5.4 $\Delta S$ over SoC. . . . . . . . . . . . . . . . . . . . . . . . . . . . . . . . . . . . . . . . . 204

B.0.1 Developed prototype used as an experimental platform for EIS measurements with switched-mode excitation. . . . . . . . . . . . . . . . . . . . . . . . . . . . . . . . . . . 205

C.4.1 Bessel function of the first kind. . . . . . . . . . . . . . . . . . . . . . . . . . . . . . . . 210
C.5.1 Modified Bessel function of the first kind. . . . . . . . . . . . . . . . . . . . . . . . . . . 212
C.6.1 Factor $j^x$. . . . . . . . . . . . . . . . . . . . . . . . . . . . . . . . . . . . . . . . . . . 213

E.1.1 Harmonics of the Battery Charger Topology determined with the Double Fourier Integral theory and a simulation with subsequent DFT. . . . . . . . . . . . . . . . . . . . . 223
E.2.1 Battery Charger Topology. . . . . . . . . . . . . . . . . . . . . . . . . . . . . . . . . . . 223
E.2.2 Generated voltage and current of the Battery Charger Topology (synthetic data). . . . 223
E.2.3 Harmonics of the Battery Charger Topology with DC-link adjustment determined with the Double Fourier Integral theory and a simulation with subsequent DFT. . . . . . . 227
E.3.1 Balancing Unit Topology. . . . . . . . . . . . . . . . . . . . . . . . . . . . . . . . . . . . 227
E.3.2 Generated voltage and current of the Balancing Unit Topology (synthetic data). . . . . 227
E.3.3 Harmonics of the Balancing Unit Topology determined with the Double Fourier Integral theory and a simulation with subsequent DFT. . . . . . . . . . . . . . . . . . . . . 230
E.4.1 Battery DC Supply Topology. . . . . . . . . . . . . . . . . . . . . . . . . . . . . . . . . . 230
E.4.2 Generated voltage and current of the Battery DC Supply Topology (synthetic data). . 230
E.4.3 Harmonics of the DC Supply Topology determined by the Double Fourier Integral theory and a simulation with subsequent DFT. . . . . . . . . . . . . . . . . . . . . . . . 237

# List of Tables

2.1 Negative electrode types, their acronyms and chemical formulas. . . . . . . . . . . . . . 8
2.2 Positive electrode types, their acronyms and chemical formulas. . . . . . . . . . . . . . . 9

3.1 Parameters $\Theta$ and $Z_{\varnothing}$ used for drawing the solid lines in figure 3.12. . . . . . . . . . . . 43
3.2 Comparison of the THD caused by an OCV change during an EIS measurement (LFP-cell A.1, NMC-cell A.2, $f_m = 1\,\mathrm{mHz}$, $\hat{I}_m = 3\,\mathrm{CA}$). . . . . . . . . . . . . . . . . . . . . . . . 69
3.3 Selected Microcycle-Impedance non-linearity measurements of the real and imaginary part fitted with the modified Butler-Volmer equation of 3.131. Parameter dependency on frequency. Raw measurements taken by [36]. . . . . . . . . . . . . . . . . . . . . . . . . 89
3.4 Selected Microcycle-Impedance non-linearity measurements of the real and imaginary part fitted with the modified Butler-Volmer equation of 3.131. Parameter dependency on temperature. Raw measurements taken by [36]. . . . . . . . . . . . . . . . . . . . . . . 90
3.5 Battery cell specific variables (1st column), their description (2nd column), from which battery cell parameter they can be derived (3rd column) and from which parameters the variable is dependent on (4th to 6th column). . . . . . . . . . . . . . . . . . . . . . . . 99

4.1 Numerical data for the correction comparison of a linear drift from figure 4.10a (corrected signal $Y_c$, $\Delta Y = \sqrt{\Delta Y_{real}^2 + \Delta Y_{imag}^2}$). . . . . . . . . . . . . . . . . . . . . . . . . . . 122
4.2 Numerical data for the correction comparison of an exponential drift from figure 4.10b (corrected signal $Y_c$, $\Delta Y = \sqrt{\Delta Y_{real}^2 + \Delta Y_{imag}^2}$). . . . . . . . . . . . . . . . . . . . . . . 122
4.3 Comparison of the total harmonic distortion and selective normalized harmonic frequency magnitudes for the Battery Charger Topology (values as factors of the measurement frequency amplitude $C_{01}$, measured values except for the ones with index 'theory'). 136
4.4 Deviation of two successive EIS measurements $Z_{BC1/2}$ measured with the Battery Charger Topology and the reference EIS measurement $Z_{ref}$ (for the first line: $\left|\frac{\Delta|Z|}{|Z|}\right| = \frac{|Z_{ref}|-|Z_{BC1}|}{|Z_{ref}|}$, $|\Delta\phi_Z| = |\phi_{Zref} - \phi_{ZBC1}|$, $\frac{|\Delta Z|}{|Z|} = \frac{|Z_{ref}-Z_{BC1}|}{|Z_{ref}|}$, for the other lines the same logic applies). . . . . . . . . . . . . . . . . . . . . . . . . . . . . . . . . . . . . . 137
4.5 Comparison of the total harmonic distortion and selective normalized harmonic frequency magnitudes of a non-modulated measurement frequency signal in the Balancing Unit Topology (values as factors of the measurement frequency amplitude, $f_m = 500\,\mathrm{Hz}$, $f_c = 8\,\mathrm{kHz}$, measured values except for the ones with index 'theory'). . . . . . . . . . . . 139
4.6 Total harmonic distortion and selective normalized harmonic frequency magnitudes of a modulated measurement frequency signal in the Balancing Unit Topology (values as factors of the measurement frequency amplitude, $f_m = 500\,\mathrm{Hz}$, $f_c = 8\,\mathrm{kHz}$, measured values except for the ones with index 'theory'). . . . . . . . . . . . . . . . . . . . . . . . 140

4.7 Comparison of the total harmonic distortion and selective normalized harmonic frequency magnitudes for the DC Supply Topology (values as factors of the measurement frequency amplitude, $f_m = 1\,\text{kHz}$, $f_c = 16\,\text{kHz}$, measured values except for the ones with index ‘theory’). . . . . . . . . . . . . . . . . . . . . . . . . . . . . . . . . . . . . 144
4.8 Deviation of two successive EIS measurements $Z_{DC1/2}$ measured with the DC Supply Topology and the reference EIS measurement $Z_{ref}$ (for the first line: $\left|\frac{\Delta|Z|}{|Z|}\right| = \frac{|Z_{ref}|-|Z_{DC1}|}{|Z_{ref}|}$, $|\Delta\phi_Z| = |\phi_{Zref} - \phi_{ZDC1}|$, $\frac{|\Delta Z|}{|Z|} = \frac{|Z_{ref}-Z_{DC1}|}{|Z_{ref}|}$, for the other lines the same logic applies). . . . . . . . . . . . . . . . . . . . . . . . . . . . . . . . . . . . . 144
4.9 Comparison of THD and the amplitude of the carrier frequency $C_{10}$ for the Battery Charger Topology switched output voltage $v_a$ and battery current $i_{bat}$ (signal amplitude $s = 1\,\text{A}$). . . . . . . . . . . . . . . . . . . . . . . . . . . . . . . . . . . . . . . . . 147

A.1 Specifications of a cylindrical LFP cell and measurements at $SoC = 50\,\%$, $\vartheta = 25\,°\text{C}$. . . 194
A.2 Microcycle-Impedance non-linearity measurements of the real and imaginary part fitted with the modified Butler-Volmer equation of 3.131. Parameter dependence on SoC. Raw measurements taken by [36]. . . . . . . . . . . . . . . . . . . . . . . . . . . . . . . . . . 196
A.3 Specifications of a cylindrical NMC cell and measurements at $SoC = 50\,\%$, $\vartheta = 25\,°\text{C}$. . 197
A.4 Specifications of a cylindrical LCO cell and measurements at $SoC = 50\,\%$, $\vartheta = 25\,°\text{C}$. . . 199
A.5 Specifications of a cylindrical NCA cell and measurements at $SoC = 50\,\%$, $\vartheta = 25\,°\text{C}$. . 201
A.6 Specifications of an NMC pouch and measurements at $SoC = 50\,\%$, $\vartheta = 25\,°\text{C}$. . . . . . 203

B.1 Specifications and components used in the developed prototype. . . . . . . . . . . . . . . 205

E.1 Numerical values to figure E.1.1. . . . . . . . . . . . . . . . . . . . . . . . . . . . . . . . 222
E.2 Numerical values to figure E.2.3. . . . . . . . . . . . . . . . . . . . . . . . . . . . . . . . 227
E.3 Numerical values to figure E.3.3. . . . . . . . . . . . . . . . . . . . . . . . . . . . . . . . 229
E.4 Numerical values to figure E.4.3. . . . . . . . . . . . . . . . . . . . . . . . . . . . . . . . 236

# Appendix

# A Battery Cells Used

## A.1 Cylindrical LFP Cell

Figure A.1.1: Photo of a cylindrical LFP cell from A123.

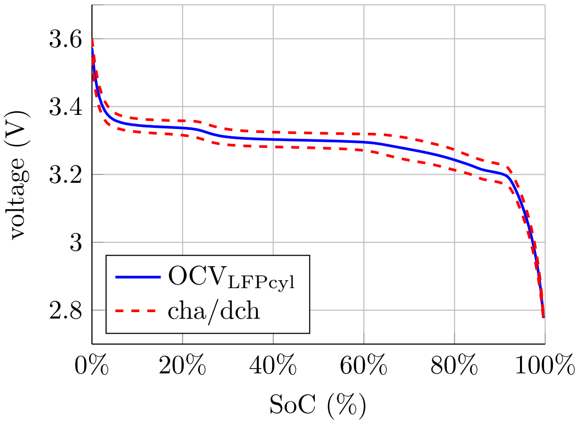

Figure A.1.2: OCV over SoC of a cylindrical LFP cell from A123.

| **parameter** | **value** | **source** |
|---|---|---|
| manufacturer | A123 systems | [4] |
| type | APR 18650 M1A | [4] |
| chemistry | $LiFePO_4$ | [5] |
| nominal capacity | 1.1 Ah | [4] |
| nominal voltage | 3.3 V | [4] |
| nominal energy | 3.63 Wh | [4] |
| outer dimensions (hxd) | 64.95x18.2 mm | [4] |
| weight | 39 g | [4] |
| voltage window | 2.0 to 3.6 V | [4] |
| std. charge current | 1.5 A | [4] |
| max. cont. charge current | 4 A | [4] |
| max. cont. discharge current | 30 A | [4] |
| $\lvert Z_i \rvert$ @ 1 kHz | N/A | |
| $R_\Omega$ | 16.2 mΩ | measurement |
| $R_{ct}$ | 18 mΩ | measurement |
| $C_{dl}$ | 0.76 F | measurement |
| $L_{bat}$ | 228 nH | measurement |
| $f_i$ | 1112 Hz | measurement |

Table A.1: Specifications of a cylindrical LFP cell and measurements at $SoC = 50\,\%$, $\vartheta = 25\,°\mathrm{C}$.

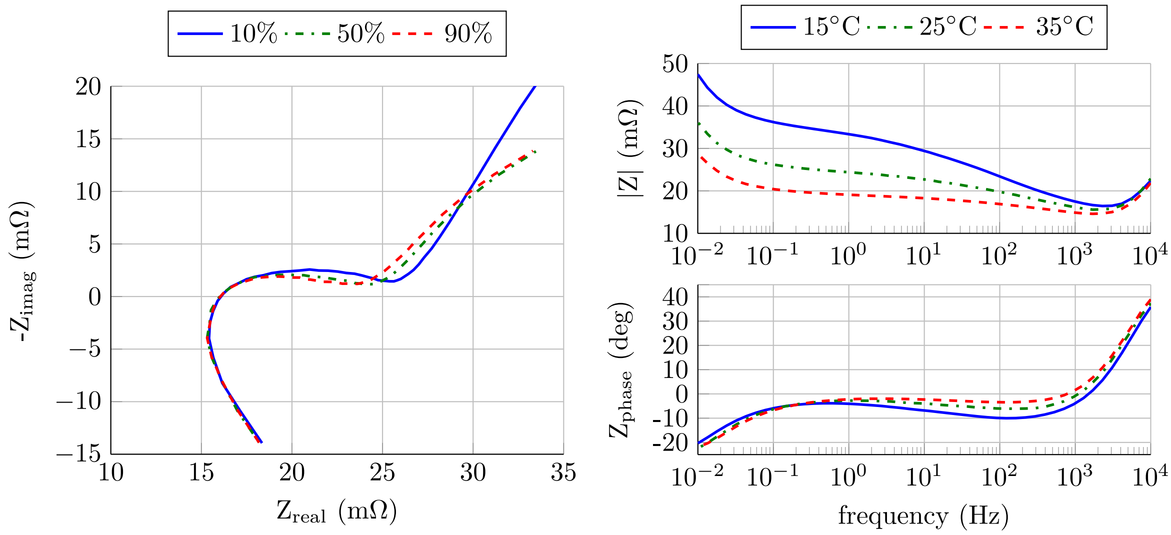

(a) Nyquist plot over SoC.

(b) Bode plot over Temperature.

Figure A.1.3: Impedance dependency on SoC and temperature.

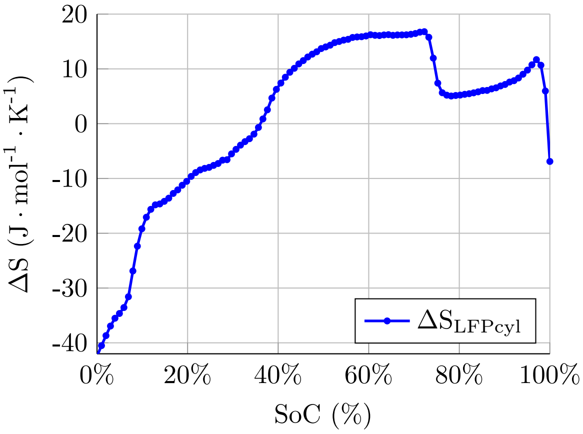

Figure A.1.4: $\Delta S$ over SoC.

| | SoC | $R_\Omega$ (m$\Omega$) | $i_0$ (A) | $\alpha$ | $r$ (m$\Omega$) | $r^2$ |
|---|---|---|---|---|---|---|
| $Z_{real}$ | 10 % | 16.2 | 0.26 | 0.39 | 17 | 0.9999 |
| | 30 % | 16.3 | 0.48 | 0.40 | 10 | 1.0000 |
| | 50 % | 16.2 | 0.33 | 0.35 | 10 | 1.0000 |
| | 70 % | 16.2 | 0.28 | 0.36 | 9 | 1.0000 |
| | 90 % | 16.2 | 0.37 | 0.38 | 10 | 1.0000 |
| $Z_{imag}$ | 10 % | 0.0 | -9.95 | 0.33 | -85 | 0.9940 |
| | 30 % | 0.0 | -18.21 | 0.05 | -20 | 0.9997 |
| | 50 % | 0.0 | -17.97 | 0.05 | -10 | 0.9968 |
| | 70 % | 0.0 | -15.44 | 0.05 | -4 | 0.9994 |
| | 90 % | 0.0 | -18.01 | 0.25 | -31 | 0.9993 |

Table A.2: Microcycle-Impedance non-linearity measurements of the real and imaginary part fitted with the modified Butler-Volmer equation of 3.131. Parameter dependence on SoC. Raw measurements taken by [36].

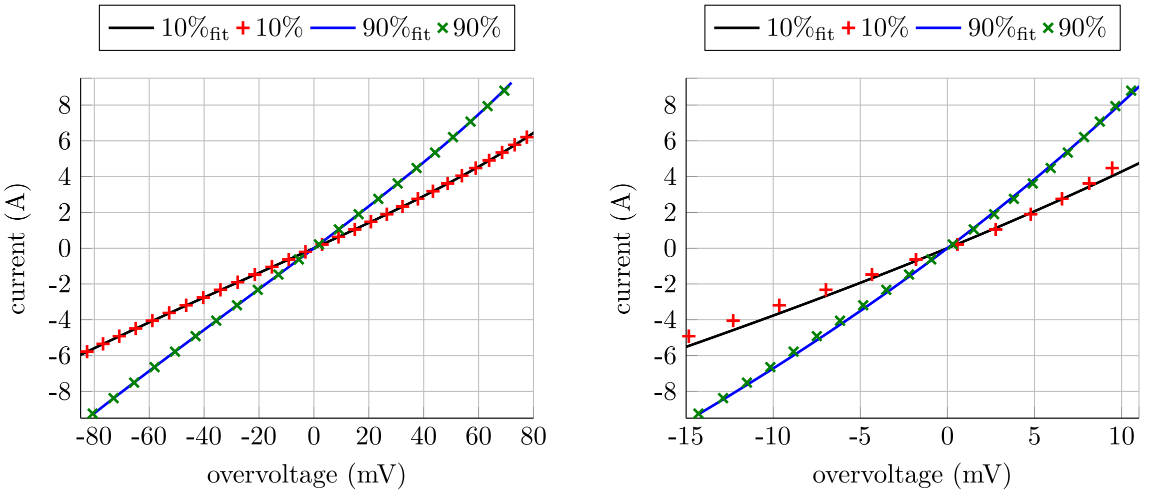

(a) Real part.

(b) Imaginary part.

Figure A.1.5: Impedance non-linearity dependence on SoC ($\vartheta = 25\,°C$, $SoC = 50\,\%$). For reasons of clarity only a subset of the measured points is shown. Raw measurements taken by [36].

## A.2 Cylindrical NMC Cell

Figure A.2.1: Photo of a cylindrical NMC cell.

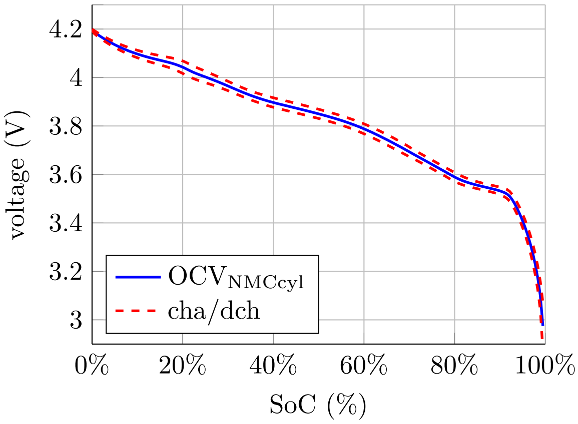

Figure A.2.2: OCV over SoC of a cylindrical NMC cell.

| **parameter** | **value** | **source** |
|---|---|---|
| manufacturer | Panasonic | [119] |
| type | UR18650 SAX | [119] |
| chemistry | $\mathrm{Li(Ni}_x\mathrm{Mn_yCo_z)O_2}$ | [120] |
| nominal capacity | 1.25 Ah | [119] |
| nominal voltage | 3.7 V | [119] |
| nominal energy | 4.625 Wh | |
| outer dimensions (hxd) | 64.8x18.1 mm | [119] |
| weight | 45 g | [119] |
| voltage window | 2.5 to 4.2 V | [119] |
| std. charge current | 0.875 A | [119] |
| max. cont. charge current | N/A | |
| max. cont. discharge current | 10 A | [119] |
| $\lvert Z_i \rvert$ @ 1 kHz | N/A | |
| $R_\Omega$ | 14.6 mΩ | measurement |
| $R_{ct}$ | 3.2 mΩ | measurement |
| $C_{dl}$ | 1.16 F | measurement |
| $L_{bat}$ | 303 nH | measurement |
| $f_i$ | 824 Hz | measurement |

Table A.3: Specifications of a cylindrical NMC cell and measurements at $SoC = 50\,\%$, $\vartheta = 25\,^\circ\mathrm{C}$.

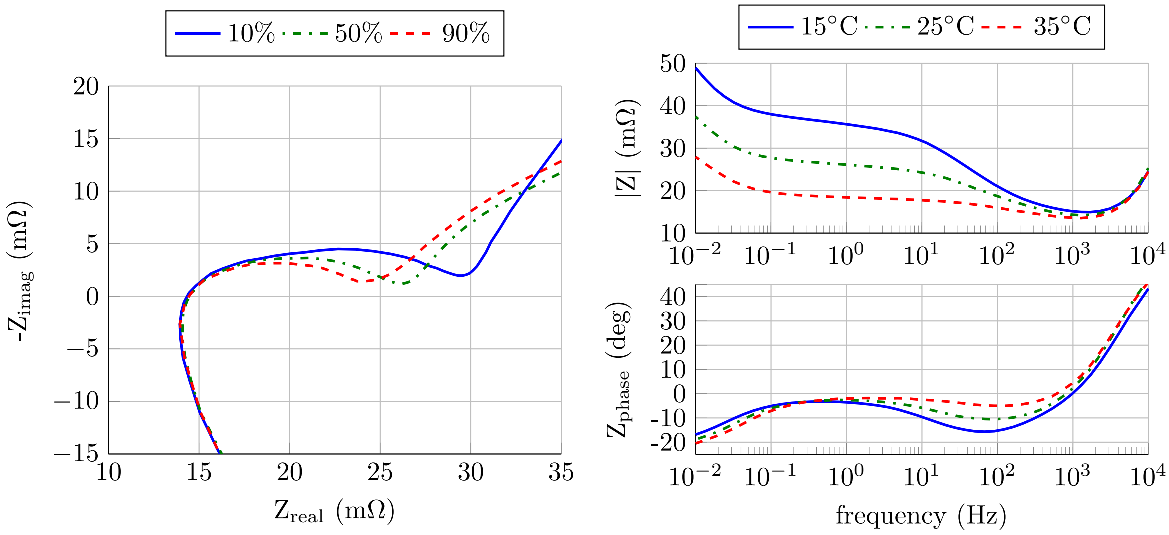

(a) Nyquist plot over SoC.

(b) Bode plot over Temperature.

Figure A.2.3: Impedance dependency on SoC and temperature.

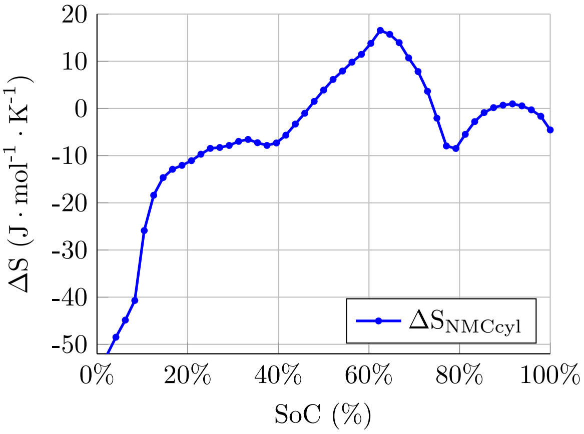

Figure A.2.4: $\Delta S$ over SoC.

## A.3 Cylindrical LCO Cell

Figure A.3.1: Photo of a cylindrical LiCoO cell.

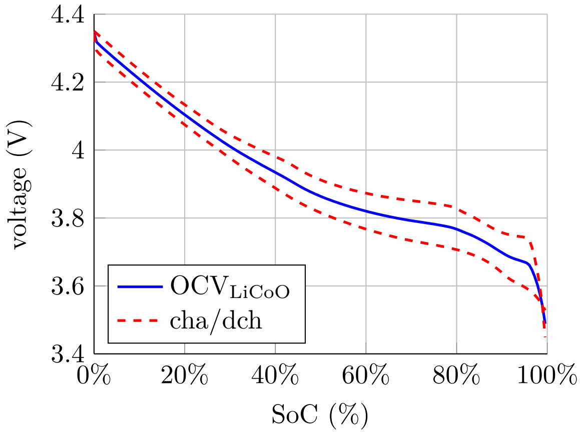

Figure A.3.2: OCV over SoC of a cylindrical LCO cell.

| parameter | value | source |
|---|---|---|
| manufacturer | Samsung SDI Co., Ltd. | [53] |
| type | ICR18650-30B | [53] |
| chemistry | $LiCoO_2$ | |
| nominal capacity | 2.95 Ah | [53] |
| nominal voltage | 3.78 V | [53] |
| nominal energy | 11.15 Wh | |
| outer dimensions (hxd) | 65.0x18.4 mm | [53] |
| weight | 48 g | [53] |
| voltage window | 2.75 to 4.35 V | [53] |
| std. charge current | 1.475 A | [53] |
| max. cont. charge current | 2.95 A | [53] |
| max. cont. discharge current | 5.9 A | [53] |
| $\lvert Z_i \rvert$ @ 1 kHz | 100 mΩ | [53] |
| $R_\Omega$ | 50 mΩ | measurement |
| $R_{ct}$ | 13 mΩ | measurement |
| $C_{dl}$ | 3.53 F | measurement |
| $L_{bat}$ | 815 nH | measurement |
| $f_i$ | 704 Hz | measurement |

Table A.4: Specifications of a cylindrical LCO cell and measurements at $SoC = 50\,\%$, $\vartheta = 25\,°\mathrm{C}$.

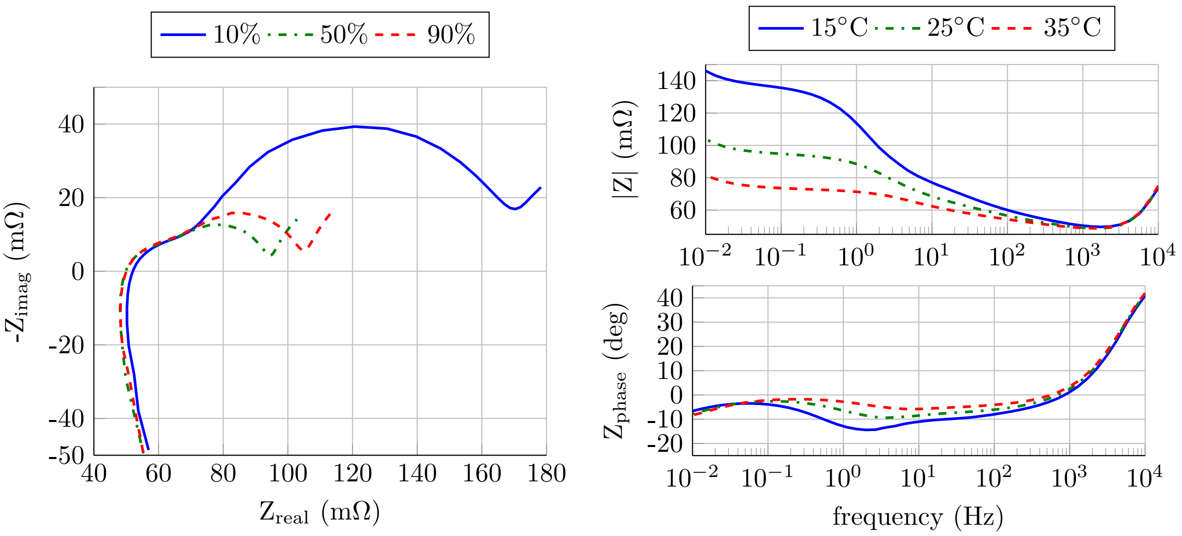

(a) Nyquist plot over SoC.

(b) Bode plot over Temperature.

Figure A.3.3: Impedance dependency on SoC and temperature.

## A.4 Cylindrical NCA Cell

Figure A.4.1: Photo of a cylindrical NCA cell.

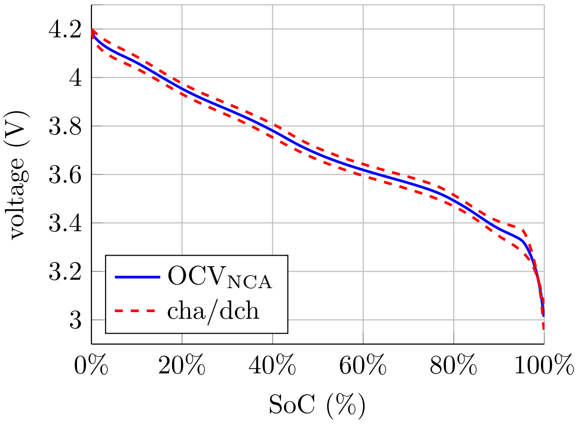

Figure A.4.2: OCV over SoC of a cylindrical NCA cell.

| parameter | value | source |
|---|---|---|
| manufacturer | Sanyo (now Panasonic) | [78] |
| type | NCR18650PD | [78] |
| chemistry | $LiNiCoAlO_2$ | |
| nominal capacity | 2.88 Ah | [78] |
| nominal voltage | 3.6 V | [78] |
| nominal energy | 10.4 Wh | [78] |
| outer dimensions (hxd) | 65.2x18.6 mm | [78] |
| weight | 46.5 g | [78] |
| voltage window | 2.5 to 4.2 V | [78] |
| std. charge current | 1.36 A | [78] |
| max. cont. charge current | N/A | |
| max. cont. discharge current | 10 A | [78] |
| $\|Z_i\|$ @ 1 kHz | 35 mΩ | [78] |
| $R_\Omega$ | 22 mΩ | measurement |
| $R_{ct}$ | 24 mΩ | measurement |
| $C_{dl}$ | 1.1 F | measurement |
| $L_{bat}$ | 412 nH | measurement |
| $f_i$ | 718 Hz | measurement |

Table A.5: Specifications of a cylindrical NCA cell and measurements at $SoC = 50\,\%$, $\vartheta = 25\,°C$.

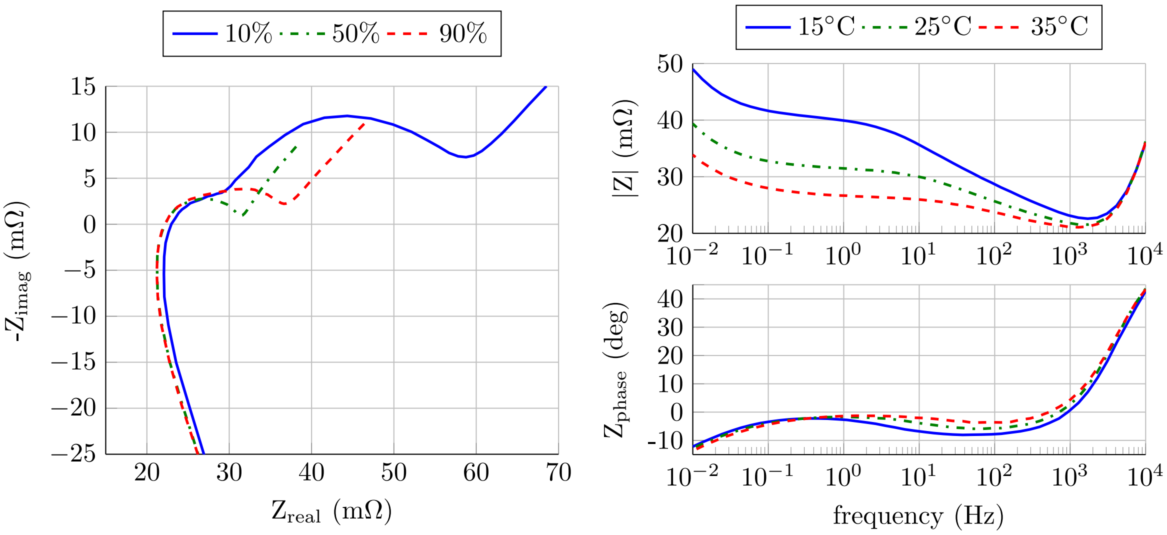

(a) Nyquist plot over SoC.

(b) Bode plot over Temperature.

Figure A.4.3: Impedance dependency on SoC and temperature.

## A.5 NMC Pouch Cell

Figure A.5.1: Photo of an NMC pouch cell from DOW KOKAM.

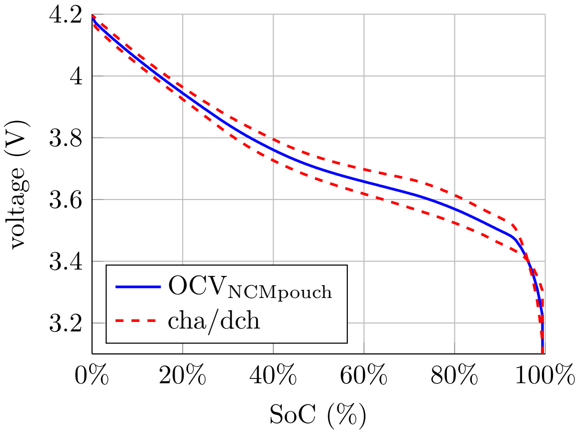

Figure A.5.2: OCV over SoC of an NMC pouch cell from DOW KOKAM.

| **parameter** | **value** | **source** |
|---|---|---|
| manufacturer | DOW KOKAM LLC | [111] |
| type | SLPB110255255H | [111] |
| chemistry | $\mathrm{Li(Ni}_x\mathrm{Mn_yCo_z)O_2}$ | [112] |
| nominal capacity | 60 Ah | [111] |
| nominal voltage | 3.7 V | [111] |
| nominal energy | 222 Wh | |
| outer dimensions (hxwxd) | 10.7x266x263 mm | [111] |
| weight | 1.49 kg | [111] |
| voltage window | 2.7 to 4.2 V | [111] |
| std. charge current | 30 A | [111] |
| max. cont. charge current | 180 A | [111] |
| max. cont. discharge current | 720 A | [111] |
| $\lvert Z_i \rvert$ @ 1 kHz | $0.45 \pm 0.10\,\mathrm{m\Omega}$ | [111] |
| $R_\Omega$ | 0.51 mΩ | measurement |
| $R_{ct}$ | 0.31 mΩ | measurement |
| $C_{dl}$ | 16.3 F | measurement |
| $L_{bat}$ | 73 µH | measurement |
| $f_i$ | 155 Hz | measurement |

Table A.6: Specifications of an NMC pouch and measurements at $SoC = 50\,\%$, $\vartheta = 25\,°\mathrm{C}$.

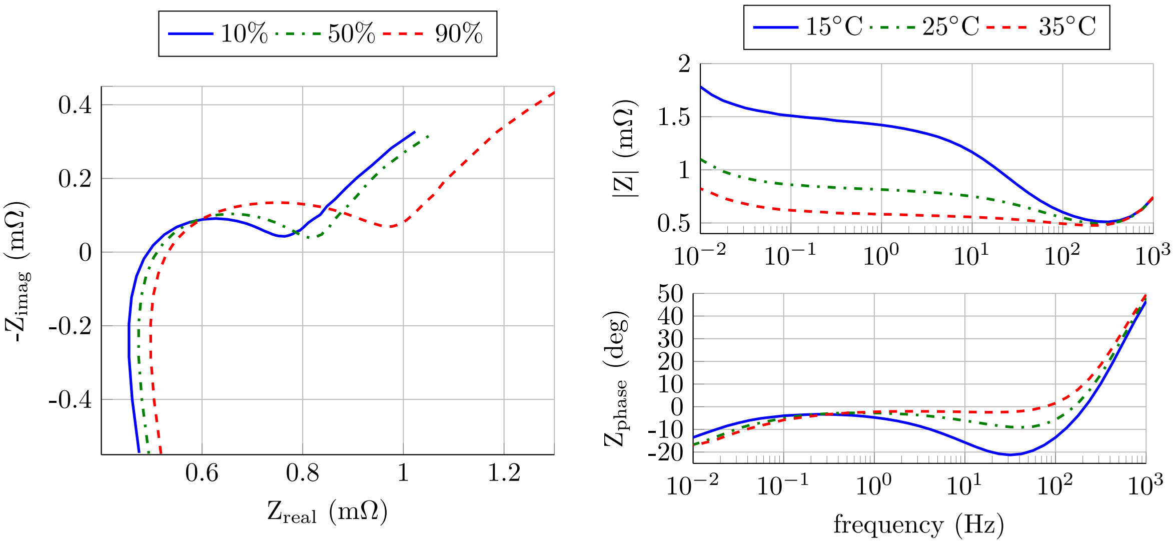

(a) Nyquist plot over SoC.

(b) Bode plot over Temperature.

Figure A.5.3: Impedance dependency on SoC and temperature.

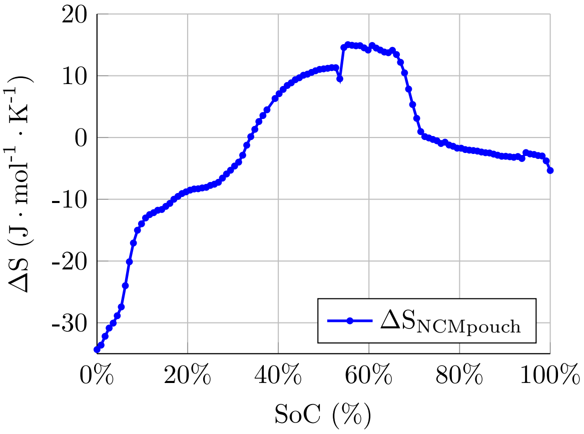

Figure A.5.4: $\Delta S$ over SoC.

# B Prototype Used

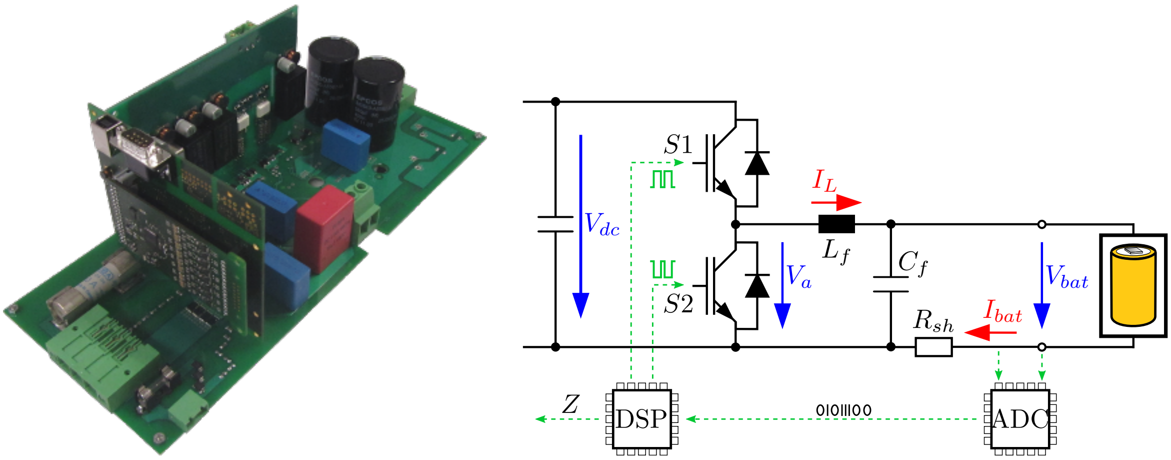

(a) Photo. (b) Simplified schematic.

Figure B.0.1: Developed prototype used as an experimental platform for EIS measurements with switched-mode excitation.

| **parameter** | **value** | **manufacturer** |
|---|---|---|
| max. Voltage (IGBT version) | 400 V | N/A |
| max. Current (IGBT version) | 20 A | N/A |
| max. Voltage (FET version) | 60 V | N/A |
| max. Current (FET version) | 40 A | N/A |
| IGBT module | FS100R07N3E4 | Infineon |
| FET module | SK85MH10T | Semikron |
| shunt $R_{sh}$ | 4 pcs., size SMT | Isabellenhütte |
| filter choke $L_f$, $R_f$ | 46 µH, 15 mΩ | self-built |
| filter capacity $C_f$ | $\Sigma = 140$ µF foil capacitors | WIMA |
| controller | STM32F407 | ST Microelectronics |
| ADC | ADS1278 Sigma-Delta | Texas Instruments |
| instrumentation amplifier | INA826 | Texas Instruments |
| operation amplifier for anti-aliasing filter | THS4521 | Texas Instruments |

Table B.1: Specifications and components used in the developed prototype.

# C Mathematical Lemmas

## C.1 Trigonometric Identities

From Barth et al. [11], page 38 to 39

$$\sin(\alpha+\beta) = \sin(\alpha)\cdot\cos(\beta) + \cos(\alpha)\cdot\sin(\beta) \tag{C.1}$$

$$\cos(\alpha+\beta) = \cos(\alpha)\cdot\cos(\beta) - \sin(\alpha)\cdot\sin(\beta) \tag{C.2}$$

$$\sin(2\alpha) = 2\cdot\sin(\alpha)\cdot\cos(\alpha) \tag{C.3}$$

$$\sin^2(\frac{\alpha}{2}) = \frac{1}{2}\cdot(1-\cos(\alpha)) \tag{C.4}$$

$$\cos^2(\frac{\alpha}{2}) = \frac{1}{2}\cdot(1+\cos(\alpha)) \tag{C.5}$$

By combining the five trigonometric identities, the following identities can be derived:
With C.1 and C.3

$$\begin{aligned}
&\cos(\alpha+\beta)\cdot\sin(\alpha+\beta)\\
&= [\cos(\alpha)\cdot\cos(\beta)-\sin(\alpha)\cdot\sin(\beta)]\cdot[\sin(\alpha)\cdot\cos(\beta)+\cos(\alpha)\cdot\sin(\beta)]\\
&= \underbrace{\cos^2(\beta)}_{\frac{1}{2}+\frac{1}{2}\cos(2\beta)} \cdot\underbrace{\cos(\alpha)\cdot\sin(\alpha)}_{\frac{1}{2}\sin(2\alpha)} + \underbrace{\cos^2(\alpha)}_{\frac{1}{2}+\frac{1}{2}\cos(2\alpha)} \cdot\underbrace{\cos(\beta)\cdot\sin(\beta)}_{\frac{1}{2}\sin(2\beta)}\\
&\underbrace{-\sin^2(\alpha)}_{-\frac{1}{2}+\frac{1}{2}\cos(2\alpha)} \cdot\underbrace{\cos(\beta)\cdot\sin(\beta)}_{\frac{1}{2}\sin(2\beta)} \underbrace{-\sin^2(\beta)}_{-\frac{1}{2}+\frac{1}{2}\cos(2\beta)} \cdot\underbrace{\cos(\alpha)\cdot\sin(\alpha)}_{\frac{1}{2}\sin(2\alpha)}\\
&= \frac{1}{2}\cdot\sin(2\alpha)\cdot\cos(2\beta) + \frac{1}{2}\cdot\cos(2\alpha)\cdot\sin(2\beta)
\end{aligned} \tag{C.6}$$

## C.2 Definite integrals

Based on the trigonometric identities of the previous section C.1 the following definite integrals can be derived:
With C.3

$$\int_0^{2\pi} \sin(ax)\cdot\cos(bx)\,\mathrm{d}x = \frac{1}{2}\cdot\sin(2ax) \quad \text{for } a=b\text{, otherwise } =0 \tag{C.7}$$

With C.4

$$\int_0^{2\pi} \underbrace{\sin(ax)\cdot\sin(bx)}_{\frac{1}{2}(=1-\cos(2ax))\text{ for }a=b\text{, otherwise }=0} \mathrm{d}x = \frac{1}{2}\cdot 2\pi \quad \text{for } a=b\text{, otherwise } =0 \tag{C.8}$$

With C.5

$$\int_0^{2\pi} \underbrace{\cos(ax) \cdot \cos(bx)}_{\frac{1}{2}(=1+\cos(2ax)) \text{ for } a=b, \text{ otherwise } =0} \mathrm{d}x = \frac{1}{2} \cdot 2\pi \quad \text{for } a = b, \text{ otherwise } = 0 \tag{C.9}$$

With C.1 and C.3

$$\begin{aligned}
&\int_0^{2\pi} \sin(ax+\varphi) \cdot \cos(bx) \, \mathrm{d}x \\
&= cos(\varphi) \cdot \int_0^{2\pi} \sin(ax) \cdot \cos(bx) \, \mathrm{d}x + \sin(\varphi) \cdot \int_0^{2\pi} \cos(ax) \cdot \cos(bx) \, \mathrm{d}x \\
&= cos(\varphi) \cdot \underbrace{\int_0^{2\pi} \frac{1}{2} \sin(2ax) \, \mathrm{d}x}_{=0} + \sin(\varphi) \cdot \int_0^{2\pi} \frac{1}{2} \left(1 + \cos(2ax)\right) \, \mathrm{d}x \text{ for } a = b, \text{ otherwise } = 0 \\
&= \sin(\varphi) \cdot \frac{1}{2} \cdot 2\pi \quad \text{for } a = b, \text{ otherwise } = 0
\end{aligned} \tag{C.10}$$

$$\begin{aligned}
&\int_0^{2\pi} \sin(ax+\varphi) \cdot \sin(bx) \, \mathrm{d}x \\
&= cos(\varphi) \cdot \int_0^{2\pi} \sin(ax) \cdot \sin(bx) \, \mathrm{d}x + \sin(\varphi) \cdot \int_0^{2\pi} \cos(ax) \cdot \sin(bx) \, \mathrm{d}x \\
&= cos(\varphi) \cdot \int_0^{2\pi} \frac{1}{2} \left(1 - \cos(2ax)\right) \, \mathrm{d}x + \sin(\varphi) \cdot \underbrace{\int_0^{2\pi} \frac{1}{2} \sin(2ax) \, \mathrm{d}x}_{=0} \text{ for } a = b, \text{ otherwise } = 0 \\
&= \cos(\varphi) \cdot \frac{1}{2} \cdot 2\pi \quad \text{for } a = b, \text{ otherwise } = 0
\end{aligned} \tag{C.11}$$

## C.3 Indefinite integrals

From Papula [85], appendix, integral 208

$$\int x \cdot \sin(ax) \, \mathrm{d}x = \frac{\sin(ax)}{a^2} - \frac{x \cdot \cos(ax)}{a} \tag{C.12}$$

From Papula [85], appendix, integral 232

$$\int x \cdot \cos(ax) \, \mathrm{d}x = \frac{\cos(ax)}{a^2} + \frac{x \cdot \sin(ax)}{a} \tag{C.13}$$

From Papula [85], appendix, integral 322

$$\int e^{ax} \cdot \sin(bx) \, \mathrm{d}x = \frac{e^{ax}}{a^2 + b^2} \left[a \cdot \sin(bx) - b \cdot \cos(bx)\right] \tag{C.14}$$

From Papula [85], appendix, integral 324

$$\int e^{ax} \cdot \cos(bx) \, \mathrm{d}x = \frac{e^{ax}}{a^2 + b^2} \left[a \cdot \cos(bx) + b \cdot \sin(bx)\right] \tag{C.15}$$

## C.4 Bessel Function of the First Kind

The following lemmas were used to solve the Double Fourier Integral for determining the harmonics of a half-bridge with varying DC-link voltage, the balancing resistor topology and the DC source topology in Appendix E. An extensive description of Bessel functions and their applications in science and engineering can be found in Watson [125] and Mc Lachlan [76].

From Holmes and Lipo [50], Appendix 2, Integral A2.12 and from it derived equations

$$\begin{aligned}&\int_{-\pi}^{\pi} e^{\pm j\xi\cos(\theta)}\cos(n\theta)\,\mathrm{d}\theta = 2\pi j^{\pm n}\mathcal{J}_n(\xi) = 2\pi(\pm 1)^n j^n \mathcal{J}_n(\xi)\\&\int_{-\pi}^{\pi} e^{\pm j\xi\sin(\theta)}\sin(n\theta)\,\mathrm{d}\theta = 2\pi j^{\pm n}\mathcal{J}_n(\xi) = 2\pi(\pm 1)^n j^n \mathcal{J}_n(\xi)\end{aligned} \tag{C.16}$$

The integration from the limits $\pi$ to $\pi$ yields the same result as from 0 and $2\pi$. For $n = 1$, shifting the integration limits by $\pi$ is equal to multiplying the exponential argument with $-1$ (because $\sin(\varphi+\pi) = -\sin(\varphi)$ and $\cos(\varphi+\pi) = -\cos(\varphi)$). The same is true for uneven values of $n$. For even values of $n$ the shift of the integration limits by $\pi$ does not change the term at all. This can be expressed by a multiplication with $(-1)^n$):

$$\int_{0}^{2\pi} e^{\mp j\xi\cos(\theta)}(-1)^n\cos(n\theta)\,\mathrm{d}\theta = 2\pi\underbrace{(-1)^n(\mp 1)^n}_{(\pm 1)^n} j^n\mathcal{J}_n(\xi)$$

$$\int_{0}^{2\pi} e^{\mp j\xi\sin(\theta)}(-1)^n\sin(n\theta)\,\mathrm{d}\theta = 2\pi\underbrace{(-1)^n(\mp 1)^n}_{(\pm 1)^n} j^n\mathcal{J}_n(\xi)$$

For $n = 1$ this equation can be stated as:

$$\int_{0}^{2\pi} e^{\pm j\xi\sin(\theta)}\sin(\theta)\,\mathrm{d}\theta = \pm j2\pi\mathcal{J}_1(\xi)$$

$$\int_{0}^{2\pi} e^{\pm j\xi\cos(\theta)}\cos(\theta)\,\mathrm{d}\theta = \pm j2\pi\mathcal{J}_1(\xi)$$

From Holmes and Lipo [50], Appendix 2, Integral A2.13 and from it derived equations

$$\begin{aligned}&\int_{-\pi}^{\pi} e^{\pm j\xi\cos(\theta)}\sin(n\theta)\,\mathrm{d}\theta = 0\\&\int_{0}^{2\pi} e^{\pm j\xi\cos(\theta)}\sin(n\theta)\,\mathrm{d}\theta = 0\\&\int_{0}^{2\pi} e^{\pm j\xi\sin(\theta)}\cos(n\theta)\,\mathrm{d}\theta = 0\end{aligned} \tag{C.17}$$

From Holmes and Lipo [50], Appendix 2, Integral A2.14 and from it derived equations

$$\int_{-\pi}^{\pi} e^{j\xi\cos(\theta)}e^{jn\theta}\,\mathrm{d}\theta = 2\pi j^n\mathcal{J}_n(\xi) \tag{C.18}$$

For equation C.16 it has been shown, that the integration limits can be shifted by $\pi$ without a change in the mathematical expression. Since $e^{jn\theta} = \cos(n\theta) + j\cdot\sin(n\theta)$ this can also be done for equation

C.18.

$$\begin{aligned}
&\int_0^{2\pi} e^{\pm j\xi cos(\theta)} e^{jn\theta}\,\mathrm{d}\theta = 2\pi j^{\pm n}\mathcal{J}_n(\xi) = 2\pi(\pm 1)^n j^n \mathcal{J}_n(\xi) \\
&\int_0^{2\pi} e^{\pm j\xi cos(\theta)} e^{-jn\theta}\,\mathrm{d}\theta = 2\pi j^{\pm n}\mathcal{J}_n(\xi) = 2\pi(\pm 1)^n j^n \mathcal{J}_n(\xi) \\
&\int_0^{2\pi} e^{\pm j\xi sin(\theta)} e^{jn\theta}\,\mathrm{d}\theta = 2\pi(\pm 1)^n j^{n+1} \mathcal{J}_n(\xi) \\
&\int_0^{2\pi} e^{\pm j\xi sin(\theta)} e^{-jn\theta}\,\mathrm{d}\theta = 2\pi(\pm 1)^n j^{n-1} \mathcal{J}_n(\xi)
\end{aligned} \tag{C.19}$$

From [76] Chapter 3, Section 3.42, equation (3) and from it derived equations

$$\begin{aligned}
&\int_{-pi}^{pi} e^{j\xi cos(\theta)}\,\mathrm{d}\theta = 2\pi\mathcal{J}_0(\xi) \\
&\int_0^{2\pi} e^{\pm j\xi cos(\theta)}\,\mathrm{d}\theta = 2\pi\mathcal{J}_0(\xi) \\
&\int_0^{2\pi} e^{\pm j\xi sin(\theta)}\,\mathrm{d}\theta = 2\pi\mathcal{J}_0(\xi)
\end{aligned} \tag{C.20}$$

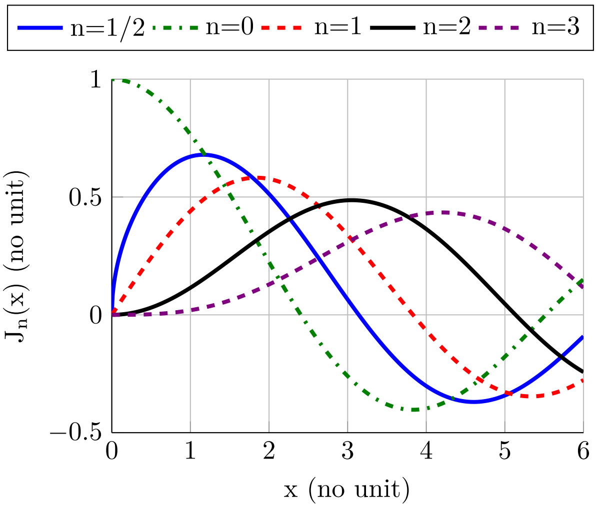

Figure C.4.1: Bessel function of the first kind.

From Holmes and Lipo [50], Appendix 2, Integral A2.17 and Integral A2.20

$$\mathcal{J}_{-n}(\xi) = (-1)^n\mathcal{J}_n(\xi) = \mathcal{J}_n(-\xi) \tag{C.21}$$

## C.5 Modified Bessel Function of the First Kind

The following lemmas were used to solve the measurement deviation caused by the temperature dependency of the impedance in section 3.2 and the measurement deviation caused by the impedance non-linearity in section 3.4. An extensive description of Bessel functions and their applications in science and engineering can be found in Watson [125] and Mc Lachlan [76].

From Mc Lachlan [76], Chapter 6, equation (8)

$$\mathcal{I}_n(x) = j^{-n}\mathcal{J}_n(jx) \tag{C.22}$$

From Mc Lachlan [76], Chapter 6, equation (9)

$$\mathcal{I}_n(-jx) = j^{-n}\mathcal{J}_n(x) = (-j)^n\mathcal{J}_n(x) \tag{C.23}$$

With equation C.22 equation C.16 can be rewritten as

$$\int_0^{2\pi} e^{\pm\xi\cos(\theta)}\cos(n\theta)\,\mathrm{d}\theta = 2\pi(\pm 1)^n\mathcal{I}_n(\xi) \tag{C.24}$$

$$\int_0^{2\pi} e^{\pm\xi\sin(\theta)}\sin(n\theta)\,\mathrm{d}\theta = 2\pi(\pm 1)^n\mathcal{I}_n(\xi) \tag{C.25}$$

With equation C.22 equation C.17 can be rewritten as

$$\int_0^{2\pi} e^{\pm\xi\cos(\theta)}sin(n\theta)\,\mathrm{d}\theta = 0 \tag{C.26}$$

$$\int_0^{2\pi} e^{\pm\xi\sin(\theta)}cos(n\theta)\,\mathrm{d}\theta = 0 \tag{C.27}$$

With equation C.22 equation C.18 can be rewritten as

$$\begin{aligned}
\int_0^{2\pi} e^{\pm\xi\cos(\theta)}e^{jn\theta}\,\mathrm{d}\theta &= 2\pi(\pm 1)^n\mathcal{I}_n(\xi) \\
\int_0^{2\pi} e^{\pm\xi\cos(\theta)}e^{-jn\theta}\,\mathrm{d}\theta &= 2\pi(\pm 1)^n\mathcal{I}_n(\xi) \\
\int_0^{2\pi} e^{\pm\xi\sin(\theta)}e^{jn\theta}\,\mathrm{d}\theta &= 2\pi(\pm 1)^n j\mathcal{I}_n(\xi) \\
\int_0^{2\pi} e^{\pm\xi\sin(\theta)}e^{-jn\theta}\,\mathrm{d}\theta &= 2\pi(\mp 1)^n j\mathcal{I}_n(\xi)
\end{aligned} \tag{C.28}$$

With equation C.22 equation C.19 can be rewritten as

$$\begin{aligned}
\int_0^{2\pi} e^{\pm\xi\cos(\theta)}\mathrm{d}\theta &= 2\pi\mathcal{I}_0(\xi) \\
\int_0^{2\pi} e^{\pm\xi\sin(\theta)}\mathrm{d}\theta &= 2\pi\mathcal{I}_0(\xi)
\end{aligned} \tag{C.29}$$

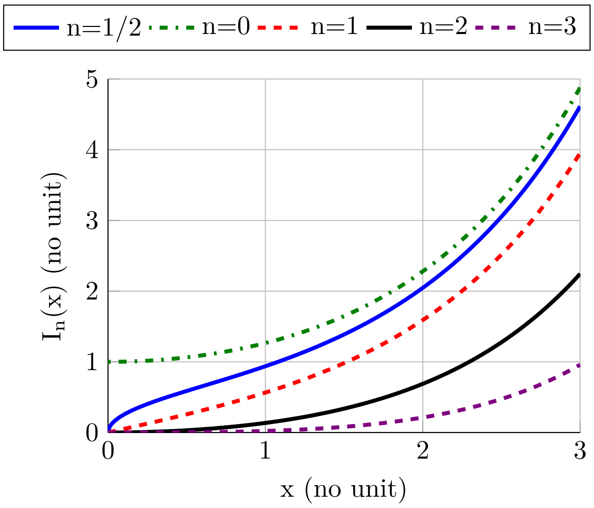

Figure C.5.1: Modified Bessel function of the first kind.

From Mc Lachlan [76] Chapter 6, equation (10) and (11)

$$\mathcal{I}_{-n}(x) = (-1)^n \mathcal{I}_n(-x) = \mathcal{I}_n(x) \tag{C.30}$$

## C.6 Imaginary Unit to the Power of a Fraction

For integer multiples of the exponent of the imaginary unit, the result is defined as:

$$\sqrt{-1} = j \tag{C.31}$$

$$(-1)^n = (j^2)^n = j^{2n} \tag{C.32}$$

For the calculation of the measurement deviation of a multi-sine measurement in section 3.4.5, an equation with the imaginary unit to the power of a variable is given. This exponent of the imaginary unit can become a fraction. Figure C.6.1 shows the complex result when the exponent has any fraction between -2 and 2. The result follows the formula:

$$j^x = cos(\frac{\pi}{2} \cdot x) + j \cdot sin(\frac{\pi}{2} \cdot x) \tag{C.33}$$

$$j^{\frac{1}{3}} = 0.866 + j0.5$$

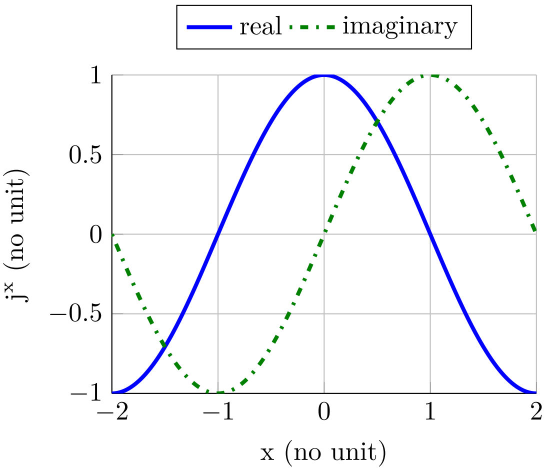

Figure C.6.1: Factor $j^x$.

# D Mathematical Derivations for Impedance Non-linearity

The Butler-Volmer equation gives the current for a certain voltage deflection from the OCV. Equation D.1 states the algebraic equation of the measurement current $i_m$ for a potentiostatic excitation. A potentiostatic excitation during the impedance measurement is first assumed (see equation D.2), since the Butler-Volmer equation cannot be analytically converted into a closed form that would give the voltage for a certain current.

$$i_m = i_0 \cdot \left[e^{\frac{(1-\alpha)zF(V_{dc}+v_{BV})}{RT}} - e^{\frac{-\alpha zF(V_{dc}+v_{BV})}{RT}}\right] + \frac{V_{dc}+v_{BV}}{r}$$

$$i_m = i_0 \cdot \left[e^{\frac{(1-\alpha)zFv_{BV}}{RT}} - e^{\frac{-\alpha zFv_{BV}}{RT}}\right] + \frac{v_{BV}}{r} \quad \text{for } V_{dc} = 0 \tag{D.1}$$

$$v_m = v_{BV} = \hat{V}_m \cdot \sin(\omega_m t) \tag{D.2}$$

## D.1 Harmonics generated by Butler-Volmer equation

This section derives the harmonics generated by a single-sine potentiostatic excitation. It therefore evaluates the Fourier transformation of the resulting measurement current $i_m$ at integer multiples $n$ of the measurement frequency $f_m$. The evaluation frequency is then $\omega_n = n \cdot \omega_m$. For deriving the harmonics $n \neq 1$ is assumed.

$$\mathrm{F}\{i_n(t)\} = \frac{2}{T_{min}} \int_0^{T_{min}} i_m(t) \cdot e^{-jn\omega_m t} \mathrm{d}t \tag{D.3}$$

$$\begin{aligned}
\mathrm{F}\{i_n(t)\} = {} & \frac{2}{T_{min}} \int_0^{T_{min}} i_0 \cdot e^{\frac{(1-\alpha)zFV_{dc}}{RT}} \cdot e^{\frac{(1-\alpha)zF\hat{V}_m}{RT} \cdot \sin(\omega_m t)} \cdot e^{-jn\omega_m t} \mathrm{d}t \\
& - \frac{2}{T_{min}} \int_0^{T_{min}} i_0 \cdot e^{\frac{-\alpha zFV_{dc}}{RT}} \cdot e^{\frac{-\alpha zF\hat{V}_m}{RT} \cdot \sin(\omega_m t)} \cdot e^{-jn\omega_m t} \mathrm{d}t \\
& + \frac{2}{T_{min}} \int_0^{T_{min}} \underbrace{\frac{V_{dc} + \hat{V}_m \cdot \sin(\omega_m t)}{r} \cdot e^{-jn\omega_m t} \mathrm{d}t}_{=0 \text{ for } n \neq 1}
\end{aligned} \tag{D.4}$$

With equation C.28 the integrals become:

$$\begin{aligned}
\mathrm{F}\{i_n(t)\} = {} & \frac{2i_0}{T_{min}} \cdot e^{\frac{(1-\alpha)zFV_{dc}}{RT}} \cdot (-j)^n \cdot T_{min} \cdot \mathcal{I}_n\left(\frac{(1-\alpha)zF\hat{V}_m}{RT}\right) \\
& - \frac{2i_0}{T_{min}} \cdot e^{\frac{-\alpha zFV_{dc}}{RT}} \cdot (-j)^n \cdot T_{min} \cdot \mathcal{I}_n\left(\frac{-\alpha zF\hat{V}_m}{RT}\right)
\end{aligned} \tag{D.5}$$

$$
\begin{aligned}
\mathrm{F}\{i_n(t)\} = (-j)^n \cdot 2i_0 \cdot e^{\frac{(1-\alpha)zFV_{dc}}{RT}} \cdot \mathcal{I}_n\left(\frac{(1-\alpha)zF\hat{V}_m}{RT}\right) \\
- (-j)^n \cdot 2i_0 \cdot e^{\frac{-\alpha zFV_{dc}}{RT}} \cdot \mathcal{I}_n\left(\frac{-\alpha zF\hat{V}_m}{RT}\right)
\end{aligned}
\tag{D.6}
$$

## D.2 Ratios of harmonics generated by Butler-Volmer equation

This section derives the ratios of the current harmonics equation from section D.1.
For the ratio of the fundamental to the third harmonic without constant voltage $V_{dc}$:

$$
\begin{aligned}
\frac{\mathrm{F}\{i_{n=1}(t)\}}{\mathrm{F}\{i_{n=3}(t)\}} &= \frac{(-j)^1 \cdot 2i_0 \cdot \left[\mathcal{I}_1\left(\frac{(1-\alpha)zF\hat{V}_m}{RT}\right) - \mathcal{I}_1\left(\frac{-\alpha zF\hat{V}_m}{RT}\right)\right]}{(-j)^3 \cdot 2i_0 \cdot \left[\mathcal{I}_3\left(\frac{(1-\alpha)zF\hat{V}_m}{RT}\right) - \mathcal{I}_3\left(\frac{-\alpha zF\hat{V}_m}{RT}\right)\right]} \\
&= \frac{-j}{(-j)^3} \cdot \left[\frac{\mathcal{I}_1\left(\frac{(1-\alpha)zF\hat{V}_m}{RT}\right) - \mathcal{I}_1\left(\frac{-\alpha zFV_{dc}}{RT}\right)}{\mathcal{I}_3\left(\frac{(1-\alpha)zF\hat{V}_m}{RT}\right) - \mathcal{I}_3\left(\frac{-\alpha zFV_{dc}}{RT}\right)}\right]
\end{aligned}
\tag{D.7}
$$

$$
\tag{D.8}
$$

For the ratio of the fundamental to the second harmonic with constant voltage. For a positive constant voltage the factor $e^{\frac{(1-\alpha)zFV_{dc}}{RT}}$ becomes large and the factor $e^{\frac{-\alpha zFV_{dc}}{RT}}$ becomes small. Therefore, the second term of equation D.6 with the latter factor is neglected.

$$
\begin{aligned}
\frac{\mathrm{F}\{i_{n=1}(t)\}}{\mathrm{F}\{i_{n=2}(t)\}} &= \frac{-j \cdot 2i_0 \cdot e^{\frac{(1-\alpha)zFV_{dc}}{RT}} \cdot \mathcal{I}_1\left(\frac{(1-\alpha)zF\hat{V}_m}{RT}\right)}{(-j)^2 \cdot 2i_0 \cdot e^{\frac{(1-\alpha)zFV_{dc}}{RT}} \cdot \mathcal{I}_2\left(\frac{(1-\alpha)zF\hat{V}_m}{RT}\right)} \\
\frac{\mathrm{F}\{i_{n=1}(t)\}}{\mathrm{F}\{i_{n=2}(t)\}} &= \frac{-j}{(-j)^2} \cdot \frac{\mathcal{I}_1\left(\frac{(1-\alpha)zF\hat{V}_m}{RT}\right)}{\mathcal{I}_2\left(\frac{(1-\alpha)zF\hat{V}_m}{RT}\right)}
\end{aligned}
\tag{D.9}
$$

## D.3 Single-sine measurement

This section derives analytically the measurement deviation introduced by a non-linear resistance described by a Butler-Volmer equation in parallel with an ohmic resistance. Equations D.1 and D.2 allow the conversion of the current response $i_m$ into the frequency-domain via the Fourier transformation:

$$\mathrm{F}\{i_m(t)\} = \frac{2}{T_m}\int_0^{T_m} i_m(t)\cdot e^{-j\omega_m t}\mathrm{d}t \tag{D.10}$$

$$\begin{aligned}
\mathrm{F}\{i_m(t)\} = &\frac{2}{T_m}\int_0^{T_m} i_0\cdot e^{\frac{(1-\alpha)zF\hat{V}_m}{RT}\cdot\sin(\omega_m t)}\cdot e^{-j\omega_m t}\mathrm{d}t\\
&-\frac{2}{T_m}\int_0^{T_m} i_0\cdot e^{\frac{-\alpha zF\hat{V}_m}{RT}\cdot\sin(\omega_m t)}\cdot e^{-j\omega_m t}\mathrm{d}t\\
&+\underbrace{\frac{2}{T_m}\int_0^{T_m}\frac{\hat{V}_m\cdot\sin(\omega_m t)}{r}\cdot e^{-j\omega_m t}\mathrm{d}t}_{\frac{2\cdot\hat{V}_m}{T_m\cdot r}\left[\underbrace{\int_0^{T_m}\sin(\omega_m t)\cdot\cos(\omega_m t)}_{=0}-j\int_0^{T_m}\sin(\omega_m t)\cdot\sin(\omega_m t)\right]\mathrm{d}t}
\end{aligned} \tag{D.11}$$

$$\begin{aligned}
\mathrm{F}\{i_m(t)\} = &\frac{2i_0}{T_m}\cdot\left[-j\cdot T_m\cdot\mathcal{I}_1\left(\frac{(1-\alpha)zF\hat{V}_m}{RT}\right)\right] \quad \text{using Lemma C.28}\\
&-\frac{2i_0}{T_m}\cdot\left[-j\cdot T_m\cdot\mathcal{I}_1\left(\frac{-\alpha zF\hat{V}_m}{RT}\right)\right] \quad \text{using Lemma C.28}\\
&+\frac{2\cdot\hat{V}_m}{T_m\cdot r}\cdot\underbrace{\left[-j\cdot\int_0^{T_m}\frac{1}{2}-\frac{1}{2}\cdot\cos(2\omega_m t)\mathrm{d}t\right]}_{\underbrace{-j\cdot\left[\frac{1}{2}t-\frac{1}{2}\frac{T_m}{4\pi}\cdot\sin(2\omega_m t)\right]_0^{T_m}}_{=-j\frac{1}{2}T_m}} \quad \text{using Lemma C.4}
\end{aligned} \tag{D.12}$$

$$\begin{aligned}
\mathrm{F}\{i_m(t)\} = &-j\frac{2i_0}{T_m}\cdot T_m\cdot\mathcal{I}_1\left(\frac{(1-\alpha)zF\hat{V}_m}{RT}\right)\\
&+j\frac{2i_0}{T_m}\cdot T_m\cdot\mathcal{I}_1\left(\frac{-\alpha zF\hat{V}_m}{RT}\right)\\
&-j\frac{\hat{V}_m}{r}
\end{aligned} \tag{D.13}$$

## D.4 Multi-sine measurement

$$\mathrm{F}\{i_m(t)\} = \frac{2}{T_{min}} \int_0^{T_{min}} \Sigma_{n=1}^{N} i_n(t) \cdot e^{-jx_n\omega_n t} \mathrm{d}t \tag{D.14}$$

$$\begin{aligned}
\mathrm{F}\{i_m(t)\} = & \frac{2}{T_{min}} \int_0^{T_{min}} \Sigma_{n=1}^{N} i_0 \cdot e^{\frac{(1-\alpha)zF\hat{V}_m}{RT} \cdot \sin(\omega_n t)} \cdot e^{-jx_n\omega_n t} \mathrm{d}t \\
& - \frac{2}{T_{min}} \int_0^{T_{min}} \Sigma_{n=1}^{N} i_0 \cdot e^{\frac{-\alpha zF\hat{V}_m}{RT} \cdot \sin(\omega_n t)} \cdot e^{-jx_n\omega_n t} \mathrm{d}t \\
& + \frac{2}{T_{min}} \underbrace{\int_0^{T_{min}} \Sigma_{n=1}^{N} \frac{\hat{V}_m \cdot \sin(\omega_n t)}{r} \cdot e^{-jx_n\omega_n t} \mathrm{d}t}_{-j \cdot \frac{\hat{V}_m}{r} \frac{1}{2} T_{min}}
\end{aligned} \tag{D.15}$$

$$\begin{aligned}
\mathrm{F}\{i_m(t)\} = & \frac{2i_0}{T_{min}} \cdot \Sigma_{n=1}^{N} (-1)^{x_n} j^{x_n} \cdot T_{min} \cdot \mathcal{I}_{x_n}\left(\frac{(1-\alpha)zF\hat{V}_m}{RT}\right) \\
& - \frac{2i_0}{T_{min}} \cdot \Sigma_{n=1}^{N} (+1)^{x_n} j^{x_n} \cdot T_{min} \cdot \mathcal{I}_{x_n}\left(\frac{\alpha zF\hat{V}_m}{RT}\right) \\
& - j\frac{\hat{V}_m}{r}
\end{aligned} \tag{D.16}$$

Entering equation D.16 into equation 3.139. Entering the resulting $Y_m$ into equation 3.142 with the approximation of $\hat{V}_m$ by $\hat{I}_m \cdot Z_0^{'}$ yields:

$$\begin{aligned}
e_Z \approx \frac{1}{Z_0^{'} + R_\Omega} \cdot \Bigg| \Bigg[ \frac{2i_0}{\hat{I}_m Z_0^{'}} \cdot \Sigma_{n=1}^{N} \Bigg( & (-1)^{x_n - 1} j^{x_n - 1} \cdot \mathcal{I}_{x_n}\left(\frac{(1-\alpha)zF\hat{I}_m Z_0^{'}}{RT}\right) - \\
& (+1)^{x_n - 1} j^{x_n - 1} \cdot \mathcal{I}_{x_n}\left(\frac{\alpha zF\hat{I}_m Z_0^{'}}{RT}\right) \Bigg) + \frac{1}{r} \Bigg]^{-1} - Z_0^{'} \Bigg|
\end{aligned} \tag{D.17}$$

With the assumption of $\alpha = 0.5$:

$$\begin{aligned}
e_Z \approx & \frac{1}{Z_0^{'} + R_\Omega} \cdot \Bigg| \Bigg[ \frac{2i_0}{\hat{I}_m Z_0^{'}} \cdot \\
& \Sigma_{n=1}^{N} \Bigg( \underbrace{\left((-1)^{x_n - 1} j^{x_n - 1} - (+1)^{x_n - 1} j^{x_n - 1}\right)}_{=2j\cos\left(\frac{\pi}{2} \cdot x_n\right)} \cdot \mathcal{I}_{x_n}\left(\frac{0.5zF\hat{I}_m Z_0^{'}}{RT}\right) \Bigg) + \frac{1}{r} \Bigg]^{-1} - Z_0^{'} \Bigg|
\end{aligned} \tag{D.18}$$

## D.5 Measurement with constant current

When the impedance is measured during charging or discharging, the constant charge/discharge current is superpositioned with a sinusoidal current. Equation D.19 assumes first that instead of a galvanostatic excitation, a potentiostatic excitation is present.

$$\begin{aligned}
\mathrm{F}\{i_m(t)\} = {} & \frac{2}{T_m}\int_0^{T_m} i_0 \cdot e^{\frac{(1-\alpha)zF(V_{dc}+\hat{V}_m\cdot\sin(\omega_m t))}{RT}} \cdot e^{-j\omega_m t}\mathrm{d}t \\
& - \frac{2}{T_m}\int_0^{T_m} i_0 \cdot e^{\frac{-\alpha zF(V_{dc}+\hat{V}_m\cdot\sin(\omega_m t))}{RT}} \cdot e^{-j\omega_m t}\mathrm{d}t \\
& + \frac{2}{T_m}\int_0^{T_m} \frac{V_{dc}+\hat{V}_m\cdot\sin(\omega_m t)}{r} \cdot e^{-j\omega_m t}\mathrm{d}t
\end{aligned} \tag{D.19}$$

$$\begin{aligned}
\mathrm{F}\{i_m(t)\} = {} & \frac{2i_0}{T_m} \cdot e^{\frac{(1-\alpha)zF\cdot V_{dc}}{RT}} \cdot \int_0^{T_m} e^{\frac{(1-\alpha)zF\cdot\hat{V}_m\cdot\sin(\omega_m t)}{RT}} \cdot e^{-j\omega_m t}\mathrm{d}t \\
& - \frac{2i_0}{T_m} \cdot e^{\frac{-\alpha zF\cdot V_{dc}}{RT}} \cdot \int_0^{T_m} e^{\frac{-\alpha zF\cdot\hat{V}_m\cdot\sin(\omega_m t)}{RT}} \cdot e^{-j\omega_m t}\mathrm{d}t \\
& + \underbrace{\frac{2}{T_m}\int_0^{T_m} \frac{V_{dc}}{r} \cdot e^{-j\omega_m t}\mathrm{d}t}_{=0} + \frac{2}{T_m}\int_0^{T_m} \frac{\hat{V}_m\cdot\sin(\omega_m t)}{r} \cdot e^{-j\omega_m t}\mathrm{d}t
\end{aligned} \tag{D.20}$$

With this equation the two superpositioned parts, constant and sinusoidal, can be separated. The overvoltage caused by the constant current is independent from time and is not integrated but treated as a constant factor. Equation D.20 only differs from equation D.11 by the factor $e^{\frac{(1-\alpha)zF\cdot V_{dc}}{RT}}$ and $e^{\frac{-\alpha zF\cdot V_{dc}}{RT}}$. Hence, all the steps for deriving equation D.21 are the same except for this factor. With Lemma C.28, the integrals of equation D.20 become:

$$\begin{aligned}
\mathrm{F}\{i_m(t)\} = {} & -j \cdot 2i_0 \cdot e^{\frac{(1-\alpha)zFV_{dc}}{RT}} \cdot \mathcal{I}_1\left(\frac{(1-\alpha)zF\hat{V}_m}{RT}\right) \\
& + j \cdot 2i_0 \cdot e^{\frac{-\alpha zFV_{dc}}{RT}} \cdot \mathcal{I}_1\left(\frac{-\alpha zF\hat{V}_m}{RT}\right) \\
& - j\frac{\hat{V}_m}{r}
\end{aligned} \tag{D.21}$$

# E Mathematical Derivation of Generated Harmonics by Switched Mode Excitation

In this appendix, the mathematical expressions for the theoretical harmonic distortions are derived. It uses the Double Fourier Integral method extensively explained by Holmes and Lipo in [50]. He derived the algebraic equation for various power converters including a half bridge converter with double the DC-link voltage. The cases used in this thesis, which were not covered in his book and are covered in this appendix, are:

1. The output voltage $v_{out}(t)$ of the DC-link voltage adjustment for the Battery Charger Topology.
2. The balancing current $i_{bal}(t)$ of the Balancing Unit Topology.
3. The input current $i_{in}(t)$ of the DC Source Topology.

## E.1 General Process

### Double Fourier Integral

Equation E.1 shows the Double Fourier Integral used by Holmes and Lipo [50].

$$C_{mn} = A_{mn} + jB_{mn} = \frac{1}{2\pi^2} \int_{-\pi}^{\pi} \int_{-\pi}^{\pi M cos y'} V_{dc} \cdot e^{j(mx+ny')} \, \mathrm{d}x \, \mathrm{d}y \tag{E.1}$$

with

$$x(t) = \omega_c t + \theta_c \tag{E.2}$$

$$y(t) = \omega_m t + \theta_m \tag{E.3}$$

It assumes an infinitely fast control circuit like an analog feedback loop would provide. For a digital controller on a processor, the reference signal is updated in a loop, making it to a discrete variable which changes in steps. Equation E.4 modifies the variable y from equation E.2 to accommodate for that fact. Among the various ways to compare the reference signal to a carrier signal, the regular trailing edge pulse width modulation was chosen.

**Time signal variables:**

$$y'(t) = y(t) - \frac{\omega_m}{\omega_c}(x - 2\pi m) \qquad \text{with } m \text{ as } m^{\text{th}} \text{ carrier interval} \tag{E.4}$$

This modifies equation E.1 for a continuous control signal to equation E.5 for a discrete regular trailing edge pulse width modulated control signal.

$$C_{mn} = A_{mn} + jB_{mn} = \frac{1}{2\pi^2}\int_{-\pi}^{\pi}\int_{-\pi}^{\pi M\cos(y)} V_{dc}\cdot e^{j\left(\left[m+n\frac{\omega_m}{\omega_c}\right]x+ny\right)}\ \mathrm{d}x\ \mathrm{d}y \tag{E.5}$$

## Verification

Figures and tables are shown for each of the three typologies to verify the derived equations. They compare the results of a simulation with the results of the derived equations. Equation E.6 shows the output voltage $v_a(t)$ with a series of sinusoidal signals according to Holmes and Lipo [50], for a half-bridge converter with DC-link voltage double has high as the mean output voltage. Its harmonics are calculated by the equation E.7 to E.11.

$$\begin{aligned} v_a(t) = {} & \frac{C_{00}}{2} \\ & + C_{01}\ e^{j\omega_m t+\theta_m} \\ & + \sum_{n=2}^{\infty} C_{0n}\ e^{jn(\omega_m t+\theta_m)} \\ & + \sum_{m=1}^{\infty} C_{m0}\ e^{jm(\omega_c t+\theta_c)} \\ & + \sum_{m=1}^{\infty}\sum_{\substack{n=-\infty \\ (n\neq 0)}}^{\infty} C_{mn}\ e^{jn(\omega_m t+\theta_m)+jm(\omega_c t+\theta_c)} \end{aligned} \tag{E.6}$$

$$C_{00} = \frac{V_{dc}}{2} \tag{E.7}$$

$$C_{01} = \frac{V_{dc}}{2}M \tag{E.8}$$

$$C_{0n} = \frac{V_{dc}}{\pi}\frac{\mathcal{J}_n\left(n\frac{\omega_m}{\omega_c}\pi M\right)}{n\frac{\omega_m}{\omega_c}}\cdot\left[\sin\left(n\frac{\pi}{2}\right) - j\cos\left(n\frac{\pi}{2}\right)\right] \tag{E.9}$$

$$C_{m0} = j\frac{V_{dc}}{m\pi}\left[\cos\left(m\pi\right) - \mathcal{J}_0\left(m\pi M\right)\right] \tag{E.10}$$

$$C_{mn} = \frac{V_{dc}}{\pi}\frac{\mathcal{J}_n\left(\left[m+n\frac{\omega_m}{\omega_c}\right]\pi M\right)}{\left[m+n\frac{\omega_m}{\omega_c}\right]}\cdot\left[\sin\left(n\frac{\pi}{2}\right) - j\cos\left(n\frac{\pi}{2}\right)\right] \tag{E.11}$$

Figure E.1.1 and table E.1 verify the equations with a simulation for which the signals were simulated in the time-domain and then Fourier-transformed into the frequency-domain to determine the harmonics.

| | $THD$ | $C_{02}$ | $C_{10}$ | $C_{1_{-1}}$ | $C_{1_{+1}}$ | $C_{20}$ | $C_{2_{-1}}$ | $C_{2_{+1}}$ |
|---|---|---|---|---|---|---|---|---|
| DFS theory | 13.7044 | 0.0098 | 12.5769 | 0.9892 | 0.9862 | 0.3065 | 0.9544 | 0.9544 |
| sim and DFT | 13.6382 | 0.0100 | 12.5144 | 0.9892 | 0.9861 | 0.3084 | 0.9542 | 0.9542 |
| difference | 0.0662 | 0.0002 | 0.0625 | 0.0001 | 0.0001 | 0.0019 | 0.0003 | 0.0003 |

Table E.1: Numerical values to figure E.1.1.

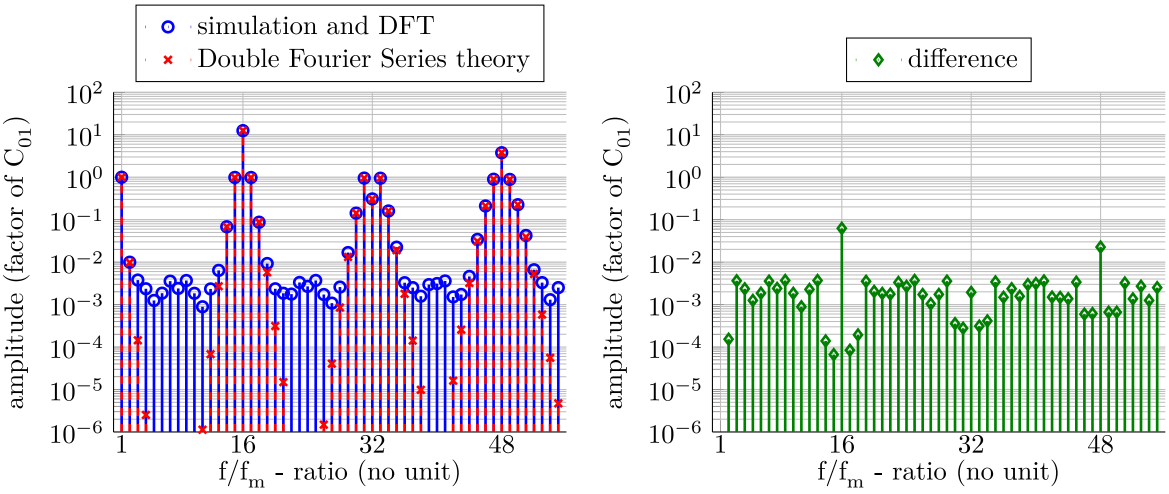

(a) Comparison.

(b) Difference.

Figure E.1.1: Harmonics of the Battery Charger Topology determined with the Double Fourier Integral theory and a simulation with subsequent DFT.

## E.2 Charger Topology Using DC-link adjustment

Section 4.3.4 shows the option to reduce the harmonic content of the switched mode excitation by reducing the DC-link voltage to levels between the battery voltage and double the battery voltage. This section derives the modified equations of the harmonics for a half-bridge converter with a varying DC-link voltage. A reduced DC-link voltage causes the effective driving voltage $v_L$ over the choke of the half-bridge converter to be unsymmetrical. This causes the positive slope of the choke current to be lower than the negative slope (see figure E.2.2).

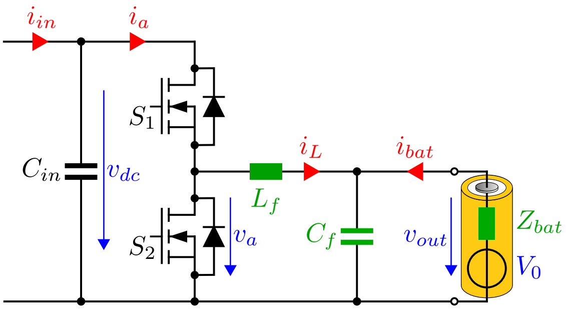

Figure E.2.1: Battery Charger Topology.

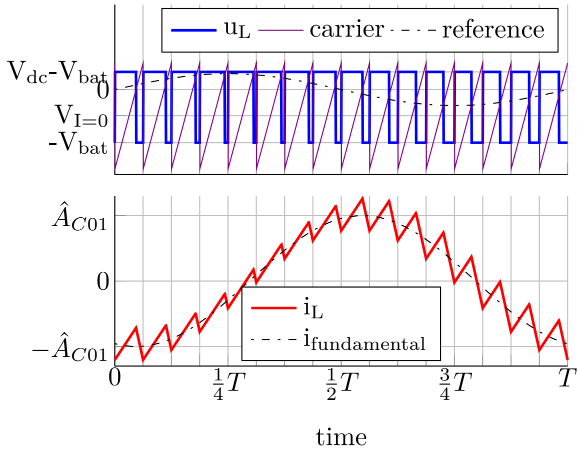

Figure E.2.2: Generated voltage and current of the Battery Charger Topology (synthetic data).

## Preconditions and Definitions

For the current to be zero the output voltage has to fulfill equation E.12.

$$V_{a,I=0} = \left(\frac{2V_{bat}}{V_{dc}} - 1\right) \cdot V_{bat} \tag{E.12}$$

Equation E.13 shows the modified modulation index $M'$ for a varying DC-link voltage. For DC-link voltages less than double the battery voltage, the modulation index can no longer take values up to 1.

$$M' = \frac{V_{dc}}{V_{bat}} - 1 \tag{E.13}$$

Figure E.2.2 shows that the sawtooth carrier signal $x(t)$ is no longer symmetrical to zero. The lower bound for the integration over $x$ of integral E.5 is no longer $-\pi$ but the larger, the smaller the DC-link voltage is (see equation E.14).

$$x_{low} = -2\frac{V_{bat}}{V_{dc}}\pi \tag{E.14}$$

## Derivation of the Harmonic Components

Starting from the double Fourier integral equation from Holmes and Lipo [50] modified by the lower bound from equation E.14:

$$C_{mn} = \frac{1}{2\pi^2}\int_{-\pi}^{\pi}\int_{-2\frac{V_{bat}}{V_{dc}}\pi}^{\pi M' \cos y'} V_{dc}\; e^{j\left(\left[m+n\frac{\omega_m}{\omega_c}\right]x+ny\right)}\; \mathrm{d}x\; \mathrm{d}y \tag{E.15}$$

The indexes m and n are set to 0 in turns to evaluate the different harmonic components.

<u>For $m = n = 0$</u> (DC offset):

$$\begin{aligned}
C_{00} &= \frac{V_{dc}}{2\pi^2}\int_{-\pi}^{\pi}\left(\pi M'\cos y + 2\frac{V_{bat}}{V_{dc}}\pi\right)\;\mathrm{d}y \\
&= \frac{V_{dc}}{2\pi^2}\left(\underbrace{\int_{-\pi}^{\pi}\pi M'\cos y\;\mathrm{d}y}_{0} + \underbrace{\int_{-\pi}^{\pi}2\frac{V_{bat}}{V_{dc}}\pi\;\mathrm{d}y}_{4\pi^2\frac{V_{bat}}{V_{dc}}}\right) \\
&= \frac{V_{dc}}{2\pi^2}\;4\pi^2\frac{V_{bat}}{V_{dc}} \\
&= 2V_{bat}
\end{aligned} \tag{E.16}$$

<u>For $m = 0,\, n > 0$</u> (fundamental and baseband harmonics):

$$\begin{aligned}
C_{0n} &= \frac{V_{dc}}{2\pi^2}\int_{-\pi}^{\pi}\int_{-2\frac{V_{bat}}{V_{dc}}\pi}^{\pi M'\cos y} e^{jn\frac{\omega_m}{\omega_c}x}e^{jny}\ \mathrm{d}x\ \mathrm{d}y \\
C_{0n} &= -j\frac{V_{dc}}{2\pi^2\left[n\frac{\omega_m}{\omega_c}\right]}\int_{-\pi}^{\pi}\left(e^{jn\frac{\omega_m}{\omega_c}\pi M'\cos y} - e^{-j2n\frac{\omega_m}{\omega_c}\frac{V_{bat}}{V_{dc}}\pi}\right)e^{jny}\ \mathrm{d}y \\
C_{0n} &= -j\frac{V_{dc}}{2\pi^2\left[n\frac{\omega_m}{\omega_c}\right]}\int_{-\pi}^{\pi} e^{jn\frac{\omega_m}{\omega_c}\pi M'\cos y}e^{jny}\ \mathrm{d}y - \int_{-\pi}^{\pi} e^{-j2n\frac{\omega_m}{\omega_c}\frac{V_{bat}}{V_{dc}}\pi}e^{jny}\ \mathrm{d}y
\end{aligned} \tag{E.17}$$

Lemma C.18 solves the first integral of E.17.

$$\begin{aligned}
C_{0n} = &-j\frac{V_{dc}}{2\pi^2\left[n\frac{\omega_m}{\omega_c}\right]}2\pi j^n\mathcal{J}_n\left(n\frac{\omega_m}{\omega_c}\pi M'\right) \\
&+j\frac{V_{dc}}{2\pi^2\left[n\frac{\omega_m}{\omega_c}\right]}e^{-j2n\frac{\omega_m}{\omega_c}\frac{V_{bat}}{V_{dc}}\pi}\cdot\underbrace{\frac{e^{jn\pi}-e^{-jn\pi}}{jn}}_{=0\text{ when }n\neq 0}
\end{aligned} \tag{E.18}$$

$\left(\frac{e^{jn\pi}-e^{-jn\pi}}{jn}\right)$ is zero for all non-zero values of $n$ and with $j^n = e^{j\frac{\pi}{2}n}$ equation E.18 becomes

$$C_{0n} = \frac{V_{dc}}{\left[n\frac{\omega_m}{\omega_c}\right]\pi}\mathcal{J}_n\left(n\frac{\omega_m}{\omega_c}\pi M'\right)\cdot\left[\sin\left(n\frac{\pi}{2}\right) - j\cos\left(n\frac{\pi}{2}\right)\right] \tag{E.19}$$

<u>For $m > 0,\, n = 0$</u> (carrier frequency and its harmonics):

$$C_{m0} = \frac{V_{dc}}{2\pi^2}\int_{-\pi}^{\pi}\int_{-2\frac{V_{bat}}{V_{dc}}\pi}^{\pi M'\cos y} e^{jmx}\ \mathrm{d}x\ \mathrm{d}y \tag{E.20}$$

$$C_{m0} = \frac{V_{dc}}{2\pi^2}\int_{-\pi}^{\pi}\left(\frac{e^{jm\pi M'\cos y} - e^{-j2m\frac{V_{bat}}{V_{dc}}\pi}}{jm}\right)\mathrm{d}y \tag{E.21}$$

$$C_{m0} = \frac{V_{dc}}{j2m\pi^2}\int_{-\pi}^{\pi} e^{jm\pi M'\cos y}\ \mathrm{d}y - \frac{V_{dc}}{j2m\pi^2}e^{-j2m\frac{V_{bat}}{V_{dc}}\pi}\int_{-\pi}^{\pi}\ \mathrm{d}y \tag{E.22}$$

Lemma C.19 solves the first integral of E.22. Eulers Formula $e^{jx} = \cos(x) - j\sin(x)$ simplifies the second term.

$$C_{m0} = -j\frac{V_{dc}}{m\pi}\cdot\mathcal{J}_0\left(m\pi M'\right) + j\frac{V_{dc}}{m\pi}\cdot cos\left(2m\frac{V_{bat}}{V_{dc}}\pi\right) + \frac{V_{dc}}{m\pi}\cdot\sin\left(2m\frac{V_{bat}}{V_{dc}}\pi\right) \tag{E.23}$$

$$C_{m0} = \frac{V_{dc}}{m\pi}\cdot\sin\left(2m\frac{V_{bat}}{V_{dc}}\pi\right) + j\frac{V_{dc}}{m\pi}\left(\cos\left(2m\frac{V_{bat}}{V_{dc}}\pi\right) - \mathcal{J}_0\left(m\pi M'\right)\right) \tag{E.24}$$

For $m > 0$, $n \neq 0$ (sidebands of carrier frequency harmonics):

$$\begin{aligned}
C_{mn} &= \frac{V_{dc}}{2\pi^2}\int_{-\pi}^{\pi}\int_{-2\frac{V_{bat}}{V_{dc}}\pi}^{\pi M'\cos y} e^{j\left(\left[m+n\frac{\omega_m}{\omega_c}\right]x+ny\right)}\ \mathrm{d}x\ \mathrm{d}y \\
C_{mn} &= \frac{V_{dc}}{2\pi^2 j\left[m+n\frac{\omega_m}{\omega_c}\right]}\cdot \\
&\quad \int_{-\pi}^{\pi}\left[e^{j\left(\pi M'\cos y\left[m+n\frac{\omega_m}{\omega_c}\right]\right)} - e^{j\left(-2\frac{V_{bat}}{V_{dc}}\pi\left[m+n\frac{\omega_m}{\omega_c}\right]\right)}\right]\cdot e^{jny}\ \mathrm{d}y \\
C_{mn} &= \frac{V_{dc}}{2\pi^2 j\left[m+n\frac{\omega_m}{\omega_c}\right]}\cdot 2\pi j^n \mathcal{J}_n\left(\pi M'\left[m+n\frac{\omega_m}{\omega_c}\right]\right) - \\
&\quad \frac{V_{dc}}{2\pi^2 j\left[m+n\frac{\omega_m}{\omega_c}\right]}\cdot e^{j\left(-2\frac{V_{bat}}{V_{dc}}\pi\left[m+n\frac{\omega_m}{\omega_c}\right]\right)}\cdot \underbrace{\frac{e^{jn\pi}-e^{-jn\pi}}{jn}}_{=0\text{ when }n\neq 0}
\end{aligned} \tag{E.25}$$

$\left(\frac{e^{jn\pi}-e^{-jn\pi}}{jn}\right)$ is zero for all non-zero values of n. Then the whole second term becomes zero. With $j^n = e^{j\frac{\pi}{2}n}$ the first term can be rewritten:

$$C_{mn} = \frac{V_{dc}}{\pi\left[m+n\frac{\omega_m}{\omega_c}\right]}\mathcal{J}_n\left(\pi M'\left[m+n\frac{\omega_m}{\omega_c}\right]\right)\left[\sin\left(n\frac{\pi}{2}\right) - j\cos\left(n\frac{\pi}{2}\right)\right] \tag{E.26}$$

## Result

$$\begin{aligned}
v_a(t) &= \frac{C_{00}}{2} \\
&\quad + \sum_{n=1}^{2} C_{0n}\ e^{jn(\omega_m t+\theta_m)} \\
&\quad + \sum_{m=1}^{\infty} C_{m0}\ e^{jm(\omega_c t+\theta_c)} \\
&\quad + \sum_{m=1}^{\infty}\sum_{\substack{n=-\infty \\ (n\neq 0)}}^{\infty} C_{mn}\ e^{jn(\omega_m t+\theta_m)+jm(\omega_c t+\theta_c)}
\end{aligned} \tag{E.27}$$

$$C_{00} = 2V_{bat} \tag{E.28}$$

$$C_{01} = \frac{V_{dc}}{\left[\frac{\omega_m}{\omega_c}\right]\pi}\mathcal{J}_1\left(\frac{\omega_m}{\omega_c}\pi M'\right) \tag{E.29}$$

$$C_{0n} = \frac{V_{dc}}{\left[n\frac{\omega_m}{\omega_c}\right]\pi}\mathcal{J}_n\left(n\frac{\omega_m}{\omega_c}\pi M'\right)\cdot\left[\sin\left(n\frac{\pi}{2}\right) - j\cos\left(n\frac{\pi}{2}\right)\right] \tag{E.30}$$

$$C_{m0} = \frac{V_{dc}}{m\pi}\cdot\sin\left(2m\frac{V_{bat}}{V_{dc}}\pi\right) + j\frac{V_{dc}}{m\pi}\left(\cos\left(2m\frac{V_{bat}}{V_{dc}}\pi\right) - \mathcal{J}_0\left(m\pi M'\right)\right) \tag{E.31}$$

$$C_{mn} = \frac{V_{dc}}{\pi\left[m+n\frac{\omega_m}{\omega_c}\right]}\mathcal{J}_n\left(\pi M'\left[m+n\frac{\omega_m}{\omega_c}\right]\right)\left[\sin\left(n\frac{\pi}{2}\right) - j\cos\left(n\frac{\pi}{2}\right)\right] \tag{E.32}$$

### Verification

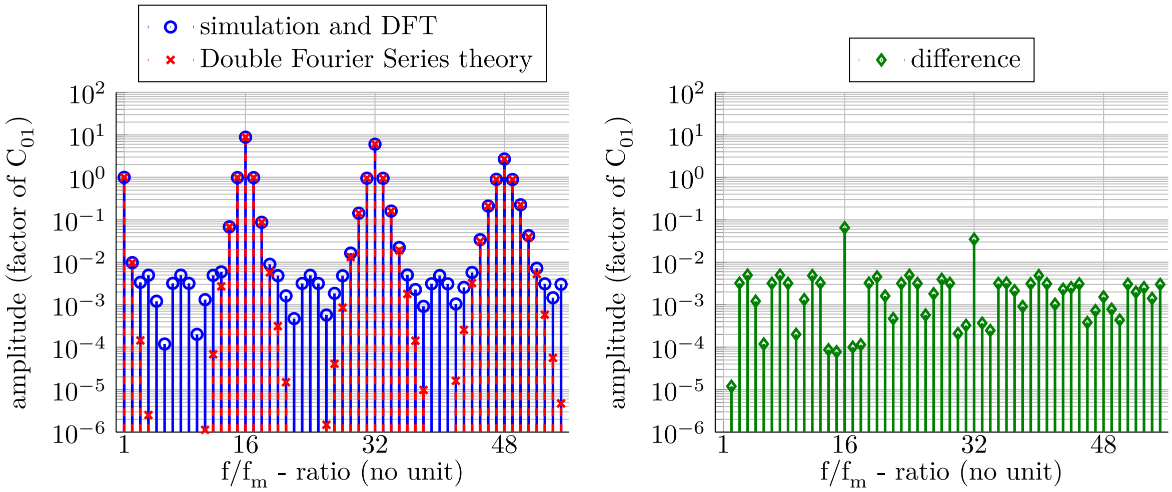

(a) Comparison.

(b) Difference.

Figure E.2.3: Harmonics of the Battery Charger Topology with DC-link adjustment determined with the Double Fourier Integral theory and a simulation with subsequent DFT.

| | $THD$ | $C_{02}$ | $C_{10}$ | $C_{1_{-1}}$ | $C_{1_{+1}}$ | $C_{20}$ | $C_{2_{-1}}$ | $C_{2_{+1}}$ |
|---|---|---|---|---|---|---|---|---|
| DFS theory | 11.7485 | 0.0098 | 8.8939 | 0.9892 | 0.9862 | 6.0600 | 0.9544 | 0.9544 |
| sim and DFT | 11.6760 | 0.0098 | 8.8289 | 0.9892 | 0.9861 | 6.0252 | 0.9541 | 0.9541 |
| difference | 0.0724 | 0.0000 | 0.0650 | 0.0001 | 0.0001 | 0.0348 | 0.0003 | 0.0003 |

Table E.2: Numerical values to figure E.2.3.

## E.3 Balancing Unit Topology

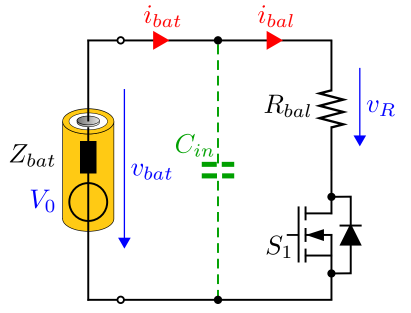

Figure E.3.1: Balancing Unit Topology.

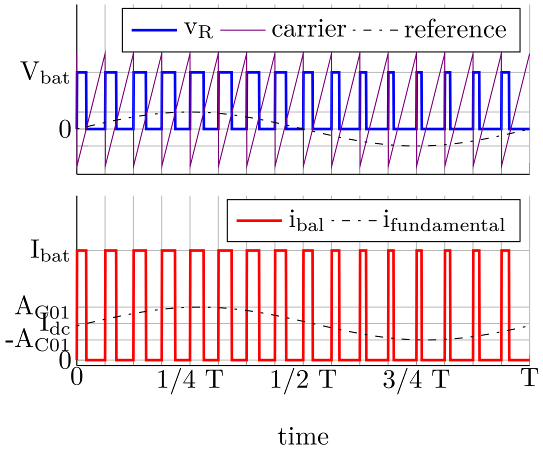

Figure E.3.2: Generated voltage and current of the Balancing Unit Topology (synthetic data).

## Preconditions and Definitions

For the Balancing Unit Topology the maximum balancing current is equal to the battery voltage over the resistor. It reaches its maximum value if the balancing switch is continuously turned on (equation E.33). For a sinusoidal current a constant current $I_{dc}$ of at least the amplitude of the sinusoidal measurement current $\hat{I}_m$ needs to be added (equation E.34) to the total excitation signal.

$$I_{bal,max} = \frac{V_{bat}}{R_{bal}} \tag{E.33}$$

$$I_{bat} = I_{dc} + \hat{I}_m \cdot \sin(2\pi\omega_m t) \tag{E.34}$$

A modified modulation index $M'$ is defined with a range depending on the maximum current $I_{bal,max}$ and the additionally applied constant current $I_{dc}$ (equation E.35). It takes into account the limits of the amplitude of the sinusoidal measurement current depending on these two current values.

$$M'_{max} = \begin{cases} \frac{2I_{dc}}{I_{bal,max}} & 0 < I_{dc} \leq \frac{I_{bal,max}}{2} \\ 1 - \frac{2I_{dc}}{I_{bal,max}} & \frac{I_{bal,max}}{2} < I_{dc} < I_{bal,max} \end{cases} \tag{E.35}$$

The second line with $\frac{I_{bal,max}}{2} < I_{dc} < I_{bal,max}$ of equation E.35 discharges the battery more than necessary. Since the goal is an EIS measurement and not balancing the cells, this case is not considered and only the first case for $I_{dc} \leq \frac{I_{bal,max}}{2}$ is used for further calculations.

Figure E.2.2 shows that the sawtooth carrier signal $x(t)$ is no longer symmetrical to zero. The lower bound for the integration over $x(t)$ in integral E.5 is no longer $-\pi$ but the larger, the smaller the constant current $I_{dc}$ is (see equation E.36).

$$x_{low} = -2\frac{I_{dc}R_{bal}}{V_{bat}}\pi \tag{E.36}$$

## Derivation of the Harmonic Components

Equation E.37 shows a similar structure as the Double Fourier Integral in appendix E.2. The solution of the integral yields the same results with $V_{dc}$ replaced with $\frac{V_{bat}}{R_{bal}}$ and $V_{bat}$ replaced with $I_{dc}$. As a proof the calculation is done for the case of $m = 0$ and $n = 0$.

$$C_{mn} = \frac{1}{2\pi^2}\int_{-\pi}^{\pi}\int_{-2\frac{I_{dc}R_{bal}}{V_{bat}}\pi}^{\pi M'\cos y} I_{bal}\ e^{j\left(\left[m+n\frac{\omega_m}{\omega_c}\right]x+ny\right)}\ \mathrm{d}x\ \mathrm{d}y \tag{E.37}$$

For $m = n = 0$ (DC offset):

$$C_{00} = \frac{V_{bat}}{R_{bal}} \frac{1}{2\pi^2} \int_{-\pi}^{\pi} \left( \pi M' \cos y + 2 \frac{I_{dc} R_{bal}}{V_{bat}} \pi \right) \, \mathrm{d}y \tag{E.38}$$

$$= \frac{V_{bat}}{R_{bal}} \frac{1}{2\pi^2} \left( \underbrace{\int_{-\pi}^{\pi} \pi M' \cos y \, \mathrm{d}y}_{0} + \underbrace{\int_{-\pi}^{\pi} 2 \frac{I_{dc} R_{bal}}{V_{bat}} \pi \, \mathrm{d}y}_{4\pi^2 \frac{I_{dc} R_{bal}}{V_{bat}}} \right) \tag{E.39}$$

$$= \frac{V_{bat}}{R_{bal}} \frac{1}{2\pi^2} \, 4\pi^2 \frac{I_{dc} R_{bal}}{V_{bat}} \tag{E.40}$$

$$= 2 I_{dc} \tag{E.41}$$

## Result

$$\begin{aligned} i_{bal}(t) = {} & \frac{C_{00}}{2} \\ & + \sum_{n=1}^{2} C_{0n} \; e^{jn(\omega_m t + \theta_m)} \\ & + \sum_{m=1}^{\infty} C_{m0} \; e^{jm(\omega_c t + \theta_c)} \\ & + \sum_{m=1}^{\infty} \sum_{\substack{n=-\infty \\ (n \neq 0)}}^{\infty} C_{mn} \; e^{jn(\omega_m t + \theta_m) + jm(\omega_c t + \theta_c)} \end{aligned} \tag{E.42}$$

$$C_{00} = 2 I_{dc} \tag{E.43}$$

$$C_{01} = \frac{V_{bat}}{R_{bal}} \frac{1}{\left[\frac{\omega_m}{\omega_c}\right] \pi} \mathcal{J}_1 \left( \frac{\omega_m}{\omega_c} \pi M' \right) \tag{E.44}$$

$$C_{0n} = \frac{V_{bat}}{R_{bal}} \frac{1}{\left[n \frac{\omega_m}{\omega_c}\right] \pi} \mathcal{J}_n \left( n \frac{\omega_m}{\omega_c} \pi M' \right) \cdot \left[ \sin \left( n \frac{\pi}{2} \right) - j \cos \left( n \frac{\pi}{2} \right) \right] \tag{E.45}$$

$$C_{m0} = \frac{V_{bat}}{R_{bal}} \frac{1}{m\pi} \cdot \sin \left( 2m \frac{I_{dc}}{I_{bal}} \pi \right) + j \frac{V_{bat}}{R_{bal}} \frac{1}{m\pi} \left( \cos \left( 2m \frac{I_{dc}}{I_{bal}} \pi \right) - \mathcal{J}_0 \left( m \pi M' \right) \right) \tag{E.46}$$

$$C_{mn} = \frac{V_{bat}}{R_{bal}} \frac{1}{\pi \left[ m + n \frac{\omega_m}{\omega_c} \right]} \mathcal{J}_n \left( \pi M' \left[ m + n \frac{\omega_m}{\omega_c} \right] \right) \left[ \sin \left( n \frac{\pi}{2} \right) - j \cos \left( n \frac{\pi}{2} \right) \right] \tag{E.47}$$

## Verification

| | $THD$ | $C_{02}$ | $C_{10}$ | $C_{1_{-1}}$ | $C_{1_{+1}}$ | $C_{20}$ | $C_{2_{-1}}$ | $C_{2_{+1}}$ |
|---|---|---|---|---|---|---|---|---|
| DFS theory | 12.8698 | 0.0098 | 10.8922 | 0.9892 | 0.9862 | 5.2503 | 0.9544 | 0.9544 |
| sim and DFT | 12.8918 | 0.0098 | 10.9172 | 0.9893 | 0.9862 | 5.2474 | 0.9546 | 0.9546 |
| difference | 0.0220 | 0.0000 | 0.0250 | 0.0000 | 0.0000 | 0.0029 | 0.0001 | 0.0001 |

Table E.3: Numerical values to figure E.3.3.

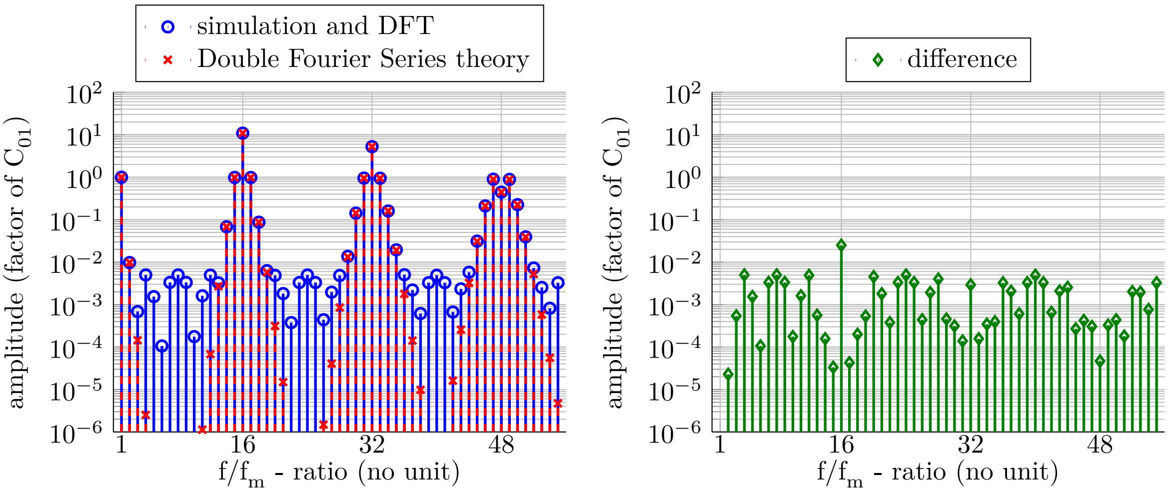

(a) Comparison.

(b) Difference.

Figure E.3.3: Harmonics of the Balancing Unit Topology determined with the Double Fourier Integral theory and a simulation with subsequent DFT.

## E.4 DC Supply Topology

When a battery is used at the input of a DC/DC-converter like the Half-Bridge-converter shown in figure E.4.1, the current of the battery is not constant but chopped into slices by the switches of the converter. During the positive half-periods of the controlled sinusoidal current, current is drawn from the battery during the ON-time of the switch S1 and freewheels over the diode of S2 during the OFF-time of S1. During the negative half-periods, the current in the inductance $L_f$ is increased during the ON-time of S2. The inductance $L_f$ continues the current during the OFF-time of S2 and pushes current into the battery over the diode of S1. Figure E.4.2 shows the current waveforms in case the current through $L_f$ is controlled to be sinusoidal.

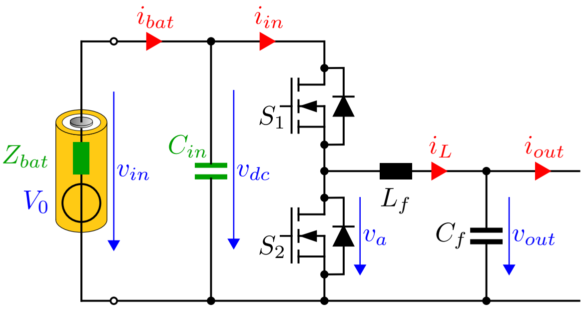

Figure E.4.1: Battery DC Supply Topology.

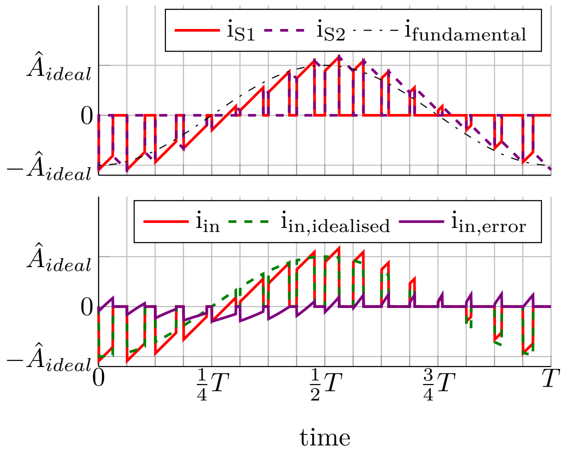

Figure E.4.2: Generated voltage and current of the Battery DC Supply Topology (synthetic data).

## Preconditions and Definitions

For the theoretical calculation of the current harmonics, the current is assumed to be sinusoidal and chopped into slices by the switches of the DC/DC-converter ($i_{in,idealised}$). This neglects the current ripple on top of the sinusoidal waveform $i_{in,error}$ which is sawtooth-like shaped with changing amplitudes shown in figure E.4.2.

The Double Fourier Integral E.1 describes how the input voltage $V_{dc}$ is switched to the output by the modulation process. In the case of a voltage source converter, a constant and stiff DC-voltage is assumed. The inductance of the DC/DC-converter creates a current source converter for the battery at the input. For calculating the current on the input of the DC/DC-converter, the current could be considered constant if a constant current $i_{out}$ would be controlled at the output of the converter. But for an EIS measurement, a sinusoidal current has to be controlled on the output of the converter according to equation E.48.

$$A_{sin}(y) \quad = \quad \frac{M \cdot V_{dc}}{|Z_{load}|} \cdot cos(y + \varphi_{load}) = A_A \cdot cos(y + \phi_{load}) \tag{E.48}$$

Therefore, in the Double Fourier Integral E.1, $V_{dc}$ is replaced by the controlled sinusoidal current through the inductance $L_f$:

$$C_{mn} = A_{mn} + jB_{mn} = \frac{1}{2\pi^2} \int_{-\pi}^{\pi} \int_{-\pi}^{\pi M \cos(y)} A_A \cdot \cos(y) \cdot e^{j(mx+ny)} \, \mathrm{d}x \, \mathrm{d}y \tag{E.49}$$

For equation E.49, the equation for a continuous control signal was used instead of a discrete regular trailing edge pulse width modulated control signal. The angle $\phi_{load}$ is set to 0 since the integration is performed over the full period.

## Lemmas for Solving the Double Fourier Integral

From [97]:

$$\begin{aligned} \cos(x) \cdot \cos(z) &= \cos(x + z) + \sin(x) \cdot \sin(z) \\ \sin(x) \cdot \sin(nx) &= -\frac{1}{2} \left( \cos[(n + 1)x] - \cos[(n - 1)x] \right) \qquad \text{(E.50)} \\ \cos(y) \cdot \cos(ny) &= \cos[(n + 1)y] - \frac{1}{2} \cos[(n + 1)y] + \frac{1}{2} \cos[(n - 1)y] \\ &= \frac{1}{2} \cos[(n + 1)y] + \frac{1}{2} \cos[(n - 1)y] \qquad \text{(E.51)} \end{aligned}$$

$$\begin{aligned}
\sin(x)\cdot\cos(z) &= \sin(x+z) - sin(z)\cdot\cos(x) \\
\sin(x)\cdot\cos(nx) &= \frac{1}{2}\left(\sin[(n+1)x] - \sin[(n-1)x]\right) \qquad \text{(E.52)} \\
\sin(y)\cdot\cos(ny) &= \sin[(n+1)y] - \frac{1}{2}\sin[(n+1)y] - \frac{1}{2}\sin[(n-1)y] \\
&= \frac{1}{2}\sin[(n+1)y] - \frac{1}{2}\sin[(n-1)y] \qquad \text{(E.53)}
\end{aligned}$$

$$\begin{aligned}
\cos(y)e^{jy} &= \cos^2(y) + j\cos(y)\cdot\sin(y) \\
\cos^2(y) &= \frac{1}{2} + \frac{1}{2}\cdot\cos(2y) \\
\cos(y)\cdot\sin(y) &= \frac{1}{2}\cdot\sin(2y) \\
\cos(y)e^{jy} &= \frac{1}{2} + \frac{1}{2}\cdot\cos(2y) + j\frac{1}{2}\cdot\sin(2y) \\
\cos(y)e^{jy} &= \frac{1}{2} + \frac{1}{2}\cdot e^{j2y} \qquad \text{(E.54)}
\end{aligned}$$

## Derivation of the Harmonic Components

The indexes m and n of equation E.49 are set to 0 in turns to evaluate the different harmonic components.

<u>For $m = 0$, $n = 0$</u> (DC offset):

$$\begin{aligned}
C_{00} &= \frac{A_A}{2\pi^2}\int_{-\pi}^{\pi}\int_{-\pi}^{\pi M\cos(y)}\cos(y)\,\mathrm{d}x\,\mathrm{d}y \\
C_{00} &= \frac{A_A}{2\pi^2}\int_{-\pi}^{\pi}(\pi M\cos(y)+\pi)\cdot\cos(y)\,\mathrm{d}y \\
C_{00} &= \frac{A_A}{2\pi^2}\left[\pi M\cdot\int_{-\pi}^{\pi}\cos^2(y)\,\mathrm{d}y + \pi\int_{-\pi}^{\pi}\cos(y)\ \mathrm{d}y\right]
\end{aligned}$$

With lemma C.5:

$$\begin{aligned}
C_{00} &= \frac{A_A}{2\pi^2}\left[\pi M\cdot\underbrace{\left[\frac{1}{2}+\frac{1}{4}\cdot\sin(2y)\right]_{-\pi}^{\pi}}_{=0} + \pi\cdot\underbrace{[\sin(y)]_{-\pi}^{\pi}}_{=\pi}\right] \\
C_{00} &= \frac{A_A}{2}\cdot M \qquad \text{(E.55)}
\end{aligned}$$

For $m = 0$, $n > 0$ (fundamental and baseband harmonics):

$$
\begin{aligned}
C_{0n} &= \frac{A_A}{2\pi^2} \int_{-\pi}^{\pi} \int_{-\pi}^{\pi M \cos(y)} \cos(y) \cdot e^{jny} \;\mathrm{d}x \;\mathrm{d}y \\
C_{0n} &= \frac{A_A}{2\pi^2} \int_{-\pi}^{\pi} (\pi M \cos(y) + \pi) \cdot \cos(y) \cdot e^{jny} \;\mathrm{d}y \\
C_{0n} &= \frac{A_A}{2\pi^2} \int_{-\pi}^{\pi} \big(\pi M \cos^2(y) + \pi \cos(y)\big) \cdot e^{jny} \;\mathrm{d}y
\end{aligned}
$$

With lemma C.5:

$$
C_{0n} = \frac{A_A}{2\pi^2} \int_{-\pi}^{\pi} \left( \frac{M\pi}{2} + \frac{M\pi}{2} \cdot cos(2y) + \pi cos(y) \right) \cdot e^{jny} \;\mathrm{d}y
$$

$$
\begin{aligned}
C_{0n} = \frac{A_A}{2\pi^2} \left[ \frac{M\pi}{2} \underbrace{\left( \frac{e^{jn\pi} - e^{-jn\pi}}{jn} ) \right)}_{=0 \text{ for } n \neq 0} \right] &+ \frac{A_A}{2\pi^2} \int_{-\pi}^{\pi} \frac{M\pi}{2} \left[ \underbrace{\cos(2y)\cos(ny) + j\cos(2y)\sin(ny)}_{=\pi \text{ for } n=2} \right] \;\mathrm{d}y \\
&+ \frac{A_A}{2\pi^2} \int_{-\pi}^{\pi} \pi \left[ \underbrace{\cos(y)\cos(ny) + j\cos(y)\sin(ny)}_{=\pi \text{ for } n=1} \right] \;\mathrm{d}y \qquad \text{(E.56)}
\end{aligned}
$$

The case $n = 1$ is solved by integrating the second line of equation E.56:

$$
\begin{aligned}
\int_{-\pi}^{\pi} \cos(y)\cos(y)\,\mathrm{d}y &= \int_{-\pi}^{\pi} \frac{1}{2} + \frac{1}{2}\cos(2y) \;\mathrm{d}y \\
&= \left[ \frac{1}{2}y + \frac{1}{4}\sin(2y) \right]_{-\pi}^{\pi} \\
&= \left( \frac{\pi}{2} + 0 + \frac{\pi}{2} - (-0) \right) \\
&= \pi \\
\int_{-\pi}^{\pi} \cos(y)\sin(y)\,\mathrm{d}y &= \int_{-\pi}^{\pi} \frac{1}{2}\sin(2y) \;\mathrm{d}y \\
&= \left[ -\frac{1}{4}\sin(2y) \right]_{-\pi}^{\pi} \\
&= \left( \frac{-1}{4} - \frac{-1}{4} \right) = \\
&= 0
\end{aligned}
$$

$$
C_{01} = \frac{A_A}{2\pi^2} \cdot \pi^2 = \frac{A_A}{2} \qquad \text{(E.57)}
$$

The case $n = 2$ is solved in the same way as the case $n = 1$ by integrating the first line of equation E.56:

$$
C_{02} = \frac{A_A}{2\pi^2} \cdot \frac{M\pi^2}{2} = \frac{A_A}{4} \cdot M \qquad \text{(E.58)}
$$

For the $n > 2$ equation E.56 becomes 0, which can be shown by using the lemmas E.51 and E.53:

$$\begin{aligned}
\int_{-\pi}^{\pi} \cos(y)\cos(ny)\ \mathrm{d}y &= \int_{-\pi}^{\pi} \frac{1}{2}\cos((n+1)y) + \frac{1}{2}\cos((n-1)y)\ \mathrm{d}y \\
&= \frac{1}{2(n+1)} \underbrace{[\sin((n+1)y)]_{-\pi}^{\pi}}_{=0} + \frac{1}{2(n-1)} \underbrace{[\sin((n-1)y)]_{-\pi}^{\pi}}_{=0} \\
&= 0 \\
\int_{-\pi}^{\pi} \cos(y)\sin(ny)\ \mathrm{d}y &= \int_{-\pi}^{\pi} \frac{1}{2}\sin((n+1)y) + \frac{1}{2}\sin((n-1)y)\ \mathrm{d}y \\
&= \frac{-1}{2(n+1)} \underbrace{[\cos((n+1)y)]_{-\pi}^{\pi}}_{=0} + \frac{-1}{2(n-1)} \underbrace{[\cos((n-1)y)]_{-\pi}^{\pi}}_{=0} \\
&= 0
\end{aligned}$$

For $m > 0,\ n = 0$ (carrier frequency and its harmonics):

$$\begin{aligned}
C_{m0} &= \frac{A_A}{2\pi^2} \int_{-\pi}^{\pi} \int_{-\pi}^{\pi M\cos(y)} \cos(y) \cdot e^{jmx}\, \mathrm{d}x\, \mathrm{d}y \\
C_{m0} &= \frac{A_A}{2\pi^2} \frac{1}{jm} \underbrace{\int_{-\pi}^{\pi} e^{jm\pi M\cos(y)} \cdot \cos(y)\, \mathrm{d}y}_{2\pi j \mathcal{J}_1(m\pi M) \text{ with C.16}} - e^{-jm\pi} \underbrace{\int_{-\pi}^{\pi} cos(y)\, \mathrm{d}y}_{=0} \\
C_{m0} &= \frac{A_A}{2\pi^2} \frac{1}{jm} 2\pi j \mathcal{J}_1(m\pi M) \\
C_{m0} &= \frac{A_A}{m\pi} \mathcal{J}_1(m\pi M) \qquad \text{(E.59)}
\end{aligned}$$

For $m > 0,\ n \neq 0$ (sidebands of carrier frequency harmonics):

$$\begin{aligned}
C_{mn} &= \frac{A_A}{2\pi^2} \int_{-\pi}^{\pi} \int_{-\pi}^{\pi M\cos(y)} cos(y) \cdot e^{j(mx+ny)}\ \mathrm{d}x\ \mathrm{d}y \\
C_{mn} &= \frac{A_A}{2\pi^2} \frac{1}{jm} \int_{-\pi}^{\pi} \cos(y) e^{jny} \left( e^{jm\pi M cos(y)} - e^{-jm\pi} \right)\ \mathrm{d}y \\
C_{mn} &= \frac{A_A}{2\pi^2} \frac{1}{jm} \int_{-\pi}^{\pi} \big( \cos(y)\cos(ny) + j\cos(y)\sin(ny) \big) \cdot \left( e^{jm\pi M\cos(y)} - e^{-jm\pi} \right)\ \mathrm{d}y \qquad \text{(E.60)}
\end{aligned}$$

Lemmas E.50 and E.52 simplify the first part of this integral:

$$\begin{aligned}
&cos(y)cos(ny) + jcos(y)sin(ny) \\
&\qquad = \frac{1}{2}\left(\cos[(n+1)x] + j\sin[(n+1)y]\right) + \frac{1}{2}\left(\cos[(n-1)y] + j\sin[(n-1)y]\right) \\
&\qquad = \frac{1}{2} e^{j(n+1)y} + \frac{1}{2} e^{j(n-1)y} \qquad \text{(E.61)}
\end{aligned}$$

With E.61 the integral E.60 is solved to:

$$\begin{aligned}
C_{mn} = &\frac{A_A}{2\pi^2}\frac{1}{jm}\int_{-\pi}^{\pi}\frac{1}{2}e^{j(n+1)y}e^{jm\pi M\cos(y)}\,\mathrm{d}y\\
&+\frac{A_A}{2\pi^2}\frac{1}{jm}\int_{-\pi}^{\pi}\frac{1}{2}e^{j(n-1)y}e^{jm\pi M\cos(y)}\,\mathrm{d}y\\
&+\frac{A_A}{2\pi^2}\frac{1}{jm}\int_{-\pi}^{\pi}-\frac{1}{2}e^{-jm\pi}e^{j(n+1)y}\,\mathrm{d}y\\
&+\frac{A_A}{2\pi^2}\frac{1}{jm}\int_{-\pi}^{\pi}-\frac{1}{2}e^{-jm\pi}e^{j(n-1)y}\,\mathrm{d}y
\end{aligned}$$

Lemma C.18 solves the first two lines

$$\begin{aligned}
C_{mn} = &\frac{A_A}{2\pi^2}\frac{1}{j2m}\left[2\pi j^{n+1}\mathcal{J}_{n+1}(m\pi M)\right]\\
&+\frac{A_A}{2\pi^2}\frac{1}{j2m}2\pi j^{n-1}\mathcal{J}_{n-1}(m\pi M)\\
&-\frac{A_A}{2\pi^2}\frac{1}{j2m}e^{-jm\pi}\underbrace{\left[\frac{e^{j(n+1)\pi}-e^{-j(n+1)\pi}}{j(n+1)}\right]}_{=0\text{ for }n\neq-1}\\
&-\frac{A_A}{2\pi^2}\frac{1}{j2m}e^{-jm\pi}\underbrace{\left[\frac{e^{j(n-1)\pi}-e^{-j(n-1)\pi}}{j(n-1)}\right]}_{=0\text{ for }n\neq1}
\end{aligned}$$

$$C_{mn} = -j\frac{A_A}{2\pi m}\left[j^{n+1}\mathcal{J}_{n+1}(m\pi M)+j^{n-1}\mathcal{J}_{n-1}(m\pi M)\right] \qquad \text{for } n\neq-1,\, n\neq1 \tag{E.62}$$

With lemma E.54, equation E.60 can be solved for $n=+1$ and $n=-1$.
For $m>0$, $n=+1$ (positive first sideband of carrier frequency harmonics):

$$\begin{aligned}
C_{m+1} = &\frac{A_A}{2\pi^2}\frac{1}{jm}\underbrace{\int_{-\pi}^{\pi}\frac{1}{2}\cdot e^{jm\pi M\cos(y)}\,\mathrm{d}y}_{=\pi\mathcal{J}_0(m\pi M)\text{ with C.19}}+\frac{A_A}{2\pi^2}\frac{1}{jm}\underbrace{\int_{-\pi}^{\pi}\frac{1}{2}e^{j2y}\cdot e^{jm\pi M\cos(y)}\,\mathrm{d}y}_{=-\pi\mathcal{J}_2(m\pi M)\text{ with C.18}}\\
&-\frac{A_A}{2\pi^2}\frac{1}{jm}\underbrace{\int_{-\pi}^{\pi}\frac{1}{2}\cdot e^{-jm\pi}\,\mathrm{d}y}_{=\frac{1}{2}e^{-jm\pi}(\pi-(-\pi))}-\frac{A_A}{2\pi^2}\frac{1}{jm}\underbrace{\int_{-\pi}^{\pi}\frac{1}{2}e^{j2y}\cdot e^{-jm\pi}\,\mathrm{d}y}_{=\frac{1}{2}e^{-jm\pi}\frac{e^{j2\pi}-e^{-j2\pi}}{j2}=0}
\end{aligned} \tag{E.63}$$

$$C_{m+1} = \frac{A_A}{2\pi m}\left[\sin(m\pi)-j\left(\mathcal{J}_0(m\pi M)-\mathcal{J}_2(m\pi M)-\cos(m\pi)\right)\right] \tag{E.64}$$

For $m > 0$, $n = -1$ (negative first sideband of carrier frequency harmonics):

$$\begin{aligned} C_{m-1} = {} & \frac{A_A}{2\pi^2}\frac{1}{jm}\underbrace{\int_{-\pi}^{\pi}\frac{1}{2}\cdot e^{jm\pi M\cos(y)}\,\mathrm{d}y}_{=\pi\mathcal{J}_0(m\pi M)\text{ with C.19}} + \frac{A_A}{2\pi^2}\frac{1}{jm}\underbrace{\int_{-\pi}^{\pi}\frac{1}{2}e^{-j2y}\cdot e^{jm\pi M\cos(y)}\,\mathrm{d}y}_{=-\pi\mathcal{J}_2(m\pi M)\text{ with C.18}} \\ & - \frac{A_A}{2\pi^2}\frac{1}{jm}\underbrace{\int_{-\pi}^{\pi}\frac{1}{2}\cdot e^{-jm\pi}\,\mathrm{d}y}_{=\frac{1}{2}e^{-jm\pi}(\pi-(-\pi))} - \frac{A_A}{2\pi^2}\frac{1}{jm}\underbrace{\int_{-\pi}^{\pi}\frac{1}{2}e^{-j2y}\cdot e^{-jm\pi}\,\mathrm{d}y}_{=\frac{1}{2}e^{-jm\pi}\frac{e^{j2\pi}-e^{-j2\pi}}{-j2}=0} \end{aligned} \tag{E.65}$$

$$C_{m-1} = \frac{A_A}{2\pi m}\left[\sin(m\pi) - j\left(\mathcal{J}_0(m\pi M) - \mathcal{J}_2(m\pi M) - \cos(m\pi)\right)\right] \tag{E.66}$$

## Result

$$\begin{aligned} i_{in}(t) = {} & \frac{C_{00}}{2} \\ & + \sum_{n=1}^{2} C_{0n}\; e^{jn(\omega_m t+\theta_m)} \\ & + \sum_{m=1}^{\infty} C_{m0}\; e^{jm(\omega_c t+\theta_c)} \\ & + \sum_{m=1}^{\infty}\sum_{\substack{n=-\infty \\ (n\neq 0)}}^{\infty} C_{mn}\; e^{jn(\omega_m t+\theta_m)+jm(\omega_c t+\theta_c)} \end{aligned} \tag{E.67}$$

$$C_{00} = \frac{A_A}{2}\cdot M \tag{E.68}$$

$$C_{01} = \frac{A_A}{2} \tag{E.69}$$

$$C_{02} = \frac{A_A}{4}\cdot M \tag{E.70}$$

$$C_{m0} = \frac{A_A}{m\pi}\mathcal{J}_1(m\pi M) \tag{E.71}$$

$$C_{m+1/-1} = \frac{A_A}{2\pi m}\left[\sin(m\pi) - j\left(\mathcal{J}_0(m\pi M) - \mathcal{J}_2(m\pi M) - \cos(m\pi)\right)\right] \tag{E.72}$$

$$C_{mn} = -j\frac{A_A}{2\pi m}\left[j^{n+1}\mathcal{J}_{n+1}(m\pi M) + j^{n-1}\mathcal{J}_{n-1}(m\pi M)\right] \qquad \text{for } n\neq -1,\, n\neq 1 \tag{E.73}$$

## Verification

| | $THD$ | $C_{02}$ | $C_{10}$ | $C_{1_{-1}}$ | $C_{1_{+1}}$ | $C_{20}$ | $C_{2_{-1}}$ | $C_{2_{+1}}$ |
|---|---|---|---|---|---|---|---|---|
| DFS theory | 1.3912 | 0.0500 | 0.0988 | 0.6249 | 0.6249 | 0.0951 | 0.0229 | 0.0229 |
| sim and DFT | 1.3925 | 0.0504 | 0.0193 | 0.6312 | 0.6320 | 0.0185 | 0.0090 | 0.0090 |
| difference | 0.0013 | 0.0004 | 0.0795 | 0.0063 | 0.0071 | 0.0766 | 0.0139 | 0.0139 |

Table E.4: Numerical values to figure E.4.3.

The difference of the carrier frequency amplitude, their harmonics and sidebands can be attributed the the additional sawtooth-like signal, which was neglected at the beginning. The larger the ratio $\frac{\omega_m}{\omega_c}$ is, the larger the influence of this additional signal becomes.

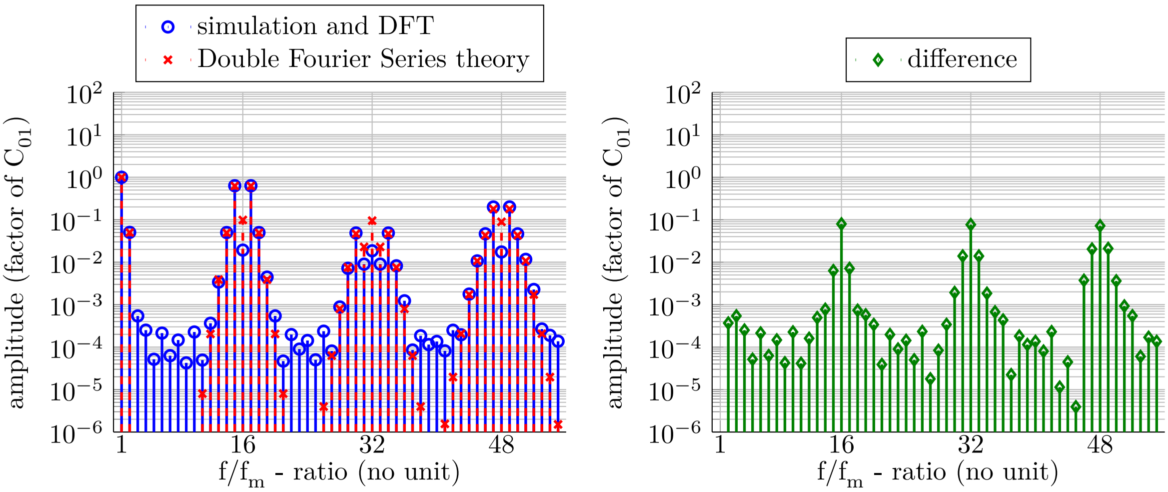

(a) Comparison.

(b) Difference.

Figure E.4.3: Harmonics of the DC Supply Topology determined by the Double Fourier Integral theory and a simulation with subsequent DFT.